Analysis and Optimization of SWIPT-Enabled RIS-Assisted UAV and V2X Communication Systems

Ph.D. Thesis

by

Manojkumar Balaji Kokare
Roll No. 2201102016



Department of Electrical Engineering
INDIAN INSTITUTE OF TECHNOLOGY INDORE

November 2026

Analysis and Optimization of SWIPT-Enabled RIS-Assisted UAV and V2X Communication Systems

A Thesis

Submitted in partial fulfillment of the
requirements for the award of the degrees
of
Doctor of Philosophy

by

Manojkumar Balaji Kokare
Roll No. 2201102016



Department of Electrical Engineering
INDIAN INSTITUTE OF TECHNOLOGY INDORE
November 2026

INDIAN INSTITUTE OF TECHNOLOGY INDORE

CANDIDATE'S DECLARATION

I hereby certify that the work which is being presented in the Thesis entitled **Analysis and Optimization of SWIPT-Enabled RIS-Assisted UAV and V2X Communication Systems** in the partial fulfillment of the requirements for the award of the degree of **Doctor of Philosophy** and submitted in the **Department of Electrical Engineering**, Indian Institute of Technology Indore, is an authentic record of my own work carried out during the time period from **July 2022** to **November 2026** under the supervision of **Dr. Sumit Gautam** and **Dr. Swaminathan R.** .

The matter presented in this Thesis has not been submitted by me for the award of any other degree of this or any other institute.

17/11/2026

Signature of the student with date

(Manojkumar Balaji Kokare)

This is to certify that the above statement made by the candidate is correct to the best of my/our knowledge.

17-Nov-2026

Signature of Thesis Supervisor with date

(Dr. Sumit Gautam)

17/11/26

Signature of Thesis Supervisor with date

(Dr. Swaminathan R.)

Manojkumar Balaji Kokare has successfully given his Ph.D. Oral Examination held on *Date of PhD Oral Examination*.

17-Nov-2026

Signature of Thesis Supervisor with date

(Dr. Sumit Gautam)

17/11/26

Signature of Thesis Supervisor with date

(Dr. Swaminathan R.)

ACKNOWLEDGEMENTS

I would like to express my deepest gratitude to all those who have supported and encouraged me throughout my Ph.D. journey.

First and foremost, I am sincerely thankful to my supervisors, Dr. Sumit Gautam and Dr. Swaminathan R., whose invaluable guidance, continuous encouragement, and unwavering support have been a constant source of inspiration. Their insightful advice and constructive feedback have shaped the direction of this research and contributed significantly to its completion. It has been a privilege to work under their respective supervisions. I am also grateful to Prof. Amod C. Umarikar and Dr. Nagendra Kumar, members of my research progress committee, for their thoughtful suggestions, critical evaluations, and motivating discussions. Their insightful comments have greatly enhanced the quality and depth of this research work.

My sincere acknowledgment to Prof. Suhas Joshi, Director, Indian Institute of Technology Indore, for providing me the opportunity to explore my research capabilities at Indian Institute of Technology Indore. I would like to thank the Head of the Department, Electrical Engineering, for kind support. I am also indebted to the administrative and technical staff at the Indian Institute of Technology Indore, India, whose support has been invaluable in overcoming many logistical and technical challenges during my research.

I would like to express my heartfelt thanks to my colleagues and friends at IIT Indore for fostering a friendly and supportive environment that greatly contributed to my learning and personal growth. I am especially grateful for the invaluable company and encouragement of Dr. Narendra Vishwakarma, Dr. Deepshikha Singh, Dr. Neha Sharma, Mr. Nayim Ahmed, Mr. Prashant Sharma, Mr. Pawan Soni, Ms. Shilpa Vishwakarma, and Mr. Sudhir Behera.

I am profoundly grateful to my family for their unconditional support, encouragement, and unwavering belief in me throughout my academic journey. I extend my heartfelt appreciation to my parents: Mr. Balaji Kokare and Mrs. Vandana Kokare, whose constant encouragement and blessings have been a continuous source of strength and motivation. I am also deeply thankful to my grandmother: Mrs. Saraswatibai Kokare, for her guidance and support. It is with sincere gratitude that I acknowledge the unwavering support of my

sister: Dr. Madhavi Kokare, and my brother: Mr. Mohitkumar Kokare, whose support, patience, understanding, and encouragement sustained me through the many challenges and milestones along the way. Their constant presence has been a source of strength and reassurance. I also gratefully acknowledge my cousins for their help and support, especially during times when I could not be physically present at home during emergencies. Finally, I fondly remember my late paternal grandfather: Mr. Topaji Kokare, my late maternal grandfather: Mr. Nivaratirao Dhage, and my late grandmother: Mrs. Sushilabai Dhage exceptional individuals whose intellect, wisdom, and passion for learning continue to inspire and influence me in both my personal and academic life.

I would like to thank all those who have contributed to this Thesis, directly or indirectly. Your support and contributions have been instrumental in the completion of my Ph.D. research work.

Manojkumar Balaji Kokare

Dedicated

to

My Parents

ABSTRACT

The evolution of Intelligent Transportation Systems (ITS) is transforming vehicular networks into highly connected and adaptive ecosystems capable of supporting reliable communication in dynamic environments. However, in emergency situations, remote regions, and infrastructure-deficient scenarios, conventional vehicular communication systems face severe challenges such as : frequent link failures, high mobility, signal blockage, and limited energy availability. To address these issues, the integration of Reconfigurable Intelligent Surfaces (RIS), Simultaneous Wireless Information and Power Transfer (SWIPT), and Uncrewed Aerial Vehicles (UAVs) has emerged as a promising solution for future wireless networks. RIS enhances signal propagation through intelligent environment reconfiguration, SWIPT enables simultaneous information transfer and Energy Harvesting (EH), while UAVs provide flexible and on-demand communication support. Motivated by these advantages, this Thesis develops unified RIS-assisted SWIPT-enabled UAV and vehicular communication frameworks to achieve reliable, energy-efficient, and high-capacity communication for next-generation ITS applications.

First, a multi-RIS-assisted Vehicle-to-Vehicle (V2V) communication system is investigated over independent and non-identically distributed double generalized Gamma (dGG) fading channels. Closed-form expressions for key performance metrics, including Outage Probability (OP), Average Symbol Error Rate (ASER), and Ergodic Capacity (EC), are derived to characterize system performance under severe fading conditions. An optimization framework based on Karush–Kuhn–Tucker (KKT) conditions is developed to maximize achievable data rate while minimizing transmit power. To further enhance computational efficiency, a Deep Neural Network (DNN)-based model is designed to predict system performance and optimal parameters using Monte-Carlo simulation data.

Next, a multi-RIS-assisted SWIPT-enabled Vehicle-to-Infrastructure (V2I) communication framework is analyzed under practical vehicular conditions, incorporating mobility through a Random Waypoint (RWP) model and imperfect Channel State Information (CSI). A Non-Linear Energy Harvesting (NL-EH) model with Power-Splitting (PS) is adopted to enable efficient simultaneous information decoding and EH. A joint optimization problem

is formulated to maximize both harvested energy and achievable rate, and is solved using iterative methods supported by closed-form solutions derived via KKT conditions and joint optimization techniques. A DNN-based approach is also employed to reduce computational complexity and facilitate real-time implementation.

Furthermore, an integrated relay-RIS-aided UAV communication framework with SWIPT capability is proposed for IoT scenarios. In this model, the UAV performs simultaneous relaying and intelligent signal reflection while harvesting energy to sustain its operation. Analytical expressions for OP, ASER, Outage Capacity (OC), and EC are derived over Nakagami-m fading channels and validated via Monte-Carlo simulations. Optimization problems are formulated to maximize achievable rate, stored energy at the UAV, and Energy Efficiency (EE) under Quality-of-Service (QoS) constraints, with solutions obtained using KKT conditions, Dinkelbach transform, and quadratic transform techniques.

Finally, a Full-Duplex (FD) UAV-assisted RIS-SWIPT framework is developed for Non-Terrestrial Networks (NTNs) under generalized $\alpha - \mu$ fading channels. The system incorporates both linear PS and NL hybrid Power–Time Splitting (PTS) EH models, while jointly optimizing RIS reflection coefficients, power allocation, and transmission parameters under QoS constraints. Closed-form expressions for OP and EC are derived and validated through simulations, and an efficient optimization algorithm is proposed to maximize system performance.

Overall, the proposed frameworks demonstrate significant improvements in reliability, spectral efficiency, EH capability, and coverage compared to conventional communication systems. The integration of optimization techniques with Machine Learning (ML) further enables scalable and real-time implementations, making the proposed solutions highly suitable for next-generation vehicular and aerial communication networks operating in complex and resource-constrained environments.

Keywords: Deep Neural Network (DNN), Energy Efficiency (EE), Energy Harvesting (EH), Intelligent Transportation Systems (ITS), Optimization, Performance Analysis, Reconfigurable Intelligent Surfaces (RIS), Relay networks, Simultaneous Wireless Information and Power Transfer (SWIPT), Uncrewed Aerial Vehicles (UAVs), Vehicle-to-Infrastructure (V2I) communication, Vehicle-to-Vehicle (V2V) communication.

LIST OF PUBLICATIONS

(A) Outcomes from Ph.D. Thesis Work

A1. In Refereed Journals

1. **M. B. Kokare**, Swaminathan R., and S. Gautam, "Performance analysis and optimization with deep learning assessment of multi-IRS-aided IoV network," *IEEE Internet of Things Journal*, vol. 12, no. 9, pp. 11581-11599, 2025.

2. **M. B. Kokare**, S. Gautam, and Swaminathan R., "Optimization for dynamic multi-RIS-assisted SWIPT-Enabled V2I networks: A deep learning approach", *Elsevier Vehicular Communications*, Volume 57, 2026.

3. **M. B. Kokare**, Swaminathan R., and S. Gautam, "Energy-efficient UAV communication via relay-RIS-aided SWIPT for disaster-resilient networks: Performance analysis and optimization", *Elsevier Internet of Things*, Volume 37, 2026.

4. **M. B. Kokare**, N. Sharma, Swaminathan R. and S. Gautam, "Performance analysis and optimization of full-duplex RIS-assisted SWIPT NTNs," submitted to *IEEE Journal on Miniaturization for Air and Space Systems*, 2026. **(Under Review-Major Revision Submitted)**

A2. In Refereed Conferences

1. **M. B. Kokare**, S. Gautam, Swaminathan R., N. Sharma, A. Kaushik, and S. Chatzinotas, "Optimizing SWIPT in multi-RIS aided V2I networks: A deep learning approach," in *proc. IEEE International Conference on Communications (ICC)*, Montreal, Canada, 2025, pp. 6167-6172.

2. **M. B. Kokare**, R. Mishra, N. Sharma, Swaminathan R., and S. Gautam, "Performance of integrated relay-RIS in UAV systems: A selection combining approach," in *proc. National Conference on Communications (NCC)*, New Delhi, India, 2025, pp. 1-6,

3. **M. B. Kokare**, S. Gautam, and Swaminathan R., "Enhancing SWIPT via IRS/RIS-assisted vehicular systems," in *proc. International Conference on Machine Learning, Image Processing, Network Security and Data Sciences (MIND)*, Goa, India, 2024.

4. **M. B. Kokare**, S. Gautam, and Swaminathan R., "On efficient resource allocation strategies for multi-RIS enhanced V2I SWIPT systems," in *proc. IEEE Wireless Communications and Networking Conference (WCNC)*, Dubai, 2024, pp. 1-6.

5. **M. B. Kokare**, Swaminathan R. and S. Gautam, "Performance of multiple IRS-enabled V2V communication over double generalized gamma fading channel," in *proc. International Conference on COMmunication Systems & NETworkS (COMSNETS)*, Bengaluru, India, 2024, pp. 913-919.

6. **M. B. Kokare**, N. Sharma, Swaminathan R., and S. Gautam, "RIS-integrated full-duplex UAV SWIPT relaying for next-generation non-terrestrial networks," in *proc. European Conference on Networks and Communications (EuCNC)*, Malaga, Spain, 2026.

7. **M. B. Kokare**, N. Sharma, Swaminathan R., and S. Gautam, "Practical RRC-based RIS-assisted full-duplex UAV SWIPT relaying for NTN," in *proc. IEEE International Symposium on Personal, Indoor and Mobile Radio Communications (PIMRC)*, Singapore, 2026, pp. 1-6.

8. **M. B. Kokare**, H. Parmale, Swaminathan R., and S. Gautam, "Mobility-aware performance analysis of RIS-assisted ISAC for V2X communications," submitted to *National Conference on Communications (NCC)*, Bengaluru, India, 2027.

A3. In Refereed Book Chapters

1. **M. B. Kokare**, P. Sharma;, Swaminathan R., V. Bhatia, S. Gautam, "Reinforcement learning and deep learning-assisted spectrum management for RIS-SWIPT-enabled 6G systems," in *Intelligent Spectrum Management: Towards 6G , IEEE*, 2025, pp.155-174.

2. **M. B. Kokare**, N. Sharma, Swaminathan R. and S. Gautam, "Integrated ISAC-RIS systems for next-generation connectivity enhancement", in *Integrated Sensing and Commu-*

nication for Sustainable Development Goals, 1st ed. Singapore: Springer, 2026.

3. **M. B. Kokare**, V. K. Malav, A. Sharma, Swaminathan R., S. Chatzinotas, and S. Gautam, "Performance Analysis of Semantic Communication Systems", in *Semantic Communications for Next-Generation Wireless Systems, IEEE*, 2026. **(Under Review)**

(B) Outcomes from Other than Ph.D. Thesis Work

B1. In Refereed Journals

1. N. Sharma, **M. B. Kokare**, Swaminathan R., A. Kaushik, S. Chatzinotas, B. Ottersten, and S. Gautam, "Energy efficient RIS-assisted SWIPT-IoT systems in smart agriculture," *IEEE Internet of Things Magazine*, 2026, doi: 10.1109/MIOT.2026.3676343.

B2. In Refereed Conferences

1. N. Sharma, **M. B. Kokare**, Swaminathan R., and S. Gautam, "Distributed RIS SWIPT-IoT systems: optimizing spectral efficiency and energy harvesting," in *proc. IEEE Wireless Communications and Networking Conference (WCNC)*, Milan, Italy, 2025, pp. 1-6.

2. N. Sharma, **M. B. Kokare**, Swaminathan R., and S. Gautam, "Maximizing weighted function in STAR-RIS aided SWIPT-IoT with discrete phase shifting," in *proc. IEEE Vehicular Technology Conference (VTC2025-Spring)*, Oslo, Norway, 2025, pp. 1-5.

3. S. Das, **M. B. Kokare**, P. Sharma, Swaminathan R., S. Gautam, and S. Ghosh, "On the joint impact of UAV orientation instability and phase errors in UAV-aided RIS systems," in *proc. International Conference on Signal Processing and Communications (SPCOM)*, Bengaluru, India, 2026, pp. 1-6.

4. H. Parmale, **M. B. Kokare**, and Swaminathan R., "Performance analysis of GBSM-based ISAC system for V2X communication," accepted to *International Conference on Advanced Networks and Telecommunications Systems (ANTS)*, Roorkee, India, 2026.

B3. In Refereed Book Chapters

1. S. Shukla, R. Gupta, S. Chavda, **M. B. Kokare**, N. Sharma, Swaminathan R., and S. Gautam, " AI/ML-driven Semantic Communication Systems", in *Semantic Communications for Next-Generation Wireless Systems, IEEE*, 2026. **(Under Review)**

Contents

ABSTRACT i

LIST OF PUBLICATIONS iii

LIST OF FIGURES xiv

LIST OF TABLES xix

LIST OF ABBREVIATIONS xxi

LIST OF SYMBOLS xxv

1 Introduction 1

1.1 Motivations 5

1.2 Contributions 7

1.3 Organization of the Thesis 11

2 Literature Review 15

2.1 Literature Review 15

2.1.1 Multi-RIS-assisted V2V Communication: Performance Analysis and Optimization Over Generalized Fading 16

2.1.2 Multi-RIS-assisted SWIPT-enabled V2I Communication with Mobility and Imperfect CSI 21

2.1.3 SWIPT-enabled Integrated Relay-RIS-aided UAV Communication . 29

2.1.4 Full-duplex SWIPT-enabled Relay–RIS UAV Communication for Non-Terrestrial Networks 34

2.2 Chapter Summary 37

3 Multi-RIS-assisted V2V Communication: Performance Analysis and Optimization Over Generalized Fading 39

3.1 Introduction 39

3.2 Organization of The Chapter 40

3.3 System and Channel Models 41

3.3.1 System Model 41

3.3.1.1 Exhaustive RIS Scheme 43

3.3.1.2 Opportunistic RIS Scheme 44

3.3.1.3 RIS Selection Strategy in ORS 44

3.3.2 Statistical Models for Mobility 45

3.3.3 Channel Model 47

3.3.3.1 Exhaustive RIS Scheme 48

3.3.3.2 Opportunistic RIS Scheme 49

3.3.3.3 PDF of Imperfect Channel Conditions 49

3.4 Performance Analysis 50

3.4.1 Exhaustive RIS Scheme 50

3.4.1.1 Outage Probability 50

3.4.1.2 Average Symbol Error Rate 51

3.4.1.3 Ergodic Capacity 52

3.4.2 Opportunistic RIS Scheme 53

3.4.2.1 Outage Probability 53

3.4.2.2 Average Symbol Error Rate 54

3.4.2.3 Ergodic Capacity 54

3.5 Optimization Outlook 55

3.5.1 Rate Maximization via Multi-RIS 55

3.5.2 Power Minimization via Multi-RIS 58

3.6 Deep Neural Network (DNN) Framework Design 59

3.6.1 Design Approach and Datasets Generation for DNN 60

3.6.2 Learning Model for DNN . . . 61
3.6.3 Real-Time Prediction . . . 62
3.6.4 Computational Complexity . . . 64
3.7 Numerical Results and Discussions . . . 65
3.7.1 ERS and ORS Comparison for Proposed Multi-RIS System . . . 67
3.7.2 DNN Results and Complexity Analysis for ORS . . . 70
3.8 Chapter Summary . . . 82

4 Multi-RIS-assisted SWIPT-enabled V2I Communication with Mobility and Imperfect CSI 85

4.1 Introduction . . . 85
4.1.1 Chapter Organization . . . 87
4.2 System and Channel Models . . . 87
4.2.1 Statistical Models for Mobility . . . 90
4.2.2 PDF of Imperfect Channel Conditions . . . 91
4.2.3 SWIPT Protocol and EH Model Considerations . . . 92
4.3 Problem Formulation and Proposed Solution . . . 94
4.4 DNN Based Optimal Solution Prediction . . . 100
4.4.1 DNN Architecture . . . 100
4.4.2 DNN Complexity Analysis . . . 102
4.5 Numerical Results and Discussions . . . 103
4.6 Chapter Summary . . . 111

5 SWIPT-enabled Integrated Relay-RIS-aided UAV Communication 113

5.1 Introduction . . . 113
5.1.1 Chapter Organization . . . 115
5.2 System Model . . . 116
5.3 Channel Model . . . 119
5.3.1 Relay-only mode . . . 119
5.3.2 RIS-only Mode . . . 122

5.3.2.1 Phase-Shift Design . . . 124
5.3.3 Integrated Relay-RIS Mode . . . 127
5.3.3.1 SC Scheme . . . 127
5.3.3.2 MRC Scheme . . . 128
5.4 Performance Analysis . . . 130
5.4.1 Outage Probability . . . 130
5.4.2 Average Symbol Error Rate . . . 131
5.4.3 Ergodic Capacity . . . 132
5.4.4 Outage Capacity . . . 133
5.5 Optimization Problem Formulation and Solutions . . . 133
5.5.1 Maximization of Rate at D . . . 134
5.5.2 Maximization of Stored Energy at UAV . . . 139
5.5.3 Energy Efficiency Maximization . . . 144
5.5.3.1 Dinkelbach Transformation . . . 145
5.5.3.2 Quadratic Transformation . . . 147
5.6 Numerical Results and Discussions . . . 148
5.7 Chapter Summary . . . 163

6 Full-duplex SWIPT-enabled Relay–RIS UAV Communication for Non-Terrestrial Networks 165

6.1 Introduction . . . 165
6.2 System and Channel Models . . . 166
6.2.1 UAV-assisted Relay transmission . . . 171
6.2.1.1 Linear Power Splitting-based EH . . . 171
6.2.1.2 Non-Linear Hybrid Power-Time Splitting-based EH . . . 174
6.2.2 UAV-assisted RIS transmission . . . 177
6.2.3 UAV-assisted Relay-RIS Transmission . . . 180
6.3 Performance Analysis . . . 181
6.3.1 Outage Probability . . . 181
6.3.2 Ergodic Capacity . . . 182

6.4 Optimization Problem Formulation 183
6.5 Numerical Results and Discussions 186
6.6 Chapter Summary 196

7 Conclusion and Future Directions **199**
7.1 Conclusion 199
7.2 Future Directions 202

A Cases of KKT Conditions **208**
A.1 Evaluation of Various Cases From KKT Conditions for Rate Maximization Problem 208
A.2 Evaluation of Various Cases From KKT Conditions for Power Minimization Problem 209

B Solution for Various Cases From KKT Conditions **210**
B.1 Evaluation of Various Cases From KKT Conditions for Unified Problem . . 210

C Closed-form Solution for Relay Link **212**
C.1 Approximate Closed-form Solution of R_1 and R_2 212
C.2 Closed-form Solution for Relay Link for $P1$ 214

List of Figures

3.1 A multi-RIS-aided V2V system model for ITS applications 42
3.2 DNN architecture. 60
3.3 Outage probability versus transmit power (dBm) for ERS and ORS schemes. 66
3.4 Average symbol error rate versus transmit power (dBm) for ERS and ORS schemes. 66
3.5 Ergodic capacity versus transmit power (dBm) for ERS and ORS schemes. . 68
3.6 Maximized rate (bits/sec/Hz) versus transmit power (dBm) for ERS and ORS schemes. 68
3.7 Minimum transmit power (dBm) versus rate threshold (bits/sec/Hz) for ERS and ORS schemes. 70
3.8 Outage probability versus transmit power (dBm) for different numbers of RIS elements and path-loss exponents. 70
3.9 Outage probability versus transmit power (dBm) for different CSI correlation coefficients. 71
3.10 Outage probability comparison for different numbers of RIS elements using gradient-based regression. 72
3.11 Outage probability versus transmit power (dBm) for different numbers of RISs. 73
3.12 Outage probability versus transmit power (dBm) for a V2V system with and without RIS. 73
3.13 Average symbol error rate versus transmit power (dBm) for different numbers of RIS elements. 74
3.14 Average symbol error rate versus transmit power (dBm) for different modulation schemes. 74

3.15 Average symbol error rate versus transmit power (dBm) for different numbers of RISs. 75
3.16 Average symbol error rate versus transmit power (dBm) for RIS, without RIS, and DF relay systems. 76
3.17 Ergodic capacity versus transmit power (dBm) for different numbers of RIS elements. 76
3.18 Ergodic capacity versus transmit power (dBm) for different numbers of RISs. 78
3.19 Ergodic capacity versus transmit power (dBm) for systems with and without RIS. 78
3.20 Maximized rate (bits/sec/Hz) versus transmit power (dBm) for different numbers of RIS elements. 79
3.21 Maximized rate (bits/sec/Hz) versus transmit power (dBm) for different numbers of RISs. 79
3.22 Minimum transmit power (dBm) versus rate threshold (bits/sec/Hz) for different numbers of RISs. 80

4.1 Multi-RIS-assisted SWIPT in a highway scenario with mobile D. 89
4.2 DNN design for optimal solution prediction in SWIPT network. 99
4.3 Convergence of harvested energy (J) and rate (bpcu) with iterations. 104
4.4 MSE vs. Epochs. 105
4.5 EH (J) versus transmit power P_t (W) for different values of L and N. 106
4.6 Achievable rate (bpcu) versus transmit power P_t (W) for different values of L and N. 106
4.7 EH (J) versus transmit power P_t (W) for different values of N and parameter a values. 107
4.8 Rate (bpcu) versus P_t (W) for various N and parameter a values. 107
4.9 EH (J) versus transmit power P_t (W) for different values of N and parameter Ω values. 109
4.10 Achievable rate (bpcu) versus transmit power P_t (W) for different values of N and parameter Ω values. 109

4.11 Achievable rate (bpcu) versus transmit power P_t (W) for different random waypoint (RWP) dimensions. 110
4.12 Achievable rate (bpcu) versus transmit power P_t (W) for perfect CSI and imperfect CSI (ICSI) under speed-dependent errors. 110

5.1 UAV-assisted integrated relay-RIS SWIPT system enabling reliable wireless connectivity in disaster recovery scenario. 117
5.2 OP versus average SNR (dB) for varying m and Ω values with $h = 100$ meters and comparison of integrated system with standalone systems. . . . 150
5.3 OP versus average SNR (dB) for varying UAV altitude (meters) with $m = 1$ and $\Omega = 1$. 150
5.4 ASER versus average SNR (dB) for varying m and Ω values with $h = 100$ meters and comparison of integrated system with standalone systems. . . . 152
5.5 ASER versus average SNR (dB) for various modulation schemes. 152
5.6 EC versus average SNR (dB) for varying m and Ω values with $h = 100$ meters and comparison of integrated system with standalone systems. . . . 154
5.7 EC versus average SNR (dB) for varying UAV altitude (meters) with $m = 1$ and $\Omega = 1$. 154
5.8 OC versus average SNR (dB) for varying m and Ω values with $h = 100$ meters and comparison of integrated system with standalone systems. . . . 156
5.9 OC versus average SNR (dB) for varying UAV altitude (meters) with $m = 1$ and $\Omega = 1$. 156
5.10 Convergence plot of rate (Algorithm 1), stored energy (Algorithm 3), EE by DT (Algorithm 5), and EE by QT (Algorithm 6). 157
5.11 R_c versus transmit power (dBW) for varying m, Ω, and h_u values. 158
5.12 R_c versus transmit power (dBW) comparison for integrated system with standalone systems. 158
5.13 S_e at UAV versus transmit power (dBW) for varying m, Ω, and h_u values. . 160
5.14 S_e at UAV versus transmit power (dBW). 160
5.15 EC versus average SNR (dB) for varying N values. 162

5.16 EE versus varying N values. 162

6.1 RIS-UAV-assisted FD SWIPT NTN communication system. 168

6.2 SWIPT-enabled simultaneous EH and ID via Linear PS protocol and NL hybrid PTS protocol in T time slot. 169

6.3 OP versus ζ for varying transmit power (dBW) values. 188

6.4 Harvested power and relay SNR versus maximum allowed transmit power P_T under the hybrid PTS-EH model for different maximum harvested power levels $P_{\max}$. The linear and saturation regions are plotted for both metrics, along with the comparative linear EH model. 188

6.5 OP versus transmit power (dBW) for varying N and α values for linear EH. 190

6.6 OP versus transmit power (dBW) for varying N and α values for NL PTS-EH. 190

6.7 OP versus transmit power (dBW) comparison for varying N and α values of linear EH and NL PTS-EH with standalone system. 191

6.8 EC versus transmit power (dBW) for varying N and α values for linear EH. 192

6.9 EC versus transmit power (dBW) comparison for varying N and α values of linear EH and NL PTS-EH with standalone system. 192

6.10 EC versus transmit power (dBW) versus N for varying h (m) values. 194

6.11 Variation of total SNR with RIS element number and maximum allowed transmit power. 195

6.12 γ_d versus γ_u^{th} for varying P_T and h_{max} values. 195

6.13 Total SNR (Υ) versus transmit power P_T comparing RIS phase configuration strategies including PRC and baseline "No RIS". 196

List of Tables

2.1 Literature summary on existing V2V system models. 22

2.2 Literature summary on existing V2I system models. 28

2.3 Literature summary on existing UAV system models 35

2.4 Comparison of existing FD UAV works with the proposed framework . . . 38

3.1 DNN training and testing input parameters. 62

3.2 dGG channel parameters and RIS_l distances (in meters) 66

3.3 Execution time (in seconds) comparison 81

4.1 DNN training input parameters. 101

5.1 Simulation parameters values for proposed UAV system 149

6.1 Simulation parameters values for proposed FD-UAV system 187

List of abbreviations

5G	Fifth-Generation
6G	Sixth-Generation
ABER	Average Bit Error Rate
Adam	Adaptive Moment Estimation
AF	Amplify-and-Forward
AI	Artificial Intelligence
AO	Alternating Optimization
ASER	Average Symbol Error Rate
AWGN	Additive White Gaussian Noise
B5G	Beyond-Fifth-Generation
BER	Bit Error Rate
BS	Base Station
C-V2X	Cellular Vehicle-to-Everything
CDF	Cumulative Distribution Function
CLT	Central Limit Theorem
CNN	Convolutional Neural Networks
CSI	Channel State Information
dGG	Double Generalized Gamma
DF	Decode-and-Forward
DL	Deep Learning
DNN	Deep Neural Network
DRL	Deep Reinforcement Learning
DSRC	Dedicated Short-Range Communication
DT	Dinkelbach Transform
EC	Ergodic Capacity
EE	Energy Efficiency
EH	Energy Harvesting
EI	External Interference

eLU	Exponential Linear Unit
ER	Energy Receiver
FD	Full-Duplex
FLOP	Floating Point Operations
FSO	Free Space Optics
FTR	Fluctuating Two-Ray
HAPS	High-Altitude Platform Stations
HD	Half-Duplex
ID	Information Decoding
IoT	Internet-of-Things
IoV	Internet-of-Vehicles
IR	Information Receiver
IRS	Intelligent Reflecting Surfaces
JO	Joint Optimization
KKT	Karush-Kuhn-Tucker
LI	Loop Interference
LoS	Line-of-Sight
MEC	Mobile Edge Computing
ML	Machine Learning
MLE	Maximum Likelihood Estimation
MRC	Maximal Ratio Combining
MSE	Mean Squared Error
MU	Multi-User
NLoS	Non-Line-of-Sight
NL-EH	Non-Linear Energy Harvesting
NOMA	Non-Orthogonal Multiple Access
NTNs	Non-Terrestrial Networks
OC	Outage Capacity
OFDMA	Orthogonal Frequency-Division Multiple Access
OP	Outage Probability

ORS	Opportunistic Relay Selection
PDF	Probability Density Function
PRC	Practical Reflection Coefficients
PS	Power-Splitting
PTS	Power-Time Switching
QoS	Quality-of-Service
QT	Quadratic Transform
RF	Radio-Frequency
RIS	Reconfigurable Intelligent Surfaces
RSMA	Rate-Splitting Multiple Access
RV	Random Variables
RWP	Random Waypoint
SAGIN	Space–Air–Ground Integrated Network
SCA	Successive Convex Approximation
SC	Selection Combining
SDN	Software-Defined Networking
SDR	Semi-definite Relaxation
SE	Spectral Efficiency
SER	Symbol Error Rate
SI	Self-Interference
SIC	Successive Interference Cancellation
SINR	Signal-to-Interference-plus-Noise Ratio
SISO	Single-Input Single-Output
SNR	Signal-to-Noise Ratio
SOP	Secrecy Outage Probability
STAR-RIS	Simultaneously Transmitting and Reflecting RIS
SWIPT	Simultaneous Wireless Information and Power Transfer
TDMA	Time Division Multiple Access
THz	Terahertz
TS	Time-Switching

UAV	Uncrewed Aerial Vehicles
URLLC	Ultra-Reliable Low-Latency Communication
V2I	Vehicle-to-Infrastructure
V2V	Vehicle-to-Vehicle
V2X	Vehicle-to-Everything
WPT	Wireless Power Transfer
WSN	Wireless Sensor Networks

List of Symbols

$\mathbb{E}[\cdot]$	Expectation operator
$f_x(\cdot)$	Probability density function (PDF) of a RV x
$F_x(\cdot)$	Cumulative distribution function (CDF) of a RV x
$I_u(\cdot)$	Modified Bessel function of the first kind with order u
$Q_v(\cdot,\cdot)$	Marcum Q-function of order v
$\Pr[\cdot]$	Probability operation
$\Upsilon(\cdot,\cdot)$	Lower incomplete gamma function
$L_k^{(\cdot)}(\cdot)$	k-point Laguerre polynomial
$\mathcal{L}(\cdot;\cdot,\cdot)$	Lagrangian
$\mathrm{eLU}(\cdot)$	Exponential linear unit activation function
$\chi(\cdot)$	Mapping function
$\mathcal{L}(\cdot)$	Loss function
$\tilde{O}_w(\cdot,\cdot)$	Unified optimization metric
$\mathcal{O}(\cdot)$	Computational complexity
$\mathcal{P}_{\mathcal{T}}$	Total power utilized
$\mathcal{F}$	Feasible region of constraint
$\mathrm{Var}(\cdot)$	Variance operator
$\mathcal{K}_\nu(\cdot)$	Modified Bessel function of second kind of order ν
$L_d^{(\cdot)}(\cdot)$	d-point Laguerre polynomial
W_l	Weight coefficient
Ψ_k	RIS PRC
$\Gamma(\cdot)$	Gamma function
$\mathrm{B}(\cdot,\cdot)$	Beta function

Chapter 1

Introduction

The rapid evolution of Sixth-Generation (6G) wireless communication systems is driving the transformation of modern connectivity toward intelligent, autonomous, and energy-efficient networks capable of supporting diverse applications across both urban and remote environments. Emerging paradigms such as the Internet-of-Vehicles (IoV), Vehicle-to-Everything (V2X) communication, Non-Terrestrial Networks (NTNs), and Internet-of-Things (IoT) ecosystems are expected to provide seamless, ultra-reliable, and low-latency connectivity for future smart transportation, disaster management, public safety, industrial automation, and remote monitoring applications. However, achieving ubiquitous and reliable communication in these scenarios remains highly challenging due to severe signal blockages, rapidly varying wireless channels, limited infrastructure availability, and stringent energy constraints, particularly in dense urban regions and disaster-prone remote areas.

In urban vehicular environments, high-rise buildings, moving vehicles, overpasses, and roadside structures often obstruct Line-of-Sight (LoS) links, resulting in severe propagation loss and unreliable communication performance. Conventional Dedicated Short-Range Communication (DSRC) technologies are increasingly unable to satisfy the growing demands for high data rates, massive connectivity, and intelligent vehicular services required

in future 6G-enabled transportation systems. Consequently, cellular Vehicle-to-Everything (C-V2X) communication has emerged as a promising solution for supporting advanced vehicular applications such as autonomous driving, intelligent traffic management, cooperative safety systems, and real-time infotainment services. Nevertheless, maintaining uninterrupted connectivity and high Quality-of-Service (QoS) in highly dynamic vehicular networks remains a major challenge.

Simultaneously, remote and disaster-affected regions often suffer from damaged or unavailable terrestrial communication infrastructure, making reliable connectivity extremely difficult during emergency and recovery operations. In such scenarios, Uncrewed Aerial Vehicles (UAVs) have gained significant attention due to their flexible deployment, adaptive mobility, and capability to rapidly establish temporary communication coverage. UAV-assisted communication systems can support a wide range of critical applications, including search-and-rescue operations, emergency response, remote sensing, surveillance, geospatial mapping, and IoT connectivity. However, UAV communication links are also vulnerable to LoS blockages, atmospheric fading, and limited onboard energy capacity, which significantly restrict long-duration operation and communication reliability.

To address these challenges, Reconfigurable Intelligent Surfaces (RISs), also referred to as Intelligent Reflecting Surfaces (IRSs), have emerged as a transformative technology for beyond-5G (B5G) and 6G wireless networks. RIS consists of programmable metasurfaces composed of low-cost passive reflecting elements capable of intelligently manipulating electromagnetic waves through dynamic adjustment of phase shifts, amplitudes, and polarization characteristics. By creating controllable wireless propagation environments, RIS can establish virtual LoS links, bypass obstacles, enhance signal strength, improve Spectral Efficiency (SE), and extend network coverage without requiring complex active Radio-Frequency (RF) chains. These characteristics make RIS particularly attractive for both ur-

ban vehicular networks and remote UAV-assisted communication systems. In dense urban environments, RIS can mitigate severe blockage effects caused by buildings and moving vehicles, while in disaster-prone and infrastructure-less areas, RIS-assisted UAV systems can provide robust and energy-efficient connectivity for emergency communication services.

Furthermore, the deployment of multiple distributed RISs introduces additional spatial diversity and macro-diversity gains, enabling more reliable communication under harsh propagation conditions. Compared with conventional relay-based architectures, RIS-assisted systems offer lower hardware complexity, reduced energy consumption, and improved scalability. These advantages are particularly important for UAV-assisted networks, where payload limitations and Energy Efficiency (EE) are critical design considerations. Moreover, RIS integration into NTNs further enhances communication resilience and ubiquitous coverage for rural and remote regions by intelligently reconfiguring the wireless environment in real time.

Alongside the connectivity enhancement, energy sustainability has become a central requirement for future wireless communication systems. The growing dependence on battery-powered sensors, vehicular communication modules, roadside infrastructure, and UAV relays necessitates efficient Energy Harvesting (EH) solutions capable of supporting long-term autonomous operation. In this context, Simultaneous Wireless Information and Power Transfer (SWIPT) has emerged as a promising technology that enables wireless devices to simultaneously decode information and harvest energy from the same RF signals. SWIPT not only prolongs network lifetime but also reduces the need for frequent battery replacement or recharging, making it highly suitable for energy-constrained vehicular and UAV-assisted communication systems.

The integration of RIS with SWIPT creates a highly synergistic framework for the next-generation wireless networks. RIS can intelligently direct reflected signals towards target

receivers, thereby enhancing both information decoding performance and EH efficiency. Such RIS-assisted SWIPT systems are capable of simultaneously improving coverage, SE, reliability, and EE in complex communication environments. Moreover, advanced SWIPT receiver architectures such as Power-Splitting (PS) and Time-Switching (TS) enable flexible trade-offs between EH and information transfer, further improving the overall system performance. In practical UAV-assisted networks, SWIPT-enabled RIS architectures can significantly extend UAV operational endurance while maintaining reliable communication links during prolonged missions in remote or disaster-affected areas.

Despite these advantages, several practical challenges remain in realizing the efficient RIS-assisted SWIPT communication systems. The highly dynamic nature of vehicular and UAV channels introduces substantial complexity in resource allocation, beamforming, phase-shift optimization, and energy management. Additionally, practical RIS deployments are constrained by discrete phase shifts, hardware impairments, and Non-Linear Energy Harvesting (NL-EH) characteristics, which significantly affect real-world system performance. The incorporation of Full-Duplex (FD) relaying in UAV-assisted systems further improves SE but also introduces Self-Interference (SI) and optimization challenges. Therefore, accurate performance analysis and efficient optimization techniques are essential for the practical deployment of RIS-assisted SWIPT-enabled communication networks.

To effectively manage these complexities, Machine Learning (ML) and Deep Neural Network (DNN)-based techniques are increasingly being integrated into RIS-assisted communication systems. Unlike conventional model-based optimization approaches, ML-driven frameworks can learn environmental dynamics from historical data and adapt network parameters in real time. These intelligent techniques enable efficient optimization of RIS phase configurations, power allocation, beamforming strategies, and SWIPT parameters under rapidly changing wireless conditions. Consequently, the ML-assisted RIS-

SWIPT systems can significantly improve network adaptability, computational efficiency, and decision-making capability while reducing processing complexity and execution time.

Motivated by these emerging research directions, this Thesis focuses on the analysis and optimization of SWIPT-enabled RIS-assisted UAV and V2X communication systems for future 6G wireless networks. The work aims to develop robust, energy-efficient, and intelligent communication frameworks capable of supporting reliable connectivity in both dense urban environments and remote disaster-prone regions. By jointly exploring RIS-assisted vehicular communication, UAV-enabled NTNs, SWIPT-based EH, and intelligent optimization techniques, this Thesis contributes toward the realization of sustainable, resilient, and high-performance next-generation wireless communication infrastructures.

1.1 Motivations

Although significant research efforts have been devoted toward RIS-assisted vehicular and UAV communication systems, several important challenges and research gaps still remain unresolved. The motivations behind the considered system models in this Thesis are summarized as follows:

- Existing studies on vehicular communication systems, such as [1], primarily focus on conventional Vehicle-to-Vehicle (V2V) performance analysis under double generalized Gamma (dGG) fading channels. Although RIS-assisted communication has been investigated in [2], the analysis was limited to a single-RIS deployment and did not consider Ergodic Capacity (EC), optimization frameworks, or DNN-assisted intelligent communication architectures.

- Multi-RIS-assisted communication systems have been studied in [3], [4], and [5]. However, these works either focused on non-vehicular or millimeter-wave scenarios

or did not investigate optimization techniques for maximizing achievable rate and minimizing transmit power consumption. Furthermore, DNN-assisted frameworks for reducing computational complexity and enabling intelligent decision-making were not explored.

- Although [6] investigated multiple RIS-assisted communication systems for Ultra-Reliable Low-Latency communication (URLLC) applications, important performance metrics such as Outage Probability (OP), Average Symbol Error Rate (ASER), and EC were not analyzed. Consequently, the joint performance evaluation, optimization, and DNN-assisted design of multi-RIS-assisted V2V communication systems over generalized dGG fading channels remain largely unexplored.

- Several studies, including [7], [8], [9], [5], [10], [2], [11], and [12], have investigated RF-EH, RIS-assisted vehicular communication, and SWIPT-enabled systems. Nevertheless, the joint analysis of multi-RIS-assisted SWIPT-enabled Vehicle-to-Infrastructure (V2I) communication under generalized dGG fading, vehicular mobility, imperfect Channel State Information (CSI), and DNN-assisted optimization frameworks remains insufficiently explored.

- Motivated by the above limitations, this Thesis investigates multi-RIS-assisted vehicular communication systems under generalized fading environments and develops optimization and Deep Learning (DL)-assisted frameworks to enhance communication reliability, achievable rate, and EE.

- UAV-assisted communication has emerged as a promising solution for remote and disaster-prone environments; however, existing literature provides limited attention to the integration of sustainable EH, RIS assistance, and intelligent communication frameworks in UAV systems.

- The RIS-assisted communication system investigated in [13], [14], and [15], whereas Outage Capacity (OC), SWIPT integration, and EH-aware optimization frameworks were not addressed. Furthermore, comprehensive performance analysis under generalized fading environments remains largely unexplored.

- Existing RIS-assisted SWIPT communication studies [16]-[17] primarily relied on linear EH models, while the joint impact of communication reliability and energy sustainability under practical NL-EH models for integrated relay-RIS-assisted UAV systems has received limited attention. In addition, Nakagami-m fading environments and EH-aware optimization techniques still remain insufficiently investigated.

- In the context of NTNs, existing FD RIS-assisted communication architectures [18], [19], [20], [21] mainly focus on terrestrial systems without SWIPT capability. Moreover, the joint integration of UAV relaying, RIS assistance, and SWIPT-enabled communication has not been comprehensively explored.

- Several prior works [22], [23], [15], [20], [21], [24], [25], [26], [27], and [28] rely on simplified propagation assumptions and static channel models. Consequently, the combined effects of residual SI, practical RIS phase-shift and amplitude responses, realistic aerial propagation environments, and EH constraints have not been comprehensively analyzed within a unified FD SWIPT-enabled relay-RIS-assisted UAV communication framework for NTNs.

1.2 Contributions

Motivated by the aforementioned research gaps and challenges in RIS-assisted vehicular and UAV communication systems, the major contributions of this Thesis are

summarized as follows:

- A comprehensive performance analysis of a multi-RIS-assisted V2V communication system over dGG fading channels is presented. Two transmission schemes, namely, Exhaustive RIS-aided Scheme (ERS) and Opportunistic RIS-aided Scheme (ORS), are proposed. In the ERS, all RISs participate in signal transmission and MRC is employed at the receiver, whereas in the ORS, the RIS providing the highest end-to-end instantaneous Signal-to-Noise Ratio (SNR) is selected for communication.
- The performance of the proposed multi-RIS-assisted V2V communication system is analyzed under both perfect and imperfect CSI conditions while incorporating vehicle mobility through the Random Waypoint (RWP) model. Closed-form analytical expressions for OP, ASER, and EC are derived by considering both path-loss and small-scale fading effects, and the analytical results are validated through extensive Monte-Carlo simulations.
- Optimization problems are formulated for maximizing the achievable data rate and minimizing the transmit power of the multi-RIS-assisted V2V communication system under practical QoS constraints. Closed-form optimal solutions are derived using Karush-Kuhn-Tucker (KKT) conditions and validated using the MATLAB optimization toolbox through the *fmincon(·)* solver. Furthermore, a DNN-based framework is developed to reduce the computational complexity and the execution time while enabling an accurate low-latency prediction of system performance in real-time vehicular communication scenarios.
- A multi-RIS-assisted SWIPT-enabled V2I communication framework is proposed under generalized dGG fading channels to improve the communication

reliability and EH efficiency. The effects of imperfect CSI and vehicular mobility are incorporated through the RWP mobility model to realistically characterize dynamic vehicular communication environments.

- A unified optimization framework is developed for jointly maximizing the harvested energy and achievable data rate in the proposed SWIPT-enabled V2I communication system. The formulated problem is solved using Joint Optimization (JO) and Alternating Optimization (AO) algorithms, and closed-form optimal solutions are obtained using KKT conditions and validated through the MATLAB *fmincon(·)* solver. In addition, a DNN-based prediction framework is proposed for low-latency estimation of system performance and optimization parameters, and its effectiveness is evaluated using Mean Squared Error (MSE) and the execution-time analysis.
- A SWIPT-enabled integrated relay-RIS-assisted UAV communication framework is proposed to enhance the communication reliability and energy sustainability in remote and disaster-prone environments. The proposed system incorporates both Selection Combining (SC) and Maximal Ratio Combining (MRC) techniques at the receiver and operates under realistic Nakagami-m fading conditions to model both LoS and Non-Line-of-Sight (NLoS) propagation environments.
- Exact closed-form analytical expressions are derived for OP, ASER, OC, and EC of the proposed UAV communication framework. Moreover, the achievable data rate, stored energy at the UAV, and overall EE are jointly optimized under practical QoS constraints using KKT-based optimization techniques. Extensive Monte-Carlo simulations are conducted to validate the analytical framework and investigate the impact of UAV altitude, Nakagami-m fading parameters, and RIS

deployment on the system performance.

– A unified FD SWIPT-enabled relay-RIS-assisted UAV communication framework for NTNs is proposed by integrating an FD Decode-and-Forward (DF) UAV relay with RIS assistance while considering practical SI effects and EH constraints. Both linear PS-based SWIPT and non-linear hybrid Power-Time Switching (PTS)-based SWIPT protocols are incorporated into the developed framework.

– Exact closed-form analytical expressions for OP and EC are derived under generalized α–μ fading channels while accounting for practical RIS amplitude and phase responses, residual SI, and realistic aerial communication environments. The developed analytical framework provides an accurate performance characterization of FD RIS-assisted UAV communication systems for NTN applications.

– A non-convex optimization problem is formulated to maximize the total received SNR through the JO of RIS phase shifts, UAV transmit power, and hybrid PTS factor under the practical QoS constraints. To efficiently solve the problem, a divide-and-conquer-based optimization algorithm is developed. The impacts of UAV altitude, fading severity parameters, residual SI, and RIS hardware impairments are comprehensively analyzed, and simulation results demonstrate significant improvements in SE, communication reliability, and energy sustainability compared with conventional standalone communication architectures.

1.3 Organization of the Thesis

This Thesis is organized into seven Chapters. The title and short summary of the Chapters are structured as follows:

Chapter 1 (Introduction)

In This Chapter, we presents the motivation, background, and significance of next-generation wireless communication systems with emphasis on 6G vehicular and non-terrestrial communication networks. The Chapter discusses the challenges associated with reliable connectivity, spectrum efficiency, and energy sustainability in urban and remote environments. Furthermore, the concepts of RIS, SWIPT, UAV-assisted communication, and V2X communication are introduced. The Chapter also outlines the research objectives, major contributions, and overall organization of the Thesis.

Chapter 2 (Literature Review)

This Chapter presents a comprehensive review of existing research related to RIS-assisted wireless communication systems, SWIPT-enabled networks, UAV-assisted communication, and V2X communication technologies. The Chapter discusses various channel models, fading environments, EH techniques, optimization approaches, and ML-based methods proposed in the literature. Additionally, the limitations of existing works and the research gaps motivating this Thesis are highlighted.

Chapter 3 (Multi-RIS-assisted V2V Communication: Performance Analysis and Optimization over Generalized Fading)

Herein, we Chapter investigate the performance of multi-RIS-assisted V2V communication systems operating under generalized fading environments. Analytical expressions for important performance metrics such as OP, ASER, and EC are derived. Furthermore, optimization techniques for RIS deployment and system parameter selection are presented to improve communication reliability and SE in dense vehicular scenarios.

Chapter 4 (Multi-RIS-assisted SWIPT-enabled V2I Communication with Mobility and Imperfect CSI)

This Chapter focuses on a SWIPT-enabled multi-RIS-assisted V2I communication system considering vehicular mobility and imperfect CSI. The impact of mobility-induced channel variations and CSI estimation errors on system performance is analyzed. Moreover, the Chapter investigates power allocation and RIS-assisted optimization strategies to enhance both information transmission reliability and EH efficiency in practical vehicular communication environments.

Chapter 5 (SWIPT-enabled Integrated Relay-RIS-aided UAV Communication)

We present the analysis of an integrated relay-RIS-assisted UAV communication system with SWIPT capability. The proposed framework is designed for remote connectivity and disaster-prone scenarios where reliable communication infrastructure may be unavailable. Performance analysis is carried out considering EH constraints, relay-assisted transmission, and RIS-based signal enhancement. The Chapter also evaluates the impact of various system parameters on OP and overall communication performance.

Chapter 6 (Full-duplex SWIPT-enabled Relay–RIS UAV Communication for Non-Terrestrial Networks)

Herein, we investigate a FD relay-RIS-assisted UAV communication framework for NTNs. Practical system considerations such as discrete RIS phase shifts, SI in FD communication, and NL-EH models are incorporated into the analysis. The Chapter derives analytical performance expressions and examines the impact of FD relaying and RIS-assisted transmission on SE, EE, and communication reliability in NTN environments.

Chapter 7 (Conclusion and Future Directions)

In this Chapter, we summarize the major contributions and key findings of the Thesis. The overall outcomes of the proposed RIS-assisted SWIPT-enabled UAV and V2X communication frameworks are discussed. In addition, several promising future research directions related to intelligent wireless communication systems, ML-based optimization, integrated sensing and communication, and next-generation 6G networks are presented.

Chapter 2

Literature Review

2.1 Literature Review

The research presented in this Thesis focuses on four interconnected areas of next-generation wireless communication systems, namely multi-Reconfigurable Intelligent Surfaces (RIS)-assisted Vehicle-to-Vehicle (V2V) communication, multi-RIS-assisted Simultaneous Wireless Information and Power Transfer (SWIPT)-enabled Vehicle-to-Infrastructure (V2I) communication, SWIPT-enabled relay-RIS-assisted Uncrewed Aerial Vehicles (UAVs) communication, and Full-Duplex (FD) SWIPT-enabled relay-RIS-assisted UAV communication for Non-Terrestrial Networks (NTNs). These technologies collectively address key challenges associated with communication reliability, Spectral Efficiency (SE), energy sustainability, and intelligent resource management in future Sixth-Generation (6G) wireless networks. This Chapter reviews the existing literature related to these research domains, discusses major analytical and optimization techniques reported in the literature, and identifies the research gaps that motivate the development of the proposed frameworks presented in subsequent Chapters.

2.1.1 Multi-RIS-assisted V2V Communication: Performance Analysis and Optimization Over Generalized Fading

Several studies have explored the performance of V2V systems using generalized fading channels. In [29], a generalized Fox's H-function was employed to evaluate the performance of an inter-vehicle communication system. In [1], the double generalized Gamma (dGG) distribution was employed to model a non-homogeneous double-scattering fading conditions commonly encountered in V2V communications. The authors introduced various statistical metrics for the bivariate dGG distribution, including the Cumulative Distribution Function (CDF), Probability Density Function (PDF), and moments. Subsequently, the resulting analytical framework was then utilized to analyze the performance of a V2V communication mode by transmit antenna selection scheme over the dGG distribution.

Several studies have explored the performance enhancements enabled by incorporating RIS into wireless systems. Authors in [30] provided a comprehensive overview comparing RIS technology with other wireless solutions, addressing current advancements and ongoing research challenges. Further, [31] elucidated the distinguishing characteristics and shared functionalities between RIS acting as reflectors and relays. The work emphasized the SE advantages of large-scale RIS configurations, suggesting potential data rate superiority over relay-based systems while simplifying the implementation complexities. In [32], the performance analysis and optimization frameworks for large RIS were reviewed. The study addressed working principles, models, and technologies, along with optimization targets like secrecy rate and Energy Efficiency (EE). Additionally, the performance metrics such as Outage Probability (OP) and data rate and highlighted open challenges in LIS-assisted networks were

also covered. In [33], recent advancements in RIS-assisted wireless systems were reviewed, with a focus on signal processing for transmission design, channel estimation, and radio localization. The review covered channel estimation for structured and unstructured models and examined three Channel State Information (CSI) estimation scenarios: fully instantaneous, fully long-term, and two-timescale. The potential of the two-timescale CSI approach was highlighted. The study also explored radio localization applications, considering channel models and deployment scenarios for both near-field and far-field conditions.

The authors in [34] reviewed RIS design and applications in wireless networks, including metasurfaces, network scenarios, and performance optimization. The review covered the use of RIS in Mobile Edge Computing (MEC), UAVs, and Wireless Power Transfer (WPT), and addressed challenges such as phase resolution and hardware limitations. Current solutions employ alternating optimization, with future research focusing on advanced algorithms to enhance performance. In [35], RIS technology for reconfigurable wireless networks was reviewed. It covered the shift to hybrid active-passive systems, challenges in signal modeling and beamforming, and applications in physical layer security, WPT, UAVs, and MEC. Dense RIS deployments with multi-hop reflections and cooperative beamforming were recommended for improved performance. Authors in [36] provides a detailed comparison between the active and passive RIS, focusing on performance under the same power budget. Active RIS, equipped with amplifiers, significantly outperforms the passive RIS by mitigating double path fading and enhancing the signal strength. Nevertheless, this improvement comes with increased complexity and noise power.

Authors in [37] investigated the benefits of employing RIS across various environments and frequency bands, from sub-6 GHz to millimeter-wave (mm-Wave). Ini-

tially, they examined single RIS system models and later expanded their analysis to incorporate multiple RISs for NLOS communication in both indoor and outdoor scenarios. Additionally, [38] utilized the Fluctuating Two-Ray (FTR) distribution to characterize small-scale fading in mm-Wave communications. The authors established statistical properties for FTR Random Variables (RV) and derived expressions for end-to-end Signal-to-Noise Ratio (SNR) for both RIS-aided and Amplify-and-Forward (AF) relay systems. Their proposed optimization methods focused on determining optimal phase shifts for RIS elements and suggested power allocation strategies for AF relay systems. In [13], the authors investigated the OP and capacity aspects in wireless networks with the assistance of multiple RISs. Employing Rayleigh fading channels, the authors derived an analytical expression for the OP and an asymptotic expression for the sum rate. This analysis is done considering two scenarios, wherein the end-to-end channel was approximated using the K_G approximation and the non-central chi-square distribution. In [39], a comprehensive examination was conducted on the current research concerning the applications of RIS in both ground and aerial-based vehicular communications, discussing challenges and prospects for the future of RIS-aided 6G vehicular communications. Authors in [40] explored a novel high-mobility vehicular communication system aided by a roadside RIS. To improve the system performance, where low-complexity passive beamforming design and an efficient channel estimation scheme was introduced.

An outage performance analysis for a single RIS-aided vehicular system considering thr Rayleigh and Rician fading channels was conducted in [41]. The analysis utilizes the Central Limit Theorem (CLT) and series expansions. The authors in [42] performed a secrecy capacity analysis on a wireless vehicular communication network aided by the RIS, discussing the impact of RIS placement and the number of RIS ele-

ments on the system performance. The authors in [2] introduced a RIS-aided system for the V2I scenario over a dGG fading channel, conducting analyses on both outage performance and Bit Error Rate (BER).

Previous studies in Vehicle-to-Everything (V2X) networks have mainly focused on evaluating the performance of single RIS-aided systems. However, given the dynamic nature of these networks, deploying multiple RIS units emerges as a preferable strategy to enhance the V2V communication effectiveness. In [10], a system model utilizing the dual-RIS to improve the V2I communication was introduced, conducting a comprehensive performance analysis considering the Nakagami-m channels. The authors derived analytical expressions for OP, SE, and EE, comparing single and dual RIS-aided V2I systems. Further, [4] evaluated the effectiveness of a multi-hop transmission system aided by RIS, employing multiple RIS units to enhance communication capabilities in a hybrid system integrating Radio-Frequency (RF) and Free-Space Optical (FSO) communications, utilizing the AF and Decode-and-Forward (DF) relaying protocols. In [5], multiple RISs alongside transmit antenna selection for mm-Wave communication systems was implemented with a focus to improve the performance at Base Station (BS) and minimize signal processing complexity at the user end. In this vein, analytical expressions were formulated for the OP and the throughput to quantify the system performance.

In [3], the authors analyzed the OP and ASER of wireless networks using multiple RISs along with the implementation of an opportunistic RIS selection strategy considering the Nakagami-m channel and formulated the optimization problems for the optimal number of RIS elements and optimal RIS placement to achieve predefined outage performance. Authors in [43] compared classic repetition-coded DF relaying with the RIS and stated that in order to outperform the DF relaying, very high data

rates and large metasurfaces are needed to minimize the total transmit power and maximize the EE. Authors in [44] explored resource allocation strategies for RIS-aided vehicular communications by taking into account varying Quality-of-Service (QoS) requirements in the V2X communications. The primary objective was to maximize the capacity of V2I links, while ensuring a minimum Signal-to-Interference-Plus-Noise Ratio (SINR) for the V2V links. A multi-RIS system was considered In [6] for URLLC applications in an industrial communication scenario focusing on average data rate and average decoding error probability analysis under finite channel block-length conditions. Extensive numerical results validate the theoretical findings and underscores the potential of multiple RIS in meeting URLLC requirements in complex industrial environments. In [45], an aerial RIS mounted on an UAV was used for relaying the transmitted signal from a terrestrial primary source node to a user on the ground using ambient backscatter communication. The performance of the proposed design framework was analyzed by deriving expressions for OP and ergodic SE.

Researchers in [46] explored short-packet communications within wireless cognitive Internet-of-Things (IoT) networks, focusing on multiple receivers. Herein an opportunistic relay selection scheme to maximize end-to-end SNR and derived closed-form expressions for average block error rate (BLER) was introduced. Additionally, Deep Learning (DL)-based evaluation model was presented showing comparable performance to the ORS scheme were introduced in [47], viz., Two novel Cooperative Reflecting Intelligent Surface (CRIS) models: $DNN_R - CRIS$ and $DNN_{R,D} - CRIS$. The $DNN_R - CRIS$ model explored the use of RIS as an IoT-based relay element in future cooperative networks, employing DL for RIS phase optimization. To mitigate maximum-likelihood complexity at the destination, they proposed a new DNN-based symbol detection method combining the $DNN_{R,D} - CRIS$ model with DNN-aided

phase optimization. The study evaluated BER performance across various relay and receiver configurations. In [48], a comprehensive review discussed deep learning-enabled RIS and suggested integrating RIS into 6G Intelligent Transportation System (ITS). Furthermore, [49] quantified the upper bounds of delay in 6G V2V communications, incorporating the hybrid communication and channel access technologies. In this work, a DNN model was formulated and trained to rapidly compute these delay bounds in real-time, devising an intelligent strategy for governing the inter-vehicle distance, especially in cooperative autonomous driving scenarios. To highlight the key distinctions between the existing studies and the proposed framework, a comparative summary of the related works is presented in Table 2.1.

2.1.2 Multi-RIS-assisted SWIPT-enabled V2I Communication with Mobility and Imperfect CSI

RISs were deployed to enhance the Energy Harvesting (EH) efficiency in [50], considering the impact of imperfect channel estimation for cascaded RIS links. The authors formulated optimization problems to improve system performance and proposed an Alternating Optimization (AO) approach. This methodology involved decomposing the original optimization problem into subproblems, which were subsequently solved using Successive Convex Approximation (SCA) and Semi-Definite Relaxation (SDR) techniques. The study presented in [41] analyzed the outage performance of an RIS-assisted vehicular communication system under both Rayleigh and Rician fading scenarios. The analysis leveraged the CLT and series expansion techniques to derive the statistical performance metrics and quantify the reliability of the system. A fractional programming-based optimization framework was introduced in [51], where the RISs were employed to enhance the efficiency of the wireless systems utilizing the

Table 2.1: Literature summary on existing V2V system models.

Ref.	System type	Channel model	OP	SER	EC	Opti.	DNN
[29]	V2V	Generalized Fox's-H function	✓	✓	×	×	×
[1]	V2V	dGG	✓	✓	✓	×	×
[37]	Single RIS-aided indoor and outdoor wireless network	Rician	×	✓	✓	×	×
[38]	Single RIS-aided mm-wave	Fluctuating Two Ray	✓	✓	×	✓	×
[13]	Multi-RIS	Rayleigh	✓	×	✓	×	×
[41]	Single RIS-aided V2I	Rayleigh and Rician	✓	×	×	×	×
[42]	Single RIS-aided V2I	Rayleigh and Double Rayleigh	×	×	✓	×	×
[2]	Single RIS-aided V2I	dGG	✓	✓	×	×	×
[10]	Dual-RIS-aided V2I	Nakagami-m	✓	×	×	×	×
[4]	Multi-RIS FSO-RF	dGG, inverse gamma	✓	✓	×	×	×
[5]	Multi-RIS-aided mm-wave	Gamma distribution	✓	×	✓	×	×
[3]	Multi-RIS	Nakagami-m	✓	✓	×	✓	×
[44]	Single RIS-aided V2I	Rician	×	×	×	✓	×
[45]	Single RIS-aided UAV networks	Nakagami-m	×	×	✓	×	×
[46]	Wireless powered Cognitive IoT networks	Rayleigh	×	✓	×	×	✓
[47]	Single RIS-aided IoT network	Rayleigh	×	✓	×	×	✓

Non-Linear Energy Harvesting (NL-EH). The study comprehensively discussed the impact of RIS-aided optimization techniques on the system performance, particularly

in terms of EE and data transmission reliability. Security aspects of RIS-assisted vehicular networks were examined in [42], where the authors investigated the secrecy capacity of the system. The study explored the effect of RIS placement and the number of RIS elements on secure communication performance, highlighting the key design considerations for ensuring robust security in vehicular networks. A multi-RIS-assisted vehicular communication framework was proposed in [8], where the system was analyzed under outdated CSI. The study applied selection strategies across all deployed RISs, thereby optimizing the performance based on maximum SNR criteria. The results demonstrated the impact of outdated CSI on vehicular communication reliability and effectiveness. In [9], the authors proposed a system model incorporating multiple RISs and conducted a rigorous statistical analysis to characterize its performance. This work provided insights into the fundamental statistical behavior of the RIS-aided wireless channels and assessed the implications of multi-RIS deployments on the overall system efficiency. The optimization of RIS-assisted SWIPT systems for IoT applications was addressed in [52]. The study focused on key performance indicators such as data rate, EH, and EE, analyzing both Time-Switching (TS) and Power-Splitting (PS) protocols to enhance the effectiveness of RIS-enabled IoT networks. A comprehensive survey on the DL-driven RIS applications for ITS was presented in [48]. The study outlined recent advancements in the integration of Artificial Intelligence (AI) with RIS technology, discussing various Machine Learning (ML) models tailored for vehicular communication enhancement. In [53] and [54], a multi-objective optimization framework for resource allocation in RIS-assisted SWIPT systems was proposed. The corresponding research works provided a thorough analysis of the trade-offs between maximizing the sum-rate for information transfer and optimizing harvested energy. The authors demonstrated the role of RISs in improving

both the communication performance and EH efficiency, highlighting the adaptability of RIS-aided SWIPT solutions to diverse system requirements and operational constraints.

Recent advancements in the RIS-assisted vehicular and wireless communication systems have been extensively investigated to enhance system performance across various application scenarios. Authors in [7] investigated the performance of RF-EH in V2V communication systems, considering both linear and NL-EH models under double-Rayleigh fading for a multi-antenna system. Specifically, the bit error probability was derived for a dual-hop DF relaying system while analyzing the impact of antenna selection at the relay node on system performance. In [1], the authors employed the dGG distribution to model non-homogeneous double-scattering fading in V2V communication channels. The study introduced fundamental statistical metrics such as the CDF, PDF, and higher-order moments to facilitate performance evaluation under a transmit antenna selection scheme. The outage performance and BER analysis of RIS-assisted V2I communication systems over dGG fading channels were examined in [2], highlighting the impact of fading severity on system reliability. The work in [5] explored the deployment of multiple RISs in mm-Wave communication systems, where transmit antenna selection was leveraged to enhance BS performance while mitigating the computational complexity at the user end.

Authors in [55] explored the Sensor-Aided Zero-Energy RIS (SAZE-RIS) for Integrated Sensing, Communication, and Powering (ISCAP) networks, highlighting the system architecture, operational strategies, and trade-offs among functionalities, with a case study demonstrating design considerations. A multi-functional RIS (MF-RIS) supporting reflection, refraction, amplification, and sensing was proposed in [56] to enhance the Integrated Sensing and Communication (ISAC) systems, with joint

beamforming and RIS configuration optimized iteratively; simulations showed the performance gains over active, passive, and Simultaneously Transmitting and Reflecting RIS (STAR-RIS), with sensing saturation beyond a certain element count. In [17], an RIS capable of dynamic transmission/reflection phase control for dual- and quad-beam patterns and polarization conversion was designed and validated through full-wave simulations and prototype measurements. Chaotic signal-based transmit waveform design for MF-RIS assisted SWIPT systems was studied in [57], with a differential chaos shift keying (DCSK)-based framework partitioning the surface for EH, transmission, and reflection; energy–BER trade-offs, element requirements, and waveform design impacts on self-sustainability were analyzed.

The authors in [47] proposed the cooperative RIS models, wherein DL techniques were integrated for the phase optimization and symbol detection. Their approach significantly improved the BER performance across varying relay and receiver configurations. Resource allocation strategies in the RIS-assisted V2X communication systems were addressed in [44], where the optimization of V2I capacity was achieved while ensuring the QoS constraints in V2V links. In [11], the authors proposed an intelligent non-convex and non-smooth optimization framework for RIS-aided mobile networks. Their work focused on enhancing the algorithmic efficiency for complex resource allocation problems, emphasizing mathematical tractability and convergence analysis. Building on this foundation, our study advances the discussion by extending the optimization scope to a joint multi-RIS and SWIPT design under realistic fading, mobility, and CSI error conditions. Authors in [12] explored the holographic counterpart computation offloading via RIS in Vehicular Edge Computing (VEC). The study demonstrated the potential of RIS to improve computation offloading efficiency and reduce latency in vehicular environment.

Additionally, the work in [45] investigated an innovative aerial RIS architecture mounted on an UAV for terrestrial-to-ground signal relaying via ambient backscatter technology, with a detailed analysis of OP and SE. Short-packet communications in cognitive IoT networks were investigated in [46], where an RIS selection mechanism was proposed to maximize the received SNR. Furthermore, a DL-based evaluation model was implemented to assess system performance under varying network conditions. Authors in [10] proposed an dual-RIS-assisted V2I system and discussed its performance. In [58], authors proposed a DNN model for UAV-aided Non-Orthogonal Multiple Access (NOMA) networks.

In [59], the authors investigated the role of Wireless Sensor Networks (WSNs) in IoT environments, focusing on the challenges imposed by resource-constrained and highly mobile sensor nodes. To address the routing efficiency in complex topologies, the authors proposed a neural network–based technique trained via Deep Reinforcement Learning (DRL) within a Software-Defined Networking (SDN) framework. The study also highlighted the importance of mitigating resource depletion in high-traffic nodes by leveraging alternative routing paths.

Authors in [60] proposed the deep processing optimization network, a novel DL framework for image processing and classification. The architecture integrates the convolutional layers, residual connections, attention mechanisms, and global average pooling to improve both accuracy and the computational efficiency. In [61], the authors reviewed the challenges of implementing DL models on edge devices with limited computing and memory resources wherein the hardware acceleration strategies were analyzed alongside the model optimization techniques. Results showed that hardware accelerators can significantly enhance the throughput and reduce the latency while maintaining the EE and accuracy. In [62], the authors proposed a neural network

model for arabic handwritten digit dataset (AHDD) classification with preprocessing, dropout regularization, and adaptive learning rates, achieving higher accuracy than a baseline model. Further suggested improvements were suggested the Convolutional Neural Network (CNNs), transfer learning, and larger datasets to enhance recognition performance. In [63], the authors analyzed Keras as a user-friendly DL application programming interface, highlighting its support for multi-graphics processing unit (GPU), distributed training, and wide applications in medical diagnosis and image recognition.

Authors in [64] discussed the application of DL in IoT-enabled healthcare networks to improve the performance through intelligent data analysis and decision-making. It is noteworthy that the WSNs were widely adopted for low-cost and real-time data exchange, though WSNs suffered from energy limitations. To overcome the shortcomings of conventional shortest-path routing, the study introduced ML-assisted SDN frameworks and proposed DRL-based algorithms to balance energy consumption and prolong network lifetime, thereby enhancing the sustainability of healthcare communication systems. In [65], authors proposed a transmission mode selection and resource block allocation for 5G-V2X communications to support mission-critical vehicular applications. The problem was formulated as a Markov decision process, and a decentralized DRL algorithm was proposed to maximize channel capacity of V2I users while ensuring the latency and reliability requirements of V2V links. Simulation results demonstrated superior performance, robustness, and convergence compared to existing state-of-the-art approaches. Authors in [59]-[65] collectively emphasize that DL not only provides powerful tools for addressing traditional optimization challenges but also enables adaptive and data-driven solutions that are particularly relevant in fast-varying vehicular channels. A comprehensive summary of these existing stud-

ies, along with a comparative analysis of their methodologies, contributions, and the novelty of the proposed approach, is presented in Table 2.2.

Table 2.2: Literature summary on existing V2I system models.

Ref.	**System Model**	**Channel Model**	**ICSI**	**SWIPT**	**DNN**
[66]	Relay assisted network	Ricean	×	✓	×
[50]	Single RIS-assisted network	Gaussian	×	✓	×
[41]	Single RIS-assisted V2I	Rayleigh & Rician	×	×	×
[51]	Multi-RIS-assisted IoT	Rayleigh	×	✓	×
[42]	Single RIS-assisted V2I	Double Rayleigh	×	×	×
[8]	Multi-RIS-assisted vehicular	Rayleigh	×	×	×
[9]	Multi-RIS-assisted network	Nakagami-m	×	×	×
[52]	Multi-RIS-assisted IoT	Rayleigh	✓	✓	×
[54]	Single RIS-assisted network	Ricean	×	✓	×
[7]	Multi-Relay assisted V2V	double-Rayleigh	×	✓	×
[1]	V2V	dGG	×	×	×
[2]	Single RIS-assisted V2I	dGG	×	×	×
[10]	Dual-RIS-assisted V2I	Nakagami-m	×	×	×
[5]	Multi-RIS-assisted mmwave	Gamma	×	×	×
[47]	Single RIS-assisted IoT	Rayleigh	×	×	✓
[44]	Single RIS-assisted V2I	Rician	×	✓	×
[45]	Single RIS-assisted UAV	Nakagami-m	×	×	×
[46]	IoT networks	Rayleigh	×	×	✓
[10]	Dual-RIS-assisted V2I	Nakagami-m	×	×	×
[58]	UAV-assisted RIS	Rician	×	×	✓
This work	Multi-RIS-assisted V2I	dGG	✓	✓	✓

2.1.3 SWIPT-enabled Integrated Relay-RIS-aided UAV Communication

Recent research has focused on leveraging RIS technology in UAV communication networks to achieve an enhanced reliability and a reasonable system performance. In [13], the authors investigated a RIS-assisted UAV communication framework wherein an RIS, deployed on a building, reflects signals from a terrestrial source towards a UAV, which subsequently relays the decoded signals to the intended destination. The study derived the PDF of the instantaneous SNR and utilized it to obtain analytical expressions for key performance metrics, including the average bit error rate (ABER), OP, and average channel capacity. The findings demonstrated that incorporating RIS into UAV communication systems substantially enhances coverage and transmission reliability. The authors in [67] analyzed the performance of a UAV-assisted NOMA network with an RIS under Nakagami-m fading. Analytical expressions for OP and EC were derived, considering diversity combining techniques and the effects of imperfect Successive Interference Cancellation (SIC) and RIS phase errors. In another study [68], a DF relaying system was analyzed to facilitate UAV communication with ground stations via RIS, highlighting its potential to improve signal quality and coverage. The authors derived closed-form expressions for performance indicators such as OP, ABER, and ergodic channel capacity, along with high-SNR approximations to characterize system performance under extreme conditions. The results reinforced the viability of RIS-assisted UAV communication, particularly in dense urban environments, where traditional Line-of-Sight (LoS) links are frequently obstructed.

The authors in [69] proposed a RIS-enabled hybrid TeraHertz (THz) or RF architecture using SC to enhance link reliability. Exact closed-form expressions for the

PDF and CDF of the output SNR were derived for both THz and RF links. Analytical expressions for OP and ASER were obtained using α-μ fading models, and asymptotic analysis revealed system diversity. Simulation results verified substantial performance and EE improvements. In [70], authors proposed network-aware RF energy transmitter positioning scheme, integrated with a robust hybrid RF wave propagation model, which effectively mitigates the energy hole problem and enhances EE in IoT networks. Simulation and experimental validations demonstrate the significant improvements in harvested energy, network coverage, and overall network lifetime. The authors in [71] proposed an RIS-aided cellular network to extend the coverage for aerial users. The proposed system integrates RISs with BS to enable efficient air-ground communication while minimizing the spread of interference signals across wide areas. The placement of RISs was optimized to enhance network performance in terms of spatial SINR and to mitigate inter-cell interference. Numerical results demonstrated that the RIS-aided network significantly outperforms the conventional systems without RISs, when the RIS positions are optimally configured.

In [72], the authors proposed a secure computation offloading framework for NOMA-enabled UAV–MEC networks subject to aerial eavesdropping, where the average secure computation capacity was maximized under user security constraints. The resulting non-convex optimization problem was handled through the worst-case security analysis, successive convex approximation, and block coordinate descent, where the proposed design achieved superior security-aware computation performance over benchmark schemes. In [73], the authors proposed an online edge learning offloading scheme for UAV-assisted MEC secure communications, which maximized the secure computation efficiency by jointly optimizing binary offloading decisions and resource allocation under task-queue stability and minimum security requirements.

The fractional and coupled optimization structure was addressed using the Dinkelbach method, DRL, and SCA, and the scheme demonstrated enhanced computational efficiency, security, and system stability relative to existing approaches.

The authors in [74] investigated physical-layer security in satellite downlink communications by formulating a secrecy rate maximization problem and solving it via joint beamforming and RIS configuration under power constraints. Simulation results demonstrated that the Satellite–Terrestrial Integrated Network (STIN)-based RIS-assisted approach improves secrecy performance compared with conventional onboard beamforming; however, the use of purely reflective RIS architectures limits robustness against the eavesdroppers. In [75], authors investigated RIS-aided hybrid satellite–terrestrial relay networks to enhance the signal reception for users experiencing blocked satellite links. By jointly optimizing the satellite and BS beamforming vectors along with RIS phase shifts, a total transmit power minimization problem was formulated under the user rate constraints. An AO framework based on singular value decomposition, the uplink–downlink duality, and penalty-based convex approximations was developed, and simulation results demonstrated the superior performance compared with the benchmark schemes. The Space–Air–Ground Integrated Network (SAGIN) was widely studied in [76] due to its wide coverage and flexible networking capability; however, its heterogeneous architecture introduced significant wireless security challenges. To address the limitations of conventional cryptographic approaches, Wireless Endogenous Security (WES) was investigated by exploiting the dynamic and heterogeneous characteristics of physical-layer resources, and hybrid-domain WES schemes were proposed to enhance both security and transmission efficiency. Furthermore, to support the massive IoT access, multiple access techniques were extensively studied. In [77], Rate-Splitting Multiple Access (RSMA)-based

multicast communication in satellite–aerial integrated networks was investigated by jointly optimizing satellite and UAV transmissions over the same frequency band, where a penalty-based sequential convex approximation algorithm was developed to maximize the system sum-rate under SINR and power constraints. Simulation results showed effective interference suppression and notable sum-rate gains over benchmark schemes.

The work in [66] introduced a dual-hop relaying scheme for SWIPT, wherein a joint optimization problem was formulated to maximize transmit power, harvested energy, and overall throughput in a hybrid active-and-passive relaying architecture. In [78], the authors proposed SWIPT-aided DF-PS Relaying (PSR) framework effectively enhances both EE and data reliability in IoT networks. Analytical and simulation results confirmed the superiority of the Adaptive PS Scheme (APSS) over the optimal and joint optimal counterparts under varying channel conditions. In [79], the authors presented a performance analysis of a UAV selection algorithm for relay networks, where randomly deployed UAVs harvest energy from a dedicated power station. Closed-form expressions for OP, throughput, and SER were derived under a NL-EH model and Nakagami-m fading. In [80], the authors presented a SWIPT-enabled MEC-assisted IoT framework that jointly optimizes energy transfer, computation offloading, and resource allocation. By decomposing the non-convex joint optimization problem into two convex sub-problems solved using the proposed AO approach that achieves an efficient energy utilization and improved computational performance of the IoT devices. A cache-assisted SWIPT cooperative system with EH relays was analyzed in [16], where time-splitting and relay selection optimize throughput and energy storage under the QoS constraints. Closed-form solutions using Karush-Kuhn-Tucker (KKT) conditions and the Lambert function demonstrated notable gains in serving

time and performance. In [81], authors proposed a UAV-WPT-assisted Space-Air-Ground Power IoT (SAG-PIoT) framework with a hybrid task offloading strategy combining partial and binary offloading under the shared energy and computation modes. By employing a Multi-Agent Distributed Deep Deterministic Policy Gradient (MAD4PG) algorithm, the joint optimization of energy replenishment and task offloading is effectively achieved, demonstrating up to 18.93% reduction in the latency and 28.14% decrease in the energy consumption compared to state-of-the-art methods. In [82], an UAV-RIS-assisted THz network was proposed for energy-efficient relay transmission, relay selection, optimizing UAV altitude, and user association to maximize sum-rate and minimize energy consumption. A three-stage AO yields quasi-optimal performance in both single and multi-user (MU) scenarios. A FSO or RF-SWIPT system employing the DF relaying was analyzed under Málaga-$\mathcal{M}$ turbulence and Rician fading, with attention to EH and physical layer security. Closed-form secrecy performance metrics were derived for both partial and full eavesdropping scenarios [17].

In [83], the authors investigated UAV-enabled SWIPT networks for IoT, analyzing the EE. The Dinkelbach transform (DT) and multi-objective evolutionary algorithm were applied to obtain the optimal solution. An RIS-assisted SWIPT system was proposed, leveraging the UAVs and buildings to simultaneously enhance both information and energy transfer. A non-convex optimization was tackled through double iteration algorithms, with performance evaluated under perfect and statistical CSI conditions [14]. UAV-mounted RIS-assisted SWIPT for IoT networks was explored to optimize the energy and information transfer using Time Division Multiple Access (TDMA) scheduling and UAV trajectory in [84]. A non-convex optimization problem was solved with iterative methods, improving the minimum achievable rate and EH

performance for multiple IoT devices. In [15], a UAV-assisted relaying system with EH capability was proposed for urban communication scenarios, wherein shadowed-Rayleigh and shadowed-Rician fading were considered to model the UAV-to-ground destination links. Under these channel conditions, closed-form expressions for the OP were derived by incorporating various urban environment parameters. Monte-Carlo simulations were conducted to validate the analytical results, which demonstrated a close match with the theoretical predictions. A comparative summary of the system model, EH model, and assessments of the most relevant prior works is presented in Table 2.3.

2.1.4 Full-duplex SWIPT-enabled Relay–RIS UAV Communication for Non-Terrestrial Networks

The integration of RIS, FD relaying, and UAVs has recently emerged as a promising paradigm for enhancing the performance of next-generation wireless networks. Several studies have investigated RIS-assisted and FD-enabled communication systems under different configurations. In [18], an RIS-assisted MU-FD two-way communication system was proposed to enhance coverage in dead zones. The work addressed both Self-Interference (SI) and co-channel interference by jointly optimizing the BS precoding and RIS reflection coefficients to maximize the weighted minimum rate. Similarly, the authors in [19] analyzed an RIS-assisted FD system in which the RIS was utilized to suppress SI. Closed-form expressions for OP and symbol error probability were derived under generalized Nakagami-m fading and validated through Monte-Carlo simulations.

The EH aspects in RIS-assisted FD systems were explored in [51], where a MU-

Table 2.3: Literature summary on existing UAV system models

Ref.	**System Model**	**EH model**	**Type of Analysis / Assessment**
[66]	Relaying	NL-EH	Optimization (sigmoidal function)
[13]	UAV-assisted relay	×	Performance analysis
[67]	UAV RIS-assisted NOMA	×	Performance analysis
[78]	UAV-assisted relay	Linear	Performance analysis
[68]	DF relay	×	Performance analysis
[69]	Hybrid RF-THz	×	Performance analysis
[71]	RIS-assisted	×	Optimization
[79]	UAV-assisted relay	NL-EH	Performance analysis and optimization (error function)
[80]	Relaying	Linear	Optimization
[41]	UAV-assisted relay	×	Performance analysis
[16]	Cache-assisted SWIPT	Linear	Optimization
[81]	UAV-assisted SWIPT	Linear	Optimization
[82]	UAV RIS-based THz	Linear	Optimization
[17]	Mixed FSO/RF SWIPT	Linear	Performance analysis
[83]	UAV-assisted SWIPT	Linear	Optimization
[14]	RIS-assisted SWIPT	Linear	Optimization
[84]	RIS-assisted SWIPT	Linear	Optimization
[15]	UAV-assisted relay	Linear	Performance analysis
This work	Integrated relay-RIS assisted UAV	NL-EH	Performance analysis, EH, and optimization (sigmoidal function)

FD communication framework with user-specific RIS deployments and hybrid NL Power-Time Switching (PTS) EH was studied under random scheduling. Reliability performance was analyzed using BLER metrics in the finite blocklength regime. In [22], the performance of an RIS-assisted FD system was examined under Weibull fading channels, while considering Practical Reflection Coefficients (PRC), Loop In-

terference (LI), residual SI, and External Interference (EI). In addition, several studies have focused on modeling the physical characteristics of RIS-assisted channels. For instance, the work in [23] analyzed a Single-Input Single-Output (SISO) RIS-assisted system under Rayleigh fading while accounting for the practical dependence between reflection amplitude and phase. Closed-form OP and EC expressions were obtained along with asymptotic approximations for the large RIS deployments. In [15], an RIS-assisted symbiotic radio system was proposed to extend the transmission coverage through cascaded channel-based phase design, and the derived outage expressions highlighted the effect of RIS size on backscatter communication performance. Further investigations on FD RIS-assisted systems were presented in [20], where the authors studied a network consisting of uplink and downlink zones in the presence of residual SI, co-channel interference, and hardware impairments. Closed-form expressions for OP, Secrecy Outage Probability (SOP), and ergodic rate were derived along with joint RIS and transmit power optimization strategies. Similarly, the work in [21] analyzed an RIS-assisted FD system with user-specific RIS deployments over correlated Nakagami-m fading channels, focusing on signal power statistics, OP, and achievable rate performance while accounting for the effects of channel correlation and residual SI.

In [24], radio resource allocation for SWIPT-enabled FD multi-antenna access points communicating with multiple EH users was studied, where a NL rectifier-based EH model and Weighted Minimum Mean Square Error (WMMSE)-based beamforming optimization were employed to maximize the system sum-rate. Similarly, an Orthogonal Frequency-Division Multiple Access (OFDMA)-based MU-FD wireless powered communication network was investigated in [25], where beamforming, power allocation, and sub-band allocation were jointly optimized to maximize the system sum-

rate. In [26], a SWIPT-powered FD DF relay system was studied under a NL-EH model, and closed-form approximations for BLER and EE were derived under the finite blocklength regime. RIS-assisted FD communication systems have also been explored in recent works. For instance, the authors in [27] proposed an RIS-assisted multi-antenna FD relay system with SWIPT, where RIS phase shifts, precoding vectors, and PS factors were jointly optimized to maximize the achievable rate. In [28], the performance of an RIS-assisted FD system with user-specific RIS deployments was analyzed over correlated Nakagami-m fading channels, where closed-form expressions for signal power statistics, OP, and achievable rates were derived. The authors in [85] analyzed an overlay FD cooperative cognitive radio network over generalized α–μ fading channels while considering hardware impairments and hybrid SWIPT receivers with both TS and PS protocols. Furthermore, a unified analytical framework for RIS-assisted two-way FD communication systems was developed in [86], supporting the multiple fading distributions and providing analytical expressions for OP, SER, and ergodic rate. To highlight the key distinctions between the existing studies and the proposed framework, a comparative summary of the related works is presented in Table 2.4.

2.2 Chapter Summary

This Chapter presented a comprehensive review of the existing literature related to RIS-assisted vehicular communication, SWIPT-enabled wireless networks, UAV-assisted communication systems, and NTNs. The review covered analytical performance evaluation, generalized fading channel models, EH techniques, optimization frameworks, and ML-based approaches reported in recent studies. The literature

Table 2.4: Comparison of existing FD UAV works with the proposed framework

Ref.	SWIPT / EH Model	Practical RIS Model	Duplex Type	Channel Model	Per. Ana.	Opti.
[19]	×	×	FD	Nakagami-m	✓	×
[18]	×	×	FD	Rayleigh	✓	✓
[51]	Hybrid NL-EH	×	FD	Rayleigh	✓	×
[22]	×	✓	FD	Weibull	✓	×
[23]	×	✓	HD	Rayleigh	✓	×
[15]	×	×	HD	Rayleigh	✓	×
[20]	×	×	FD	Nakagami-m	✓	✓
[21]	×	×	FD	Correlated Nakagami-m	✓	×
[24]	NL-EH	×	FD	Rayleigh	✓	✓
[25]	Wireless power transfer	×	FD	Rayleigh	✓	✓
[26]	NL-EH (PS + TS SWIPT)	×	FD	Rayleigh	✓	✓
[27]	PS-SWIPT	×	FD	Rayleigh	✓	✓
[28]	×	×	FD	Correlated Nakagami-m	✓	×
[85]	Hybrid TS + PS SWIPT	×	FD	α–μ	✓	✓
[86]	×	×	FD	Rayleigh, Nakagami-m, Weibull, κ–μ	✓	×
This Work	Linear PS-SWIPT +NL PTS-SWIPT	✓	FD	α–μ	✓	✓

survey revealed several important research gaps, including limited investigations on multi-RIS-assisted vehicular communication under generalized fading environments, insufficient consideration of vehicular mobility and imperfect CSI in SWIPT-enabled systems, inadequate exploration of practical EH models in UAV-assisted communication, and the lack of unified frameworks incorporating FD operation, RIS assistance, SWIPT, and UAV relaying for NTN applications. These identified limitations provide the primary motivation for the analytical, optimization, and intelligent communication frameworks developed in the subsequent Chapters of this Thesis.

Chapter 3

Multi-RIS-assisted V2V Communication: Performance Analysis and Optimization Over Generalized Fading

3.1 Introduction

The rapid advancement of intelligent transportation systems has led to the emergence of the Internet-of-Vehicles (IoV) as a fundamental component of next-generation wireless communication networks. IoV integrates vehicles with communication, sensing, and computing capabilities, enabling seamless connectivity among vehicles, infrastructure, and network entities. With the evolution towards Sixth-Generation (6G) wireless systems, IoV is expected to support ultra-reliable, low-latency, and high-data-rate communication services.

Traditional vehicular communication systems, primarily based on Dedicated Short-Range Communication (DSRC), suffer from limitations in terms of scalability, cover-

age, and reliability. cellular Vehicle-to-Everything (C-V2X) has emerged as a promising alternative, offering improved Spectral Efficiency (SE), enhanced coverage, and higher reliability. However, vehicular environments are characterized by rapid mobility, severe multipath fading, and frequent blockage, which degrade the system performance.

To address these challenges, Reconfigurable Intelligent Surfaces (RISs) have been introduced as a key enabling technology. RISs consist of programmable passive elements capable of controlling the phase and amplitude of incident electromagnetic waves. By intelligently reconfiguring the wireless environment, RISs can establish virtual Line-of-Sight (VLoS) links and significantly enhance signal quality.

In addition, Deep Learning (DL) techniques, particularly Deep Neural Network (DNN), have shown significant potential in handling complex optimization problems in wireless communications. DNNs enable fast and efficient prediction of system performance, thereby reducing computational complexity.

Motivated by these developments, this Chapter investigates a multi-RIS-assisted Vehicle-to-Vehicle (V2V) communication system, focusing on the performance analysis, optimization, and DL-based prediction.

3.2 Organization of The Chapter

The remainder of the Chapter is structured as follows. In Section 3.3, the system model and the channel models both Exhaustive RIS-aided Scheme (ERS) and Opportunistic RIS-aided Scheme (ORS) schemes are discussed. Section 3.4 evaluates the Outage Probability (OP), Average Symbol Error Rate (ASER), and Ergodic Capacity (EC) performance metrics. Section 3.5 formulates the rate maximization and power

minimization optimization problem and subsequently its solutions are provided. Section 3.6 gives a detailed explanation of the proposed DNN model for prediction of performance metric and optimization problems results. Section 3.7 presents the numerical results followed by concluding remarks of this Chapter are given in Section 3.8.

3.3 System and Channel Models

In this section, we describe the proposed system and channel models for multi-RIS-aided V2V wireless communication.

3.3.1 System Model

As shown in Fig. 3.3, we consider a multi-RIS-aided V2V wireless communication system, consisting of a single antenna source vehicle (S), that communicates with a single-antenna destination vehicle (D) with the assistance of L passive RISs (RIS$_l$, l=$1, 2, \ldots, L$). It is important to note that the lth RIS is equipped with a total of N passive reflecting elements. Let $\Theta_l = \text{diag}([\kappa_1^{(1)} e^{j\theta_l^{(1)}}, \ldots, \kappa_l^{(n)} e^{j\theta_l^{(n)}}, \ldots, \kappa_L^{(N)} e^{j\theta_L^{(N)}}])$, where $\kappa_l^{(n)} \in (0, 1]$ and $\theta_l^{(n)} \in [0, 2\pi)$.[1] In practice, independently controlling the reflection amplitude and phase shift is costly. Therefore, each element is typically designed to maximize signal reflection for simplicity [87], [88], [89]. Due to the high path loss, it is assumed that the power of signals reflected by the RIS two or more times is negligible and therefore ignored. Given that the direct transmission between S and D is impeded by the obstacles, we deploy RISs to assist the transmission. Furthermore, we assume that the perfect Channel State Information (CSI) is available

[1] In practice, each element of the RIS is usually designed to maximize the signal reflection. Thus, we set $\kappa_l^{(n)} = 1, \forall N$, in this paper for simplicity.

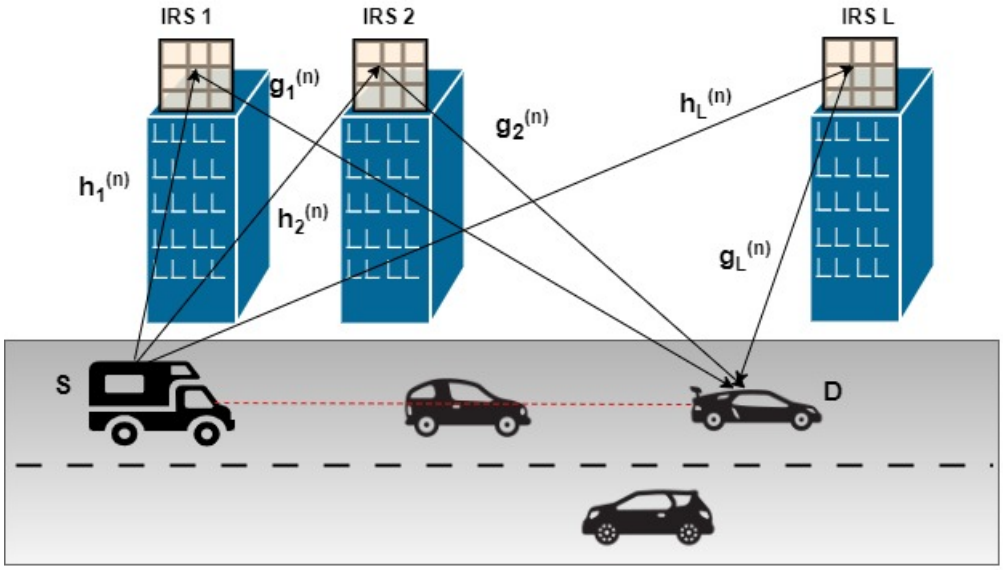

Fig. 3.1: A multi-RIS-aided V2V system model for ITS applications

at the receiver. By creating a VLoS path, the RISs attempt to improve the Signal-to-Noise Ratio (SNR) at D. The real-time tunable RISs are used to reduce the rapid fluctuations in the received signal strength, which occurs due to the Doppler effect and the multipath fading effect caused by the mobility of vehicles [90].

Let $\bar{h}_l^{(n)}$ and $\bar{g}_l^{(n)}$ be represented in terms of polar form as : $\bar{h}_l^{(n)} = h_l^{(n)} e^{j\phi_l^{(n)}}$ and $\bar{g}_l^{(n)} = g_l^{(n)} e^{j\xi_l^{(n)}}$, respectively, where $h_l^{(n)}$ and $g_l^{(n)}$ are the magnitudes of the channel fading coefficients and $\phi_l^{(n)}$ and $\xi_l^{(n)}$ are the phases with $\{\phi_l^{(n)}, \xi_l^{(n)}\} \in [0, 2\pi)$. We consider the full reflection assumption and hence, $\Theta_l^{(n,n)} = e^{j\theta_l^{(n)}}$. The free-space path loss p_l is given by

$$p_l = \frac{\lambda^2 \sqrt{G_t G_r}}{16\pi d_{1,l} d_{2,l}}. \tag{3.1}$$

The propagation of waves in V2V communications entails scattering and re-scattering within the local environments of both the transmitter and receiver, given their mobile nature [91]. This double-bouncing phenomenon is commonly characterized by mod-

eling it as a product of fading amplitudes. Commonly employed distributions for representing the double-bouncing scattering phenomenon includes the double-Rayleigh [92], double-Nakagami [93], double-Weibull, log-normal, and gamma-gamma distributions [94]. However, it is noteworthy that all these aforementioned double-bouncing distributions are special cases of a more comprehensive double generalized Gamma (dGG) distribution [1], [94], which provides a versatile channel model capable of accurately representing various mobile propagation conditions. Consequently, it is assumed that both the fading channel coefficients from the S to the RIS$_l$ and from RIS$_l$ to the D follows a dGG distribution.

3.3.1.1 Exhaustive RIS Scheme

In the ERS, all RISs assist the transmission from S to D by reflecting the replicas of transmitted signal over the same time-frequency channel. Each RIS directs its beam to the D, preventing interference. Consequently, D receives a combined signal from all RISs. Using a coherent combination, the received signal at D, consisting of the reflected signals from all L RISs, can be written as

$$\hat{y} = \sqrt{P_t} p_l \left[\sum_{l=1}^{L} \sum_{n=1}^{N} \bar{h}_l^{(n)} \bar{g}_l^{(n)} \right] x + w, \tag{3.2}$$

where P_t denotes the average transmit power of signal, x represents the transmitted signal/symbol with $\mathbb{E}[|x^2|] = 1$, and w denotes the Additive White Gaussian Noise (AWGN).

The instantaneous SNR at D is represented as

$$\hat{\gamma}_l = \frac{P_t p_l^2 \left| \sum_{l=1}^{L} \sum_{n=1}^{N} h_l^{(n)} g_l^{(n)} \right|^2}{N_0} = \frac{P_t p_l^2 \hat{t}_l^2}{N_0}, \tag{3.3}$$

where $\hat{t}_l = \left|\sum_{l=1}^{L}\sum_{n=1}^{N} s_l^{(n)}\right|$ and $s_l^{(n)} = h_l^{(n)} g_l^{(n)}$. The positive Random Variables (RV) $\hat{t}_l^2$ is used to obtain the Probability Density Function (PDF) of $\hat{\gamma}_l$ using transformation of RVs technique.

3.3.1.2 Opportunistic RIS Scheme

Instead of using all the RISs, we propose the ORS to reduce the resource usage. In this scheme, only the most suitable RIS assists in the transmission. The ORS offers a low-complexity and energy-efficient protocol at the receiver, handling fewer reflecting signals than the ERS. The signal received at D from RIS$_l$ can be expressed as

$$y = \sqrt{P_t} p_l \left[\sum_{n=1}^{N} \bar{h}_l^{(n)} \bar{g}_l^{(n)}\right] x + w. \tag{3.4}$$

The instantaneous SNR at D is represented as

$$\gamma_l = \frac{P_t p_l^2 \left|\sum_{n=1}^{N} h_l^{(n)} g_l^{(n)}\right|^2}{N_0} = \frac{P_t p_l^2 t_l^2}{N_0}, \tag{3.5}$$

where $t_l = \left|\sum_{n=1}^{N} s_l^{(n)}\right|$. The PDF of γ_l is obtained by applying the transformation of RVs technique, using the positive RV t_l^2.

3.3.1.3 RIS Selection Strategy in ORS

The transmission of the information signal originating from S undergoes reflection by a network comprising L individual RISs, directing it towards D. From the array of received signals at D, the signal acquired from the RIS demonstrating the maximum end-to-end instantaneous SNR is designated for subsequent processing, while signals received from the remaining RISs will be disregarded. The end-to-end instantaneous

SNR pertaining to the chosen RIS in ORS can be expressed as

$$\gamma^*_{max} = \max_{l=1,\ldots,L} \{\gamma_l\}. \tag{3.6}$$

The channel corresponding to maximum SNR is represented as t^*_{max}. Furthermore, it is assumed that the CSI is estimated at D by using pilot symbols prior to each transmission phase, enabling the calculation of the instantaneous SNR at D to select the best RIS. Additionally, the RIS selection strategy in ORS ensures that only one RIS, possessing the best end-to-end SNR, will be active at any given time. Therefore, this will avoid the inter-RIS reflection [95]. As per the order statistics theory, the CDF of γ^*_{max} is given by

$$F_{\gamma^*_{max}}(\gamma) = \prod_{l=1}^{L} F_{\gamma_l}(\gamma). \tag{3.7}$$

3.3.2 Statistical Models for Mobility

We analyze the effect of mobility on the received signal power in S to RIS$_l$ and RIS$_l$ to D link using the Random Waypoint (RWP) model. The average received power is represented as $P_t r^{-a}$, where a ($2 \leq a \leq 5$) is the path-loss exponent and r denotes distance. For a stationary vehicle, the distance-based path-loss term r^{-a} remains constant. However, for a mobile vehicle, the distance r varies randomly. The RWP model assumes that D can be at random coordinates relative to S, based on the network's layout. The PDF of r is represented as [96]

$$f_r(x) = \sum_{k=1}^{K} \frac{C_k}{x^{\beta_k} d^{\beta_k+1}}, \tag{3.8}$$

where parameters k, C_k , and β_k depend on the number of dimensions considered in the topology and distance indicates the separation between S and RIS$_l$ (i.e. $d_{1,l}$) as well as the separation between RIS$_l$ and D (i.e. $d_{2,l}$). For One-dimensional (1-D) topology : $k = 2$, $C_k = [6, 6]$, and $\beta_k = [1, 2]$; for Two-dimensional (2-D) : topology $k = 3$, $C_k = 173 \times [324, 420, 96]$, and $\beta_k = [1, 3, 55]$; and for Three-dimensional (3-D) : topology $k = 3$, $C_k = 172 \times [735, 1190, 455]$, and $\beta_k = [2, 4, 6]$.

The signal received at D from RIS$_l$ can be expressed as

$$\ddot{y} = \sqrt{P_t} \left[\sum_{n=1}^{N} h_l^{(r)} \bar{h}_l^{(n)} g_l^{(r)} \bar{g}_l^{(n)} \right] x + w, \tag{3.9}$$

where $h_l^{(r)}$ and $g_l^{(r)}$ are path-loss induced by S and D, respectively, due to mobility.

The instantaneous SNR at D is represented as

$$\ddot{\gamma}_l = \frac{P_t \left| \sum_{n=1}^{N} h_l^{(r)} h_l^{(n)} g_l^{(r)} g_l^{(n)} \right|^2}{N_0} = \frac{P_t \left| \sum_{n=1}^{N} \ddot{t}_l \right|^2}{N_0} \tag{3.10}$$

where $\ddot{t}_l = h_l^{(r)} h_l^{(n)} g_l^{(r)} g_l^{(n)}$ is the product of four RVs.

$$f_Z(z) = \Psi z^{\alpha_2 m_2 - 1} H_{0,2}^{2,0} \left[\varphi z^{\alpha_2} \;\middle|\; \begin{matrix} - \\ (0,1), (\frac{\alpha_1 m_1 - \alpha_2 m_2}{\alpha_1}, \frac{\alpha_2}{\alpha_1}) \end{matrix} \right], \tag{3.11}$$

$$f_{s_l^{(n)}}(z) = A_l^{(n)} z^{\alpha_{2,l}^{(n)} m_{2,l}^{(n)} - 1} \times H_{0,4}^{4,0} \left[B_l^{(n)^{-1}} z^{\alpha_{2,l}^{(n)}} \;\middle|\; \begin{matrix} - \\ (0,1), \left(m_{1,l}^{(n)} - \frac{\alpha_{2,l}^{(n)} m_{2,l}^{(n)}}{\alpha_{1,l}^{(n)}}, \frac{\alpha_{2,l}^{(n)}}{\alpha_{1,l}^{(n)}} \right), \left(m_{3,l}^{(n)} - \frac{\alpha_{2,l}^{(n)} m_{2,l}^{(n)}}{\alpha_{3,l}^{(n)}}, \frac{\alpha_{2,l}^{(n)}}{\alpha_{3,l}^{(n)}} \right) \\ \left(m_{4,l}^{(n)} - \frac{\alpha_{2,l}^{(n)} m_{2,l}^{(n)}}{\alpha_{4,l}^{(n)}}, \frac{\alpha_{2,l}^{(n)}}{\alpha_{4,l}^{(n)}} \right) \end{matrix} \right], \tag{3.12}$$

$$M_{s_l^{(n)}}(r) = A_l^{(n)} r^{-\alpha_{2,l}^{(n)} m_{2,l}^{(n)}} \times H_{1,4}^{4,1}\left[B_l^{(n)^{-1}} r^{-\alpha_{2,l}^{(n)}} \middle| \begin{matrix} (1-\alpha_{2,l}^{(n)} m_{2,l}^{(n)}, \alpha_{2,l}^{(n)}) \\ (0,1), \left(m_{1,l}^{(n)} - \frac{\alpha_{2,l}^{(n)} m_{2,l}^{(n)}}{\alpha_{1,l}^{(n)}}, \frac{\alpha_{2,l}^{(n)}}{\alpha_{1,l}^{(n)}}\right), \left(m_{3,l}^{(n)} - \frac{\alpha_{2,l}^{(n)} m_{2,l}^{(n)}}{\alpha_{3,l}^{(n)}}, \frac{\alpha_{2,l}^{(n)}}{\alpha_{3,l}^{(n)}}\right) \\ \left(m_{4,l}^{(n)} - \frac{\alpha_{2,l}^{(n)} m_{2,l}^{(n)}}{\alpha_{4,l}^{(n)}}, \frac{\alpha_{2,l}^{(n)}}{\alpha_{4,l}^{(n)}}\right) \end{matrix} \right]. \tag{3.13}$$

3.3.3 Channel Model

The PDF of the dGG RV $X(\alpha_1, m_1, \alpha_2, m_2)$ expressed in terms of Fox's H-function [2], is represented by (3.11) at the top of this page.

In (3.11), α_1, m_1, α_2, m_2 are Gamma distribution shaping parameters, $\Psi = \frac{\alpha_2}{\left(\left(\frac{\Omega_1}{m_1}\right)^{\frac{\alpha_2 m_2}{\alpha_1}} \left(\frac{\Omega_2}{m_2}\right)^{m_2} \Gamma(m_1)\Gamma(m_2)\right)}$, $\varphi = \left(\frac{m_2}{\Omega_2}\right)\left(\frac{m_1}{\Omega_1}\right)^{\frac{\alpha_2}{\alpha_1}}$, and $\Omega_j = \left(\frac{\left(E\left[X_j^2\right]\right)\Gamma(m_j)}{\Gamma\left(m_j + \frac{2}{\alpha_j}\right)}\right)^{\frac{\alpha_j}{2}}$ is the $\alpha_j{}^{th}$ root mean value, $j = 1, 2$. Based on its four shaping parameters, the dGG distribution becomes more flexible, making it highly effective for accurately modeling the diverse V2V channel.

Next that $s_l^{(n)} = h_l^{(n)} g_l^{(n)}$ with mean and variance of μ_s and σ_s^2, respectively. In addition, $h_l^{(n)}$ is the dGG distributed with shaping parameters $(\alpha_{1,l}^{(n)}, m_{1,l}^{(n)}, \alpha_{2,l}^{(n)}, m_{2,l}^{(n)})$ and $\Psi_{1,l}^{(n)}$, $\varphi_{1,k}^{(n)}$. Likewise, $g_l^{(n)}$ follows a dGG distribution with shaping parameters $(\alpha_{3,l}^{(n)}, m_{3,l}^{(n)}, \alpha_{4,l}^{(n)}, m_{4,l}^{(n)})$ and $\Psi_{2,l}^{(n)}$, $\varphi_{2,l}^{(n)}$. Assuming $\Psi_{j,l}^{(n)} = \Psi$ and $\varphi_{j,l}^{(n)} = \varphi$, the PDF of $s_l^{(n)}$ is given by (3.12) at the top of this page.

In (3.12), $B_l^{(n)} = \left(\varphi_{1,l}^{(n)}\right)^{-1} \left(\varphi_{2,l}^{(n)}\right)^{-\frac{\alpha_{2,l}^{(n)}}{\alpha_{4,l}^{(n)}}}$, $A_l^{(n)} = \frac{\Psi_{1,l}^{(n)} \Psi_{2,l}^{(n)}}{\alpha_{4,l}^{(n)}} \left(\varphi_{2,l}^{(n)}\right)^{\frac{\alpha_{2,l}^{(n)} m_{2,l}^{(n)} - \alpha_{4,l}^{(n)} m_{4,l}^{(n)}}{\alpha_{4,l}^{(n)}}}$, and r^{th} moment of $s_l^{(n)}$ is given by (3.13) at the top of the next page.

$$f_{\hat{\gamma}_l}(\gamma) = \frac{1}{2\sigma_1^2}\left(\frac{\gamma}{\rho_1}\right)^{-\frac{1}{4}}\left(\frac{1}{\overline{\gamma}}\right)^{3/4}\exp\left(-\frac{\gamma+\rho_1\overline{\gamma}}{2\overline{\gamma}\sigma_1^2}\right)I_{-\frac{1}{2}}\left(\frac{\sqrt{\gamma\rho_1}}{\sqrt{\overline{\gamma}}\sigma_1^2}\right), \tag{3.17}$$

3.3.3.1 Exhaustive RIS Scheme

As $\hat{t}_l = \sum_{l=1}^{L}\sum_{n=1}^{N} s_l^{(n)}$, the Central Limit Theorem (CLT) implies that for sufficiently large values of L and N (i.e., $L, N >> 1$), $\hat{t}_l$ converges to a Gaussian distribution with mean and variance given by $\hat{\mu}_t = LN\mu_s$ and $\hat{\sigma}_t^2 = LN\sigma_s^2$, respectively, i.e., $\hat{t}_l \sim \mathcal{N}(\hat{\mu}_t, \hat{\sigma}_t^2)$.

The PDF and CDF of $\hat{t}_l$ are respectively given by

$$f_{\hat{t}_l}(z) = \begin{cases} \frac{1}{\sqrt{2\pi\hat{\sigma}_t^2}}\exp\left(-\frac{(z-\hat{\mu}_t)^2}{2\hat{\sigma}_t^2}\right) & \text{if } z > 0, \\ 0 & \text{if } z = 0, \end{cases} \tag{3.14}$$

and

$$\begin{aligned} F_{\hat{t}_l}(z) &= \int_{-\infty}^{z} f_{\hat{t}_l}(z)dz \\ &= \begin{cases} 1 - Q\left(\frac{z-\hat{\mu}_t}{\sqrt{2\hat{\sigma}_t^2}}\right) & \text{if } z > 0, \\ 0, & \text{if } z = 0. \end{cases} \end{aligned} \tag{3.15}$$

The PDF of $\hat{\gamma}_l$ is given by (3.17) at the top of the next page. In (3.17), $\bar{\gamma} = \frac{P_t}{N_o}$ is the average SNR, $\rho_1 = \hat{\mu}_t^2$, and $\sigma_1^2 = \hat{\sigma}_t^2$.

The CDF of $\hat{\gamma}_l$ is represented as

$$F_{\hat{\gamma}_l}(\gamma) = 1 - Q_{\frac{1}{2}}\left(\frac{\sqrt{\rho}_1}{\sigma_1}, \frac{\sqrt{\gamma}}{\sqrt{\overline{\gamma}}\sigma_1}\right), \tag{3.16}$$

$$f_{\gamma_l}(\gamma) = \frac{1}{2\sigma^2}\left(\frac{\gamma}{\rho}\right)^{-\frac{1}{4}}\left(\frac{1}{\overline{\gamma}}\right)^{3/4}\exp\left(-\frac{\gamma+\rho\overline{\gamma}}{2\overline{\gamma}\sigma^2}\right)I_{-\frac{1}{2}}\left(\frac{\sqrt{\gamma\rho}}{\sqrt{\overline{\gamma}}\sigma^2}\right), \tag{3.20}$$

3.3.3.2 Opportunistic RIS Scheme

As $t_l = \sum_{n=1}^{N} s_l^{(n)}$ and applying CLT for large vaules of N (i.e., $N >> 1$), t_l coincide to a Gaussian distribution with mean and variance as $\mu_t = N\mu_s$ and ${\sigma_t}^2 = N\sigma_s^2$, respectively, i.e., $t_l \sim \mathcal{N}(\mu_t, \sigma_t^2)$.

The PDF and CDF of t_l are, respectively, given by

$$f_{t_l}(z) = \begin{cases} \frac{1}{\sqrt{2\pi{\sigma_t}^2}}\exp\left(-\frac{(z-\mu_t)^2}{2{\sigma_t}^2}\right) & \text{if } z > 0, \\ 0 & \text{if } z = 0, \end{cases} \tag{3.18}$$

and

$$\begin{aligned} F_{t_l}(z) &= \int_{-\infty}^{z} f_{t_l}(z)dz \\ &= \begin{cases} 1 - Q\left(\frac{z-\mu_t}{\sqrt{2{\sigma_t}^2}}\right) & \text{if } z > 0, \\ 0, & \text{if } z = 0. \end{cases} \end{aligned} \tag{3.19}$$

and the PDF of γ_l is given by (3.20) expressed at the top of this page. Here $\rho = {\mu_t}^2$ and $\sigma^2 = {\sigma_t}^2$. As a result, the CDF of γ_l can be represented as

$$F_{\gamma_l}(\gamma) = 1 - Q_{\frac{1}{2}}\left(\frac{\sqrt{\rho}}{\sigma}, \frac{\sqrt{\gamma}}{\sqrt{\overline{\gamma}}\sigma}\right). \tag{3.21}$$

3.3.3.3 PDF of Imperfect Channel Conditions

In practical scenarios, the Radio-Frequency (RF) channel changes rapidly due to the mobility of S and D. Due to this, there arises channel estimation errors leading to an

imperfect CSI. Hence, the imperfect channel gain of the cascaded link is written as [97]

$$\tilde{s}_l^{(n)} = \delta s_l^{(n)} + \sqrt{1-\delta^2}\epsilon, \tag{3.22}$$

where $\delta \in [0, 1]$. Here, $\delta = 1$ represents perfect CSI with no errors. Moreover, ϵ is a RV, which is independent of $s_l^{(n)}$, following zero-mean Gaussian distribution with variance equal to σ_e^2.

3.4 Performance Analysis

This section furnishes an elaborative discussion on deriving the closed-form expressions for OP, ASER, and EC considering a CSI.

3.4.1 Exhaustive RIS Scheme

3.4.1.1 Outage Probability

The proposed ERS is considered to be in outage, when the instantaneous SNR falls below a specific threshold value γ_{th} and the corresponding OP is given by

$$P_{out} = \Pr[\hat{\gamma}_l \leq \gamma_{\text{th}}] = F_{\hat{\gamma}_l}(\gamma_{\text{th}}). \tag{3.23}$$

The above equation is reformulated using $F_{\gamma_l}(\gamma)$ as follows

$$P_{out} = F_{\hat{\gamma}_l}(\gamma_{\text{th}})\,, \tag{3.24}$$

where $F_{\hat{\gamma}_l}(\gamma_{\text{th}})$ is computed by substituting $\gamma = \gamma_{\text{th}}$ in (3.16).

$$\hat{P}_{\text{out}} = \exp\left(-\frac{\rho_1}{2\sigma_1^2}\right)\sum_{\varsigma=0}^{\infty}\frac{(-1)^{\varsigma}(\varsigma+\vartheta-1)!}{\varsigma!(\vartheta-\varsigma)!}\frac{\vartheta^{1-2\varsigma}}{\Gamma(\varsigma+1/2)}j^{2\varsigma}\left(\frac{1}{2\sigma_1^2}\right)^{\varsigma}\rho_1^{\varsigma}\Upsilon\left(\varsigma+\frac{1}{2},\frac{\gamma_{th}}{2\bar{\gamma}\sigma_1^2}\right) \tag{3.25}$$

The exact closed-form expression for the OP is complex and lacks clear insights. Therefore, we provide an asymptotic analysis for the outage in the high-SNR region, considering ERS. The $I_e(d)$ in (3.17) can be expressed as $I_e(d) = \sum_{\vartheta=0}^{\infty} j^{-e}(-1)^{\vartheta}\frac{(\vartheta+\varsigma-1)!}{\varsigma!(\vartheta-\varsigma)!}\vartheta^{1-2\varsigma}\,\Gamma(e+\varsigma+1)\left(\frac{jd}{2}\right)^{2\varsigma+e}$, where j represents the imaginary number. The asymptotic expression is given by (3.25) at the top of this page.

3.4.1.2 Average Symbol Error Rate

The ASER for the ERS, employing M-ary Phase-Shift Keying (MPSK) modulation, is computed by utilizing the CDF of $\hat{\gamma}_l$ and is expressed as [98]

$$P_{\text{ser}} = \frac{p\sqrt{q}}{2\sqrt{2\pi}}\int_0^{\infty}\frac{F_{\hat{\gamma}_l}(\gamma)}{\sqrt{\gamma}}e^{\frac{-p\gamma}{2}}\,d\gamma\,, \tag{3.26}$$

where p and q are modulation scheme parameters and it changes accordingly for different modulation schemes. For example, $\{p = 1, q = 2\}$ for BPSK, $\{p = 2, q = 1\}$ for QPSK, $\{p = 2, q = 0.3\}$ for 8-PSK, and $\{p = 2, q = 0.076\}$ for 16-PSK.

The integral in equation (3.26) is approximated by employing a k-point Gauss–Laguerre quadrature method [98], and consequently, the ASER expression is expressed as

$$P_{\text{ser}} \approx \frac{p\sqrt{q}}{2\sqrt{2\pi}}\sum_{j=1}^{k}W_j F_{\hat{\gamma}_l}(\phi_j), \tag{3.27}$$

where W_j represents the weight coefficient and ϕ_j denotes the jth zero of the Laguerre

polynomial $L_k^{(-1/2)}(x)$, which is expressed as

$$L_k^{(-1/2)}(x) = \frac{2}{k}\sum_{b=0}^{k}\binom{k-\frac{1}{2}}{k-b}\left(\frac{-x^b}{b!}\right). \tag{3.28}$$

The weight coefficient W_j is defined as

$$W_j = \frac{\Gamma(k+1/2)\,\phi_j}{k!\left[(k+1)\,L_{k+1}^{(-1/2)}(\phi_j)\right]^2}. \tag{3.29}$$

By substituting (3.16) in (3.27), we obtain the final expression for ASER as follows

$$P_{\text{ser}} \approx \frac{p\sqrt{q}}{2\sqrt{2\pi}}\sum_{j=1}^{k} W_j F_{\hat{\gamma}_l}(\phi_j). \tag{3.30}$$

3.4.1.3 Ergodic Capacity

The EC for the ERS is given by [99]

$$C = \frac{1}{\ln 2}\int_0^\infty \frac{1-F_{\hat{\gamma}_l}(\gamma)}{1+\gamma}d\gamma. \tag{3.31}$$

Due to the mathematical intractability of (3.31), we utilize the generalized Gauss-Laguerre quadrature method [98] and reformulate the EC as

$$C = \frac{1}{\ln 2}\sum_{j=1}^{k} W_j F_{\hat{a}_1}(\phi_j), \tag{3.32}$$

where $F_{\hat{a}_1}(\phi_j) = \frac{1-F_{\hat{\gamma}_1}(\phi_j)}{(1+x_j)x^{(-\frac{1}{2})}e^{-x_j}}$.

By substituting (3.16) into (3.32), we obtain the final expression for the EC as

$$C = \frac{1}{\ln 2}\sum_{j=1}^{k} W_j F_{\hat{a}_1}(\phi_j). \tag{3.33}$$

$$P_{\text{out}} = \prod_{l=1}^{L} \exp\left(-\frac{\rho}{2\sigma^2}\right) \sum_{\varsigma=0}^{\infty} \frac{(-1)^{\varsigma}(\varsigma+\vartheta-1)!}{\varsigma!(\vartheta-\varsigma)!} \frac{\vartheta^{1-2\varsigma}}{\Gamma(\varsigma+1/2)} j^{2\varsigma} \left(\frac{1}{2\sigma^2}\right)^{\varsigma} \rho^{\varsigma} \Upsilon\left(\varsigma+\frac{1}{2}, \frac{\gamma_{th}}{2\bar{\gamma}\sigma^2}\right). \tag{3.36}$$

3.4.2 Opportunistic RIS Scheme

3.4.2.1 Outage Probability

The proposed ORS is considered to be in outage, when the instantaneous SNR of the best link, which corresponds to the highest end-to-end instantaneous SNR, falls below a specific threshold value γ_{th} and the OP is given by

$$P_{out} = \Pr[\gamma^*_{max} \leq \gamma_{\text{th}}] = F_{\gamma^*_{max}}(\gamma_{\text{th}}). \tag{3.34}$$

By substituting (3.7) into (3.34), it can be rewritten in terms of $F_{\gamma_l}(\gamma)$ as follows

$$P_{out} = \prod_{l=1}^{L} F_{\gamma_l}(\gamma_{th}), \tag{3.35}$$

where $F_{\gamma_l}(\gamma_{\text{th}})$ is computed by substituting $\gamma = \gamma_{\text{th}}$ in (3.21).

It is to be noted that the exact closed-form expression for the OP is quite intricate and do not readily yield any meaningful insights. By substituting the $I_w(d)$ expansion in (3.35), asymptotic expression of outage considering ORS in the high-SNR region can be expressed as (3.36), shown at the top of this page.

3.4.2.2 Average Symbol Error Rate

The ASER for the considered ORS, employing MPSK modulation, is computed by utilizing the CDF of γ^*_{max} and is expressed as [98]

$$P_{\text{ser}} = \frac{p\sqrt{q}}{2\sqrt{2\pi}} \int_0^\infty \frac{F_{\gamma^*_{max}}(\gamma)}{\sqrt{\gamma}} e^{\frac{-p\gamma}{2}} \, d\gamma. \tag{3.37}$$

The integral in equation (5.48) can be approximated by employing a k-point Gauss–Laguerre quadrature method [98], and consequently, the ASER expression can be expressed as

$$P_{\text{ser}} \approx \frac{p\sqrt{q}}{2\sqrt{2\pi}} \sum_{j=1}^{k} W_j F_{\gamma^*_{max}}(\phi_j). \tag{3.38}$$

By substituting (3.7) in (5.49), we obtain the final expression for ASER as follows

$$P_{\text{ser}} \approx \frac{p\sqrt{q}}{2\sqrt{2\pi}} \sum_{j=1}^{k} W_j \prod_{l=1}^{L} F_{\gamma_l}(\phi_j). \tag{3.39}$$

3.4.2.3 Ergodic Capacity

The EC for the ORS is given by [99]

$$C = \frac{1}{\ln 2} \int_0^\infty \frac{1 - F_{\gamma^*_{max}}(\gamma)}{1+\gamma} \, d\gamma. \tag{3.40}$$

Due to the mathematical intractability of (5.52), we utilize the generalized Gauss-Laguerre quadrature method [98] and reformulate the EC as

$$C = \frac{1}{\ln 2} \sum_{j=1}^{k} W_j F_a(\phi_j) \, , \tag{3.41}$$

where $F_a(\phi_j) = \frac{1-F_{\gamma^*_{max}}(\phi_j)}{(1+x_j)x^{(-\frac{1}{2})}e^{-x_j}}$.

By substituting (3.7) into (5.53), we obtain the final expression for the EC as

$$C = \frac{1}{\ln 2}\sum_{j=1}^{k} W_j \prod_{l=1}^{L} F_a(\phi_j). \tag{3.42}$$

To achieve higher data transmission rates, employing a high-order modulation scheme is necessary. However, such schemes typically demand increased transmit power to uphold signal quality and reliability, especially over longer distances. In the subsequent section, we introduce two optimization problems aimed at optimizing transmit power for the multi-RIS aided V2V system under consideration.

3.5 Optimization Outlook

Herein, we present the problem formulation and potential solutions for optimizing two objectives: rate and power using multi-RIS. Our aim is to determine the optimal transmit power values, while adhering to constraints on both rate and power. Subsequent subsections delve into detailed discussions of the optimization problems and their corresponding solutions.

3.5.1 Rate Maximization via Multi-RIS

The achievable information rate at D aided by the multiple RISs is given by

$$R_u = \log_2(1+\gamma). \tag{3.43}$$

It is to be noted that, here $\gamma = \hat{\gamma}_l$ for ERS and $\gamma = {\gamma^*}_{max}$ for ORS. Our objective is to maximize the information rate between S and D, while simultaneously ensuring

compliance with the rate constraint and limiting the total transmit power at S. The corresponding optimization problem is mathematically represented as follows

$$\begin{aligned} \text{(P3.1)} : \underset{P_t}{\text{maximize}} \quad & R_u \\ \text{subject to} \quad & \text{(C1)} : \ 0 < P_t \leq P_{max}, \\ & \text{(C2)} : \ R_u \geq R_{th}, \end{aligned} \tag{3.44}$$

where P_{max} and R_{th} are the maximum transmit power and maximum rate threshold value, respectively.

The problem (P3.1) is a concave maximation problem aiming to maximize the information data by optimizing the power, while ensuring that the transmit power does not surpass P_{max} and the rate remains above a predefined threshold R_{th}. Despite R_u being a complex expression of the optimization variable, in our optimization problem, it becomes a concave objective function, making it easy to apply all the Karush-Kuhn-Tucker (KKT) conditions.

The Lagrangian corresponding to (P3.1) is expressed as

$$\mathcal{L}(P_t; \nu_1, \nu_2) = f(P_t) - \nu_1 g(P_t) - \nu_2 h(P_t), \tag{3.45}$$

where $f(P_t) = \log_2(1+\gamma)$, $g(P_t) = P_t - P_{max}$, and $h(P_t) = R_{th} - \log_2(1+\gamma)$ with ν_1, ν_2 are the Lagrange multipliers associated with their respective constraints (C1) and (C2). For optimal value, the following must hold: $\nabla\mathcal{L}(P_t; \nu_1, \nu_2) = 0$, i.e.,

$$\frac{\partial\mathcal{L}(P_t; \nu_1, \nu_2)}{\partial P_t} \Rightarrow \frac{1}{ln2(1+\gamma)} - \nu_1 + \nu_2 \frac{1}{ln2(1+\gamma)} = 0. \tag{3.46}$$

The complementary slackness expressions are given by

$$\nu_1 \cdot g(P_t) = 0, \tag{3.47}$$

$$\nu_2 \cdot h(P_t) = 0. \tag{3.48}$$

The possible solutions are outlined in the subsequent theorems.

Theorem 1. *If* $\nu_1 \neq 0 \Rightarrow g(P_t) = 0; \nu_2 = 0 \Rightarrow h(P_t) \neq 0$ *then, we obtain the following optimized value*

$$P_{t,1} = P_{max}. \tag{3.49}$$

Theorem 2. *If* $\nu_1 \neq 0 \Rightarrow g(P_t) = 0; \nu_2 \neq 0 \Rightarrow h(P_t) = 0$ *then, we obtain the following optimized values*

$$P_{t,1} = P_{max}, \tag{3.50}$$

$$P_{t,2} = \frac{(2^{R_{th}} - 1)N_o}{(p_l \tilde{\tilde{t}}_l)^2}, \tag{3.51}$$

where $\tilde{\tilde{t}}_l = \hat{t}_l$ for ERS and $\tilde{\tilde{t}}_l = t^*{}_{max}$ for ORS.

Based on the above-mentioned findings, the optimal value of the transmit power is given by

$$P^{\circ} = \max(P_{t,1}, P_{t,2}). \tag{3.52}$$

Proof. See Appendix A.1. ■

3.5.2 Power Minimization via Multi-RIS

In this subsection, the objective is to minimize the transmit power between S and D by concurrently satisfying the rate constraint, while ensuring that the total transmit power at S remains within the prescribed limit. The optimization problem (P3.2) is formulated as follows

$$\begin{aligned} \text{(P3.2)} : \underset{P_t}{\text{minimize}} \quad & P_t \\ \text{subject to} \quad & \text{(C1)} - \text{(C2)}. \end{aligned} \tag{3.53}$$

Problem (P3.2) is a convex minimization problem, whose primary aim is to minimize the transmit power by optimizing the power, while ensuring that the transmit power does not surpass P_{max} and the rate remains above R_{th}. Subsequently, the Lagrangian associated with (P3.2) is represented as

$$\mathcal{L}(P_t; \mu_1, \mu_2) = f_1(P_t) + \mu_1 g(P_t) + \mu_2 h(P_t), \tag{3.54}$$

where $f_1(P_t) = P_t$, with μ_1, μ_2 being the Lagrange multipliers associated with their respective constraints (C1) and (C2). To attain an optimal value, the following condition must be satisfied: $\nabla \mathcal{L}(P_t; \mu_1, \mu_2) = 0$,

$$\frac{\partial \mathcal{L}(P_t; \mu_1, \mu_2)}{\partial P_t} \Rightarrow 1 + \mu_1 - \mu_2 \frac{1}{ln2(1+\gamma)} = 0. \tag{3.55}$$

The expressions for complementary slackness are written as

$$\mu_1 \cdot g(P_t) = 0, \tag{3.56}$$

$$\mu_2 \cdot h(P_t) = 0. \tag{3.57}$$

The possible solutions are outlined in the subsequent theorems.

Theorem 3. *If* $\mu_1 = 0 \Rightarrow g(P_t) \neq 0; \mu_2 \neq 0 \Rightarrow h(P_t) = 0$*, then we obtain the optimized value* $P_{t,1}$.

Theorem 4. *If* $\mu_1 \neq 0 \Rightarrow g(P_t) = 0; \mu_2 \neq 0 \Rightarrow h(P_t) = 0$*, then we obtain the optimized value* $P_{t,1}$ *and* $P_{t,2}$.

Based on the above-mentioned findings, the optimal value of the transmit power is given by

$$P^{\bullet} = \min(P_{t,1}, P_{t,2}). \tag{3.58}$$

Proof. See Appendix A.2. ■

As noted earlier, simulations typically demand significant time investment. Additionally, the previous sections have outlined the derivation of complex equations for various performance metrics and optimizations, processes renowned for their intricacy and time-consuming nature. In the following section, we introduce a framework crafted to tackle these challenges, emphasizing reduced computational complexity and shorter execution times.

3.6 Deep Neural Network (DNN) Framework Design

This section presents the DNN framework designed for forecasting the OP, ASER, EC, and optimization problems for ORS. Notably, the framework aims at reducing the computational complexity and shortening the execution times. This approach

stands in contrast to the challenges posed by analytical evaluations and Monte-Carlo simulations, which are known for their complex and time-consuming nature.

3.6.1 Design Approach and Datasets Generation for DNN

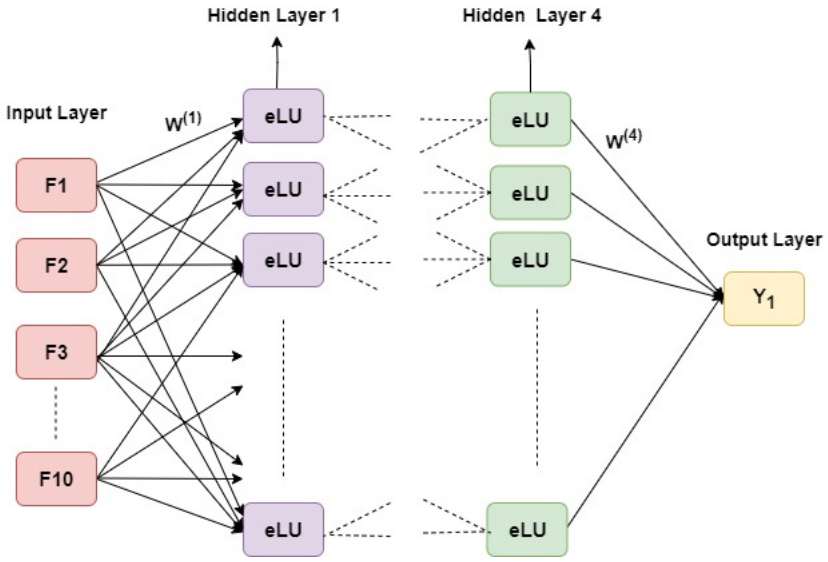

Fig. 3.2: DNN architecture.

We introduce the design of a DNN for performance assessment, where the criterion for RIS selection is formulated as a regression problem for $L = 2$ surfaces. The architecture of the DNN model is depicted in Fig. 3.2, comprising an input layer, several hidden layers, and an output layer.

The system parameters for OP, ASER, and EC with their respective values are given in Table 3.1. For the rate maximization problem, we consider $P_t \in [0, 40]$, and for the power minimization problem, we assume $R_{th} \in [1, 5]$ instead of varying P_t while all the other system parameters remain the same as given in Table 3.1. The OP, ASER, and EC values are generated through Monte-Carlo simulation and an iterative algorithm is employed for R_{max} and P_{min} optimization problem values, treating it as the

output variable within their respective training dataset. The resultant dataset G comprises a row vector containing the dataset $\mathbf{g} = [F[g], Y_{\text{sim}}]$, where each sample g is characterized by the feature vector $F[g]$ encompassing all specified input variables. Each feature vector $F[g]$ undergoes simulation, producing a distinct output Y_{sim}.

In terms of model architecture, linear functions are applied to the output units, while NL activation functions are employed for the hidden-level units. We randomly generate 10^5 samples, eventually partitioning them into the training and testing sets with an allocation of 80% for training and the remaining 20% for testing.

3.6.2 Learning Model for DNN

As illustrated in Fig. 3.2, a conventional DNN architecture is composed of a single input layer, multiple hidden layers, and a single output layer. The 10 parameters under consideration in dataset generation corresponds to individual neurons within the input layer. For every input parameter x, a threshold operation is carried out at each hidden layer using an exponential linear unit (eLU) activation function [100]. The eLU activation function scales any value below zero to zero, as shown below

$$\text{eLU}(x) = \begin{cases} a_1(e^x - 1), & \text{if } x < 0, \\ x, & \text{if } x \geq 0, \end{cases} \tag{3.59}$$

where a_1 is an arbitrary constant set to value 1. The eLU activation function presents numerous advantages when compared to alternative functions such as the Scaled exponential Linear Unit (SeLU), Rectified exponential Linear Unit (ReLU), hyperbolic tangent (Tanh), Softmax, and Softplus activation functions. These advantages stem from its near-linear characteristics, which facilitate easier optimization, computational simplicity, and the mitigation of vanishing gradient problems. Specifically,

Table 3.1: DNN training and testing input parameters.

Input parameters	**Values**	***Input parameters***	**Values**
P_t	[-20,25]	$d_{2,1}$	[10,50]
N	[16,80]	$\alpha_{1,2}^{(n)}$	[1,3]
$\alpha_{1,1}^{(n)}$	[1,3]	$\beta_{1,2}^{(n)}$	[1,3]
$\beta_{1,1}^{(n)}$	[1,3]	$d_{1,2}$	[10,50]
$d_{1,1}$	[10,50]	$d_{2,2}$	[10,50]

the Tanh activation function encounters challenges related to vanishing gradients, when the input data exhibit extremes, resulting in increased computational complexity [101]. The fading ReLU issue becomes apparent, as inputs approach zero or turn negative [101]. Since there is only one neuron in the output layer, it directly predicts numerical values without utilizing any modification or activation functions. We assume a fully connected layer, where the activation $X_{u,v}$ of the vth neuron in the uth layer is linked to the activation in the $(u-1)^{th}$ layer as

$$X_{u,v} = \text{eLU}\left(\sum_{i=1}^{U_{Fu-1}} W_{u,v,i} x_{u-1,i} + C_{u,v}\right), \tag{3.60}$$

where U_{u-1} represents the total number of neurons in the $(u-1)^{th}$ layer. The weight linking to the ith neuron is denoted by $W_{u,v,i}$ in the $(u-1)^{th}$ layer, and a scalar bias is represented by $C_{u,v}$ in the uth layer.

3.6.3 Real-Time Prediction

The DNN framework comprises two distinct phases: training and prediction. During the training phase, the neural network learns the input-output relationships offline. This process employs the adaptive moment estimation (Adam) optimization technique, aiming to optimize model parameters based on the provided dataset. Throughout the back-propagation operation, Adam is employed for the computation and up-

dating of weights and biases within the designated DNN model. This choice of optimization method, in comparison to alternative learning optimization techniques such as Nesterov, stochastic gradient descent, momentum, and RMSProp accelerated gradient, is made to enhance the efficiency of the model's parameter adjustments. Adam demonstrates superior performance advantages in terms of training speed. We denote ${Y_{\text{sim}}}^{(k)}$ and $\widetilde{Y}_{\text{sim}}^{(k)}$ as the actual and expected output values, respectively. For the kth testing dataset within the DNN model, the MSE between the actual and expected output values can be computed using the following loss function

$$(K) = \frac{1}{K}\sum_{k=1}^{K}\left(Y_{\text{sim}}^{(k)} - \widetilde{Y}_{\text{sim}}^{(k)}\right)^2, \tag{3.61}$$

where K, ${Y_{\text{sim}}}^{(k)}$, $\widetilde{Y}_{\text{sim}}^{(k)}$ are the training samples, the expected value, and the predicted value, respectively. The Adam estimation optimization algorithm is employed during the back-propagation process to iteratively update the weights and biases. This iterative updating aims to minimize the overall training loss [102].

Once the offline training concludes, the resulting DNN model, encapsulating weights and biases, can be compactly depicted as $\chi(\cdot)$ within a mapping function. A properly trained DNN demonstrates the capability to generate highly precise real-time predictions. Upon the availability of new input data, the DNN model is employed to predict the associated performance metric values. During the training phase, DNN settings can be dynamically adjusted to minimize the errors, as the DNN's capacity can be enhanced by incorporating additional neurons in each hidden layers or number of hidden layers within the network.

3.6.4 Computational Complexity

In the DNN model, the computational complexity primarily hinges on the number of Floating Point Operations (FLOPs). During the estimation process, the computational cost is assessed through two main metrics: the number of FLOPs and the total number of parameters. The FLOPs per second, which dependS on the number of weights and biases within the network, serve as a key indicator of the computational complexity of the proposed DNN model. Essentially, more weights and biases lead to a higher number of FLOPs required, thereby increasing the computational burden. This metric provides a comprehensive measure of the model's efficiency and scalability, offering insights into the resources needed for real-time processing and deployment. In the proposed DNN model, the number of input variables is $\varpi_{in} = 10$, with $\varpi_o = 150$ neurons in the input layer, $\varpi_{hid}[m] = 150$ neurons in each of the four hidden layers ($m \in \{1, \ldots, 4\}$), and $\varpi_{out} = 1$ neuron in the output layer.

The DNN has the following number of parameters ($\bar{\bar{\eta}}$)

$$\begin{aligned}\bar{\bar{\eta}} = &(\varpi_{in}.\varpi_o) + \varpi_o + (\varpi_o.\varpi_{hid}[1]) + \varpi_{hid}[1] \\ &+ ..... + (\varpi_{hid}[m].\varpi_{hid}[m+1]) + \varpi_{hid}[m+1] \\ &+ ..... + (\varpi_{hid}[4].\varpi_{out}) + \varpi_{out},\end{aligned} \tag{3.62}$$

where $(a.b)$ indicates the scalar multiplication between any two variables.

The DNN has the following number of FLOPs ($\hat{\hat{\eta}}$)

$$\begin{aligned}\hat{\hat{\eta}} &= (\varpi_{in}.\varpi_o.2) + \varpi_o + (\varpi_o.\varpi_{hid}[1].2) + \varpi_{hid}[1] \\ &+ ..... + (\varpi_{hid}[m].\varpi_{hid}[m+1].2) + \varpi_{hid}[m+1] \\ &+ ..... + (\varpi_{hid}[4].\varpi_{out}.2) + \varpi_{out}. \end{aligned} \tag{3.63}$$

For the given network, the total parameters and FLOPs are calculated to be 69,601 and 138,901, respectively.

3.7 Numerical Results and Discussions

Herein, we provide numerical results for the V2V system enhanced by the multi-RIS and corroborate the derived analytical equations through Monte-Carlo simulations. Unless explicitly indicated otherwise, the gain of the transmitting antennas is set at G_t = 10 dBi and the gain of the receiving antenna is set at G_r = 0 dBi, while the carrier frequency is fixed at $f_c = 6$ GHz. Additionally, the channel bandwidth of 20 MHz is assumed and a noise margin is set at 6 dBm. It is imperative to emphasize that identical dGG fading channel parameters are assumed for both the links from S to RIS$_l$ and RIS$_l$ to D, as well as for each element of RIS (i.e. $\alpha_{1,l}^{(n)} = \alpha_{2,l}^{(n)} = \alpha_1^{(n)}$, $m_{1,l}^{(n)} = m_{2,l}^{(n)} = m_1^{(n)}$). This simplification is made to enhance the clarity and does not entail any loss of generality. Table 3.2 provides specific dGG channels fading parameters and distances for various RIS$_l$.

Table 3.2: dGG channel parameters and RIS$_l$ distances (in meters)

l	**Case-1**		**Case-2**		**Distances (m)**	
	$\alpha_1^{(n)}$	$m_1^{(n)}$	$\alpha_1^{(n)}$	$m_1^{(n)}$	$d_{1,l}$	$d_{2,l}$
1	2.5	2	2.5	1.5	10	50
2	2	2	2	1.5	20	40
3	1.5	2	1.5	1.5	30	30
4	1	2	1	1.5	40	20

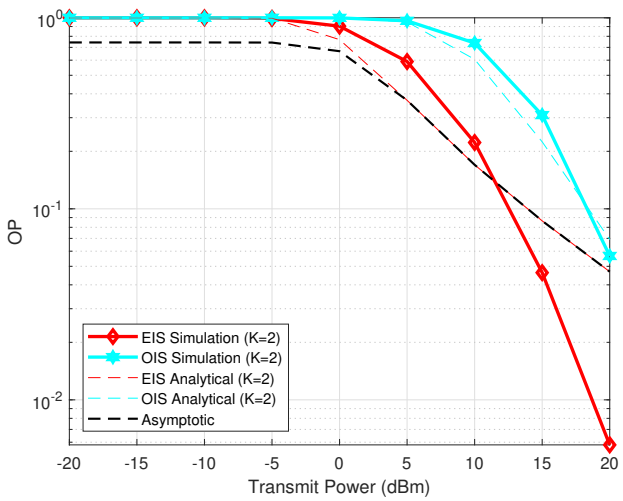

Fig. 3.3: Outage probability versus transmit power (dBm) for ERS and ORS schemes.

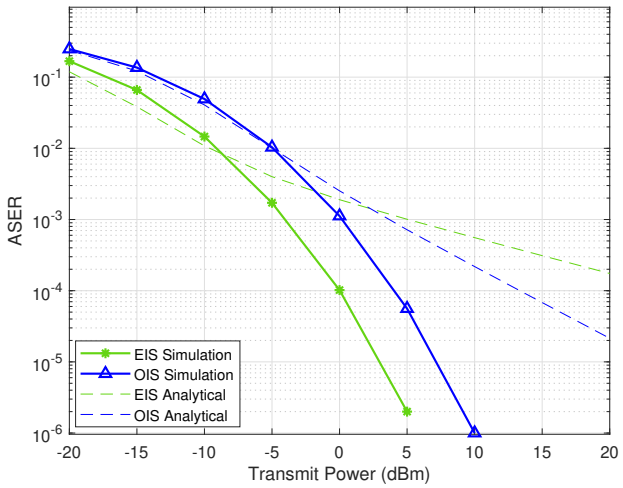

Fig. 3.4: Average symbol error rate versus transmit power (dBm) for ERS and ORS schemes.

3.7.1 ERS and ORS Comparison for Proposed Multi-RIS System

In Fig. 3.3, we plot the OP for the ERS and ORS by incorporating two RISs (i.e., $L = 2$) situated between S and D each consisting of $N = 32$ RIS elements and all RIS_l are identical. As observed in the plots, ERS outperforms ORS for the same number of elements due to MRC being performed at D. However, this comes at the cost of increased system complexity and higher resource usage. The analytical results deviates from the simulations, especially at the high-SNR region, due to the CLT approximation. Additionally, the asymptotic curves align with the analytical results at high transmit power levels.

In Fig. 3.4, we plot the ASER for the ERS and ORS by incorporating two RISs (i.e., $L = 2$) situated between S and D each consisting of $N = 32$ RIS elements and all RIS_l are identical. As observed in the plots, ERS outperforms ORS for the same number of elements due to MRC being performed at D. However, this comes at the cost of increased system complexity and higher resource usage. The analytical results deviate from the simulations, especially at the high-SNR region, due to the CLT approximation. Additionally, the asymptotic curves align with the analytical results at high transmit power levels.

In Fig. 3.5, we plot the EC for the ERS and ORS by incorporating two RISs (i.e., $L = 2$) situated between S and D each consisting of $N = 32$ RIS elements and all RIS_l are identical. As observed in the plots, ERS outperforms ORS for the same number of elements due to MRC being performed at D. However, this improvements results in higher system complexity and greater resource usage. The analytical results deviates from the simulations, especially at the high-SNR region, due to the CLT approximation. Additionally, the asymptotic curves align with the analytical results

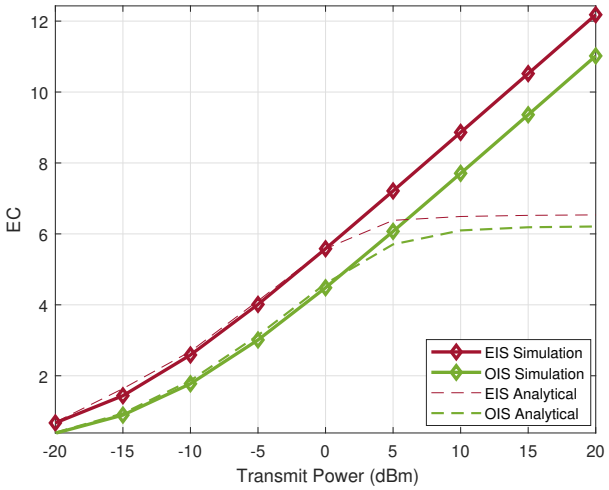

Fig. 3.5: Ergodic capacity versus transmit power (dBm) for ERS and ORS schemes.

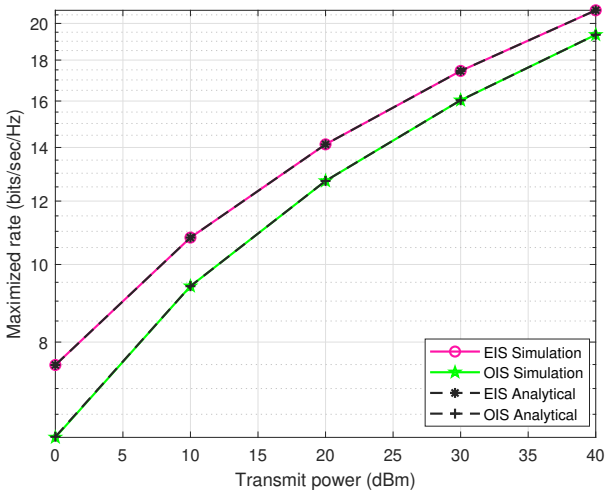

Fig. 3.6: Maximized rate (bits/sec/Hz) versus transmit power (dBm) for ERS and ORS schemes.

at high transmit power levels.

In Fig. 3.6, we assess the performance of the proposed V2V system based on the optimization solutions, as outlined in Section 3.5. All results are derived from 500 Monte-Carlo random channel realizations, considering identical surfaces. We depict in Fig. 3.6 the maximized rate against transmit power for ERS and ORS considering $N = 32$ and $L = 2$ assuming a noise power of -130 dBm and a rate threshold of

$R_{th} = 5$ bits/sec/Hz. The theoretical results obtained from the KKT conditions are align with the simulation results.

Fig. 3.7 compares the minimized power against the rate threshold for ERS and ORS assuming $N = 32$ and $L = 2$ considering a maximum transmit power of $P_t = 40$ dBm and a noise power of -90 dBm. The analytical results match the simulation for both schemes, with ERS demonstrating better performance than ORS in terms of rate, as more signal copies are received at D. However, ERS requires more resources compared to ORS.

Fig. 3.8 shows the OP versus transmit power plots by considering the mobility and imperfect CSI in the proposed system. In Fig. 3.8, the performance of the proposed V2V system has been analyzed by considering mobility of S and D vehicles, as outlined in Section 3.4. Note that $L = 2$ non-identical surfaces are assumed in between mobile S and D vehicles, which follows the 1-D RWP model. As the path-loss coefficient increases, the performance of the system degrades with decrease in received power. For a moving vehicle, random variations in distance r, combined with an increase in the path-loss exponent, cause the system's performance to deteriorate further because the received power, which is inversely related to r^a, decreases more significantly. Further, by increasing the number of elements in each RIS$_l$, the performance is improved.

In Fig. 3.9, the performance of the proposed V2V system has been analyzed considering the imperfect CSI between S to RIS$_l$ and RIS$_l$ to D. The OP performance is shown under imperfect CSI condition for three different CSI correlation coefficient values $\delta = 0.7, 0.8, 0.9$. It is seen that the increasing values of the CSI correlation coefficient enhances the OP performance. It is due to the fact that high value of δ implies less errors in channel estimation.

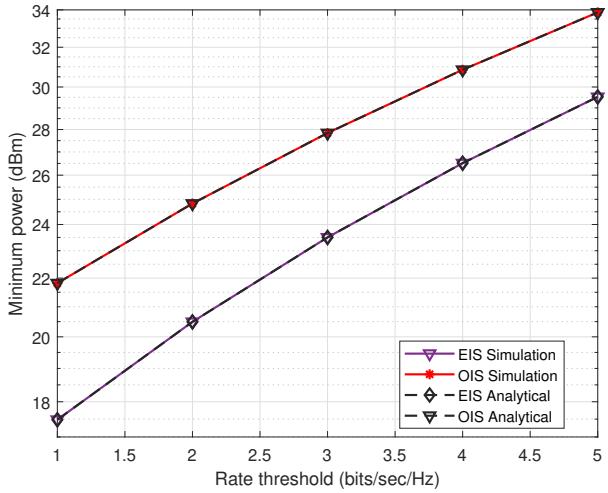

Fig. 3.7: Minimum transmit power (dBm) versus rate threshold (bits/sec/Hz) for ERS and ORS schemes.

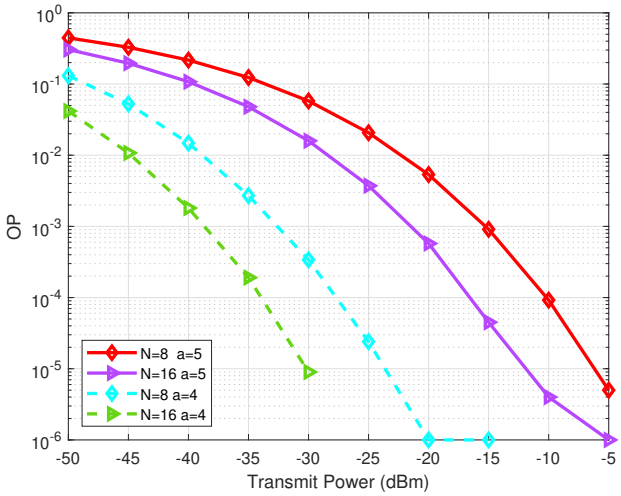

Fig. 3.8: Outage probability versus transmit power (dBm) for different numbers of RIS elements and path-loss exponents.

3.7.2 DNN Results and Complexity Analysis for ORS

In Fig. 3.10, the validation of our proposed V2V system is conducted incorporating two non-identical RISs (i.e., $L = 2$) situated between S and D. Specifically, the OP for the proposed system is plotted by increasing the RIS elements count. It is noted that the system outage performance improves as the RIS elements count increases

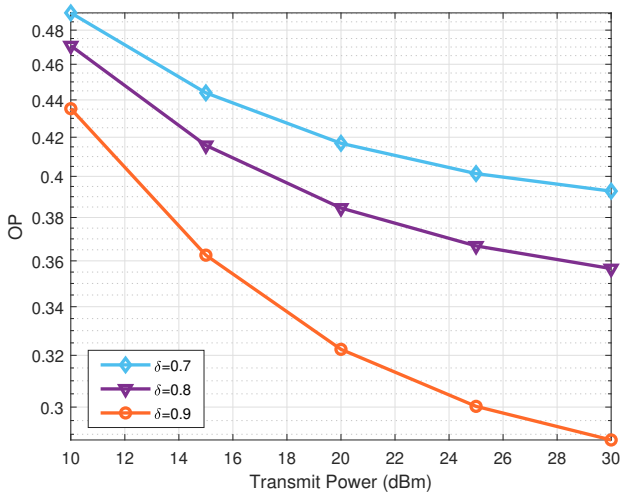

Fig. 3.9: Outage probability versus transmit power (dBm) for different CSI correlation coefficients.

due to the reception of more signal copies at D. When switching from $N = 16$ to $N = 64$, a 12 dBm transmit power gain occurs in order to attain an OP of 10^{-1}. The plots also indicate that as the number of RIS elements is doubled, a reduction in transmit power of 6 dBm is noticed to maintain the same OP. Moreover, the asymptotic curves comply with the analytical curves at high transmit power values. It is noteworthy that the simulation curves closely adhere to the predictions made by the DNN model. The strong correlation between the two sets of results indicates that the DNN model can effectively predict the performance metrics, reducing the need for time-consuming simulations, while maintaining precision. We additionally compare our proposed model with the gradient-based regression model, and the results demonstrate that the proposed model outperforms the gradient-based regression model.

In Fig. 3.11, the OP plots are presented for two scenarios assuming ORS, wherein the number of RISs ranges from $L = 1$ to $L = 4$, each made up of 32 RIS elements. According to Table 5.1, the channel parameters are presumed for each RIS. The plots reveal an enhancement in the OP with an increased number of RIS$_l$ posi-

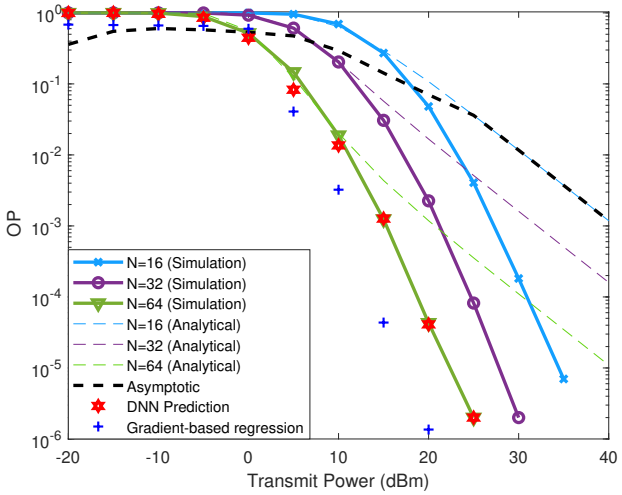

Fig. 3.10: Outage probability comparison for different numbers of RIS elements using gradient-based regression.

tioned between S and D. The selected optimal RIS, which maximises the end-to-end instantaneous SNR, is responsible for this improvement. To achieve an OP of 10^{-2}, transmission power gain values of 5 dBm (for Case-1) and 11 dBm (for Case-2) are noticed.[2]

Fig. 3.12 indicates that an OP of 10^{-1} for the multi-RIS-aided V2V system with $L = 2$ is achieved with 8 dBm less transmit power than the direct transmission system without RIS. Therefore, the proposed multi-RIS-aided V2V system demonstrates superior performance than the existing direct transmission systems documented in the literature [2].[3] Moreover, the outage performance improves as the number of reflecting surfaces increases, enhancing the signal strength.

In Fig. 3.13, we illustrate the ASER for BPSK modulation scheme with respect to transmit power for varying number of RIS elements. The observed performance trends in Fig. 3.13 are consistent with those in Fig. 3.10. The required transmit power to achieve an ASER of 10^{-2}, is $P_t = -11$ dBm for $N = 16$. For $N = 32$ and $N = 64$,

[2]The parameters for Case-1 and Case-2 are mentioned in Table 3.2.
[3]For a fair comparison, we have considered a V2V system with a direct link in [2].

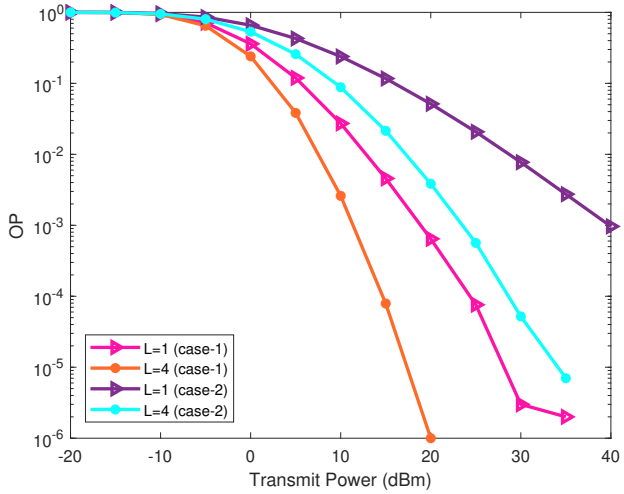

Fig. 3.11: Outage probability versus transmit power (dBm) for different numbers of RISs.

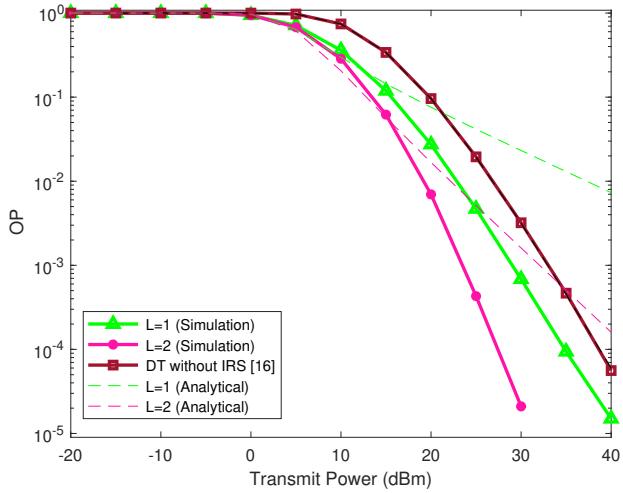

Fig. 3.12: Outage probability versus transmit power (dBm) for a V2V system with and without RIS.

the corresponding transmit power values are -5 dBm and 2 dBm, respectively. Interestingly, the DNN prediction results align with the Monte-Carlo simulations with high precision and reduced computation time.

Fig. 3.14 shows the ASER performance for various MPSK modulation schemes, considering a fixed number of RIS elements (i.e., $N = 32$) in RIS$_l$. As the modulation order increases, the system's performance decreases, as expected. For achieving an

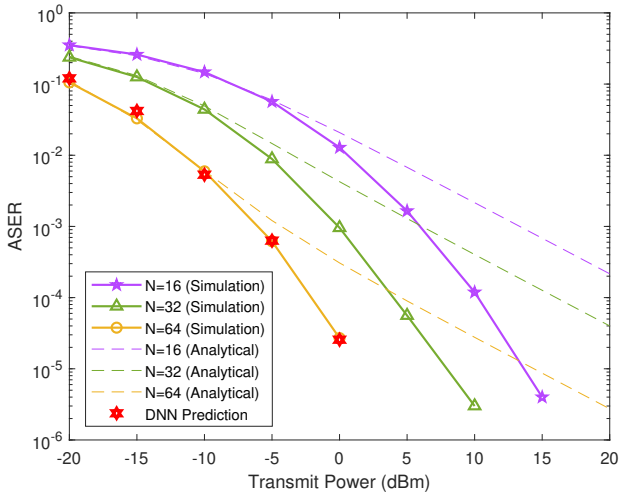

Fig. 3.13: Average symbol error rate versus transmit power (dBm) for different numbers of RIS elements.

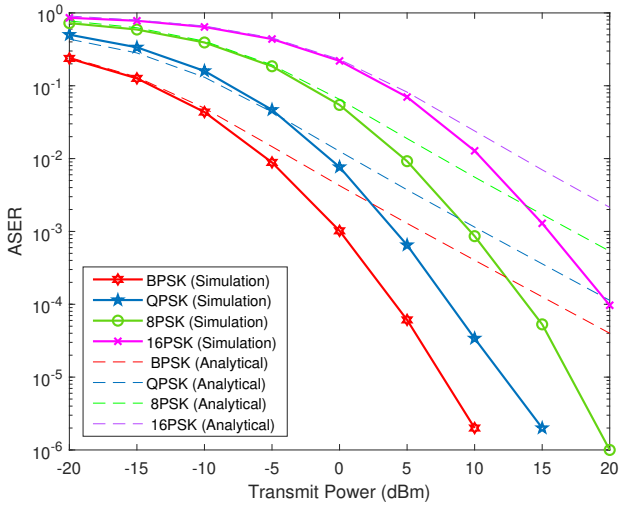

Fig. 3.14: Average symbol error rate versus transmit power (dBm) for different modulation schemes.

ASER of 10^{-2}, BPSK requires a transmit power of $P_t = -13$ dBm. In contrast, QPSK requires -8 dBm, 8-PSK requires -3 dBm, and 16-PSK demands 4 dBm. Nevertheless, the deviation between the analytical and simulation curves is attributed to approximations in (5.49) and the CLT.

Likewise, it is observed from Fig. 3.15 that the transmit power gains of 3 dBm and

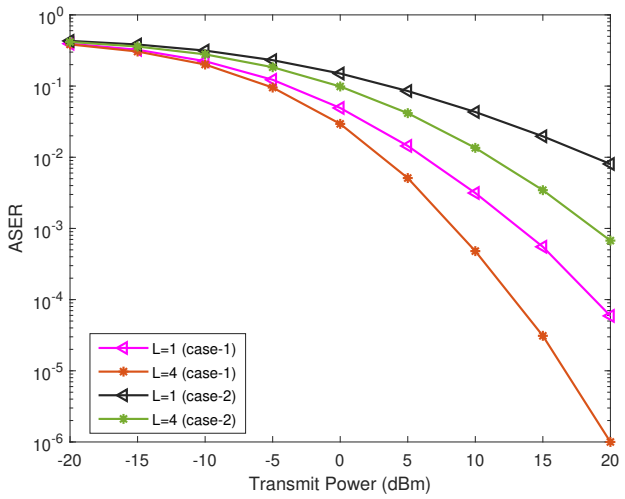

Fig. 3.15: Average symbol error rate versus transmit power (dBm) for different numbers of RISs.

7 dBm are required for Case-1 and Case-2, respectively, to achieve an ASER of 10^{-2} for the scenario where $L = 4$ compared to the scenario where $L = 1$. Through a comparison between Case-1 and Case-2, it becomes evident that the system performance deteriorates as the shaping parameter value $m_1^{(n)}$ decreases from 2 to 1.5. The noticed performance degradation primarily stems from a rise in the fading severity. Moreover, with the decrease in the shaping parameter, the required transmit power is raised by 10 dBm to attain the ASER of 10^{-2} for the case when $L = 1$. Similarly, only 8 dBm of excess transmit power is required to achieve the same ASER in case where $L = 4$. The ASER, similar to OP, improves with N and L due to the improved signal strength at the receiver.

In Fig. 3.16, the ASER performance comparison of various system models are shown and for comparison, we consider a multi-relay system under DF relaying protocol, incorporating the opportunistic relay selection to designate the most optimal relay for data transmission [103].[4] The comparative analysis reveals a notable enhance-

[4]The system model presented in [103] has undergone modifications to accommodate a V2V scenario, specifically considering the dGG fading channel for the sake of comparison.

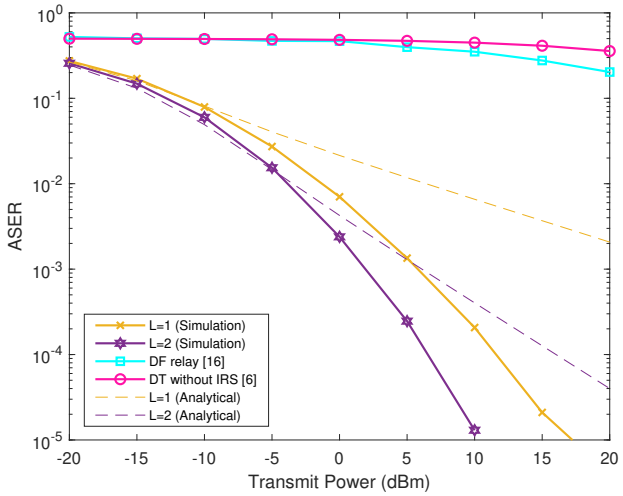

Fig. 3.16: Average symbol error rate versus transmit power (dBm) for RIS, without RIS, and DF relay systems.

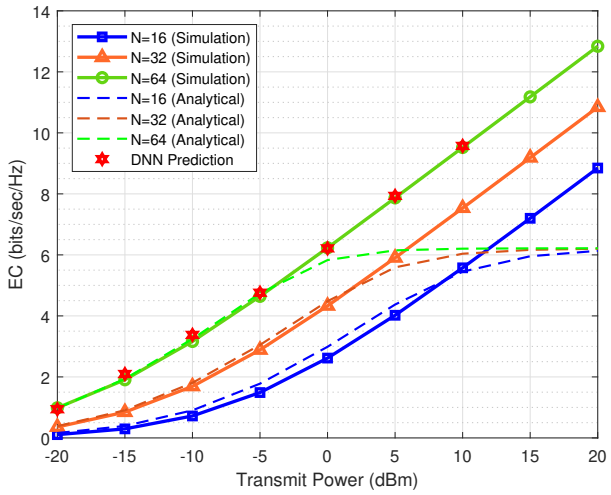

Fig. 3.17: Ergodic capacity versus transmit power (dBm) for different numbers of RIS elements.

ment in the performance advantage of the proposed multi-RIS system over the multi-relay system is primarily attributed to decoding errors occurring at the relay node selected through opportunistic relay selection. The transmit power necessary to attain the ASER of 10^{-1} for the multi-RIS V2V system aided by RIS$_l$ with $L = 2$ is observed to be 15 dBm lesser compared to the power requirement of the multi-relay system assuming a scenario involving two DF relay nodes. Furthermore, the per-

formance of the proposed multi-RIS-aided V2V system surpasses the existing V2V system with direct transmission without RIS [1] and the V2V system aided by a single RIS ($L = 1$) [2][5].

In Fig. 3.17, we illustrate the EC performance of the proposed system. Specifically, in Fig. 3.17, we increase the number of elements in each RIS to plot the EC of the multi-RIS-aided V2V system with ORS assuming $L = 2$. It is observed that an increase in the number of elements in each RIS correlates with the improvement in capacity. In order to achieve an EC of 5 bits/sec/Hz, a transmit power gain of 11 dBm is noticed as the number of RIS elements increases from $N = 16$ to $N = 64$. Moreover, the plot depicts that doubling the number of RIS elements results in 6 dBm reduction in transmit power, while maintaining the same capacity. It is significant to highlight that the predictions generated by the DNN closely match the simulation curves.

Fig. 3.18 illustrates the EC plots for two distinct scenarios, where the number of RISs is varied from $L = 1$ to 4 with each RIS comprising 32 elements, and the channel parameters for both the scenarios are given in Table 5.1. The plots clearly indicate that the EC performances of the system exhibit improvement with increase in the number of RIS$_l$ positioned between the S and D vehicles. The transmit power gains to achieve the EC of 8 bits/sec/Hz in a proposed V2V system with $L = 4$ compared to the system with $L = 1$ are observed to be equal to 2 dBm and 4 dBm, for Case-1 and Case-2, respectively.

Fig. 3.19 shows the comparison of the proposed multi-RIS-aided V2V system with the direct transmission V2V system without RIS. It is inferred that the transmit power needed to attain the EC of 5 bits/sec/Hz for the RIS-aided V2V system with $L = 2$ is

[5]For a fair comparison, we modified the system model in [2] to accommodate a single-RIS-aided V2V scenario without direct link.

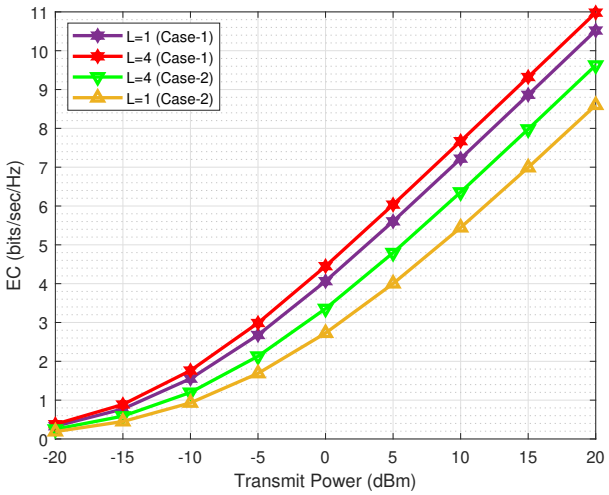

Fig. 3.18: Ergodic capacity versus transmit power (dBm) for different numbers of RISs.

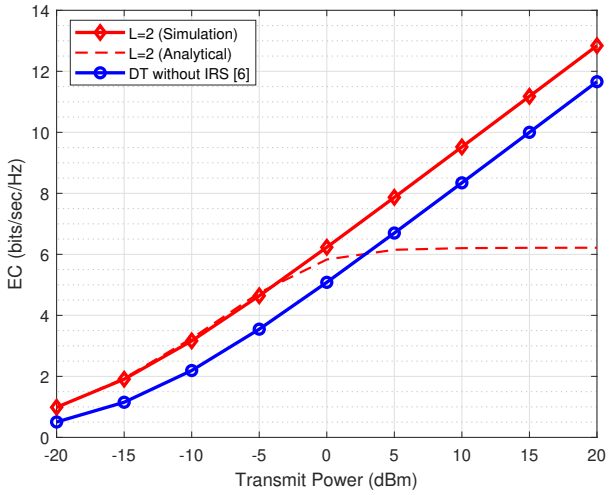

Fig. 3.19: Ergodic capacity versus transmit power (dBm) for systems with and without RIS.

3 dBm less than the direct transmission system without RIS.

We assess in Fig. 3.20 the performance of the proposed V2V system based on the optimization solutions, as outlined in Section 3.5. All results are derived from 500 Monte-Carlo random channel realizations, considering non-identical surfaces. In Fig. 3.20, we depict the maximized rate against transmit power for various RIS elements N with two RISs between S and D (i.e., $L = 2$). With a noise power of -130 dBm and a rate threshold of $R_{th} = 5$ bits/sec/Hz, increasing reflecting elements substantially

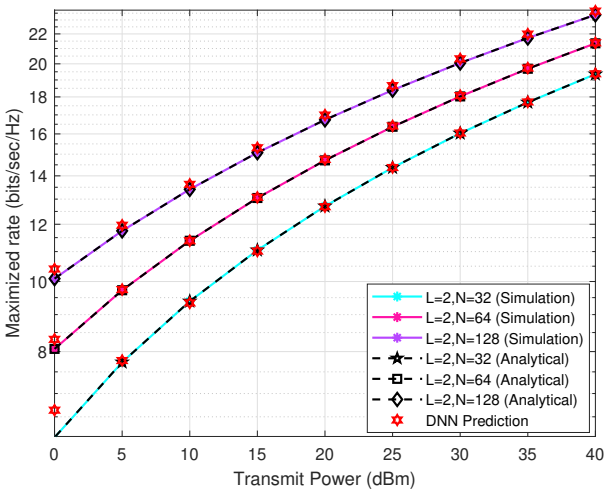

Fig. 3.20: Maximized rate (bits/sec/Hz) versus transmit power (dBm) for different numbers of RIS elements.

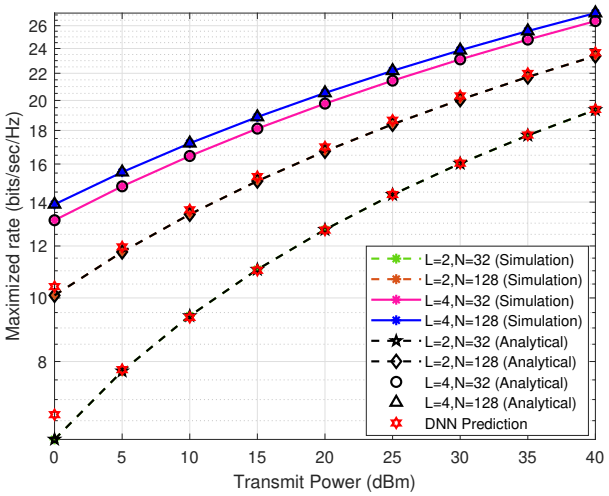

Fig. 3.21: Maximized rate (bits/sec/Hz) versus transmit power (dBm) for different numbers of RISs.

enhances the rate. At a constant transmit power P_t of 20 dBm, a normalized rate gain of 4 bits/sec/Hz is observed when transitioning from $N = 32$ to $N = 128$ elements.

Fig. 3.21 compares the maximized rate versus transmit power for different RISs (i.e., $L = 2$ and $L = 4$) with varying element counts. The plot illustrates that increasing the number of elements and RISs in ORS boosts the rate of the system. The RIS selection based on the maximum instantaneous SNR is the primary reason for this

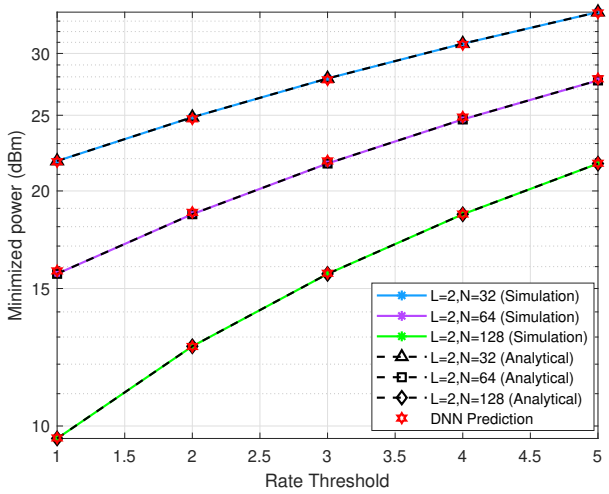

Fig. 3.22: Minimum transmit power (dBm) versus rate threshold (bits/sec/Hz) for different numbers of RISs.

improvement. A normalized rate gain of 7 bits/sec/Hz is observed when the number of RISs increases from $L = 2$ to $L = 4$ by keeping $N = 32$.

In Fig. 3.22, we plot the minimized power against the rate threshold for varying element numbers N assuming $L = 2$. Considering a maximum transmit power of $P_t = 40$ dBm and a noise power of -90 dBm, increasing reflecting elements from $N = 32$ to $N = 128$ markedly reduces the transmit power requirement. DNN prediction results align very well with the analytical solutions obtained through the KKT conditions and the simulation results obtained through MATLAB optimization toolbox (via fmincon(·) solver).

A comparative analysis between the DNN assessment of the proposed system and its simulations is conducted concerning their respective execution times and the MSE values as shown in Table 3.3. The results indicate that obtaining OP values through DNN prediction requires only 0.0856 seconds. In contrast, the Monte-Carlo simulation takes 6.8397 seconds to obtain the OP values for $N = 32$, which shows approximately a 98.75% decrease in the execution time. Further, as we increase $N = 32$ to

Table 3.3: Execution time (in seconds) comparison

Metric	***Scenario***	***Simulation***	***DNN***	***MSE***
OP	N=32	6.8397	0.0858	0.0139
	N=64	11.3194	0.0937	0.0139
ASER	N=32	5.1682	0.0798	0.0011
	N=64	10.6825	0.0947	0.0011
EC	N=32	6.0880	0.0848	1.2101
	N=64	10.4031	0.1147	1.2101
Rate maximization	N=32	4.3819	0.0743	0.0237
	N=64	6.5881	0.0928	0.0237
Power minimization	N=32	4.3484	0.07189	0.0521
	N=64	6.7157	0.0818	0.0521

$N = 64$, the simulation time increases by almost 4 seconds, but the DNN prediction time almost remains the same. The simulation values and the DNN prediction values are used to calculate the MSE, which is 0.0139. Similarly, the Monte-Carlo simulation requires 5.1682 seconds and 6.0880 seconds for calculating ASER and EC, respectively, when $N = 32$ and the corresponding times increase to 10.6825 seconds and 10.4031 seconds, respectively, when we double the number of RIS elements. The DNN prediction shows that the execution time corresponding to ASER and EC decrease to 0.0798 seconds and 0.0848 seconds, which yields approximately 98.46% and 98.60% faster results compared to the Monte-Carlo simulations, respectively, for $N = 32$, and 0.0947 seconds and 0.1147 seconds, respectively, for $N = 64$. The corresponding MSE values for ASER and EC are 0.0011 and 1.2101, respectively.

For the R_{max} optimization problem, the findings reveal that acquiring R_{max} values through the optimization solver takes 4.3819 seconds. Meanwhile, DNN prediction requires only 0.0743 seconds, which takes approximately 98.30% less time to obtain R_{max} values for $N = 32$. As we transition from $N = 32$ to $N = 64$, the simulation time escalates by nearly 2 seconds. In contrast, the DNN prediction time remains

relatively constant. The simulation values and DNN prediction values are employed to compute the MSE, resulting in a value of 0.0237. Similar to the R_{max} optimization problem, P_{min} values through DNN prediction require only 0.07189 seconds. Conversely, the optimization solver takes 4.3484 seconds, which requires approximately 98.34% more time to obtain P_{min} values for $N = 32$. With an increase in the number of RIS elements from $N = 32$ to $N = 64$, the simulation time rises by approximately 2 seconds, however, DNN prediction time remains the same. The MSE between the simulation values and DNN prediction values is determined to be 0.0521.

The proposed multi-RIS-aided V2V communication system has significant practical applications in advancing intelligent transportation and autonomous vehicle technologies by improving signal reliability for real-time communication in both urban and rural environments. It enables VLoS communication, supports seamless IoV interactions, and contributes to safety applications. Additionally, the energy-efficient RIS technology aligns with green communication goals, making it a sustainable solution for future 6G-enabled vehicular networks.

3.8 Chapter Summary

In this Chapter, we analyzed the performance of a multi-RIS-aided V2V system comprehensively over a dGG fading channel. Moreover, we formulated and resolved optimization problems to maximize the rate and minimize the transmit power of the proposed V2V system. In addition, a DNN framework was also designed to evaluate the proposed system. Our primary objective was to incorporate multiple RISs by proposing two schemes, namely ERS and ORS, to enhance the overall system performance. To achieve this, end-to-end instantaneous SNR values were utilized. Further-

more, closed-form analytical expressions for the PDF and CDF of the instantaneous SNR were derived. Building upon these expressions, we derived the analytical expressions for OP, ASER, and EC using the CLT and Gauss-Laguerre approximations. In addition, closed-form solutions for the optimization problems were derived by applying the KKT conditions for both the ERS and ORS. We also analyzed the impact of imperfect CSI with channel estimation errors and mobility of S and D vehicles on the system performance. The numerical results validated that both the number of reflecting elements within each RIS and the total number of RISs played a substantial role in improving the system performance. It was observed that DNN has emerged as a revolutionary approach to predict the system performance with low computational time and high accuracy. Therefore, the deployment of DNN stands as a promising and effective technique for assessing the system performance. This approach is particularly advantageous in URLLC scenarios, where computing closed-form expressions obtained for various performance metrics can be impractical.

Chapter 4

Multi-RIS-assisted SWIPT-enabled V2I Communication with Mobility and Imperfect CSI

4.1 Introduction

The rapid advancement of vehicular communication systems has catalyzed the development of Sixth-Generation (6G) vehicular networks, envisioned to support ultra-reliable, low-latency, and high-capacity wireless connectivity. These networks are fundamental to enable emerging applications such as autonomous driving, real-time traffic control, and Vehicle-to-Everything (V2X) communication. However, realizing these goals in practical deployments is challenged by the highly dynamic and obstructed wireless propagation environment, particularly in dense urban areas. Physical barriers such as buildings, overpasses, and other vehicles cause severe signal attenuation and blockage, which degrade communication reliability and system performance [104], [105]. To mitigate these challenges, spectrum resources with both

robust propagation and high capacity are essential. In this regard, the upper midband spectrum (7–24 GHz) has emerged as a strong candidate for 6G, since it offers larger bandwidth than sub-6 GHz while retaining more favorable propagation characteristics than millimeter-wave (mm-Wave) frequencies, making it well-suited for the vehicular communication scenarios.

Moreover, the inclusion of Machine Learning (ML) techniques introduce a powerful dimension to the optimization of Reconfigurable Intelligent Surfaces (RIS)-assisted Simultaneous Wireless Information and Power Transfer (SWIPT) vehicular networks. The vehicular environment is highly dynamic, characterized by rapidly changing topologies and fluctuating channel conditions. As a result, conventional model-based approaches may fail to fully capture the complexity of real-world scenarios. ML algorithms offer the ability to learn from historical data and adapt in real-time, enabling the network to make intelligent decisions on power allocation, and RIS configuration without requiring explicit models of the environment.

As a result, the integration of RIS technology, SWIPT mechanisms, and ML-driven control fosters the evolution of autonomous and energy-efficient 6G vehicular networks. Such networks are capable of operating with minimal human intervention, adapting autonomously to environmental and operational variations, and ensuring high reliability, low latency, and Energy Efficiency (EE). This holistic approach does not only address the performance bottlenecks of current vehicular communication systems but also aligns with the broader vision of green, sustainable, and resilient communication infrastructures in the era of 6G and beyond.

4.1.1 Chapter Organization

The Chapter is organized as follows. Section 4.2 presents the system architecture and corresponding channel models that serve as the foundation for the proposed framework. Section 4.3 formulates the optimization problem and outlines the proposed solution methodology. Section 4.4 describes the design of the Deep Neural Network (DNN) architecture employed to solve the optimization problem efficiently, along with relevant implementation details. Simulation results and performance evaluations, including parameter sensitivity analysis and comparisons with existing methods, are provided in Section 4.5. Finally, Section 4.6 concludes the Chapter with a summary of key findings and potential directions for future work.

4.2 System and Channel Models

We consider a multi-RIS-assisted Vehicle-to-Infrastructure (V2I) SWIPT system, which operates based on a Power-Splitting (PS) scheme. In this model, a roadside unit equipped with a single antenna, referred to as the source node (S), simultaneously transmits both information and energy to a vehicle, referred to as the destination node (D). The transmission takes place exclusively through the assistance of L multiple RISs, denoted as $\{RIS_l\}_{l=1,\dots,L}$, each consisting of N passive reflecting elements, as illustrated in Fig. 4.1. It is assumed that the direct Line-of-Sight (LoS) path between the source and the vehicle is obstructed due to environmental blockages such as buildings, trees, or other vehicles. As a result, the communication link between the S and the D is entirely established through the cascaded reflection paths created by the multiple intelligent surfaces.

Let $\bar{g}_{n,l} = g_{n,l}e^{j\varphi_{n,l}}$ and $\bar{h}_{n,l} = h_{n,l}e^{j\zeta_{n,l}}$ represent the complex channel fading co-

efficients between the S and the nth reflecting element of the lth RIS, and between the nth reflecting element of the lth RIS and the D, respectively. Here, $g_{n,l}$ and $h_{n,l}$ respectively denote the amplitude gains, while $\varphi_{n,l}$ and $\zeta_{n,l}$ are the respectively associated phase components, assumed to be independent and uniformly distributed over the interval $[0, 2\pi]$. The amplitude fading coefficients $g_{n,l}$ and $h_{n,l}$ are modeled as independent and non-identically distributed random variables that follow the double generalized Gamma (dGG) distribution. Specifically, $g_{n,l}$ follows a distribution parameterized by $(\alpha_{n,l}^{(1)}, \beta_{n,l}^{(1)}, \alpha_{n,l}^{(2)}, \beta_{n,l}^{(2)})$, and $h_{n,l}$ follows a distribution parameterized by $(\alpha_{n,l}^{(3)}, \beta_{n,l}^{(3)}, \alpha_{n,l}^{(4)}, \beta_{n,l}^{(4)})$. The dGG distribution is a highly flexible and unified statistical distribution that encompasses several widely used fading models as special cases, including the double-Nakagami, double-Weibull, double-Rayleigh, Weibull-Gamma, and Gamma-Gamma distributions. Due to this versatility, the dGG distribution is well-suited to characterize a broad range of practical wireless fading scenarios, particularly in dynamic V2I environments where mobility, multi-path propagation, and random blockages lead to significant variations in the channel conditions. The Maximum Likelihood Estimation (MLE) framework can be employed to estimate the parameters of the dGG channel model; however, the primary focus of this work has been on the analytical development of the model to characterize small-scale fading under the generalized conditions. We recognize that the experimental validation using real vehicular networking data such as measurements collected in urban, highway, or intersection scenarios would substantially enhance the practical relevance of the proposed model.

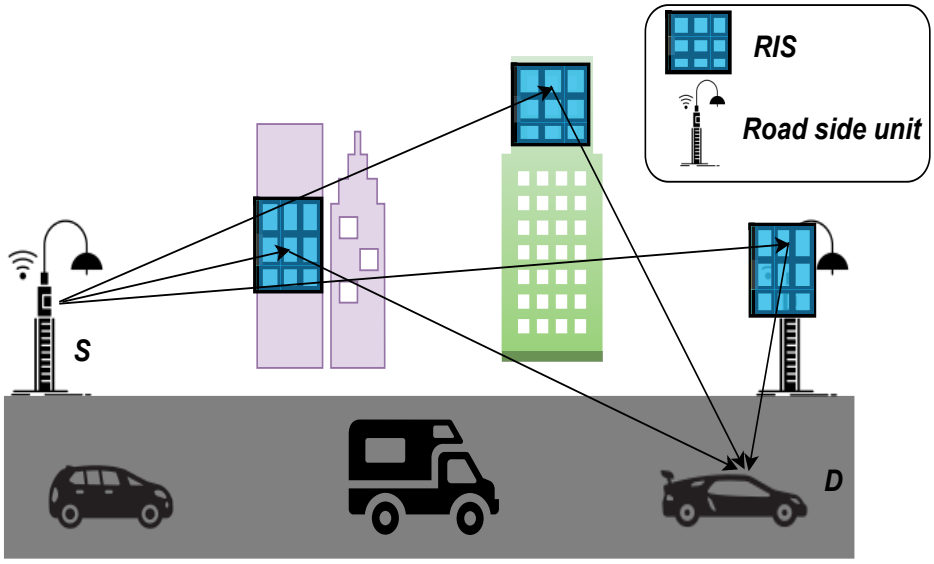

Fig. 4.1: Multi-RIS-assisted SWIPT in a highway scenario with mobile D.

The signal received at D is expressed as

$$\begin{aligned} y_d &= \sqrt{P_t}\left(\sum_{n=1}^{N}\sum_{l=1}^{L} g_{n,v}\bar{g}_{n,l}h_{n,v}\bar{h}_{n,l}e^{j\theta_{n,l}}\right)x + n_d, \\ &= \sqrt{P_t}g_{n,v}\left(\sum_{n=1}^{N}\sum_{l=1}^{L} r_{n,l}e^{j(\varphi_{n,l}+\zeta_{n,l}+\theta_{n,l})}\right)x + n_d, \end{aligned} \tag{4.1}$$

where $r_{n,l}{=}g_{n,l}h_{n,v}h_{n,l}$, P_t represents the transmit power of the signal, $e^{j\theta_{n,l}}$ is the phase shift of the lth reflecting element of the RIS$_n$, $\theta_{n,l}{\in}[0, 2\pi)$, x is the transmit signal/symbol, n_d denotes the Additive White Gaussian Noise (AWGN) with zero-mean and variance N_0 , and $g_{n,v}$ and $h_{n,v}$ represents the path-loss between S to RIS_n and RIS_n to D, respectively. Note that

$$g_{n,v}{=}d_{sn}^{-\frac{a}{2}}\left(\frac{cG_tG_r}{4\pi f_c}\right), \tag{4.2}$$

where d_{sn} represents the distance from S to RIS_n, a is the path-loss exponent, c denotes the speed of light, G_t and G_r are the transmit and receive antenna gains, respectively, and f_c denotes the carrier frequency. The term $h_{n,v}$ varies randomly

with distance v and is defined by Random Waypoint (RWP) model, as discussed in the subsequent subsection.

4.2.1 Statistical Models for Mobility

Mobility plays a crucial role in determining the received signal power in the wireless communication systems, particularly in the RIS-assisted V2I networks. In this study, we analyze the impact of mobility on the received signal power in the RIS_n-to-D communication link by employing the RWP mobility model. The received power at the destination node D is modeled as

$$P_r = P_t r^{-a}, \tag{4.3}$$

where P_t denotes the transmit power, r represents the distance between the RIS and the receiver D, and a is the path-loss exponent, which typically falls within the range : $a \in [2, 5]$, depending on the propagation environment.

For a stationary receiver, the path-loss term v^{-a} remains unchanged over time. However, in the case of a mobile receiver, the distance v varies dynamically based on the movement of D. The RWP model assumes that D can be positioned randomly within the network topology relative to RIS_n, leading to random variations in v. Consequently, the Probability Density Function (PDF) of v is expressed as (3.8). The values of these parameters for different spatial dimensions are summarized as follows

- 1-D topology: In a linear network topology, the distance distribution follows a simpler form with $k = 2$, $B_i = [6, -6]$, and $\delta_i = [1, 2]$.
- 2-D topology: In a planar network, the distance distribution becomes more complex, with parameters given by $k = 3$, $B_i = 173 \times [324, -420, 96]$, and

$\delta_i = [1, 3, 55]$.

- 3-D topology: In a volumetric network where the receiver moves in three spatial dimensions, the distance distribution follows $k = 3$, $B_i = 172 \times [735, -1190, 455]$, and $\delta_i = [2, 4, 6]$.

The parameters B_i and δ_i define the weight and decay rate of the probability distribution of v, respectively, which governs how frequently certain distances occur within the mobility model. As the number of dimensions increases, the complexity of the distance distribution also increase, leading to a more intricate variation of the received signal power.

By characterizing mobility-induced variations in the signal power using the RWP model, this analysis provides an insight into the statistical behavior of the received power fluctuations in the RIS-assisted networks. These findings are intended to be leveraged for the performance optimization.

4.2.2 PDF of Imperfect Channel Conditions

In practical wireless communication systems, the Radio-Frequency (RF) channel undergoes rapid variations due to the mobility of the destination node D. These fluctuations introduce challenges in accurate channel estimation, leading to imperfections in the available Channel State Information (CSI). The presence of channel estimation errors affects the reliability of communication links, particularly in RIS-assisted networks, where perfect CSI is crucial for effective beamforming and signal enhancement.

To model the impact of imperfect Channel State Information (ICSI) on the cascaded link $r_{n,l}$, the estimated channel gain $\tilde{r}_{n,l}$ is expressed by Gauss–Markov model as

given in (3.22). We adopt the Gauss–Markov model with a single correlation coefficient Ω since it offers a statistically grounded, measurement-interpretable, and analytically tractable representation of channel estimation errors, unlike overly conservative ellipsoidal or worst-case approach models.

In realistic scenarios, however, vehicles' speeds vary due to acceleration, deceleration, and traffic conditions, leading to time-varying relative velocities and dynamic Doppler shifts. Consequently, CSI estimation errors increase with higher speeds, affecting the performance of both analytical optimization and learning-based frameworks. The presence of ICSI due to mobility-induced variations can degrade the performance of RIS-assisted systems, affecting the key metrics such as received signal power, beamforming gain, and OP.

The received instantaneous SNR at D is expressed as

$$\gamma_d = \frac{P_t g_{n,v}^2 \left| \sum_{n=1}^{N} \sum_{l=1}^{L} \tilde{r}_{n,l} \right|^2}{N_0} = \frac{P_t s_{n,l}}{N_0}, \tag{4.4}$$

where $s_{n,l} = g_{n,v}^2 \left| \sum_{n=1}^{N} \sum_{l=1}^{L} \tilde{r}_{n,l} \right|^2$ and the phase shift of lth element in RIS_n is adjusted such that the total phase shift $\varphi_{n,l} + \zeta_{n,l} + \theta_{n,l} = 0$.

4.2.3 SWIPT Protocol and EH Model Considerations

We consider the PS scheme for SWIPT, which operates based on block transmission over a time duration of T seconds. In this scheme, the signal received at the D is divided into two distinct components. A fraction $\sqrt{\rho} y_d$ of the received signal power is allocated for Energy Harvesting (EH), while the remaining portion, $(\sqrt{1-\rho}) y_d$, is utilized for Information Decoding (ID). The parameter $\rho \in [0, 1]$ represents the PS factor, which determines the trade-off between EH and ID at the receiver.

To accurately model the Non-Linear (NL) nature of EH circuits, we employ the sigmoidal function-based practical EH model, which is given by

$$E_h = \frac{T\xi}{1-\Phi}\left(\frac{1}{1+\exp(-\rho u P_t s_{n,l}+uv)}-\Phi\right), \tag{4.5}$$

where $\Phi = \frac{1}{1+\exp(pq)}$ is a constant that accounts for the zero-input zero-output response of the EH circuit. The parameters u and v are system-specific constants determined by the circuit design and hardware specifications, while ρ denotes the PS factor. Additionally, ξ represents the saturation point of the EH circuit, which defines the maximum energy conversion efficiency under high received power conditions.

The overall achievable data rate at the vehicle destination is expressed as

$$R_d = \log_2(1+(1-\rho)\gamma_d), \tag{4.6}$$

where γ_d denotes the received SNR ratio at the ID unit. This expression characterizes the trade-off between information transfer and EH, as increasing the PS factor ρ enhances the EH at an expense of reduced data rate.

In the conventional Wireless Power Transfer (WPT) models, a linear EH assumption is often made, wherein the energy conversion efficiency is independent of the input RF power, leading to a direct linear relationship between the harvested energy and the received signal power. However, this linear model is only accurate under specific conditions where the received power relatively remains constant and within a certain operational range. In the practical scenarios, particularly in dynamic vehicular communication environments, the NL characteristics of EH circuits must be taken into account. To overcome the limitations of the linear EH model and accurately capture the NL behavior of RF to direct current power conversion, we adopt a sigmoidal

function-based Non-Linear Energy Harvesting (NL-EH) model [106]. This model provides a more realistic representation of the EH efficiency, particularly in cases where the received power varies significantly due to mobility and fluctuating channel conditions.

In the subsequent section, we formulate a unified optimization problem aimed at jointly optimizing the transmit power at the source and the PS factor at the vehicle destination. The objective of this optimization framework is to enhance the overall system performance in the envisioned multi-RIS-assisted V2I communication system by efficiently balancing the EH and information rate.

4.3 Problem Formulation and Proposed Solution

Herein, we present a unified problem formulation for optimizing two distinct objectives : (i) harvested energy, and (ii) the data rate, by jointly optimizing P_t and ρ under the same set of constraints. We define a metric $\tilde{O}_j(P_t, \rho)$, which encompasses two different cases : $\tilde{O}_w(P_t, \rho)$ as the harvested energy, and $\tilde{O}_z(P_t, \rho)$ as the rate. These cases are expressed as follows

$$\underset{\forall j \in [w,z]}{\tilde{O}_j(P_t, \rho)} := \begin{cases} \tilde{O}_w(P_t, \rho) = E_h(P_t, \rho) & \text{: Harvested energy} \\ \tilde{O}_z(P_t, \rho) = R_d(P_t, \rho) & \text{: Rate} \end{cases} \tag{4.7}$$

Problem $(P1)$ aims to maximize the metric $\tilde{O}_j(P_t, \rho)$, with the unified optimization

problem defined as

$$\text{(P4.1)} : \underset{P_t,\rho}{\text{maximize}} \quad \tilde{O}_j(P_t,\rho) \quad \forall j \in [w,z] \tag{4.8}$$

$$\text{subject to:} \quad \text{(C1)} : \; R_d \geq R_{th}, \tag{4.9}$$

$$\text{(C2)} : \; E_h \geq E_{th}, \tag{4.10}$$

$$\text{(C3)} : \; 0 < P_t \leq P_{max}, \tag{4.11}$$

$$\text{(C4)} : \; 0 \leq \rho \leq 1, \tag{4.12}$$

where P_{max}, R_{th}, and E_{th} are the maximum transmit power, rate threshold, and harvested energy threshold, respectively.

Owing to the simultaneous presence of the variables P_t and ρ in both the individual objective functions and the associated constraints, the original optimization problem (P4.1) becomes non-convex in nature. Such non-convexity renders the problem to be analytically intractable while exploring the standard convex optimization frameworks, since it may posses multiple local optimas. To effectively address this complexity, a Divide-and-Conquer (DAC) strategy is employed as one of the strategies. This methodological approach involves the partitioning of original primal problem (P4.1), which jointly optimizes over the set of decision variables into more tractable sub-problems. Each sub-problem focuses on optimizing a specific subset of variable while holding the remaining variables fixed, based on their values from the previous iteration.

In particular, the original problem is divided into two interrelated sub-problems

$(\text{P4.1})_a$ and $(\text{P4.1})_b$. The mathematical representation is as follows

$$(\text{P4.1})_a : \underset{P_t}{\text{maximize}} \quad \tilde{O}_j(P_t) \quad \forall j \in [w, z] \tag{4.13}$$

$$\text{subject to:} \quad (\text{C3}) : \ 0 < P_t \leq P_{max}, \tag{4.14}$$

$$(\text{C5}) : \ R_d(P_t) \geq R_{th}, \tag{4.15}$$

$$(\text{C6}) : \ E_h(P_t) \geq E_{th}, \tag{4.16}$$

$$(\text{P4.1})_b : \underset{\rho}{\text{maximize}} \quad \tilde{O}_j(\rho) \quad \forall j \in [w, z] \tag{4.17}$$

$$\text{subject to:} \quad (\text{C4}) : \ 0 \leq \rho \leq 1, \tag{4.18}$$

$$(\text{C7}) : \ R_d(\rho) \geq R_{th}, \tag{4.19}$$

$$(\text{C8}) : \ E_h(\rho) \geq E_{th}, \tag{4.20}$$

where the constraints (C5) and (C6) in sub-problem $(\text{P4.1})_a$ represents the achievable data rate and EH constraints, respectively, with respect to the optimization variable P_t. Similarly, the constraints (C7) and (C8) in sub-problem $(\text{P4.1})_b$ represents the achievable data rate and EH constraints, respectively, considering the optimization variable as : ρ.

To address the non-convexity of (P4.1), we use an iterative optimization approach based on AO, outlined in Algorithm 4.1. We initialize $\tilde{O}_j(P_t, \rho)$ for all $j \in [w, z]$, then fix ρ to compute P_t^*, and find ρ^* using the updated P_t^*. The process iterates until either the current value of $\tilde{O}_j(P_t, \rho)$ falls below that of the previous iteration, or the maximum number of iterations is reached. The computational complexity is $\mathcal{O}(m(\mathcal{S} + \mathcal{T}))$, where m is the number of iteration, and $\mathcal{S}$ and $\mathcal{T}$ are number of computational steps for Step 3. and Step 4., respectively. As a second method, we

incorporate the JO methodology, where multiple optimization variables are optimized simultaneously rather than being solved sequentially or independently. Instead of addressing each parameter in isolation, the JO optimizes all the relevant parameters together, ensuring that their inter-dependencies are considered. Next, we discuss an alternative method to obtain a closed-form solution for the aforementioned problem (P4.1), wherein we solve the problem directly using the Karush-Kuhn-Tucker (KKT) conditions [107]. It provides necessary and sufficient conditions for the optimality in convex problems, but in the case of non-convex problems, they are only necessary for local optima, identifying candidate solutions that may or may not be globally optimal. Despite this limitation, the KKT-based methods are computationally faster due to their gradient-based nature. To proceed, the Lagrangian corresponding to (P4.1) is denoted as follows

$$\mathcal{L}(P_t, \rho; \Delta) = \tilde{O}_j(P_t, \rho) - \mu_1 g(P_t, \rho) - \mu_2 h(P_t, \rho) - \mu_3 i(P_t, \rho) - \mu_4 j(P_t, \rho), \tag{4.21}$$

where $\Delta = (\mu_1, \mu_2, \mu_3, \mu_4)$ is the set of Lagrange multipliers corresponding to the constraints (C1)-(C4), $g(P_t, \rho) = R_{th} - R_h$, $h(P_t, \rho) = E_{th} - E_h$, $i(P_t, \rho) = P_t - P_{max}$, $j(P_t, \rho) = \rho - 1$.

For optimality, it must hold that $\nabla\mathcal{L}(P_t, \rho; \Delta) = 0$, such that the optimality conditions are represented as

$$\frac{\partial\mathcal{L}(P_t, \rho; \Delta)}{\partial P_t} \Rightarrow \frac{\partial\tilde{O}_j(P_t, \rho)}{\partial P_t} + \mu_2\rho\lambda_2 + \mu_1(1-\rho)\lambda_1 - \mu_3 = 0, \tag{4.22}$$

$$\frac{\partial\mathcal{L}(P_t, \rho; \Delta)}{\partial \rho} \Rightarrow \frac{\partial\tilde{O}_j(P_t, \rho)}{\partial \rho} - \mu_1 P_t\lambda_1 + \mu_2 P_t\lambda_2 - \mu_4 = 0, \tag{4.23}$$

Algorithm 4.1 Iterative AO Algorithm.

1: Initialize $\tilde{O}_j(P_t,\rho) \quad \forall j \in [u,v]$
2: **Repeat**
3: Solve (4.8) for fixed ρ to find P_t^*
4: Solve (4.8) by putting P_t^* obtained in 3:, to find ρ^*
5: Find $\tilde{O}_j(P_t,\rho)$ using P_t^* and ρ^*, save $\tilde{O}_j(P_t,\rho)(n)$ and $n = n+1$
6: **Until**: $\tilde{O}_j(P_t,\rho)(n) \geq \tilde{O}_j(P_t,\rho)(n-1)$

where $\frac{\partial \tilde{O}_w(P_t,\rho)}{\partial P_t} = \rho\lambda_2$, $\lambda_2 = \frac{T\xi p s_{n,l} e^{(-pP_t\rho s_{n,l}+pq)}}{(1-\phi)\left(1+e^{(-\rho pP_t s_{n,l}+pq)}\right)^2}$, $\frac{\partial \tilde{O}_z(P_t,\rho)}{\partial P_t} = (1-\rho)\lambda_1$, $\lambda_1 = \frac{s_{n,l}}{\ln 2 \cdot N_0(1+\frac{(1-\rho)P_t s_{n,l}}{N_o})}$, $\frac{\partial \tilde{O}_w(P_t,\rho)}{\partial \rho} = P_t\lambda_2$, and $\frac{\partial \tilde{O}_z(P_t,\rho)}{\partial \rho} = -P_t\lambda_1$.

The conditions for feasibility are given by $\{g(P_t,\rho), h(P_t,\rho), i(P_t,\rho), j(P_t,\rho)\} \leq 0$.

The complementary slackness expressions are represented as follows

$$\mu_1 \cdot g(P_t,\rho) = \mu_2 \cdot h(P_t,\rho) = \mu_3 \cdot i(P_t,\rho) = \mu_4 \cdot j(P_t,\rho) = 0. \tag{4.24}$$

The non-negativity constraints are given by $\{P_t, \rho, \Delta\} \geq 0$, along with the additional constraint $j(P_t,\rho) \geq 0$. If $\mu_4 \neq 0$, the complementary slackness requires $j(P_t,\rho) = 0$, which would imply $\rho = 1$. However, $\rho = 1$ is generally not applicable in the SWIPT scenario and is only permissible in a pure EH problem. Therefore, the Lagrange multiplier μ_4 must be zero for the considered SWIPT setup. Analyzing (4.21)-(4.24) using standard KKT procedures yields feasible solutions outlined in Theorem 5.

Theorem 5. The optimal values of P_t^* and ρ^* for $\tilde{O}_j(P_t,\rho)$ are, respectively, given by

$$\tilde{O}_j(P_t,\rho) := \begin{cases} P_t^* = P_{t_1} \quad ; \qquad j \in [w,z], \\ \rho^* = \begin{cases} \max(\rho_1,\rho_2) \quad ; \quad j = w, \\ \min(\rho_1,\rho_2) \quad ; \quad j = z. \end{cases} \end{cases} \tag{4.25}$$

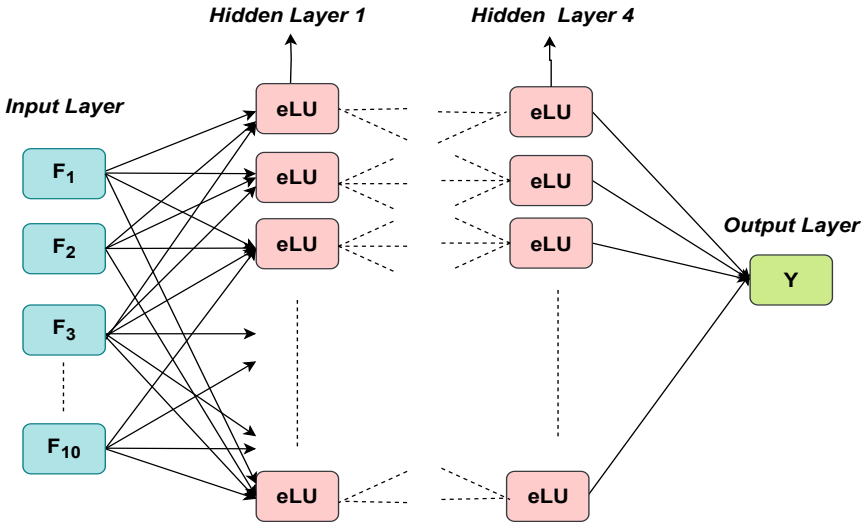

Fig. 4.2: DNN design for optimal solution prediction in SWIPT network.

Proof. See Appendix B. ■

While this section addresses conventional optimization methods, which, although effective, are often computationally intensive and time-consuming. The following section introduces a DNN framework as an alternative and complementary approach to the analytical optimization framework, rather as a replacement. Unlike iterative optimization, which requires repeated problem decomposition and parameter updates, the DNN leverages data-driven learning to directly approximate the complex input–output relationships. This approach significantly reduces the computational burden, improves scalability to large-scale systems, and enables real-time adaptability in dynamic environments.

4.4 DNN Based Optimal Solution Prediction

We now introduce a DNN framework for efficiently predicting optimal solutions, reducing computational complexity, execution time, and the need for extensive mathematical analysis and Monte-Carlo simulations.

4.4.1 DNN Architecture

We now present a DNN design that formulates the prediction of optimal solutions for (P4.1) as a regression problem within the context of supervised learning, specifically for the case where $L = 2$ surfaces. The DNN architecture comprises a single input layer, four hidden layers, and a single output layer [58]. The DNN model is implemented using Python 3.10.13, Keras 2.18.0, and TensorFlow 3.8.0 within the Jupyter Notebook environment. The experiments are conducted on a 64-bit system equipped with an Intel Core i5-8400 CPU @ 2.80 GHz, 32 GB RAM, and integrated Intel UHD Graphics 630. An ablation study was performed to evaluate the impact of network depth and width on the model's performance. The number of hidden layers was varied from 2 to 6, and the number of neurons per layer was tested at 50, 100, 150, and 200. The configuration comprising four hidden layers with 150 neurons each yielded the best trade-off between prediction accuracy, convergence stability, and inference latency. Consequently, this architecture was adopted for the final implementation due to its superior balance between performance and computational efficiency. The input features for the model include system parameters which are given in Table 4.1. The model's outputs are the optimal values derived from the KKT solutions for the rate and EH optimization, which serves as a ground truth during supervised learning. The dataset $\mathcal{M}$ is structured as a row vector $m{=}[F[m], Y_{\mathrm{d}}]$, where each sample h con-

Table 4.1: DNN training input parameters.

Input parameters	**Values**	***Input parameters***	**Values**
P_t	[5,10]	$d_{2,1}$	[100,500]
N	[4,64]	$\alpha_{1,l}^{(1)}$	[1,3]
$\alpha_{1,l}^{(1)}$	[1,3]	$\beta_{1,l}^{(2)}$	[1,3]
$\beta_{1,l}^{(1)}$	[1,3]	$d_{1,2}$	[100,500]
$d_{1,1}$	[100,500]	$d_{2,2}$	[100,500]

sists of a feature vector $F[m]$, representing all the 10 input variables, and an output Y_{d}, which is the ground truth value generated through simulations using the offline KKT-based solutions.

To avoid overfitting during training and to achieve accurate results on the test set, the output Y_{d} is normalized using logarithmic normalization for the harvested energy data. Linear functions are applied to the output layer, while NL activation functions are employed in the hidden layers. A total of 10^5 samples are generated, with 80% used for training and 20% for testing. To ensure the generalization of the proposed DNN model, additional training was done using the extended dataset of 10^6 samples. However, the results showed no significant improvement in prediction accuracy and convergence behavior. Therefore, for practical considerations, such as reduced training time and reduced computational overhead, the final implementation uses the 10^5 samples dataset. The eLU activation function is utilized in each hidden layer, offering advantages over ReLU, such as simplified optimization, reduced computational complexity, and mitigation of vanishing gradient issues [58]. The eLU activation function scales any value below zero to zero, as shown below

$$\mathrm{eLU}(a) = \begin{cases} c_1(e^a - 1), & \text{if } a < 0 \\ a, & \text{if } a \geq 0 \end{cases}, \tag{4.26}$$

where c_1 is an arbitrary constant set to value 1.

The DNN framework consists of two phases : training and prediction. During the training phase, the Adam optimizer is employed to learn the input-output relationships efficiently. Adam's ability to update model parameters through the back-propagation enhances the training speed compared to methods like stochastic gradient descent and Nesterov. The training is performed with an initial learning rate of 0.001, a batch size of 500, and 150 epochs, ensuring stable convergence and generalization performance of the model. The model's performance on the tth testing dataset for predicted output $\widetilde{Y}_{\text{o}}$ is evaluated by calculating the MSE between the actual ${Y_{\text{d}}}^{(t)}$ and predicted $\widetilde{Y}_{\text{o}}^{(t)}$ values given by

$$L(t)=\frac{1}{t}\sum_{k=1}^{t}\left({Y_{\text{d}}}^{(t)}-\widetilde{Y}_{\text{o}}^{(t)}\right)^{2}. \tag{4.27}$$

Adam optimization is used during the back-propagation to iteratively adjust weights and biases, minimizing the training loss. A well-trained DNN allows for precise real-time predictions. When new input data is available, the DNN model predicts the corresponding optimal values. During the training phase, the DNN configuration is tuned by adding neurons or hidden layers to minimize errors and enhance capacity.

4.4.2 DNN Complexity Analysis

During the estimation process, the complexity is evaluated via two key metrics : the total number of Floating Point Operations (FLOPs) and the total number of parameters. The FLOPs per second, which are influenced by the number of weights and biases in the network, serve as a crucial measure of the model's computational demands. A greater number of weights and biases results in a higher FLOP count, thereby increasing the computational load. This metric provides a comprehensive as-

sessment of the model's efficiency and scalability, offering valuable insights into the resources required for real-time processing and deployment.

In the proposed model, there are $\bar{\kappa}$=10 input variables, with κ=150 neurons in the input layer, $\tilde{\kappa}[b]$=150 neurons in each of the four hidden layers ($b \in \{1, \ldots, 4\}$), and $\hat{\kappa}$=1 neuron in the output layer.

The DNN has the following number of parameters ($\tilde{\eta}$)

$$\tilde{\eta}=(\bar{\kappa}\times\kappa)+\kappa+(\kappa\times\tilde{\kappa}[1])+\tilde{\kappa}[1]+.....+(\tilde{\kappa}[b]\times\tilde{\kappa}[b+1]) \\ +\tilde{\kappa}[b+1]+.....+(\tilde{\kappa}[4]\times\hat{\kappa})+\hat{\kappa}, \tag{4.28}$$

The DNN has the following number of FLOPs ($\hat{\eta}$)

$$\hat{\eta}=(\bar{\kappa}\times\kappa\times2)+\kappa+(\kappa\times\tilde{\kappa}[1]\times2)+\tilde{\kappa}[1]+...+(\tilde{\kappa}[b]\times\tilde{\kappa}[b+1]\times2) \\ +\tilde{\kappa}[b+1]+...+(\tilde{\kappa}[4]\times\hat{\kappa}\times2)+\hat{\kappa}. \tag{4.29}$$

The total number of parameters and FLOPs for the specified network are computed to be 69,601 and 138,901, respectively.

4.5 Numerical Results and Discussions

In this section, we evaluate the numerical results for the considered multi-RIS-assisted V2I system. Unless stated otherwise, the simulation parameters used to obtaining the results are P_{max}=10 W, E_{th}=1μW, R_{th}=5 bpcu, G_t=G_r = 10 dBi, f_c=6 GHz, N_o= $-$ 120 dBW, ρ=0.5, ξ=2.8 mW, u=1500, and v=0.0022 [108]. For simplicity and without loss of generality, we assume identical dGG fading channel parameters for all links (i.e. $\alpha_{n,l}^{(1)}$=$\alpha_{n,l}^{(2)}$ and $\rho_{n,l}^{(1)}$=$\rho_{n,l}^{(2)}$). Distances in meters and dGG fading

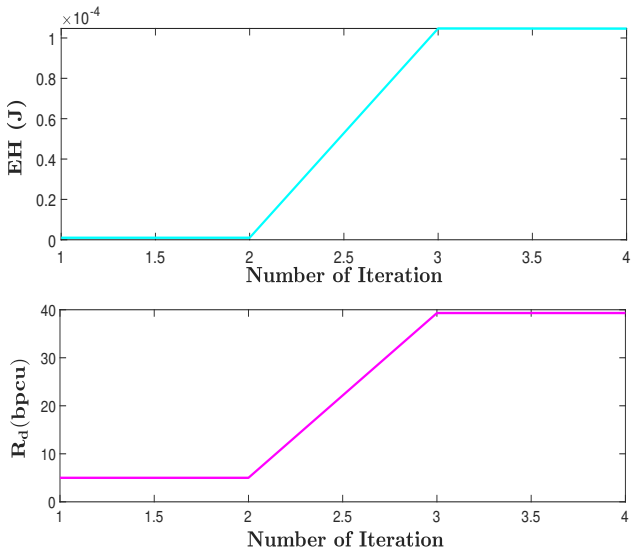

Fig. 4.3: Convergence of harvested energy (J) and rate (bpcu) with iterations.

channel parameters for various RISs are given by d_{s1}=100, d_{1d}=500, $\alpha_{1,l}^{(1)}$=1, $\rho_{1,l}^{(1)}$=2, d_{s2}=200, d_{2d}=400, $\alpha_{2,l}^{(1)}$=2, $\rho_{2,l}^{(1)}$=2. Here, we considered a 1-D-topology with parameters given by $k = 2$, $B_i = [6, -6]$, and $\delta_i = [1, 2]$.

Fig. 4.3 illustrates the convergence of both the maximized harvested energy and rate, averaged over 500 Monte-Carlo channel realizations. The maximized harvested energy converges in approximately five iterations, while the rate requires nearly four iterations. These algorithmic results, derived from Algorithm 1, are obtained using MATLAB's $fmincon(\cdot)$ NL solver [109], and the convergence plot presented in Fig. 4.3 further substantiates the validation of Algorithm 1.

Fig. 4.4 illustrates the training and validation performance of the proposed DNN models for both the information rate and EH prediction tasks. The curves demonstrate the convergence behavior of the training process and confirm that the validation performance closely follows the training trends, thereby indicating that the designed DNNs are well-trained without overfitting. This validates the effectiveness of the adopted network architecture, activation functions, and the optimization strategy in accurately

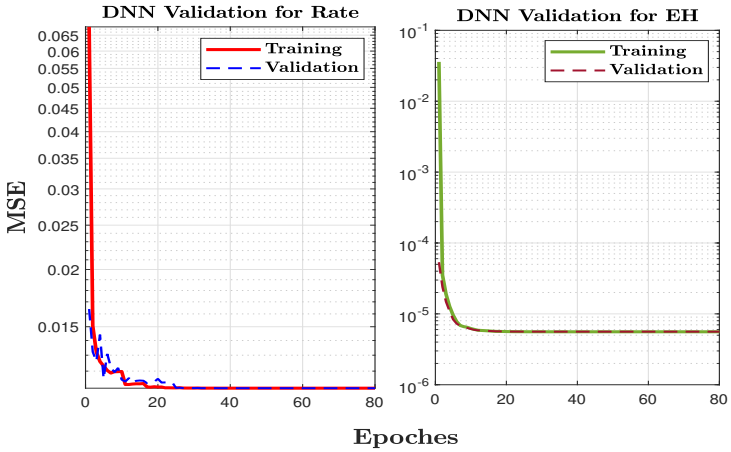

Fig. 4.4: MSE vs. Epochs.

learning the underlying NL mapping between the system parameters and the performance metrics.

In Fig. 4.5, we access the performance of the proposed V2I system based on the optimization solutions. The variations in maximized harvested energy with respect to transmitted power P_t are shown for four different methods. The results of the AO and KKT solutions closely align, while the JO method, which optimizes both variables simultaneously, shows comparable results to AO but is more sensitive to the selection of the initial point. Notably, the proposed DNN model outperforms both the JO and KKT solutions. As L increases, harvested energy appreciates with the results of $N = 2$ outperforming $N = 1$. The presence of additional RIS elements significantly improves the harvested energy due to the reception of multiple signals at D. The DNN predictions closely align with the simulation results, achieving a 98.54% reduction in computation time.

Fig. 4.6 shows the rate change with P_t for various L and N values. Higher transmitted power leads to an increased rate, with greater L and N values significantly enhancing the rate due to improved instantaneous SNR at the receiver. For $P_t = 6$ W, increasing

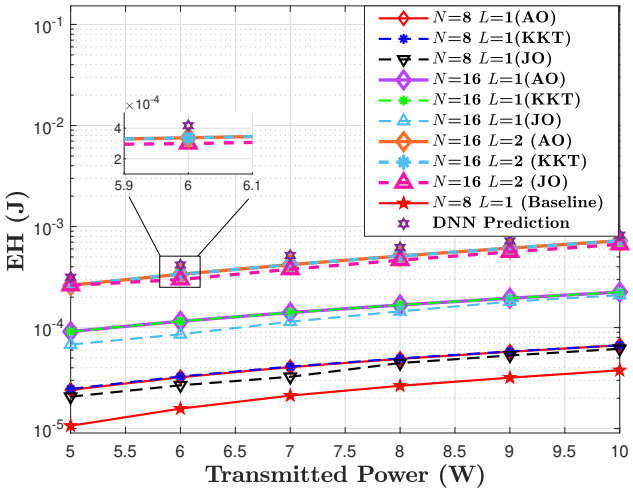

Fig. 4.5: EH (J) versus transmit power P_t (W) for different values of L and N.

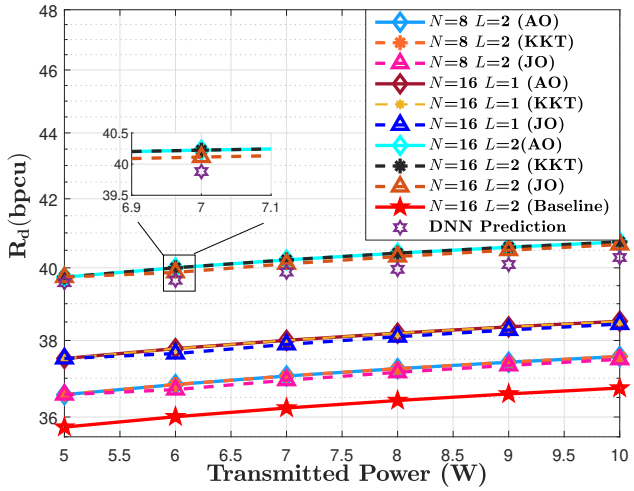

Fig. 4.6: Achievable rate (bpcu) versus transmit power P_t (W) for different values of L and N.

L to 16 results in an approximately 2 bpcu gain, while transitioning from $N = 1$ to $N = 2$ yields nearly a 3 bpcu gain. The DNN model's predictions are approximately 99.46% more efficient in time reduction compared to simulations. Compared to the baseline with partial optimization of a single variable (fixing $\beta = 0.5$), increasing L and N improves both the harvested energy and information rate. Simulation results illustrate the trade-off between information rate and EH in the PS-based SWIPT sys-

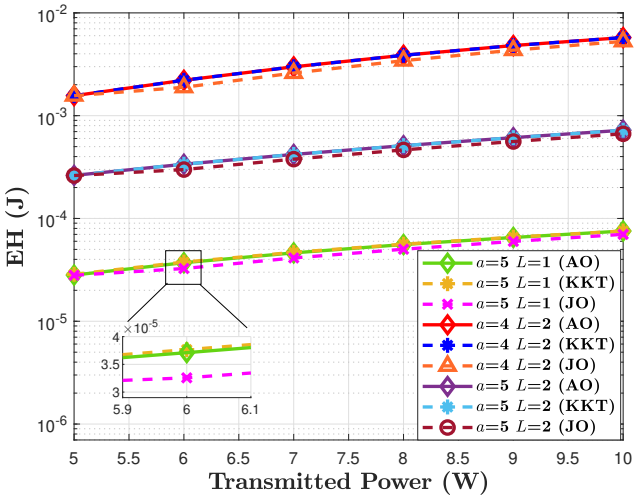

Fig. 4.7: EH (J) versus transmit power P_t (W) for different values of N and parameter a values.

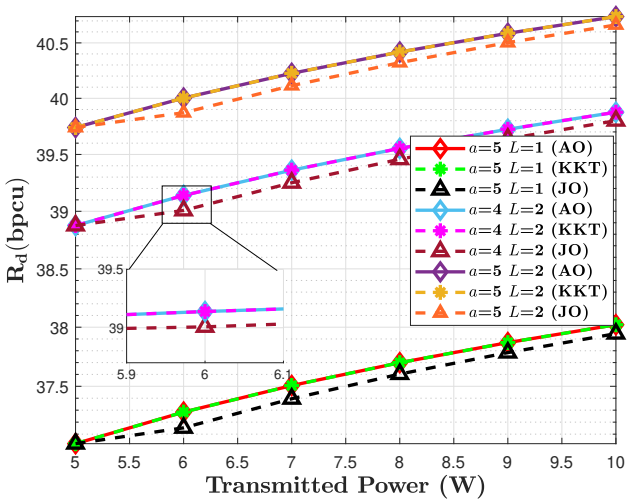

Fig. 4.8: Rate (bpcu) versus P_t (W) for various N and parameter a values.

tem, which is critical for practical deployments. In the PS framework, the received signal is split between EH and ID according to the PS factor, ρ. A higher ρ allocates a larger fraction of the received power to EH, improving the harvested energy, while reducing the power available for ID and lowering the achievable information rate. Conversely, a smaller ρ favors ID over EH, enhancing the data rate but limiting the harvested energy. The trade-off between the information rate and EH efficiency

is strongly influenced by the PS factor ρ. The deployment of multiple RISs further enhances the overall system performance, improving both the harvested energy and achievable data rate. These results highlight the critical role of multi-RIS deployments in improving system performance and the EH–ID trade-off incurred due to the PS factor in practical SWIPT systems.

In Fig. 4.7, the performance of the proposed V2I system is analyzed by considering the mobility of the destination vehicle, as outlined in Section II. Note that we have considered a 1-D RWP mobility model. As the path-loss coefficient increases, the performance of the system degrades with decrease in the received power. For a moving vehicle, random variations in distance v, combined with an increase in the path-loss exponent a, further degrades the system performance because the received power, which is inversely related to r^a, decreases more significantly. Further, by increasing the number of elements in each RIS_n, the performance is improved.

Fig. 4.8 shows the variations in maximized rate with respect to P_t for different N and a values. As P_t increases, the SNR for $N = 2$ surpasses that for $N = 1$, resulting in an enhanced rate. Further, the analytical solutions using KKT conditions are validated by simulations.

In Fig. 4.9, the performance of the proposed V2I system has been analyzed considering the ICSI. The harvested energy and rate performance is shown under the ICSI condition for two different CSI correlation coefficient values : $\Omega = 0.8, 0.9$. It is observed that increasing the values of the CSI correlation coefficient enhances the performance. It is due to the fact that high value of Ω implies less errors in channel estimation. Fig. 4.9 illustrates how the maximized harvested energy varies with P_t for different N and Ω values. An increase in N and Ω leads to higher harvested energy.

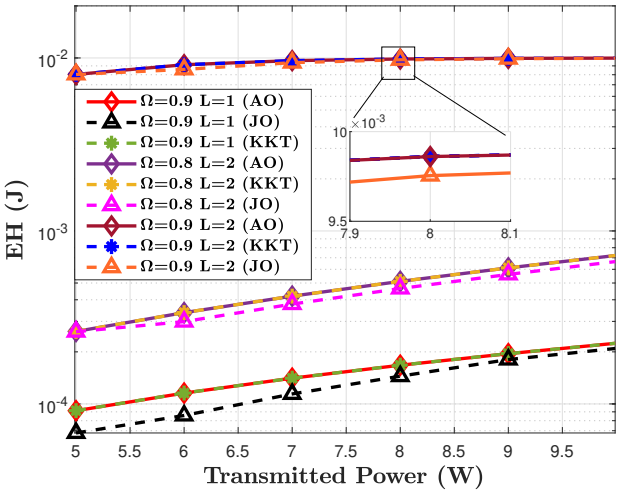

Fig. 4.9: EH (J) versus transmit power P_t (W) for different values of N and parameter Ω values.

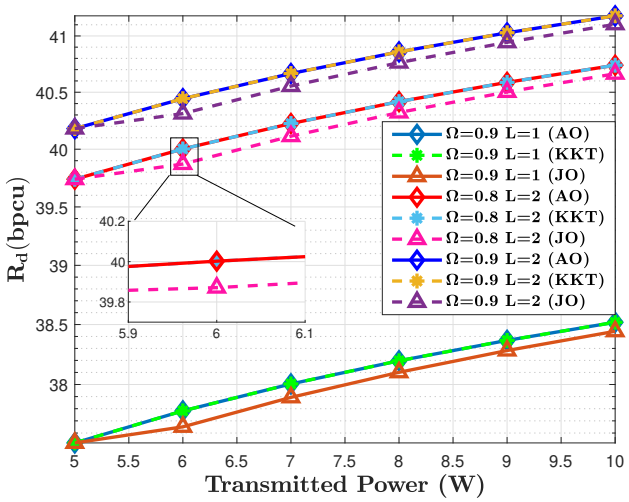

Fig. 4.10: Achievable rate (bpcu) versus transmit power P_t (W) for different values of N and parameter Ω values.

Fig. 4.10 shows the rate variation with P_t across different N and Ω values. As expected, higher transmitted power improves the rate. Additionally, increasing the Ω significantly enhances the rate due to less channel estimation errors. For a practical frame structure, Ω can be modeled as a function of both training length and reuse factor, where higher training overhead and lower reuse improve the correlation, while reduced training or excessive pilot reuse result in weaker correlation and degraded

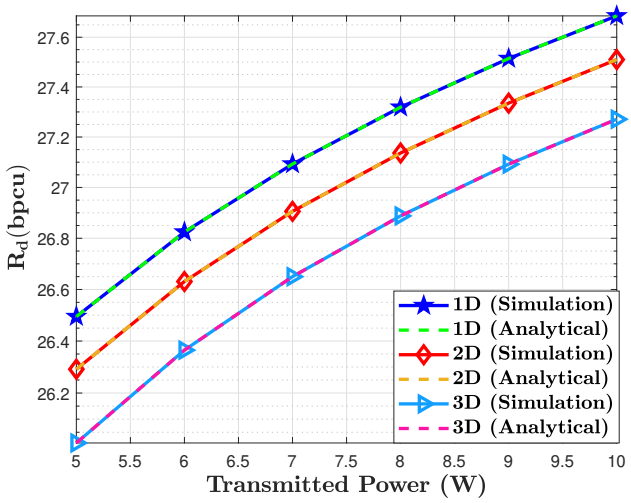

Fig. 4.11: Achievable rate (bpcu) versus transmit power P_t (W) for different random waypoint (RWP) dimensions.

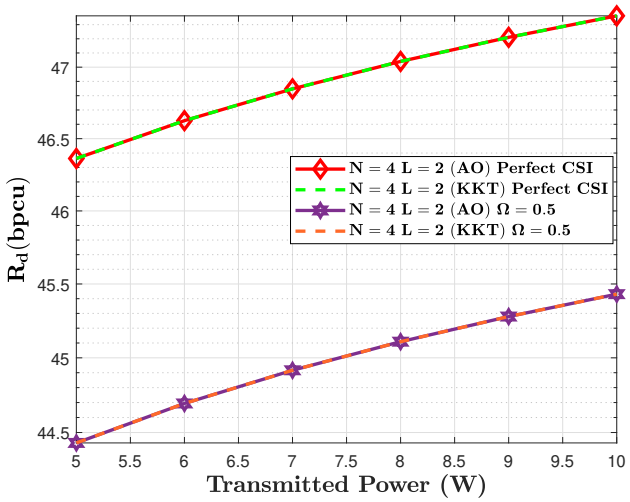

Fig. 4.12: Achievable rate (bpcu) versus transmit power P_t (W) for perfect CSI and imperfect CSI (ICSI) under speed-dependent errors.

CSI quality.

In Fig. 4.11, the performance of the proposed V2I system is evaluated under 1-D, 2-D, and 3-D RWP mobility models, as discussed in Section II for $L = 2, K = 4$. For a moving vehicle, random variations in distance v and speed introduce additional performance degradation since the received power decreases more sharply with mobility. The estimation errors induced by vehicular speed are explicitly analyzed. Fig. 4.11

illustrates the variation of the maximized rate across different RWP dimensions. It is observed that increasing the mobility dimension from 1-D to 3-D reduces the achievable rate, as higher-dimensional mobility leads to more complex distance distributions and larger fluctuations in received signal power.

Fig. 4.12 depicts the rate performance with different values of the CSI correlation coefficient, $\Omega = \{0.5, 1\}$. As expected, higher vehicular speeds result in larger channel estimation errors and lower achievable rates. Conversely, increasing Ω improves the system performance by mitigating estimation errors, with $\Omega = 1$ representing the perfect CSI scenario.

4.6 Chapter Summary

In this Chapter, we proposed a unified optimization framework for a V2I-SWIPT system employing multiple RIS. We maximized both the harvested energy, and the achievable data rate, by leveraging the PS protocol under a NL-EH model. To achieve this, we designed an iterative AO algorithm to solve the formulated optimization problem efficiently. The closed-form solutions for the key optimization variables were derived using the KKT conditions, ensuring optimality in resource allocation. Numerical evaluations were conducted to validate the proposed analytical framework, demonstrating the impact of system parameters on overall performance. Specifically, the results highlighted the sensitivity of both harvested energy and achievable data rate to the number of reflecting elements and the number of RISs. While an increase in the number of surfaces and passive elements leads to improved system performance, it also introduces significant computational complexity due to the high-dimensional optimization space. To mitigate this challenge, we introduced a DNN-based model

capable of efficiently predicting the optimized values with high precision. The integration of DL significantly reduced the computational time while maintaining near-optimal performance, making the proposed approach practical for real-time vehicular applications. Our analysis demonstrates that multi-RIS-assisted PS-SWIPT frameworks can significantly enhance both EH and information rate in vehicular networks. The findings provide practical insights for deployment, highlighting that spatially distributed RISs can mitigate blockage and coverage issues while supporting multiple vehicles simultaneously. Moreover, the proposed framework accounts for realistic fading, mobility, and imperfect CSI, making it applicable for real-world V2I scenarios.

Chapter 5

SWIPT-enabled Integrated Relay-RIS-aided UAV Communication

5.1 Introduction

Uncrewed Aerial Vehicles (UAVs) have become integral to Internet-of-Things (IoT) ecosystems due to their ability to deliver flexible, on-demand, and wide-area connectivity for diverse devices [110]. Their deployment spans a broad range of applications, from commercial domains such as remote sensing, logistics, and cinematography to governmental and emergency services involving disaster management, search and rescue, geospatial mapping, and surveillance [111]. These diverse roles highlight the growing relevance of UAVs in smart infrastructure and public safety. Nevertheless, operating at low altitudes in dense urban environments exposes UAVs to frequent Line-of-Sight (LoS) blockages caused by high-rise structures, which degrades the communication reliability and hinders mission-critical operations [112]. Further-

more, the limited onboard energy capacity of UAVs restricts their endurance, creating a bottleneck for long-term IoT support. To overcome this challenge, Simultaneous Wireless Information and Power Transfer (SWIPT) has emerged as a promising solution allowing the UAVs to harvest energy from Radio-Frequency (RF) signals while concurrently transmitting data. By leveraging SWIPT, UAV-assisted IoT networks become capable of extending the operational duration, reduce dependence on frequent recharging, and maintain reliable connectivity for energy-constrained IoT nodes, particularly in scenarios requiring uninterrupted service such as disaster recovery.

The Reconfigurable Intelligent Surfaces (RISs) are emerging as a technology to dynamically optimize wireless propagation in next-generation 5G-and-beyond networks. Comprising an array of programmable metasurfaces, RIS can intelligently manipulate wireless signals by inducing software-controlled reflections. Each RIS element is engineered with functionalities such as reflection, refraction, transmission, and absorption, which can be selectively utilized to meet diverse operational requirements [113]. Compared with the conventional relay-assisted communication systems, which suffer from high power consumption due to active RF chains, increased hardware complexity, amplified noise propagation, limited scalability, and reduced Energy Efficiency (EE) particularly in the UAV-assisted and disaster-prone environments where energy and payload constraints are critical, RIS-based architectures provide a compelling alternative with multiple advantages. RIS structures consist of cost-efficient, integrated components such as polymer-based diodes, switchable conductive patches, and other programmable elements that facilitate efficient signal redirection with minimal hardware overhead. Due to their compact form factor and lightweight design, RIS arrays support highly flexible 3-D deployments. Furthermore, the adjustable number of RIS elements provides additional degrees of freedom for the

channel optimization, thereby enhancing overall communication performance. Notably, RIS-based signal reflection operates independently of dedicated frequency allocation, mitigating network-wide spectrum congestion. Additionally, RIS achieves an energy-efficient operation by reflecting incoming signals without requiring extensive signal amplification, thereby conserving power [114]. This capability also enables UAV mounted transmitters to enter power-saving modes when the RIS-assisted transmission ensures adequate communication quality. The integration of RIS and UAV systems necessitates rigorous performance modeling and evaluation to fully exploit their synergistic potential.

The incorporation of a relay-assisted RIS-equipped UAV introduces unparalleled flexibility in communication networks, especially in environments where the traditional communication infrastructure is either absent or rendered inoperative, such as in disaster-affected areas. RIS technology enhances signal propagation by employing reconfigurable surfaces that mitigate obstructions, create virtual LoS pathways, and minimize interference in complex environments. The fusion of relay stations with RIS amplifies these advantages further, enabling the UAVs to function as dynamic network nodes while RIS optimizes the wireless connectivity with the ground stations. This hybrid architecture significantly enhances the network coverage, reduces latency, and improves overall communication reliability, presenting a superior alternative to the conventional standalone systems [66].

5.1.1 Chapter Organization

The structure of this paper is outlined as follows. Section 5.2 describes the system architecture, while Section 5.3 details the corresponding channel models that forms the basis of the proposed framework. Performance analysis is conducted in Section

5.4. The optimization and its solutions are outlined in Section 5.5. Simulation results and performance evaluations, including the parameter sensitivity analysis and comparisons with the existing approaches, are presented in Section 5.6. Finally, Section 5.7 summarizes the key findings and discusses the potential directions for future research.

5.2 System Model

We consider an integrated relay–RIS SWIPT network in which a UAV is equipped with a passive RIS, an independent DF relay acts as an Information Receiver (IR), and an Energy Receiver (ER) acts as a separate SWIPT architecture. This UAV enables communication between a base station (S) and a ground IoT device (D), under the assumption that no direct S–D link exists. Specifically, the RIS reflects the incident signal towards D with minimal power consumption [115], while the DF relay operates solely as an IR to ensure reliable data transmission between S and D, as shown in Fig. 5.1. Energy harvested by the ER is stored in a rechargeable unit and subsequently utilized to support both the relay's signal forwarding and the on-board processing requirements. The relay decodes the information received from S and further forwards it to D, where D, functioning as an additional IR, performs joint decoding of the signal received from both the relay and the RIS. A Time-Division Multiplexing (TDM)-based orthogonal reception framework is assumed between the relay-assisted and RIS-assisted links, enabling the destination to independently estimate the instantaneous SNR of each branch. Accordingly, at the D, SC is performed based on the maximum of the instantaneous SNRs observed across the two transmission paths. DF relay is preferred over AF relay in proposed system as they mitigate noise amplifica-

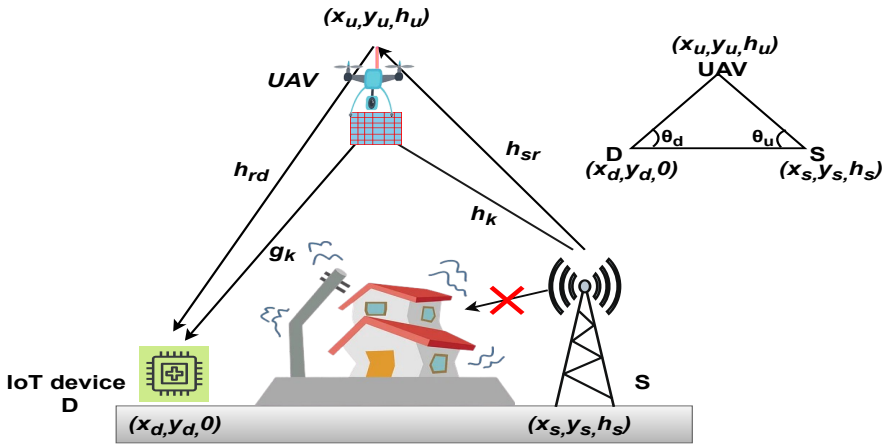

Fig. 5.1: UAV-assisted integrated relay-RIS SWIPT system enabling reliable wireless connectivity in disaster recovery scenario.

tion, thereby enhancing both communication reliability and Energy Harvesting (EH). Although DF relays introduce additional decoding complexity and processing delay, these drawbacks are outweighed by the performance benefits, particularly in critical applications such as disaster recovery.

Following the cartesian coordinates, positions of S and D are represented by $\mathbf{v}_s = (x_s, y_s, h_s)$ and $\mathbf{v}_d = (x_d, y_d, 0)$, respectively. Next, we make the assumption of UAV operating at any altitude h_u within the range $h_u \in [h_{\min}, h_{\max}]$, where $h_{\min}$ and $h_{\max}$ are the permissible altitudes for the UAV. The RIS is horizontally and rigidly mounted on the UAV platform and modeled as a uniform rectangular array with equal elements along both the horizontal and vertical axes. Consequently, it shares the same 3-D coordinates as the UAV. The UAV coordinates are given by $\mathbf{v}_u = (x_u, y_u, h_u)$. The UAV is assumed to remain stationary at a fixed location during the operation, neglecting the mobility effects. This assumption is practical in the disaster scenarios such as search-and-rescue or emergency communication recovery, where UAVs typically hover in a fixed position to maintain reliable connectivity with the ground users while minimizing the energy consumption. In the two-dimensional cartesian plane, the lo-

cations of the S, D, and UAV are represented by $\mathbf{w}_s = (x_s, y_s)$, $\mathbf{w}_d = (x_d, y_d)$, and $\mathbf{w}_u = (x_u, y_u)$, respectively.

The communication between the UAV and S, as well as between the UAV and D, depends on the elevation angle between the communicating nodes (or the UAV's altitude) and environmental factors, such as the height of surrounding buildings. The signal transmission to ground users can experience either LoS or Non-Line-of-Sight (NLoS) conditions, depending on the elevation angle (in radians) between the UAV and S or D. This elevation angle is given by the following expression.

$$\theta_u = \arctan\left(\frac{h_u}{|\mathbf{w}_u - \mathbf{w}_s|}\right), \quad \theta_d = \arctan\left(\frac{h_u}{|\mathbf{w}_u - \mathbf{w}_d|}\right). \tag{5.1}$$

For every link, the LoS probability is a function of elevation angle (θ_i), given by

$$p_L(\theta_i) = \left(1 + l_i \exp(-n_i(\theta_i - l_i))\right)^{-1}, \quad \forall i \in \{u, d\}, \tag{5.2}$$

where, l_u, l_d, n_u, and n_d are environment-dependent parameters determined through curve fitting technique utilizing the Damped Least-Squares (DLS) method, as described in [116].

The path-loss exponent α is a function of θ_i [116], and are expressed as

$$\alpha(\theta_i) = p_L(\theta_i)k_i + w_i, \quad \forall i \in \{u, d\}, \tag{5.3}$$

where k_u, w_u, k_d, and w_d are the constants, which depend on the uplink and downlink scenarios [117]. We further present the transmission and channel models corresponding to each mode of operations.

The energy gathered in real-life scenarios is a NL function of the input RF signal.

Normally, when the input power increases, the efficiency of converting RF energy to direct current (RF-to-DC) the energy rises to a peak and then levels out at a constant amount. In a high power regime, the harvesting of energy could be overestimated, when the traditional linear EH model is applied. In order to eliminate the inaccuracy of the conventional linear EH receiver model and capture the NL characteristic of the RF-to-DC power conversion, we adopt a sigmoidal function based NL-EH mechanism [106]. The SWIPT receiver yields an expression for the harvested energy as

$$EH = \frac{\varepsilon}{1-\Phi}\left(\frac{1}{1+exp(-aP_t z^2+ab)}-\Phi\right), \tag{5.4}$$

where $\Phi = \frac{1}{1+exp(ab)}$ is a constant for the zero-input/zero-output response of EH, z is the channel corresponding to the instantaneous SNR, ε is the EH circuit saturation point, and a and b are the constants related to the underlying circuit components, such as the resistance, capacitance, and diode turn-on voltage. Since the EH hardware at each ER is fixed, the values of a and b remain constant and are accurately estimated using the standard curve-fitting techniques based on experimentally obtained RF-EH measurements, as widely adopted in prior works [106] and [19].

5.3 Channel Model

In this section, we discussed the channel models for the relay-only, RIS-only, and integrated relay-RIS modes under both SC and MRC schemes.

5.3.1 Relay-only mode

To ensure a consistent system performance, the relay is assumed to be powered by both an external power supply, with energy E_{ext}, and harvested energy, thereby ensur-

ing a reliable communication between the UAV and D. This generalized model facilitates the analysis of diverse practical scenarios, including a purely SWIPT-enabled relay, which is represented by setting $E_{\text{ext}} = 0$.

The harvested energy at the UAV is given by

$$E_h = \frac{\varepsilon}{1-\Phi}\left(\frac{1}{1+exp(-aP_t h_{sr}^2 + ab)} - \Phi\right), \tag{5.5}$$

where P_t denotes the transmission power of S, and h_{sr} represents the fading channel coefficient between S and the UAV, modeled using the Nakagami-m distribution.

The transmissions from S to UAV can be expressed as

$$y_u = \sqrt{AP_t d_u^{-\alpha(\theta_u)}} h_{sr} x + n_u, \tag{5.6}$$

where x is the transmitted signal from S to UAV. The separation between the S and the UAV is denoted by d_u, expressed as $d_u = \sqrt{|\mathbf{w}_u - \mathbf{w}_s|^2 + h_u^2}$, where $\mathbf{w}_u$ and $\mathbf{w}_s$ are their respective horizontal coordinates and h_u is the UAV altitude. The constant A encapsulates the physical system parameters such as the carrier frequency and antenna characteristics. The term n_u corresponds to zero-mean AWGN with a power spectral density of N_0. Additionally, the received signal at D from UAV is expressed as

$$y_d = \sqrt{AP_u d_d^{-\alpha(\theta_d)}} h_{rd} \bar{y}_u + n_d, \tag{5.7}$$

Here, $\bar{y}_u$ represents the decoded and forwarded signal by the UAV to D, while P_u denotes the UAV's transmission power. The UAV-to-D distance is given by $d_d = \sqrt{|\mathbf{w}_u - \mathbf{w}_d|^2 + h_u^2}$. The term n_d corresponds to additive white Gaussian noise (AWGN) with zero mean and power spectral density N_0, and h_{rd} represents the channel fading coefficient for relay-to-D link, following the Nakagami-m distribution.

The PDF of the Nakagami-m, characterized by fading severity (i.e., shape) parameter (m) and average power (i.e., scale) parameter (Ω), is given by [118]

$$f_X(x) = \frac{2m^m}{\Gamma(m)\Omega^m} x^{2m-1} \exp\left(-\frac{m}{\Omega}x^2\right), \quad x \geq 0. \tag{5.8}$$

The Nakagami-m model's flexibility in adjusting the fading parameter m enables accurate representation of different propagation environments. This adaptability is particularly important for SWIPT-enabled UAV systems, where EH efficiency is highly sensitive to fading severity. Hence, Nakagami-m provides a more accurate and versatile characterization of UAV channels compared to the Rayleigh and Rician fading models. The Nakagami-m fading model reduces exactly to a Rayleigh fading when $m = 1$, while for $m > 1$, it converts to an accurate approximation of Rician fading [119].

The instantaneous SNRs for S-to-relay link and relay-to-D link are, respectively, given by

$$\gamma_u = \frac{AP_t d_u^{-\alpha(\theta_u)} Y_u}{N_0}, \quad \gamma_d = \frac{AP_u d_d^{-\alpha(\theta_d)} Y_d}{N_0}, \tag{5.9}$$

where $Y_u = |h_{sr}|^2$ and $Y_d = |h_{rd}|^2$ follow a Gamma distribution. Hence, the PDF of γ_j also follows Gamma distribution, which is given as

$$f_{\gamma_j}(x) = \frac{m^m}{\Gamma(m)\Omega^m k^m} x^{m-1} \exp\left(-\frac{m}{\Omega k}x\right), \tag{5.10}$$

where $k = \frac{AP_j d_j^{-\alpha(\theta_j)}}{N_0}, \quad j \in (u, d)$.

The CDF of γ_j is given by

$$F_{\gamma_j}(x) = \frac{\Upsilon\left(m, \frac{m}{\Omega k}\gamma_j\right)}{\Gamma(m)}, \tag{5.11}$$

where $\Upsilon(\cdot,\cdot)$ is the lower incomplete Gamma function.

The end-to-end instantaneous SNR $\hat{\gamma}$ from S to D for DF relaying can be written as

$$\hat{\gamma} = \min\{\gamma_u, \gamma_d\}. \tag{5.12}$$

While the DF relaying mode relies on an active signal forwarding through the UAV, the RIS-only mode leverages passive reflection to enhance the signal quality without additional power consumption for forwarding. In the following subsection, we present the channel model for RIS-Only Mode.

5.3.2 RIS-only Mode

Herein, it is assumed that the relay does not participate in the transmission process, and instead, the RIS adapts the phase shifts of its elements to improve the signal quality. The phase optimization is carried out to achieve a constructive signal combining at the destination. The signal received at D via N RIS elements is given by

$$y_i = \sum_{k=1}^{N} \sqrt{AP_t d_u^{-\alpha(\theta_u)}}\bar{h}_k e^{j\phi_k} \sqrt{Ad_d^{-\alpha(\theta_d)}}\bar{g}_k x + n_i. \tag{5.13}$$

The channels from S to RIS and from the RIS to D are expressed as $\bar{h}_k = h_k e^{j\zeta_k}$ and $\bar{g}_k = g_k e^{j\xi_k}$, respectively.

The end-to-end instantaneous SNR $\bar{\gamma}$ for RIS-only mode is given as

$$\bar{\gamma} = \frac{A^2 P_t}{N_0} \left(\sum_{k=1}^{N} d_u^{-\frac{\alpha(\theta_u)}{2}} d_d^{-\frac{\alpha(\theta_d)}{2}} h_k g_k e^{j(\zeta_k + \xi_k + \phi_k)} \right)^2. \tag{5.14}$$

It is evident from (5.14) that the maximum SNR is obtained by setting the channel phases as $\phi_k = -(\zeta_k + \xi_k)$, which maximizes the exponential term to unity, since $|e^{j(\zeta_k+\xi_k+\phi_k)}|^2$=1. Consequently, (5.14) simplifies to

$$\bar{\gamma} = \mathcal{B} \left(\sum_{k=1}^{N} h_k g_k \right)^2 = \mathcal{B} v_k^2, \tag{5.15}$$

where $\mathcal{B} = \frac{A^2 P_t}{N_0} d_u^{-\theta_u} d_d^{-\theta_d}$ and $v_k = \sum_{i=1}^{N} h_k g_k$.

Let $z_k = h_k g_k$, where both h_k and g_k are assumed to follow independent Nakagami-m distributions, with $h_k \sim$ Nakagami$(m_{k,1}, \Omega_{k,1})$ and $g_k \sim$ Nakagami$(m_{k,2}, \Omega_{k,2})$, representing distinct fading conditions on the separate links. Then, the PDF of z_k is written as

$$f_{z_k}(x) = \frac{4(\Theta_{k,1}\Theta_{k,2})^{m_{k,1}+m_{k,2}}}{\Gamma(m_{k,1})\Gamma(m_{k,2})} \mathcal{K}_{m_{k,1}-m_{k,2}}(2\Theta_{k,1}\Theta_{k,2}x) \times x^{m_{k,1}+m_{k,2}-1}, \tag{5.16}$$

where $\Theta_{k,j} = \sqrt{\frac{m_{k,j}}{\Omega_{k,j}}}$ for $j = 1, 2$, and $\mathcal{K}_\nu(\cdot)$ is the modified Bessel function of the second kind of order ν [120]. The r-th moment of z_k is given by

$$\mathbb{E}\left((z_k)^r\right) = \frac{\Gamma\left(m_{k,1} + \frac{r}{2}\right) \Gamma\left(m_{k,2} + \frac{r}{2}\right) (\Theta_{k,1}\Theta_{k,2})^r}{\Gamma(m_{k,1})\Gamma(m_{k,2})}. \tag{5.17}$$

Now, let $v_k = \sum_{i=1}^{N} z_k$. As v_k is the sum of independent and identically distributed (i.i.d.) positive RVs, and according to [121], the PDF of v_k can be well approximated by the first term of a Laguerre series expansion, resulting in a Gamma distribution

with PDF given by

$$f_{v_k}(x) \approx \frac{1}{\Gamma(a_k) b_k^{a_k}} x^{a_k - 1} \exp\left(-\frac{x}{b_k}\right), \tag{5.18}$$

where the shape parameter $a_k = \frac{(\mathbb{E}(v_k))^2}{\mathrm{Var}(v_k)}$ and the scale parameter $b_k = \frac{\mathrm{Var}(v_k)}{\mathbb{E}(v_k)}$. Since the expectation is a linear operator, $\mathbb{E}(v_k) = N\mathbb{E}(z_k)$, and due to the independence, $\mathrm{Var}(v_k) = N\,\mathrm{Var}(z_k)$.

By applying the transformation of Random Variables (RV) technique, the PDF of $\bar{\gamma}$ is given by

$$f_{\bar{\gamma}}(\gamma) \approx \frac{1}{2\Gamma(a_k) b_k^{a_k}} \mathcal{B}^{-\frac{a_k}{2}} \gamma^{\frac{a_k}{2}-1} \exp\left(-\frac{1}{b_k}\sqrt{\frac{\gamma}{\mathcal{B}}}\right). \tag{5.19}$$

The CDF expression of $\bar{\gamma}$ is given by

$$F_{\bar{\gamma}}(\gamma) \approx \frac{\Upsilon\left(a_k, \sqrt{\frac{\gamma}{b_k^2 \mathcal{B}}}\right)}{\Gamma(a_k)}. \tag{5.20}$$

5.3.2.1 Phase-Shift Design

In the ideal configuration, the phase shift of the k-th reflecting element is selected as : $\phi_k = \phi_k^{\mathrm{opt}} = -(\zeta_k + \xi_k)$, so that the exponential term is maximized to unity, i.e., $\left|e^{j(\zeta_k + \xi_k + \phi_k)}\right|^2 = 1$.

In practice, however, a perfect phase alignment is difficult to realize due to impairments such as UAV jitter, vibration, and airflow turbulence. As a result, the implemented phase may be expressed as

$$\phi_k = \phi_k^{\mathrm{opt}} + \phi_k^{\mathrm{err}}, \tag{5.21}$$

where $\phi_k^{\text{opt}} = -(\zeta_k + \xi_k)$ and ϕ_k^{err} denotes the residual phase error.

The phase estimation error ϕ_k^{err} is typically characterized by a von Mises distribution with zero mean and concentration parameter η, which is inversely related to the phase-error variance. A smaller value of η represents more severe disturbance-induced phase fluctuations. The corresponding PDF and moment generating function are given by [122]

$$f_{\phi_k^{\text{err}}}(x) = \frac{e^{\eta \cos(x)}}{2\pi I_0(\eta)}, \tag{5.22}$$

$$\varphi_p = \mathbb{E}\big(e^{jp\phi_k^{\text{err}}}\big) = \frac{I_p(\eta)}{I_0(\eta)}, \tag{5.23}$$

where $I_0(\cdot)$ and $I_p(\cdot)$ denotes the modified Bessel functions of the first kind of order 0 and p, respectively.

Under an imperfect phase adjustment, the received SNR at node D is given by

$$\bar{\gamma}_{ip} = \frac{A^2 P_t}{N_0} \left(\sum_{k=1}^{N} d_u^{-\frac{\alpha(\theta_u)}{2}} d_d^{-\frac{\alpha(\theta_d)}{2}} h_k g_k e^{j\phi_k^{\text{err}}} \right)^2. \tag{5.24}$$

Let $\bar{\gamma}_{ip} = C_{ip} H_D$,

$$H_D = \left| \sum_{k=1}^{N} h_k g_k e^{j\phi_k^{\text{err}}} \right|^2 = |U_m + jV_m|^2, \tag{5.25}$$

where the in-phase and quadrature components are given by

$$U_m = \sum_{k=1}^{N} h_k g_k \cos(\phi_k^{\text{err}}), \qquad V_m = \sum_{k=1}^{N} h_k g_k \sin(\phi_k^{\text{err}}). \tag{5.26}$$

The corresponding mean values are obtained as

$$\mathbb{E}[U_m] = N\,\mathbb{E}[h_k]\mathbb{E}[g_k] J_1 = N \xi_g^2 J_1, \tag{5.27}$$

where $\mathbb{E}[h_k] = \frac{\Gamma(m_1+\frac{1}{2})}{\Gamma(m_1)\sqrt{m_1}}$, $\mathbb{E}[g_k] = \frac{\Gamma(m_2+\frac{1}{2})}{\Gamma(m_2)\sqrt{m_2}}$.

$$\mathbb{E}[V_m] = N\xi_g^2\mathbb{E}[\sin(\phi_k^{\text{err}})] \approx 0 \quad \Rightarrow \quad \mathbb{E}[V_m] = 0, \tag{5.28}$$

where $\xi_g = \sqrt{\mathbb{E}[h_k]\mathbb{E}[g_k]}$.

The variance of U_m is obtained as

$$\text{Var}[U_m] = \frac{N}{2}\Big(1 + J_2 - 2\xi_g^4 J_1^2\Big), \tag{5.29}$$

By employing the Gamma approximation, the PDF of H_D is expressed as

$$f_{H_D}(x) = x^{m_h-1}\frac{m_h^{m_h}}{\Gamma(m_h)\Omega_h^{m_h}}\exp\left(-\frac{m_h}{\Omega_h}x\right), \tag{5.30}$$

where the shaping parameter and mean power are

$$m_h = \frac{\mathbb{E}^2(U_m)}{4\,\text{Var}(U_m)} = \frac{N\xi_g^4 J_1^2}{2\big(1 + J_2 - 2\xi_g^4 J_1^2\big)}, \tag{5.31}$$

$$\Omega_h = \mathbb{E}^2(U_m) = N^2\xi_g^4 J_1^2. \tag{5.32}$$

Accordingly, the CDF of H_D is obtained as

$$F_{H_D}(x) = \frac{\Upsilon\Big(m_h, \frac{m_h}{\Omega_h}x\Big)}{\Gamma(m_h)}, \tag{5.33}$$

where $\Upsilon(\cdot,\cdot)$ denotes the lower incomplete Gamma function.

The CDF of the instantaneous SNR under imperfect phase adjustment is obtained as

$$F_{\tilde{\gamma}_{ip}}(\gamma) = \Pr(C_{ip}H_D \leq \gamma) = F_{H_D}\left(\frac{\gamma}{C_{ip}}\right) = \frac{\Upsilon\left(m_h,\ \frac{m_h}{\Omega_h}\frac{\gamma}{C_{ip}}\right)}{\Gamma(m_h)}, \qquad \gamma \geq 0. \quad (5.34)$$

To harness the complementary benefits of active relaying and passive reflection, we now consider an integrated relay-RIS mode. This hybrid configuration is designed to enhance the communication reliability, and its corresponding channel models for the SC and MRC schemes are presented in the following subsection.

5.3.3 Integrated Relay-RIS Mode

In this mode, two schemes are considered to characterize the system behavior. These schemes are described in detail as follows.

5.3.3.1 SC Scheme

In this mode, both the relay transceiver and RIS in UAV forward the signal transmitted from S, with D employing SC based on maximum instantaneous SNR. Hence, the output instantaneous SNR at the receiver is given by

$$\tilde{\gamma}_{sc} = \max\left(\hat{\gamma}, \bar{\gamma}\right). \quad (5.35)$$

The CDF of $\tilde{\gamma}_{sc}$ can be expressed as

$$\begin{aligned} F_{\tilde{\gamma}_{sc}}(\gamma) &= \Pr\left[\max\left(\hat{\gamma}, \bar{\gamma}\right) < \gamma\right] \\ &= \Pr\left[\hat{\gamma} < \gamma, \bar{\gamma} < \gamma\right], \end{aligned} \quad (5.36)$$

where $\Pr(\cdot)$ denotes the probability. By substituting (5.12) in the above align, the CDF of $\tilde{\gamma}_{sc}$ is represented as

$$\begin{aligned} F_{\tilde{\gamma}_{sc}}(\gamma) &= \Pr\left[\min\{\gamma_u, \gamma_d\} < \gamma, \bar{\gamma} < \gamma\right] \\ &= (1 - (1 - F_{\gamma_u}(\gamma))(1 - F_{\gamma_d}(\gamma))) \times F_{\bar{\gamma}}(\gamma), \end{aligned} \tag{5.37}$$

where $F_{\gamma_u}(\gamma)$ and $F_{\gamma_d}(\gamma)$ are the CDFs of instantaneous SNRs of relay-only mode given by (5.11) and $F_{\bar{\gamma}}(\gamma)$ is the CDF of instantaneous SNR of RIS-only mode expressed in (6.42).

Due to the imperfect phase adjustment, the received instantaneous SNR of RIS-only mode is denoted by $\bar{\gamma}_{ip}$, and its corresponding CDF is expressed as $F_{\bar{\gamma}_{ip}}(\gamma)$, as given in (5.34).

The CDF of $\tilde{\gamma}_{sc}^{ip}$ considering imperfect phase adjustment under SC scheme is represented as

$$\begin{aligned} F_{\tilde{\gamma}_{sc}^{ip}}(\gamma) &= \Pr\left[\min\{\gamma_u, \gamma_d\} < \gamma, \bar{\gamma}_{ip} < \gamma\right] \\ &= (1 - (1 - F_{\gamma_u}(\gamma))(1 - F_{\gamma_d}(\gamma))) \times F_{\bar{\gamma}_{ip}}(\gamma). \end{aligned} \tag{5.38}$$

5.3.3.2 MRC Scheme

In this mode, both the relay transceiver and RIS in UAV forward the signal transmitted from S, with D employing MRC scheme. Hence, the output instantaneous SNR at the receiver is given by

$$\tilde{\gamma}_{mrc} = \hat{\gamma} + \bar{\gamma}. \tag{5.39}$$

The CDF of $\tilde{\gamma}_{mrc}$ is expressed as

$$F_{\tilde{\gamma}_{mrc}}(\gamma) = \Pr\left[(\hat{\gamma} + \bar{\gamma}) < \gamma\right]. \tag{5.40}$$

The CDF corresponding to the MRC scheme is formulated as

$$F_{\tilde{\gamma}_{mrc}}(\gamma) = \int_0^{\gamma} \int_0^{\gamma - x} f_{\hat{\gamma},\bar{\gamma}}(x, y)\, dx\, dy. \tag{5.41}$$

Since the above integral is not straightforward to calculate, we use an approximation method in which the region of integration is divided into L rectangular sub-regions to facilitate the solution of the integral [69]. For the mth sub-region among the total L regions, the integral is expressed as

$$I_m = \int_{\frac{(m-1)\gamma}{L}}^{\frac{m\gamma}{L}} f_{\hat{\gamma}}(x)\, dx \int_0^{\gamma - \frac{(m-1)\gamma}{L}} f_{\bar{\gamma}}(y)\, dy \tag{5.42}$$

$$= \left[F_{\hat{\gamma}}\left(\frac{m\gamma}{L}\right) - F_{\hat{\gamma}}\left(\frac{(m-1)\gamma}{L}\right)\right] F_{\bar{\gamma}}\left(\frac{(L-m+1)\gamma}{L}\right). \tag{5.43}$$

Hence, the expression in (5.43) is rewritten as

$$F_{\tilde{\gamma}_{mrc}}(\gamma) = \sum_{m=1}^{L} I_m. \tag{5.44}$$

The final expression for the CDF is written as

$$F_{\tilde{\gamma}_{mrc}}(\gamma) = \sum_{m=1}^{L} \left[F_{\hat{\gamma}}\left(\frac{m\gamma}{L}\right) - F_{\hat{\gamma}}\left(\frac{(m-1)\gamma}{L}\right)\right] \times F_{\bar{\gamma}}\left(\frac{(L-m+1)\gamma}{L}\right), \tag{5.45}$$

where $F_{\hat{\gamma}}(\cdot)$ and $F_{\bar{\gamma}}(\cdot)$ are the CDFs given in (5.11) and (6.42), respectively. In this section, Similarly, for the analysis under imperfect phase adjustment, the instantaneous received SNR in the RIS-only mode is denoted by $\bar{\gamma}_{ip}$, and its CDF is expressed

as $F_{\tilde{\gamma}_{ip}}(\gamma)$, as previously defined in (5.34) and derived in the earlier section.

The CDF of $\tilde{\gamma}^{ip}_{mrc}$ considering imperfect phase adjustment under MRC scheme is represented as

$$F_{\tilde{\gamma}^{ip}_{mrc}}(\gamma) = \sum_{m=1}^{L} \left[F_{\hat{\gamma}} \left(\frac{m\gamma}{L} \right) - F_{\hat{\gamma}} \left(\frac{(m-1)\gamma}{L} \right) \right] \times F_{\tilde{\gamma}_{ip}} \left(\frac{(L-m+1)\gamma}{L} \right) \tag{5.46}$$

5.4 Performance Analysis

In this section, the performance of the integrated relay–RIS mode is evaluated using the OP, ASER, EC, and OC metrics. In particular, OP and ASER are employed to capture the reliability and link-level error behavior of the system under practical fading and interference conditions, which are especially important for latency- and Quality-of-Service (QoS)-constrained applications. In contrast, EC and OC serve as throughput-oriented indicators that characterize the long-term Spectral Efficiency (SE) and capacity performance under statistical channel variations. Together, these metrics enable a comprehensive and complementary assessment of the proposed system.

5.4.1 Outage Probability

The proposed integrated relay-RIS UAV system is deemed to be in outage if the instantaneous SNR of the optimal link drops below the threshold value γ_{th}. The OP of

the integrated relay-RIS system is expressed as

$$\widehat{P} = \Pr[\tilde{\gamma}_t < \gamma_{\text{th}}] = F_{\tilde{\gamma}_t}(\gamma_{th}), \tag{5.47}$$

where γ is replaced with γ_{th}. By setting $\tilde{\gamma}_t = \tilde{\gamma}_{sc}$ and $\tilde{\gamma}_t = \tilde{\gamma}_{mrc}$, the OP for the SC and MRC schemes under perfect phase adjustment are obtained. Likewise, by setting $\tilde{\gamma}_t = \tilde{\gamma}_{sc}^{ip}$ and $\tilde{\gamma}_t = \tilde{\gamma}_{mrc}^{ip}$, the corresponding OP for the SC and MRC schemes under imperfect phase adjustment are obtained.

5.4.2 Average Symbol Error Rate

For the proposed relay-RIS integrated system, employing M-ary PSK modulation, ASER is evaluated using the CDF of instantaneous SNR. The CDF-based ASER expression for MPSK scheme is given by

$$\widetilde{P} = \frac{p\sqrt{q}}{2\sqrt{2\pi}} \int_0^\infty \frac{F_{\tilde{\gamma}_t}(\gamma)}{\sqrt{\gamma}} e^{\frac{-q\gamma}{2}} \, d\gamma \,, \tag{5.48}$$

where p and q represent parameters specific to the modulation scheme, with their values defined as follows: BPSK ($p = 1, q = 2$), QPSK ($p = 2, q = 1$), 8-PSK ($p = 2, q = 0.3$), and 16-PSK ($p = 2, q = 0.076$). Note that substituting $\tilde{\gamma}_t = \tilde{\gamma}_{sc}$ and $\tilde{\gamma}_t = \tilde{\gamma}_{mrc}$, we get ASER for the SC scheme and the MRC scheme under perfect phase adjustment, respectively. Similarly by substituting $\tilde{\gamma}_t = \tilde{\gamma}_{sc}^{ip}$ and $\tilde{\gamma}_t = \tilde{\gamma}_{mrc}^{ip}$, the corresponding OP for the SC and MRC schemes under imperfect phase adjustment are obtained.

The integral in (5.48) is approximated using the n-point Gauss–Laguerre quadrature

method, leading to the final expression for the ASER as

$$\widetilde{P} = \frac{p\sqrt{q}}{2\sqrt{2\pi}} \sum_{l=1}^{n} W_l F_{\tilde{\gamma}_t}(\phi_l). \tag{5.49}$$

Here, W_l represents the weight coefficient and ϕ_l denote the lth zero of the Laguerre polynomial $L_d^{(-1/2)}(x)$, which is given by

$$L_d^{(-1/2)}(x) = \frac{2}{d} \sum_{j=0}^{d} \begin{pmatrix} d - \frac{1}{2} \\ d - j \end{pmatrix} \left(\frac{-x^j}{j!} \right). \tag{5.50}$$

The weight coefficient W_l is defined as

$$W_l = \frac{\Gamma\left(j + \frac{1}{2}\right) \phi_l}{j! \left[(j+1) L_{j+1}^{(-1/2)}(\phi_l) \right]^2}. \tag{5.51}$$

5.4.3 Ergodic Capacity

The EC for the integrated Relay-RIS is given by

$$C = \frac{1}{\ln 2} \int_0^{\infty} \frac{1 - F_{\tilde{\gamma}_t}(\gamma)}{1 + \gamma} \, d\gamma. \tag{5.52}$$

Due to the mathematical intractability of (5.52), we utilize the generalized Gauss-Laguerre quadrature method and reformulate the EC as follows

$$C = \frac{1}{\ln 2} \sum_{l=1}^{n} W_l F_a(\phi_l), \tag{5.53}$$

where $F_a(\phi_l) = \frac{1 - F_{\tilde{\gamma}_t}(\phi_l)}{(1+x_l) x^{(-\frac{1}{2})} e^{-x_l}}$. By substituting $\tilde{\gamma}_t = \tilde{\gamma}_{sc}$ and $\tilde{\gamma}_t = \tilde{\gamma}_{mrc}$, we get EC for SC scheme and MRC scheme under perfect phase adjustment, respectively. Similarly by substituting $\tilde{\gamma}_t = \tilde{\gamma}_{sc}^{ip}$ and $\tilde{\gamma}_t = \tilde{\gamma}_{mrc}^{ip}$, the corresponding OP for the SC and MRC schemes under imperfect phase adjustment are obtained.

5.4.4 Outage Capacity

The OC of the proposed system is interpreted as the probability that the system's instantaneous transmission rate lies below a given minimum capacity requirement. The OC is expressed as

$$\tilde{C} = \Pr[C_{\tilde{\gamma}_t} \leq C_{th}] = F_{\tilde{\gamma}_t}\left(2^{C_{th}} - 1\right), \tag{5.54}$$

where C_{th} is the threshold capacity value. By substituting $\tilde{\gamma}_t = \tilde{\gamma}_{sc}$ and $\tilde{\gamma}_t = \tilde{\gamma}_{mrc}$, the OC expressions for the SC and MRC schemes under perfect phase adjustment are obtained. In a similar manner, substituting $\tilde{\gamma}_t = \tilde{\gamma}_{sc}^{ip}$ and $\tilde{\gamma}_t = \tilde{\gamma}_{mrc}^{ip}$ yields the corresponding results for the SC and MRC schemes in the presence of imperfect phase adjustment.

To achieve higher data transmission rates and prolong the UAV's hovering time, it is crucial to optimize the transmit power and relay link power. This ensures an efficient EH, thereby extending the UAV's operational life. In the following section, three distinct optimization problems are formulated: the first aims to maximize the achievable data rate at the D, the second focuses on enhancing the amount of energy stored at the UAV, while the third addresses the maximization of EE.

5.5 Optimization Problem Formulation and Solutions

Herein, our primary goal is to maximize the information rate at D, the energy stored at the UAV, and EE. To achieve this, we derive the closed-form expressions for the optimization problem by applying the KKT conditions.

5.5.1 Maximization of Rate at D

In this subsection, we aim at maximizing the information rate between the S and the D via integrated relay-RIS considering MRC scheme, while assuring the rate constraint, power for UAV to D link, and the total transmit power at the S does not exceed the limit. The overall sum rate at the D is given by

$$R_u = \log_2(1 + \tilde{\gamma}_{mrc}). \tag{5.55}$$

Here, $\tilde{\gamma}_{mrc}$ denotes the instantaneous SNR from MRC scheme. This expression shows that maximizing the achievable rate is equivalent to maximizing the effective received SNR at node D. Hence, the optimization of P_t and P_u directly influences the rate performance through their impact on $\tilde{\gamma}_{mrc}$.

The corresponding optimization problem is mathematically represented as

$$\text{(P5.1)} : \max_{P_t,\, P_u} \quad R_u \tag{5.56}$$

$$\text{subject to: (C1)} : \; R_u \geq R_{th}, \tag{5.57}$$

$$\text{(C2)} : \; P_{min} \leq P_u \leq E_h + E_{ext}, \tag{5.58}$$

$$\text{(C3)} : \; 0 \leq P_t \leq P_{max}, \tag{5.59}$$

where R_{th}, P_{min}, E_{ext}, E_h, and P_{max} are the maximum rate threshold value, minimum power required for UAV to D link, input energy at UAV, harvested energy at UAV, and maximum transmit power, respectively.[1] Constraints (C1)-(C3) jointly ensure QoS, UAV power feasibility, and source transmit power limitations. Therefore, the optimization balances rate maximization with practical energy and hardware restrictions. The Problem (P5.1) is non-convex because the variables in the objective function and

[1]Here, the energy term and power term are used interchangeably, assuming a unit time duration.

constraints are interdependent, making a direct solution intractable. To obtain the closed-form solution, we invoke the KKT conditions to find the sub-optimal solution, which may be the optimal solution in some cases.

For MRC reception, the equivalent received SNR is

$$\tilde{\gamma}_{mrc} = \begin{cases} \gamma_d + \bar{\gamma}, & \gamma_d \leq \gamma_u, \\ \gamma_u + \bar{\gamma}, & \gamma_u \leq \gamma_d, \end{cases} \tag{5.60}$$

This formulation reflects that MRC combines signals from two independent paths, and the effective SNR is determined by the weaker hop, which acts as the system bottleneck.

To deal with the non-convexity of (P5.1) from joint optimization of P_u and P_t, we use an iterative approach, optimizing one parameter while fixing the other until a convergence of the objective function is reached. The proposed Algorithm 5.2 has a computational complexity of $\mathcal{O}(s(\mathcal{A}+\mathcal{B}))$, where S is number of iterations, and $\mathcal{A}$ and $\mathcal{B}$ denotes the number of computational time for Step 3 and Step 4, respectively.

Next, we discuss an alternative method to obtain a closed-form solution for the aforementioned problem (P5.1) wherein we solve it directly using the KKT conditions [107].

Let $\tilde{\gamma}_{mrc} = \gamma_d + \bar{\gamma};\ \gamma_d \leq \gamma_u$, the Lagrangian corresponding to (P5.1) be denoted as follows

$$\mathcal{L}(P_t, P_u; \Delta) = f(P_t, P_u) - \lambda_1 g(P_t, P_u) - \lambda_2 h(P_t, P_u) - \lambda_3 i(P_t, P_u) - \lambda_4 j(P_t, P_u), \tag{5.61}$$

where $\Delta = (\lambda_1, \lambda_2, \lambda_3, \lambda_4)$ is the vector comprising Lagrange multipliers, $f(P_t, P_u) = \log_2(1+\bar{\gamma}) + \log_2(1+\gamma_d)$, $g(P_t, P_u) = R_{th} - (\log_2(1+\bar{\gamma}) + \log_2(1+\gamma_d))$,

$h(P_t, P_u) = P_u - \frac{\varepsilon}{1-\Phi}\left(\frac{1}{1+exp(-aP_t h_{sr}^2+ab)} - \Phi\right) - E_{ext}$, $i(P_t, P_u) = P_{min} - P_u$, and $j(P_t, P_u) = P_t - P_{max}$, and λ_1, λ_2, λ_3, λ_4 are the Lagrange Multipliers. The Lagrangian incorporates the objective function and constraints into a single expression, enabling the use of KKT conditions to determine the stationary points that satisfy optimality under power and rate constraints.

For optimal value, $\nabla\mathcal{L}(P_t, P_u; \Delta) = 0$ must hold

$$\frac{\partial\mathcal{L}(P_t, P_u; \Delta)}{\partial P_t} \Rightarrow (1+\lambda_1)\frac{v_k^2}{\ln 2 \cdot N_0(1+\bar{\gamma})} - \lambda_4 + \lambda_2 \frac{\varepsilon a h_{sr}^2 e^{(-aP_t z_k^2+ab)}}{(1-\phi)\left(1+e^{(-aP_t h_{sr}^2+ab)}\right)^2} = 0 \tag{5.62}$$

$$\frac{\partial\mathcal{L}(P_t, P_u; \Delta)}{\partial P_u} \Rightarrow (1+\lambda_1)\frac{h_{rd}^2}{\ln 2 \cdot N_0(1+\gamma_d)} - \lambda_2 + \lambda_3 = 0 \tag{5.63}$$

These conditions indicate how the optimal transmit powers are influenced by channel gains, noise power, and the EH characteristics, while being regulated by the associated Lagrange multipliers.

To satisfy the KKT conditions, the complementary slackness expressions are described as follows

$$\begin{aligned} \lambda_1 \cdot g(P_t, P_u) = 0; \quad & \lambda_2 \cdot h(P_t, P_u) = 0; \\ \lambda_3 \cdot i(P_t, P_u) = 0; \quad & \lambda_4 \cdot j(P_t, P_u) = 0. \end{aligned} \tag{5.64}$$

The complementary slackness conditions determine which constraints are active at optimality, leading to the case-by-case analysis presented in the subsequent lemmas. To satisfy the non-negativity conditions : $\{P_t, P_u, \Delta\} \geq 0$, a comprehensive case analysis of (5.61)–(5.64) is performed under standard KKT procedures.

Algorithm 5.2 AO Algorithm for rate

1: **Initialization:** Choose an initial feasible value for R_u and initialize iteration counter $n = 0$.
2: **repeat**
3: Solve (P5.1) to Optimize P_t with fixed P_u, and obtain P_t^*.
4: Obtain optimal P_u^* by solving (P5.1) using P_t^*.
5: Compute R_u using the updated P_t^* and P_u^*.
6: Store the result: $R_u(n)$.
7: Increment iteration counter: $n \leftarrow n + 1$.
8: **until** convergence: $R_u(n) \geq R_u(n-1)$

Among the sixteen possible cases, the four potential optimal solutions are outlined in Lemmas 1–4.

Lemma 1. If $\lambda_1 = 0 \Rightarrow (R_u - R_{\text{th}}) \neq 0$; $\lambda_2 \neq 0 \Rightarrow (P_u - E_h - E_{ext}) = 0$; $\lambda_3 = 0 \Rightarrow (P_{min} - P_u) \neq 0$; $\lambda_4 \neq 0 \Rightarrow (P_t - P_{max}) = 0$, then the optimal values are

$$P_t^{(1)} = P_{max}, \;\; P_u^{(1)} = \frac{\varepsilon}{1-\Phi}\left(\frac{1}{1+exp(-aP_t^{(1)}h_{sr}^2 + ab)} - \Phi\right) + E_{ext}. \tag{5.65}$$

Lemma 2. If $\lambda_1 = 0 \Rightarrow (R_u - R_{\text{th}}) \neq 0$; $\lambda_2 \neq 0 \Rightarrow (P_u - E_h - E_{ext}) = 0$; $\lambda_3 \neq 0 \Rightarrow (P_{min} - P_u) = 0$; $\lambda_4 \neq 0 \Rightarrow (P_t - P_{max}) = 0$, then the optimal values are

$$P_t^{(2)} = P_t^{(1)}, \;\; P_u^{(2)} = \max\left(P_u^{(1)}, P_{min}\right) \tag{5.66}$$

Lemma 3. If $\lambda_1 \neq 0 \Rightarrow (R_u - R_{\text{th}}) = 0$; $\lambda_2 \neq 0 \Rightarrow (P_u - E_h - E_{ext}) = 0$; $\lambda_3 = 0 \Rightarrow (P_{min} - P_u) \neq 0$; $\lambda_4 \neq 0 \Rightarrow (P_t - P_{max}) = 0$, then the optimal values are

$$P_t^{(3)} = P_t^{(1)}, \;\; P_u^{(3)} = \max\left(P_u^{(1)}, \frac{(2^{R_{th} - \log_2(1+\bar{\gamma})} - 1)N_o}{h_{rd}^2}\right) \tag{5.67}$$

Lemma 4. If $\lambda_1 \neq 0 \Rightarrow (R_u - R_{\text{th}}) = 0$; $\lambda_2 \neq 0 \Rightarrow (P_u - E_h - E_{ext}) = 0$;

Algorithm 5.3 Rate Maximization Algorithm

Input: Parameters $\varepsilon, a, b, \xi, N, R_{th}, E_{th}, P_{max}, P_{min}$
Output: Maximized rate $\mathcal{R}$
if $\gamma_d \leq \gamma_u$ **then**
  Compute $\mathcal{R}_1$ using (5.65)
  Compute $\mathcal{R}_2$ using (5.66)
  Compute $\mathcal{R}_3$ using (5.67)
  Compute $\mathcal{R}_4$ using (5.68)
  $\mathcal{R} \leftarrow \max(\mathcal{R}_1, \mathcal{R}_2, \mathcal{R}_3, \mathcal{R}_4)$
else
  Compute $\mathcal{R}_5$ using (5.69)
  Compute $\mathcal{R}_6$ using (5.70)
  Compute $\mathcal{R}_7$ using (5.71)
  $\mathcal{R} \leftarrow \max(\mathcal{R}_5, \mathcal{R}_6, \mathcal{R}_7)$
end if
return $\mathcal{R}$

$\lambda_3 \neq 0 \Rightarrow (P_{min} - P_u) = 0$; $\lambda_4 \neq 0 \Rightarrow (P_t - P_{max}) = 0$, then the optimal values are

$$P_t^{(4)} = P_t^{(1)}, \quad P_u^{(4)} = \max\left(P_u^{(3)}, P_{min}\right) \tag{5.68}$$

Similarly, for the MRC-based equivalent SNR, $\tilde{\gamma}_{mrc} = \gamma_u + \bar{\gamma}$, under the condition $\gamma_u \leq \gamma_d$, the KKT conditions are applied. Among the sixteen possible cases, the following three are identified as the optimal solutions outlined in Lemmas 5–7.

Lemma 5. If $\lambda_1 = 0 \Rightarrow (R_u - R_{\text{th}}) \neq 0$; $\lambda_2 \neq 0 \Rightarrow (P_u - E_h - E_{ext}) = 0$; $\lambda_3 \neq 0 \Rightarrow (P_{min} - P_u) = 0$; $\lambda_4 \neq 0 \Rightarrow (P_t - P_{max}) = 0$, then the optimal values are

$$P_t^{(1')} = P_t^{(1)}, \quad P_u^{(1')} = P_u^{(2)} \tag{5.69}$$

Lemma 6. If $\lambda_1 \neq 0 \Rightarrow (R_u - R_{\text{th}}) = 0$; $\lambda_2 \neq 0 \Rightarrow (P_u - E_h - E_{ext}) = 0$; $\lambda_3 \neq 0 \Rightarrow (P_{min} - P_u) = 0$; $\lambda_4 = 0 \Rightarrow (P_t - P_{max}) \neq 0$, then the optimal values are

$$P_t^{(2')} = \frac{\left(2^{R_{\text{th}} - \log_2(1+\bar{\gamma})} - 1\right) N_0}{h_{sr}^2}, \quad P_u^{(2')} = P_u^{(1')} \tag{5.70}$$

Lemma 7. If $\lambda_1 \neq 0 \Rightarrow (R_u - R_{\text{th}}) = 0$; $\lambda_2 \neq 0 \Rightarrow (P_u - E_h - E_{ext}) = 0$; $\lambda_3 \neq 0 \Rightarrow (P_{min} - P_u) = 0$; $\lambda_4 \neq 0 \Rightarrow (P_t - P_{max}) = 0$, then the optimal values are

$$P_t^{(3')} = P_t^{(1')}, \quad P_u^{(3')} = \max\left(P_u^{(2')}, \frac{\left(2^{R_{\text{th}} - \log_2(1+\bar{\gamma})} - 1\right) N_0}{h_{sr}^2}\right). \tag{5.71}$$

To summarize the solutions obtained via two cases, we introduce the Algorithm 5.3, aimed at maximizing the $(P5.1)$. The execution complexity of Algorithm 2 is $\mathcal{O}(N^2 + 1)$. The computational complexity of the proposed KKT-based algorithm has been explicitly analyzed and quantified, revealing that the optimization involves only a limited number of arithmetic operations and simple iterative updates that can be efficiently handled at a centralized controller. Consequently, the IoT devices incur only negligible computational overhead during online operation, respectively, making the proposed approach suitable for resource-constrained deployments.

While maximizing the data rate at D ensures an efficient information delivery, sustaining UAV operation is equally critical. Therefore, we now focus on optimizing the energy stored at the UAV to support prolonged and autonomous flight in energy-constrained environments.

5.5.2 Maximization of Stored Energy at UAV

In this subsection, our objective is to maximize the energy stored S_e at the UAV. The stored energy is obtained by

$$S_e = E_h + E_{ext} - E_u, \tag{5.72}$$

where E_{ext} represents the externally supplied energy and E_u is the output energy used by the UAV to forward information to D located at ground.[2] Equation (5.72) highlights the trade-off between communication performance and energy preservation at the UAV, since higher relay transmit power improves the achievable rate but reduces the stored energy. The motivation for this subsection stems from the fact that the stored energy at the UAV can be utilized for additional processing tasks, such as on-board processing, or to recharge its battery for future operations. Specifically, an optimization problem is formulated to maximize the stored energy while ensuring that the rate constraint is met, the power allocated to the UAV–D link is maintained, and the total transmit power at the S remains within the allowable limits. The corresponding optimization problem is mathematically represented as

$$\text{(P5.2)}: \max_{P_t,\, P_u} \quad S_e \tag{5.73}$$

$$\text{subject to:} \quad \text{(C1)} - \text{(C3)}. \tag{5.74}$$

Similar to (P5.1), Problem (P5.2) is non-convex since the variables in the objective function and constraints are interdependent, which makes it difficult to obtain a direct solution. To tackle the non-convexity of (P5.2) from joint optimization of P_u and P_t, we use an iterative approach, optimizing one parameter while fixing the other until convergence. The proposed Algorithm 5.4 has a computational complexity of $\mathcal{O}(s'(\mathcal{C}+\mathcal{D}))$, where s' is number of iterations, and $\mathcal{C}$ and $\mathcal{D}$ are number of computational time for Step 3 and Step 4, respectively.

We next discuss an alternative method to solve Problem (P5.2) to obtain a closed form solution by leveraging the KKT conditions [107]. The Lagrangian for (P5.2) is given by

[2]Here, the energy term E_u and power term P_u are used interchangeably, assuming a unit time duration.

Algorithm 5.4 AO Algorithm for Stored Energy

1: **Initialization:** Choose an initial feasible value for S_e and initialize iteration counter $n = 0$.
2: **repeat**
3: Solve (P5.2) to Optimize P_t with fixed P_u, obtaining P_t^*.
4: Obtain optimal P_u^* by solving (P5.2) using P_t^*.
5: Compute R_u using the updated P_t^* and P_u^*.
6: Store the result: $S_e(n)$.
7: Increment iteration counter: $n \leftarrow n + 1$.
8: **until** convergence: $S_e(n) \geq S_e(n-1)$

$$\mathcal{L}(P_t, P_u; \Psi) = k(P_t, P_u) - \mu_1 g(P_t, P_u) - \mu_2 h(P_t, P_u) - \mu_3 i(P_t, P_u) - \mu_4 j(P_t, P_u) \tag{5.75}$$

where $\Psi = (\mu_1, \mu_2, \mu_3, \mu_4)$ is the Lagrange multipliers, $k(P_t, P_u) = \frac{\varepsilon}{1-\Phi}\left(\frac{1}{1+exp(-aP_t h_{sr}^2+ab)} - \Phi\right) + E_{ext} - P_u$.

For an optimal value, $\nabla\mathcal{L}(P_t, P_u; \Psi) = 0$ must hold

$$\frac{\partial\mathcal{L}(P_t, P_u; \Psi)}{\partial P_t} \Rightarrow \mu_1 \frac{v_k^2}{\ln 2 \cdot N_0(1+\bar{\gamma})} - \mu_4 + (1+\mu_2)\frac{\varepsilon a h_{sr}^2 e^{(-aP_t z_k^2+ab)}}{(1-\phi)\left(1+e^{(-aP_t h_{sr}^2+ab)}\right)^2} = 0 \tag{5.76}$$

$$\frac{\partial\mathcal{L}(P_t, P_u; \Delta)}{\partial P_u} \Rightarrow -1 + \mu_1 \frac{h_{rd}^2}{\ln 2 \cdot N_0(1+\gamma_d)} - \mu_2 + \mu_3 = 0 \tag{5.77}$$

To satisfy the KKT conditions, the complementary slackness expressions are described as follows

$$\begin{aligned} &\mu_1 \cdot g(P_t, P_u) = 0; \quad \mu_2 \cdot h(P_t, P_u) = 0; \\ &\mu_3 \cdot i(P_t, P_u) = 0; \quad \mu_4 \cdot j(P_t, P_u) = 0. \end{aligned} \tag{5.78}$$

To satisfy the non-negativity conditions $\{P_t, P_u, \Delta\} \geq 0$, a comprehensive case anal-

Algorithm 5.5 Maximizing Stored Energy Algorithm

Input: Parameters $\varepsilon, a, b, \xi, N, R_{th}, E_{th}, P_{max}, P_{min}$
Output: Maximized value of stored energy at UAV $\mathcal{S}_e$
Compute $\mathcal{S}_{e1}$ using (5.79) and (5.80).
Compute $\mathcal{S}_{e2}$ using (5.81) and (5.82).
Compute $\mathcal{S}_{e2}$ using (5.83) and (5.84).
Compute $\mathcal{S}_{e4}$ using (5.85) and (5.86).
Compute $\mathcal{S}_{e5}$ using (5.87) and (5.88).
Compute $\mathcal{S}_{e6}$ using (5.89) and (5.90).
Optimal Value: $\mathcal{S}_e \leftarrow \max(\mathcal{S}_{e1}, \mathcal{S}_{e2}, \mathcal{S}_{e3}, \mathcal{S}_{e4}, \mathcal{S}_{e5}, \mathcal{S}_{e6})$
return $\mathcal{S}_e$

ysis of (5.75)–(5.78) is performed under the standard KKT procedures.

Among the sixteen possible cases, the six potential optimal solutions are outlined in Lemmas 8–13.

Lemma 8. If $\mu_1 = 0 \Rightarrow (R_u - R_{\text{th}}) \neq 0$; $\mu_2 = 0 \Rightarrow (P_u - E_h - E_{ext}) \neq 0$; $\mu_3 \neq 0 \Rightarrow (P_{min} - P_u) = 0$; $\mu_4 \neq 0 \Rightarrow (P_t - P_{max}) = 0$, then the optimal values are

$$P_t^{(5)} = P_{max}, \tag{5.79}$$

$$P_u^{(5)} = P_{min}. \tag{5.80}$$

Lemma 9. If $\mu_1 = 0 \Rightarrow (R_u - R_{\text{th}}) \neq 0$; $\mu_2 \neq 0 \Rightarrow (P_u - E_h - E_{ext}) = 0$; $\mu_3 \neq 0 \Rightarrow (P_{min} - P_u) = 0$; $\mu_4 \neq 0 \Rightarrow (P_t - P_{max}) = 0$, then the optimal values are

$$P_t^{(6)} = P_{max}, \tag{5.81}$$

$$P_u^{(6)} = \min\left(E_h + E_{ext}, P_{min}\right). \tag{5.82}$$

Lemma 10. If $\mu_1 \neq 0 \Rightarrow (R_u - R_{\text{th}}) = 0$; $\mu_2 = 0 \Rightarrow (P_u - E_h - E_{ext}) \neq 0$;

$\mu_3 = 0 \Rightarrow (P_{min} - P_u) \neq 0$; $\mu_4 \neq 0 \Rightarrow (P_t - P_{max}) = 0$, then the optimal values are

$$P_t^{(7)} = P_t^{(5)}, \tag{5.83}$$

$$P_u^{(7)} = \frac{(2^{R_{th} - \log_2(1+\hat{\gamma})} - 1) N_o}{h_{rd}^2}, \tag{5.84}$$

Lemma 11. If $\mu_1 \neq 0 \Rightarrow (R_u - R_{\text{th}}) = 0$; $\mu_2 = 0 \Rightarrow (P_u - E_h - E_{ext}) \neq 0$; $\mu_3 \neq 0 \Rightarrow (P_{min} - P_u) = 0$; $\mu_4 \neq 0 \Rightarrow (P_t - P_{max}) = 0$, then the optimal values are

$$P_t^{(8)} = P_t^{(5)}, \tag{5.85}$$

$$P_u^{(8)} = \min\left(P_u^{(7)}, P_{min}\right), \tag{5.86}$$

Lemma 12. If $\mu_1 \neq 0 \Rightarrow (R_u - R_{\text{th}}) = 0$; $\mu_2 \neq 0 \Rightarrow (P_u - E_h - E_{ext}) = 0$; $\mu_3 = 0 \Rightarrow (P_{min} - P_u) \neq 0$; $\mu_4 \neq 0 \Rightarrow (P_t - P_{max}) = 0$, then the optimal values are

$$P_t^{(9)} = P_t^{(5)}, \tag{5.87}$$

$$P_u^{(9)} = \min\left(P_u^{(7)}, E_h + E_{ext}\right), \tag{5.88}$$

Lemma 13. If $\mu_1 \neq 0 \Rightarrow (R_u - R_{\text{th}}) = 0$; $\mu_2 \neq 0 \Rightarrow (P_u - E_h - E_{ext}) = 0$; $\mu_3 \neq 0 \Rightarrow (P_{min} - P_u) = 0$; $\mu_4 \neq 0 \Rightarrow (P_t - P_{max}) = 0$, then the optimal values are

$$P_t^{(10)} = P_t^{(5)}, \tag{5.89}$$

Algorithm 5.6 Dinkelbach-Based EE Maximization Algorithm

1: Initialize feasible powers $P_t^{(0)}$, $P_u^{(0)}$, and set iteration index $k = 0$.
2: Compute initial $t^{(0)} = \dfrac{R_u(P_t^{(0)}, P_u^{(0)})}{\mathcal{P}_{\mathcal{T}}(P_t^{(0)}, P_u^{(0)})}$.
3: **repeat**
4: Solve the transformed problem: $(P_t^{(k+1)}, P_u^{(k+1)}) = \arg\max_{P_t, P_u \in \mathcal{F}} \Big(R_u(P_t, P_u) - t^{(k)} \mathcal{P}_{\mathcal{T}}(P_t, P_u) \Big)$
5: Update $t^{(k+1)} = \dfrac{R_u(P_t^{(k+1)}, P_u^{(k+1)})}{\mathcal{P}_{\mathcal{T}}(P_t^{(k+1)}, P_u^{(k+1)})}$, $\quad k \leftarrow k + 1$.
6: **until** $R_u(P_t^{(k)}, P_u^{(k)}) - t^{(k)} \mathcal{P}_{\mathcal{T}}(P_t^{(k)}, P_u^{(k)}) \leq \epsilon$
7: Return optimal (P_t^*, P_u^*) and t^*.

$$P_u^{(10)} = \min \left(P_u^{(9)}, P_{min} \right), \tag{5.90}$$

To summarize the solutions given in Lemmas 8–13, we introduce the following Algorithm, aimed at maximizing the $(P5.2)$. The execution complexity of Algorithm 5.5 is $\mathcal{O}(N^2 + 1)$.

5.5.3 Energy Efficiency Maximization

Another critical performance metric for assessing the feasibility and robustness of the UAV-RIS-assisted SWIPT system is the EE. In this subsection, we formulate and address an optimization problem aimed at maximizing the EE. By definition, the EE is expressed as the ratio of the achievable data rate to the total power consumed by the BS, RIS, and relay.

The achievable rate R_c is obtained from (5.55). The overall power consumption comprises the BS transmit power P_t, the dynamic circuit power of the RIS $\bar{P}_{RIS}$, the static circuit power of the RIS $\bar{\bar{P}}_{RIS}$, the relay's operational power P_u, the circuit power of BS $\tilde{P}_b$, and the circuit power of IoT device $\tilde{P}_i$. Hence, the total power expenditure is

written as

$$\mathcal{P}_{\mathcal{T}} = P_t + \bar{P}_{RIS} + \bar{\bar{P}}_{RIS} + P_u + \tilde{P}_b + \tilde{P}_i. \tag{5.91}$$

This model captures both transmission and hardware-related power consumption, ensuring that the EE metric reflects practical system energy costs.

Based on (5.91), the EE maximization problem is formulated as

$$\begin{aligned} \text{(P5.3)}: \max_{P_t,\, P_u} \quad & \frac{R_u(P_t, P_u)}{\mathcal{P}_{\mathcal{T}}} \\ \text{subject to: (C1)} - \text{(C4)}, \end{aligned} \tag{5.92}$$

where the constraints ensure feasible data rate, relay power, and BS transmit power allocations.

Since (P5.3) is a non-convex fractional program, conventional convex optimization techniques cannot be directly applied. To address this, we employ a fractional programming strategy, specifically the Dinkelbach-based method and Quadratic Transform (QT)-based method which has been widely adopted for EE optimization in wireless systems.

5.5.3.1 Dinkelbach Transformation

Problem (P5.3) belongs to the concave-convex fractional class and can be efficiently tackled using the DT. The main idea is to reformulate the fractional objective into a subtractive parametric form by introducing an auxiliary variable t. The equivalent problem can be expressed as [123]

$$f_d(t) = \max_{P_t,\, P_u \in \mathcal{F}} \Big(R_u(P_t, P_u) - t\, \mathcal{P}_{\mathcal{T}}(P_t, P_u) \Big), \tag{5.93}$$

Algorithm 5.7 Quadratic Transform-Based EE Maximization Algorithm

1: **Initialize:** $\{P_t, P_u\} \in \mathcal{F}$, iteration index $j = 2$, maximum iterations.
2: **repeat**
3: Update auxiliary variable $q = \frac{\sqrt{R_u(P_t,P_u)}}{\mathcal{P}_\mathcal{T}(P_t,P_u)}$.
4: **Inner AO Iterations:**
Solve (P5.4) with given $P_t^{(j)}$ to obtain $P_u^{(j+1)}$.
Solve (P5.4) with obtained $P_u^{(j+1)}$ to update $P_t^{(j+1)}$.
Evaluate $Q(P_t, P_u)^{(j+1)}$ using $P_u^{(j+1)}$ and $P_t^{(j+1)}$.
if $Q(P_t, P_u)^{(j+1)} \geq Q(P_t, P_u)^{(j)}$ and $j \leq M$
Set $P_t^{(j)} = P_t^{(j+1)}$, $j = j + 1$, repeat inner AO loop.
else
Stop inner AO loop.
end if
5: Obtain optimized $\{P_u^{(j-1)}, P_t^{(j-1)}\}$ for the current q.
6: **until** convergence of objective function
7: **Output:** Optimized $\{P_u^\star, P_t^\star, q^\star\}$.

where $\mathcal{F}$ denotes the feasible region defined by constraints (C1)-(C4). This transformation converts the fractional objective into a sequence of parametric convex problems, which are efficiently solved while preserving the optimality.

The optimal solution of (P5.3) is characterized by $\{P_t^*, P_u^*\}$, which corresponds to the auxiliary parameter

$$t^* = \frac{R_u(P_t^*, P_u^*)}{\mathcal{P}_\mathcal{T}(P_t^*, P_u^*)}. \tag{5.94}$$

At the convergence, the following condition holds

$$f_d(t^*) = \max_{P_t,\, P_u \in \mathcal{F}} \Big(R_u(P_t, P_u) - t^* \mathcal{P}_\mathcal{T}(P_t, P_u) \Big) \tag{5.95}$$

$$= R_u(P_t^*, P_u^*) - t^* \mathcal{P}_\mathcal{T}(P_t^*, P_u^*) = 0. \tag{5.96}$$

The Dinkelbach method iteratively updates t until this condition is satisfied. Owing to its super-linear convergence, the algorithm guarantees the globally optimal solution

of the original EE maximization Problem (P5.3). The step-by-step procedure of the adopted Dinkelbach-based algorithm is outlined in Algorithm 5.6. The execution complexity of Algorithm 5.6 is $\mathcal{O}(I_D I_1)$, where I_1 denotes the execution time of Step 4 and I_D represents the number of iterations required for Dinkelbach algorithm to converge.

5.5.3.2 Quadratic Transformation

The QT, inspired by the DT, introduces an auxiliary optimization variable into the fractional programming framework, while keeping the objective function unchanged [123]. Unlike DT, which achieves the optimum at t^*, QT provides a more interpretable solution by enhancing the objective function representation and directly yielding the optimal value. The reformulated Problem (P5.4), derived from (P5.3), incorporates an additional variable q, consistent with the principles of QT.

$$\begin{aligned} \text{(P5.4)}: \max_{P_t,\, P_u,\, q} \; & 2q\sqrt{R_u(P_t, P_u)} - q^2 \mathcal{P}_{\mathcal{T}}(P_t, P_u) = Q(P_t, P_u) \\ \text{subject to: (C1)} - \text{(C4)} \;\; & q \in \mathbb{R}, \end{aligned} \tag{5.97}$$

The auxiliary variable q decouples the fractional structure, allowing AO over q, P_t, and P_u for efficient convergence. The optimal solution is efficiently obtained using the Algorithm 5.7. The execution complexity of Algorithm 5.7 is $\mathcal{O}(I_Q I_2)$, where I_2 denotes the execution time of Step 4 and I_Q represents the number of iterations required for quadratic algorithm to converge.

5.6 Numerical Results and Discussions

This section discusses the performance evaluation of the integrated relay-RIS system through analytical derivations and simulation results. The performance is evaluated in terms of key metrics, including the OP, ASER, OC, and EC. Additionally, three optimization problems are addressed viz., maximizing the achievable rate at D, enhancing the energy stored at the UAV, and maximization of EE. The derived analytical expressions are validated through the Monte-Carlo simulation results, and comprehensive insights are provided into the effects of system parameters, such as the UAV altitude and the channel conditions, on the overall system performance. Unless stated otherwise, the simulation parameter values are provided in Table 5.1, and are taken from the previously published work [66]. We assume identical Nakagami-m channel parameters for both the S-to-UAV and UAV-to-D communication links in relay mode. For each RIS element, the parameters are considered to be equal, such that $m_{k,1} = m_{k,2} = m$ and $\Omega_{k,1} = \Omega_{k,2} = \Omega$, for simplicity, without any loss of generality.

In Figs. 5.2–5.9, the performance analysis of the integrated relay-RIS assisted UAV system is presented. The UAV altitude is fixed at $h = 100$ meters. The simulation results indicate that as the Nakagami-m fading parameter increases, the system's OP, ASER, OC, and EC improve, owing to the reduced severity of fading. Moreover, an increase in the UAV altitude leads to higher OP, ASER, and OC, while the EC decreases. This is attributed to the reduced probability of establishing an LoS link between the S and UAV, and between the UAV and D, as the altitude increases. The proposed integrated relay-RIS architecture is benchmarked against the conventional RIS-only and relay-only configurations. The results demonstrate that the proposed scheme performs superior than the existing systems. The integration of relay and RIS

Table 5.1: Simulation parameters values for proposed UAV system

Parameter	**Value**
Antenna gain A	10 dB
Coordinates of S (x_s, y_s, h_s)	(0,0,30) m
Coordinates of UAV (x_u, y_u, h_u)	(200,200,100) m
Coordinates of D (x_d, y_d)	(1000,1000) m
Threshold SNR γ_{th}	10 dB
Number of RIS elements N	4
Uplink constant k_u and k_d	-1.7
Downlink constant w_u and w_d	0.12
Maximum transmit power P_{max}	5 dBW
Input energy E_{ext}	50 μJ
Rate threshold R_{th}	1 bpcu
Circuit saturation point ϵ	4.4 dBm
Circuit parameters a	1500
Circuit parameters b	0.0022
Noise variance N_o	-120 dBW
Dynamic circuit power of RIS $\bar{P}_{RIS}$	-4.8 dBm
Static circuit power of RIS $\bar{\bar{P}}_{RIS}$	20 dBm
Circuit power of BS $\tilde{P}_b$	0 dBm
Circuit power of IoT device $\tilde{P}_i$	6.9 dBm

technologies significantly enhances the communication reliability and improves the OP, ASER, OC, and EC performance by dynamically adapting to varying channel conditions. Furthermore, the analytical expressions matches well with the Monte-Carlo simulation results, thereby validating the reliability of the theoretical analysis.

In particular, Fig. 5.2 presents the OP versus average SNR (dB) for various Nakagami-m fading parameters m and Ω. When transitioning from $m = 1$ to $m = 2$, an SNR gain of approximately 5 dB is observed corresponding to OP of 10^{-3} for both SC and MRC schemes. Additionally, among the considered schemes, MRC provides the most favorable performance, surpassing that of SC. This improvement is attributed to the optimal nature of MRC, which maximizes the output SNR by coherently combining signals from multiple branches. The proposed integrated relay-RIS system is compared with standalone RIS-only and relay-only configurations. To achieve an OP

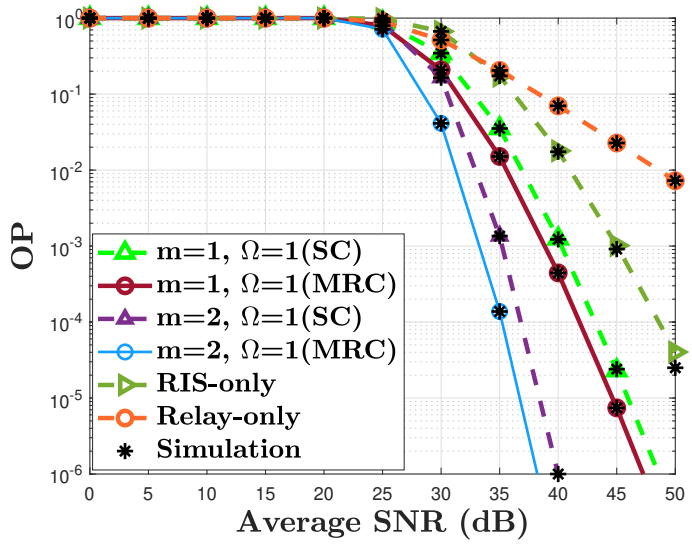

Fig. 5.2: OP versus average SNR (dB) for varying m and Ω values with $h = 100$ meters and comparison of integrated system with standalone systems.

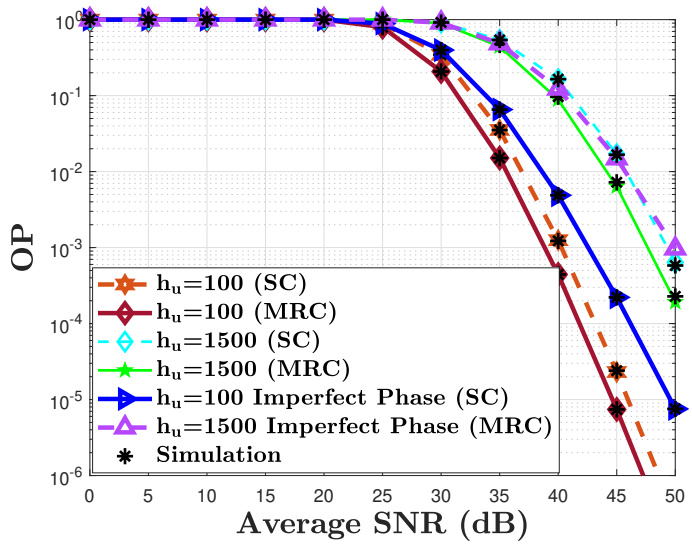

Fig. 5.3: OP versus average SNR (dB) for varying UAV altitude (meters) with $m = 1$ and $\Omega = 1$.

of 10^{-3}, the RIS-only and relay-only systems require approximately 5 dB and 13 dB higher SNR, respectively, than the integrated system under the SC scheme. These SNR gaps further increase to approximately 7 dB and 15 dB, respectively, for the MRC scheme. This performance gap arises because the integrated architecture simultaneously exploits the RIS-induced passive beamforming gain and relay-assisted

diversity gain, thereby strengthening both the uplink and downlink hops and reducing the probability that either hop becomes the performance bottleneck. In contrast, the RIS-only scheme lacks active relaying gain, while the relay-only scheme cannot benefit from the additional passive array gain, making the outage events more likely in the moderate-to-low SNR region where fading effects dominate. This performance gap highlights the efficacy of the proposed integrated approach in mitigating the limitations associated with individual RIS or relay deployments.

Fig. 5.3 presents the variation in OP with respect to the UAV altitude, assuming $m = 1$ and $\Omega = 1$. To maintain an OP of 10^{-2}, the system requires an additional 10 dB and 9 dB SNR at an altitude of $h = 1500$ meters compared to $h = 100$ meters, for SC and MRC schemes, respectively. Furthermore, the results obtained under the perfect phase adjustment for the SC and MRC schemes are compared with their counterparts under an imperfect phase adjustment. The plots clearly show that the phase imperfections lead to a performance degradation; however, we additionally obtain results that are more realistic and practically meaningful.

Fig. 5.4 depicts the ASER versus average SNR (dB) under various Nakagami-m fading conditions m and Ω. For $\Omega = 1$, transitioning from $m = 1$ to $m = 2$ results in a reduction of approximately 5 dB in the desired SNR to attain an ASER of 10^{-4} under the SC scheme. In comparison, the MRC scheme achieves better ASER performance than the SC scheme. Furthermore, the ASER performance of the proposed integrated relay-RIS system is compared with that of standalone RIS-only and relay-only schemes. The results indicate that, to attain an ASER of 10^{-2}, the RIS-only and relay-only configurations require approximately 4 dB and 7 dB higher SNR, respectively, than the integrated system under both SC and MRC schemes. This improvement is attributed to the simultaneous utilization of RIS-assisted passive beamforming

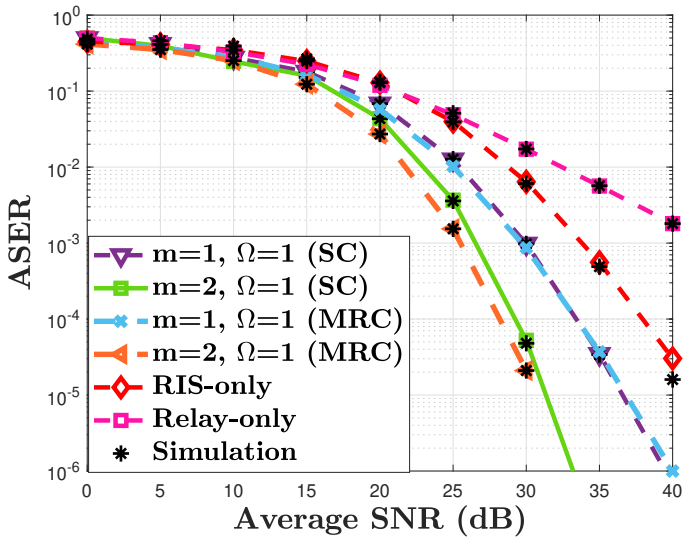

Fig. 5.4: ASER versus average SNR (dB) for varying m and Ω values with $h = 100$ meters and comparison of integrated system with standalone systems.

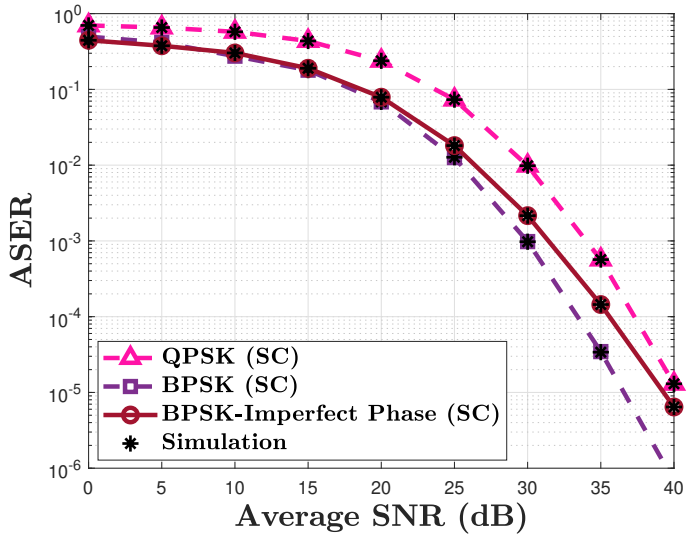

Fig. 5.5: ASER versus average SNR (dB) for various modulation schemes.

and relay-induced diversity gain, which together strengthen the received signal power and enhance link reliability. By contrast, RIS-only schemes do not provide active signal forwarding, whereas relay-only systems cannot leverage an additional array gain or the channel reconfiguration offered by the RIS, resulting in comparatively higher error rates. The performance advantage becomes more pronounced in the moderate

SNR regime, where fading effects are dominant and symbol error probability is highly sensitive to the link quality improvements, thereby demonstrating the effectiveness of the integrated approach in improving the error performance.

Fig. 5.5 illustrates a comparison between BPSK and QPSK modulation schemes. As expected, the system performance degrades with increasing the modulation order. To obtain an ASER of 10^{-2}, the QPSK scheme under the SC requires an additional 5 dB SNR compared to BPSK. The ASER analysis considering BPSK scheme under SC are compared with their counterparts under imperfect phase adjustment, and it is observed that the system performance degrades in the presence of phase errors.

Fig. 5.6 presents the EC versus average SNR (dB) for different Nakagami-m fading severity m and Ω. It is observed that increasing $m = 1$ to $m = 2$ results in an approximate SNR gain of 4 dB to achieve an EC of 3 bits/sec/Hz for both SC and MRC schemes. The MRC scheme consistently exhibits a superior capacity performance compared to the SC, primarily due to its ability to optimally combine the received signals across multiple branches, thereby maximizing the resultant SNR. A comparison of the EC performance between the integrated relay-RIS system and standalone configurations employing RIS-only or relay-only under a fixed SNR of 30 dB is presented. The standalone RIS-only and relay-only systems achieve approximately 1 bit/s/Hz and 2 bits/s/Hz EC, respectively. In contrast, the integrated system achieves significantly higher capacities, with the SC scheme reaching 4 bits/s/Hz and the MRC scheme attaining 5 bits/s/Hz. This improvement occurs because the integrated architecture simultaneously exploits the RIS-assisted passive beamforming gain and relay-assisted diversity gain, which jointly enhance the effective channel quality and reduce the impact of fading on both transmission hops. These results clearly demonstrate the efficacy of the proposed integrated relay-RIS architecture in enhancing the

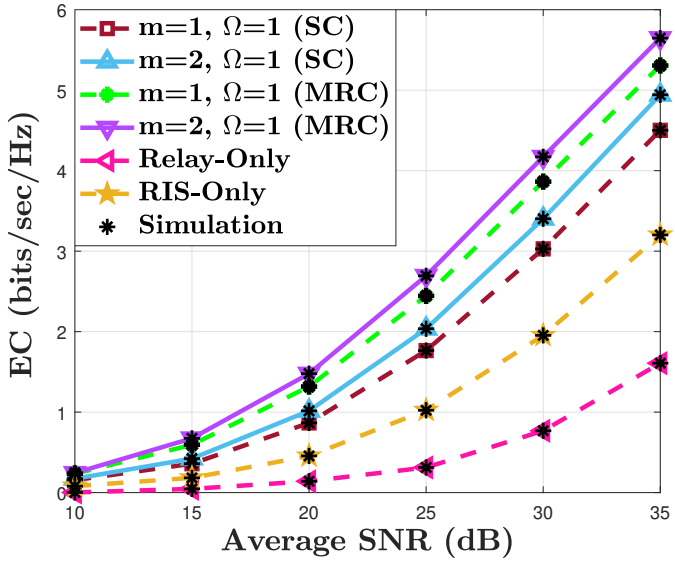

Fig. 5.6: EC versus average SNR (dB) for varying m and Ω values with $h = 100$ meters and comparison of integrated system with standalone systems.

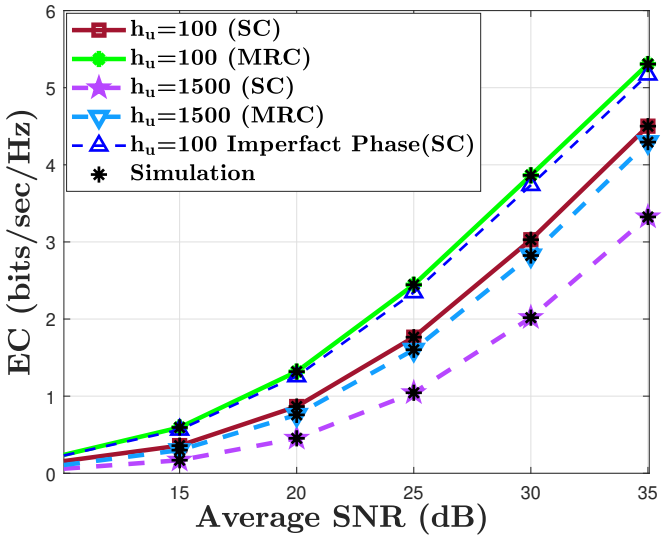

Fig. 5.7: EC versus average SNR (dB) for varying UAV altitude (meters) with $m = 1$ and $\Omega = 1$.

SE by leveraging the complementary advantages of both techniques to overcome the limitations inherent in standalone configurations.

Fig. 5.7 illustrates the impact of UAV altitude on EC, assuming $m = 1$ and $\Omega = 1$. As the altitude increases from $h = 100$ meters to $h = 1500$ meters, the system re-

quires an additional 8 dB and 9 dB of SNR to maintain an EC of 3 bits/sec/Hz for SC and MRC schemes, respectively. This degradation in EC with increasing altitude is attributed to the reduced probability of LoS links, which diminishes the overall channel quality. The EC analysis considering perfect phase in SC scheme is compared with the imperfect phase adjustment, and it is observed that the system performance degrades in the presence of phase errors. Fig. 5.8 illustrates the OC versus average SNR (dB) under various Nakagami-m fading conditions m and Ω. When transitioning from $m = 1$ to $m = 2$, an SNR gain of approximately 4 dB is necessary to attain an OC of 10^{-3} for both the SC and MRC schemes. The MRC scheme consistently outperforms SC due to its optimal signal combining capability, which maximizes the output SNR through coherent summation across multiple branches. The performance of the proposed integrated relay-RIS system is benchmarked against the standalone RIS-only and relay-only configurations. To achieve an OC of 10^{-1}, the RIS-only and relay-only systems require approximately 3 dB and 5 dB higher SNR, respectively, than the integrated system under the SC scheme. For the MRC scheme, these SNR gaps further widen to approximately 20 dB and 22 dB, respectively. This performance gain is achieved because the proposed architecture jointly harnesses the passive array gain provided by the RIS and the diversity benefits introduced by relay, thereby strengthening the overall channel conditions and mitigating fading effects across both the communication links. These results underscore the effectiveness of the proposed integrated architecture in addressing the limitations of individual RIS or relay-based systems.

Fig. 5.9 presents the variation in the OC with respect to UAV altitude, assuming $m = 1$ and $\Omega = 1$. To sustain an OC of 10^{-1}, the system necessitates an additional 7 dB and 9 dB of SNR at a UAV altitude of $h = 1500$ meters compared to $h = 100$ meters,

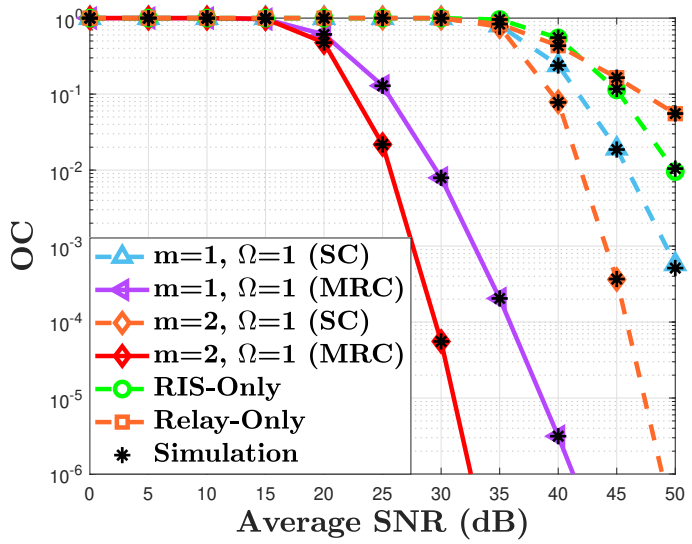

Fig. 5.8: OC versus average SNR (dB) for varying m and Ω values with $h = 100$ meters and comparison of integrated system with standalone systems.

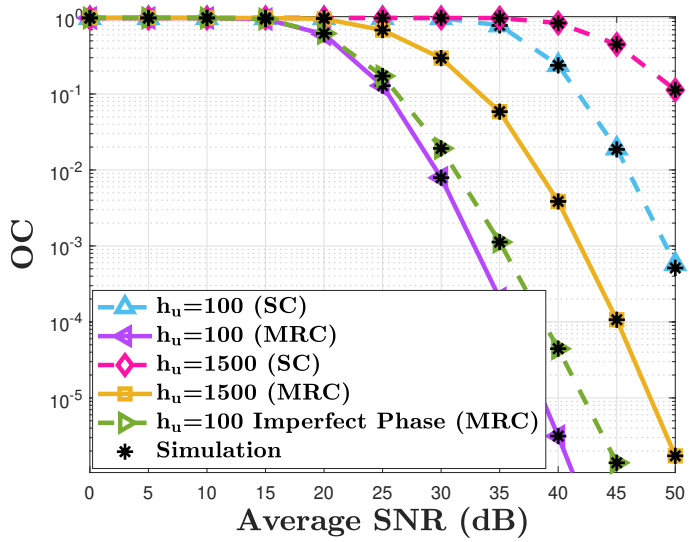

Fig. 5.9: OC versus average SNR (dB) for varying UAV altitude (meters) with $m = 1$ and $\Omega = 1$.

under the SC and MRC schemes, respectively. Similar to the EC analysis presented in Fig. 5.7, the OC performance with perfect phase alignment is compared to that with imperfect phase adjustment, and the analysis indicates that system performance degrades in the presence of phase errors, as observed for the EC.

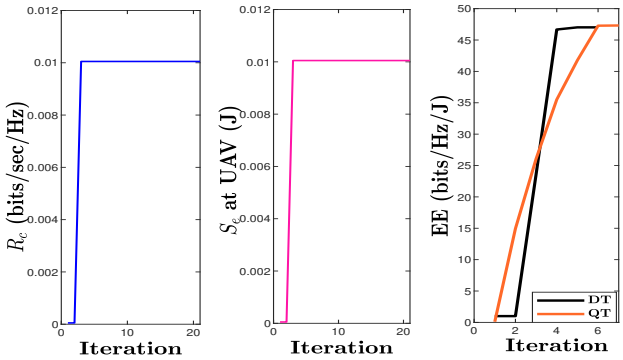

Fig. 5.10: Convergence plot of rate (Algorithm 1), stored energy (Algorithm 3), EE by DT (Algorithm 5), and EE by QT (Algorithm 6).

In Fig. 5.10, the convergence performance of the proposed algorithms is illustrated for different optimization objectives. Specifically, both the rate maximization (Algorithm 1) and stored energy maximization (Algorithm 3) exhibit convergence within three iterations, indicating rapid stabilization of their respective solutions. For EE maximization, the DT (Algorithm 5) converges in three iterations, while the QT (Algorithm 6) requires around six iterations to achieve stability. These results clearly demonstrate the computational advantage of DT over QT in terms of convergence speed. Moreover, the fast convergence of all algorithms within a limited number of iterations highlights the robustness and practical applicability of the proposed optimization framework in UAV–RIS-assisted IoT networks.

In Fig. 5.11, the achievable rate is depicted as a function of the transmit power under different Nakagami-m fading scenarios. As expected, the rate increases with appreciating transmit power. Moreover, a larger m value indicating less severe fading yields a noticeable improvement in the achievable rate. For instance, at a fixed transmit power of 3 dBW, increasing m provides approximately a 2% rate loss. Similarly, raising the UAV altitude from $h = 100$ m to $h = 1500$ m results in a rate reduction of about 4 bits/sec/Hz due to the deterioration in channel quality. The analytical results

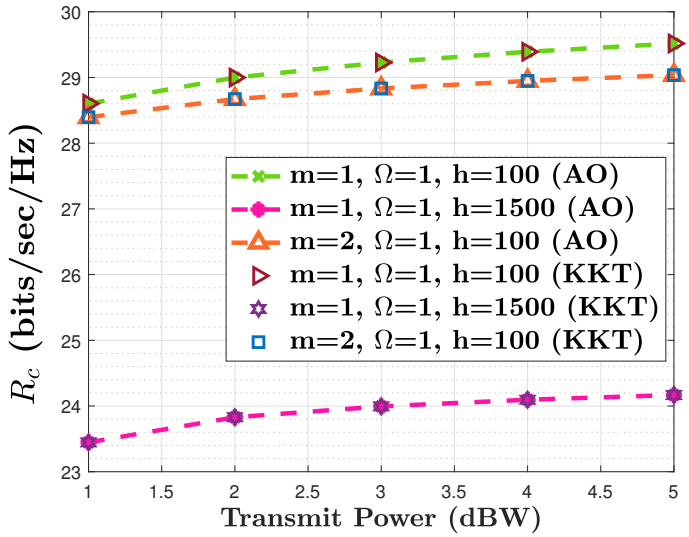

Fig. 5.11: R_c versus transmit power (dBW) for varying m, Ω, and h_u values.

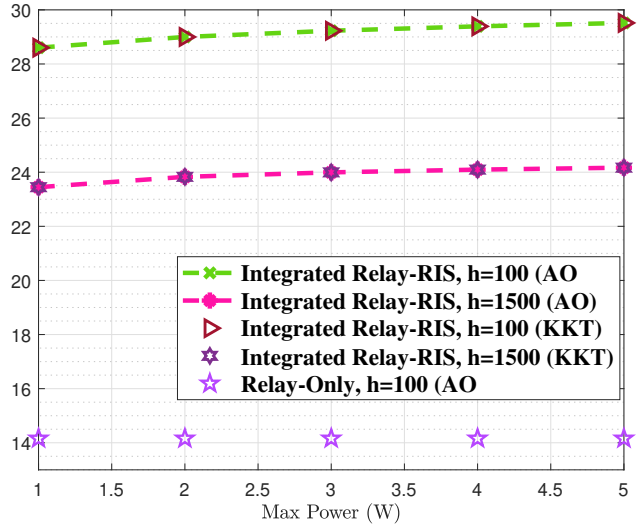

Fig. 5.12: R_c versus transmit power (dBW) comparison for integrated system with standalone systems.

obtained from the KKT-based optimization closely match the Monte-Carlo simulation outcomes, validating the accuracy and robustness of the proposed optimization framework.

Fig. 5.12 illustrates a comparison of the achievable rate at node D for the proposed integrated relay-RIS system and the standalone relay-only architecture at a

fixed transmit power of 3 dBW. The relay-only setup achieves an approximate rate of 14 bits/s/Hz, whereas the integrated design attains a significantly higher rate of 19 bits/s/Hz. This performance gain arises from the additional passive beamforming and channel shaping capabilities introduced by the RIS, which enhances the effective channel strength beyond the diversity benefits offered by relaying alone. Consequently, the integrated approach more effectively suppresses the fading and improves link reliability, thereby demonstrating its superiority in enhancing the SE and mitigating channel impairments.

Fig. 5.13 illustrates the variation in the maximized stored energy at the UAV as a function of transmit power for different values of fading parameter m and UAV altitude h_u. As m increases, the harvested and subsequently stored energy at the UAV also increases due to improved signal conditions. The integrated relay-RIS system further enhances the harvested energy by constructively combining the reflected and relayed signals. Nevertheless, raising the UAV altitude from $h = 100$ m to $h = 1500$ m leads to diminished energy storage capacity, primarily due to the deterioration of the channel conditions. The variation in the stored energy (S_e) with respect to the UAV altitude is relatively small. At a transmit power of 3 dBW, increasing the UAV altitude from 100 m to 1500 m results in only about a 4% reduction in the S_e. This limited percentage variation indicates that the effect of altitude-dependent RF energy attenuation on the total stored energy is minor under the considered system settings. The primary reason for this behavior is that the total stored energy at the UAV is dominated by the external onboard battery, while the energy harvested via SWIPT constitutes only a very small fraction of the overall energy budget. Consequently, although the harvested SWIPT energy itself is affected by increased propagation distance, its contribution is insufficient to noticeably alter the total stored energy. As

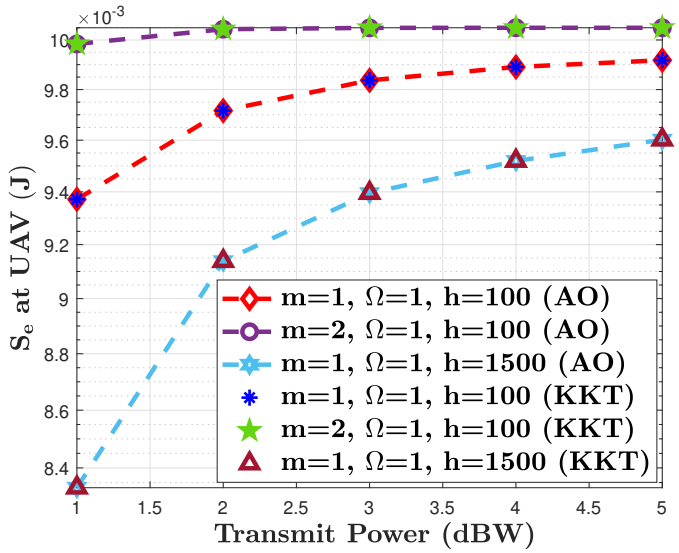

Fig. 5.13: S_e at UAV versus transmit power (dBW) for varying m, Ω, and h_u values.

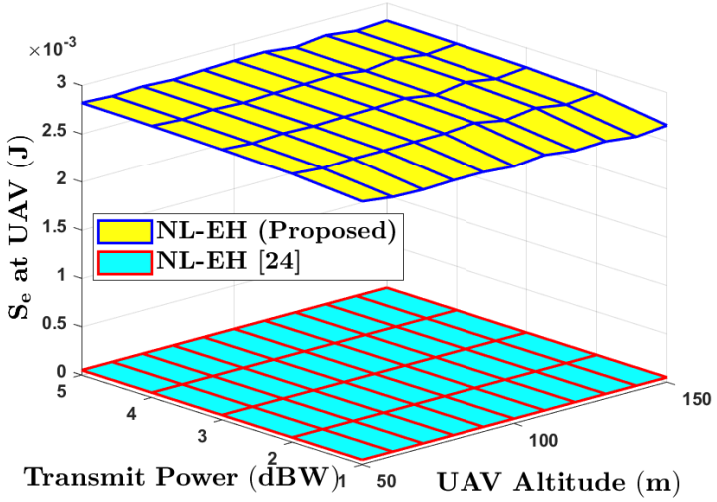

Fig. 5.14: S_e at UAV versus transmit power (dBW).

a result, altitude-induced variations in SWIPT energy translate into only marginal changes in S_e. Consistent with Fig. 5.11, the KKT-based analytical results closely match the simulations, validating the theoretical model.

In Fig. 5.14, the stored energy at the UAV is plotted as a function of transmit power and UAV altitude. The harvested energy at the UAV is typically on the order of mil-

lijoules $S_e \approx 10^{-3}$ J. As expected, the stored energy increases with growing transmit powers. Since, SWIPT-enabled EH is sensitive to the propagation conditions, its impact on the overall stored energy remains limited due to the dominance of the UAV's external power source. Furthermore, a comparison between the EH circuit parameters of the proposed system and those of existing configurations demonstrate that the selected parameters yields superior performance, illustrating how the hardware imperfections, including current leakage and circuit sensitivity limitations, contributes to the NL behavior.

Fig. 5.15 illustrates a comparative analysis of the EC and the stored energy in an integrated relay-RIS-assisted UAV communication system. Specifically, Fig. 5.15 depicts the EC as a function of average SNR and UAV altitude for different values of the number of RIS elements N. As anticipated, increasing N leads to improvement in EC. By increasing $N = 4$ to $N = 16$ the EC is increased by approximately 4 bits/sec/Hz. In-line with the earlier observations, an increase in the UAV altitude results in a decline in EC. However, to maintain a constant EC at higher altitudes, it is necessary to correspondingly increase the number of RIS elements.

In Fig. 5.16, the EE performance is illustrated as a function of the number of RIS elements N, while fixing the maximum transmit power at $P_{max} = 5$ dBW at altitude $h = 100$ m. The plots compare the outcomes of two optimization frameworks, namely DT and QT, against a benchmark case without RIS deployment. As the number of RIS elements increases, both DT and QT based solutions exhibit a consistent improvement the EE, highlighting the significant role of RIS in enhancing the system performance by providing additional passive beamforming gain. Furthermore, DT consistently outperforms the QT in terms of computational efficiency, making it a more practical choice for large-scale RIS-assisted networks. The gap between the RIS-enabled and

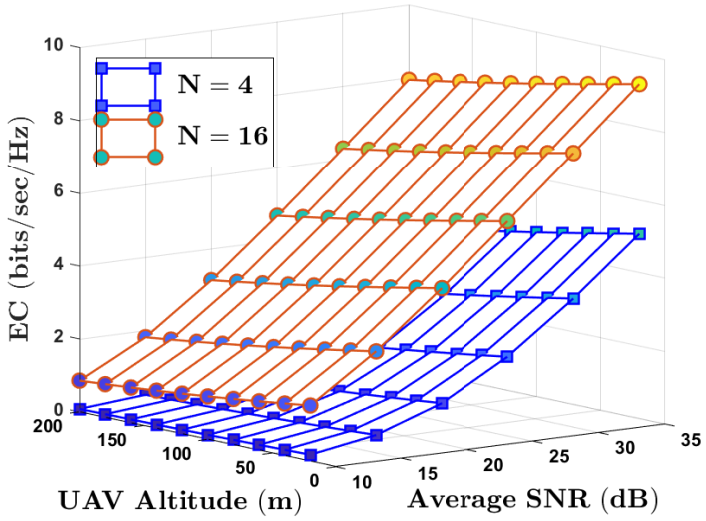

Fig. 5.15: EC versus average SNR (dB) for varying N values.

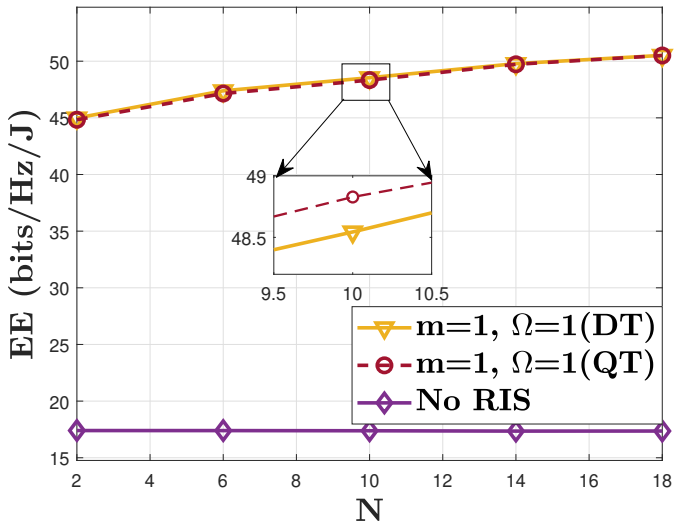

Fig. 5.16: EE versus varying N values.

no RIS scenarios further emphasizes the importance of RIS in achieving higher EE under constrained transmit power conditions.

5.7 Chapter Summary

This Chapter introduced an efficient integration of UAVs with relay and RIS technologies to improve the performance of UAV-enabled communication systems. The proposed system, operating in an integrated relay-RIS configuration and evaluated under SC and MRC schemes, demonstrates notable improvements in communication reliability and efficiency. Significant reductions in key performance metrics such as OP, ASER, and OC, along with enhancements in EC, have been achieved when compared to conventional RIS-only and relay-only UAV systems. These gains are primarily attributed to the system's ability to dynamically adapt to varying channel conditions, thereby optimizing the communication paths through real-time CSI. The adaptability and robustness of the proposed system are especially beneficial for critical applications that demand high reliability, such as autonomous vehicular communication and remote healthcare services. Furthermore, three optimization problems were formulated and solved to maximize the achievable rate, the stored energy at the UAV, and EE. The analytical formulations derived in this work have been thoroughly validated through Monte-Carlo simulations for performance evaluation. Additionally, the solutions obtained from the KKT conditions for the formulated optimization problems exhibit a strong agreement with the simulation results, thereby confirming the effectiveness and accuracy of the proposed analytical closed-form solutions. Since the RIS elements reflect the signals without active power consumption, they enhance the EE and supports long-duration UAV operations in the energy-constrained or remote environments.

Chapter 6

Full-duplex SWIPT-enabled Relay–RIS UAV Communication for Non-Terrestrial Networks

6.1 Introduction

Non-Terrestrial Networks (NTNs) are a key enabler of beyond-5G (B5G) and Sixth-Generation (6G) systems, providing ubiquitous connectivity and resilient communication in remote, rural, and disaster-affected areas where terrestrial infrastructure is limited [124]. To support the growing demands for high data rates and massive connectivity, technologies such as Uncrewed Aerial Vehicles (UAVs) and Reconfigurable Intelligent Surfaces (RISs) are being widely explored. UAVs offer flexible deployment and adaptive positioning as aerial Base-Station (BS) or relays, while RIS can intelligently reconfigure the wireless environment to enhance the signal strength, mitigate blockages, and improve Spectral Efficiency (SE) in challenging NTN scenarios [125]. However, practical deployment of the RIS-assisted UAV systems faces notable

challenges. Most existing works assume ideal continuous RIS phase shifts, which are unrealistic due to hardware and environmental constraints. Incorporating practical discrete phase shift is therefore essential for accurate performance evaluation. Moreover, integrating Full-Duplex (FD) relaying in UAV-assisted NTN enables simultaneous bidirectional transmission over a single frequency band, improving the SE [19].

Energy sustainability remains a critical concern, as the UAVs are inherently power-hungry due to propulsion, communication, and onboard processing. Simultaneous Wireless Information and Power Transfer (SWIPT) offers a promising solution by enabling the UAV relays to harvest energy from the ambient Radio-Frequency (RF) signals while maintaining a reliable data transmission [108]. The effectiveness of SWIPT depends on the adopted Energy Harvesting (EH) model. While the linear EH models are analytically convenient, practical harvesters exhibits Non-Linear (NL) characteristics due to circuit saturation and sensitivity threshold, necessitating a comparative analysis for realistic system design [106].

6.2 System and Channel Models

We consider an aerial FD-NTN communication system comprising a UAV-mounted RIS, as illustrated in Fig. 6.1. The RIS consists of N passive reflecting elements that assist the communication from the base station B_s to the ground Internet-of-Things (IoT) node G_d. The B_s is equipped with a single transmit antenna, while the ground user G_d employs a single receive antenna. The UAV carries an RIS and simultaneously operates as an independent FD Decode-and-Forward (DF) relay with dedicated transmit and receive antennas, respectively, enabling the concurrent reception from

B_s and transmission towards G_d over the same frequency band. Due to severe blockage and large path losses in the NTN environments, the direct $B_s - G_d$ link is assumed to be unavailable. The RIS passively reflects the incident signal towards G_d with negligible power consumption, thereby improving the coverage and link reliability. Concurrently, the FD relay at the UAV decodes the signal received from the B_s and forwards the regenerated signal to G_d. To ensure an interference-free reception, a Time-Division Multiplexing (TDM)-based orthogonal transmission protocol is adopted between the relay-assisted and RIS-assisted communication paths. This enables the destination G_d to individually evaluate the instantaneous Signal-to-Noise Ratio (SNR) of each received signal, after which Selection Combining (SC) is applied by choosing the branch corresponding to the largest instantaneous SNR. To enhance the energy sustainability, a SWIPT architecture is considered, where an energy receiver co-located with the relay harvests RF energy from the received signals. The harvested energy is stored in a rechargeable unit and later utilized to support relay forwarding operations and onboard processing at the UAV.

The UAV is capable of harvesting energy by employing SWIPT. For the linear EH model, the relay adopts the Power-Splitting (PS)-SWIPT protocol. Specifically, a fraction ρ of the received signal power is allocated to the EH, while the remaining portion $(1 - \rho)$ is utilized for Information Decoding (ID), where $\rho \in [0, 1]$ denotes the PS ratio. In contrast, to capture the practical circuit behavior and a more realistic RF-EH, a Non-Linear Energy Harvesting (NL-EH) model based on hybrid Power-Time Switching (PTS) architecture is also considered at the UAV. In this scheme, the UAV operates over three sequential phases to accomplish EH, ID, and data forwarding. During the EH phase, denoted by τ_e, the UAV employs a Time-Switching (TS) mechanism in which the received RF signal is exclusively used for EH. In the subse-

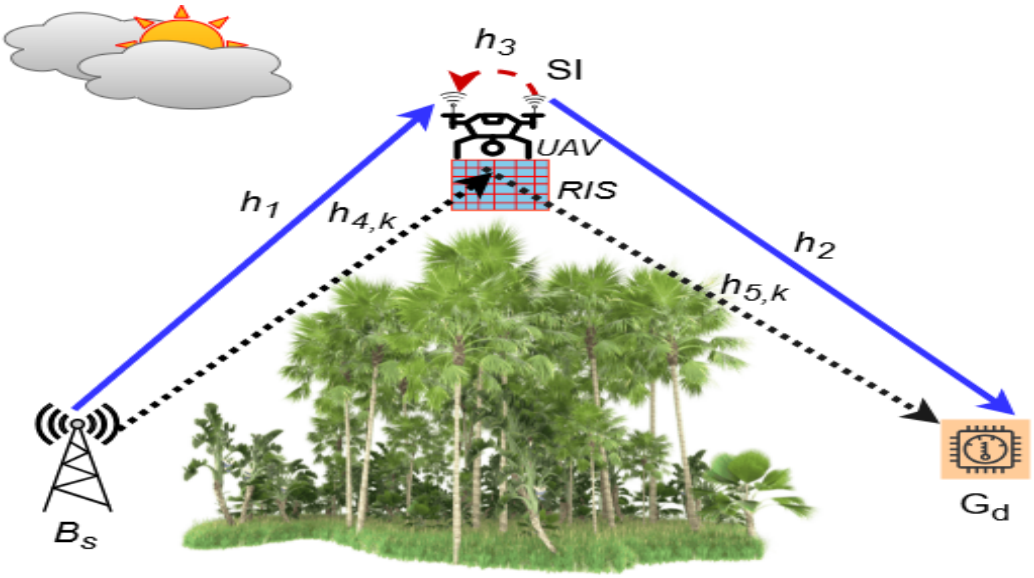

Fig. 6.1: RIS-UAV-assisted FD SWIPT NTN communication system.

quent phase τ_p, the UAV adopts the PS protocol with a PS factor $\eta \in [0, 1]$, such that a fraction η of received power is directed to EH, while the remaining portion $(1 - \eta)$ is used for ID. Finally, in the transmission phase τ_t, the UAV utilizes the harvested energy to forward the decoded information to G_d, as shown in Fig. 6.2.

The wireless channels between communicating nodes are modeled using the generalized $\alpha - \mu$ fading distribution, which effectively characterizes a wide range of propagation conditions. The channel gain is assumed to remain constant within a transmission block and to vary independently across different blocks. Accordingly, the channel coefficient between any pair of nodes is denoted by h_j, characterized by fading parameters α_j and μ_j, for $j \in \{1, 2, 3, (4, k), (5, k)\}$, corresponding to the respective communication as shown in Fig. 6.1.

The Probability Density Function (PDF) of the channel gain associated with the j-th transmission hop is modeled using the α–μ fading distribution [126], which is

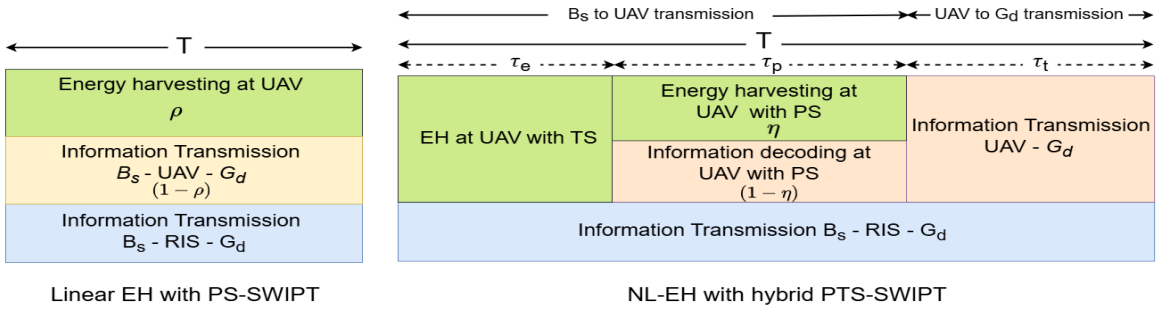

Fig. 6.2: SWIPT-enabled simultaneous EH and ID via Linear PS protocol and NL hybrid PTS protocol in T time slot.

expressed as

$$f_{h_j}(x) = \frac{\alpha_j \mu_j^{\mu_j} x^{\alpha_j \mu_j - 1}}{\hat{a}^{\alpha_j \mu_j} \Gamma(\mu_j)} \exp\left(-\mu_j \left(\frac{x}{\hat{a}}\right)^{\alpha_j}\right), \tag{6.1}$$

where $\hat{a}$ denotes the α_j-root mean value defined as $\hat{a} = \left(\mathbb{E}[h_j^{\alpha_j}]\right)^{1/\alpha_j}$. The parameter $\alpha_j > 0$ controls the fading non-linearity, while $\Gamma(\cdot)$ represents the Gamma function, $\Gamma(s) = \int_0^\infty t^{s-1} e^{-t} dt$ [120]. The parameter $\mu_j \geq \frac{1}{2}$ characterizes the clustering of multipath components and is related to the normalized variance of $h_j^{\alpha_j}$ as

$$\mu_j = \frac{\left(\mathbb{E}[h_j^{\alpha_j}]\right)^2}{\mathbb{E}[h_j^{2\alpha_j}] - \left(\mathbb{E}[h_j^{\alpha_j}]\right)^2}. \tag{6.2}$$

The α–μ distribution serves as a generalized fading model that encompasses several classical channel models as special cases. For example, Rayleigh fading is obtained when $\alpha = 2$ and $\mu = 1$, Weibull fading arises for $\mu = 1$ with variable α, and Nakagami-m fading corresponds to $\alpha = 2$ and $\mu = m$ [126]. Owing to this flexibility, the α–μ model is well suited for capturing small-scale fading effects in diverse environments.

In the Cartesian coordinate system, the positions of B_s and G_d are denoted by $\mathbf{p}_s = (x_s, y_s, 0)$ and $\mathbf{p}_d = (x_d, y_d, 0)$, respectively. The UAV operates at an adjustable altitude h, constrained within $h \in [h_{\min}, h_{\max}]$, where $h_{\min}$ and $h_{\max}$ define the per-

missible flight limits. Accordingly, the UAV's three-dimensional position is given by $\mathbf{p}_u = (x_u, y_u, h)$. For analytical convenience, the projections of these nodes onto the horizontal plane are expressed as $\mathbf{q}_s = (x_s, y_s)$, $\mathbf{q}_d = (x_d, y_d)$, and $\mathbf{q}_u = (x_u, y_u)$.

The wireless links between B_s and the UAV, as well as between the UAV and G_d, depends on the elevation angles and surrounding environmental conditions such as building density and height. The elevation angles (in radians) are defined as

$$\phi_u = \arctan\left(\frac{h}{\|\mathbf{q}_u - \mathbf{q}_s\|}\right), \ \phi_d = \arctan\left(\frac{h}{\|\mathbf{q}_u - \mathbf{q}_d\|}\right). \tag{6.3}$$

The probability of establishing an Line-of-Sight (LoS) link is modeled as a function of the elevation angle ϕ_i and is given by

$$p_L(\phi_i) = \big(1 + l_i \exp\big(-n_i(\phi_i - l_i)\big)\big)^{-1}, \quad i \in \{u, d\}, \tag{6.4}$$

where l_i and n_i are environment-dependent parameters obtained via Damped Least-Squares (DLS) fitting [116].

The path-loss exponent is influenced by the elevation angle and can be expressed as [116]

$$\sigma(\phi_i) = p_L(\phi_i) m_i + v_i, \tag{6.5}$$

where m_i and v_i are the empirical constants associated with the propagation environment for the respective links [117]. This elevation-dependent model captures the transition between LoS and Non-Line-of-Sight (NLoS) conditions, enabling a more accurate characterization of the UAV-assisted NTN channels.

6.2.1 UAV-assisted Relay transmission

In the proposed system model, G_d receives the message transmitted from B_s, where UAV employs the FD-DF based relaying technique and then forwards the message to G_d. Thus, the received signal at the UAV is composed of the signal emitted from B_s to UAV plus SI. This can be expressed as

$$y_u = \sqrt{d_u^{-\sigma(\phi_u)} P_s} h_1 x_s + \sqrt{P_r} h_3 x_r + w_u, \tag{6.6}$$

where x_s and x_r are the transmitted signal from source B_s and UAV, respectively, P_s and P_r are the transmission power of B_s and UAV, respectively, and d_u represents the distance between B_s and UAV, defined as $d_u = \sqrt{|\mathbf{q}_u - \mathbf{q}_s|^2 + h^2}$. The term $h_1 = |h_1|e^{j\theta_1}$ and $h_3 = |h_3|e^{j\theta_3}$ represents the complex fading channel coefficient between B_s to UAV and SI, respectively. The term w_u denotes the complex AWGN with zero-mean and variance N_0.

6.2.1.1 Linear Power Splitting-based EH

The energy harvested at the UAV can be expressed as [66]

$$\bar{E}_r = \zeta \rho T d_u^{-\sigma(\phi_u)} P_s |h_1|^2, \tag{6.7}$$

where $\zeta \in (0, 1]$ represents the energy conversion efficiency, accounting for the losses incurred by the EH, decoding, and signal processing circuitry, and T denotes the transmission time interval.

Consequently, the average transmit power of the UAV by linear EH is given by

$$\bar{P}_r = \frac{\bar{E}_r}{T} = \zeta \rho d_u^{-\sigma(\phi_u)} P_s |h_1|^2. \tag{6.8}$$

Additionally, the received signal at G_d from UAV is expressed as

$$\bar{y}_d = \sqrt{d_d^{-\sigma(\phi_d)} \bar{P}_r}\, h_2 \tilde{y}_u + w_d, \tag{6.9}$$

where $\tilde{y}_u$ is the decoded signal at the relay, d_d is the distance between the UAV and G_d, i.e., $d_d = \sqrt{|\mathbf{q}_u - \mathbf{q}_d|^2 + h^2}$, $h_2 = |h_2| e^{j\theta_2}$ represents the complex channel fading coefficient for UAV to G_d link, and w_d denotes complex AWGN with zero-mean and variance N_0. The instantaneous SINR at the B_s to UAV link is

$$\bar{\gamma}_u = \frac{(1-\rho) d_u^{-\sigma(\phi_u)} P_s |h_1|^2}{\bar{P}_r |h_3|^2 + N_0}. \tag{6.10}$$

Substituting (6.8) in (6.10) and considering $N_o << \bar{P}_r$, we get,

$$\bar{\gamma}_u = \frac{1-\rho}{\zeta \rho |h_3|^2}. \tag{6.11}$$

By using (6.1) and employing transformation of RVs technique, the PDF of $|\bar{h}_3|^2$ is written as

$$f_{|h_3|^2}(x) = \frac{\alpha_3 \mu_3^{\mu_3} x^{\frac{\alpha_3 \mu_3}{2} - 1}}{2 \Omega_3^{\alpha_3 \mu_3} \Gamma(\mu_3)} \exp\left(-\frac{\mu_3}{\Omega_3} x^{\frac{\alpha_3}{2}} \right), \tag{6.12}$$

where $\Omega_3 = a^{\alpha_3}$.

The Cumulative Distribution Functions (CDF) of $\bar{\gamma}_u$ can be easily obtained employing

$$F_{\bar{\gamma}_d}(r) = \frac{\lambda_1^{\frac{3\mu_1-\mu_2}{2}}\lambda_2^{\frac{3\mu_2-\mu_1}{2}}}{\Gamma(\mu_1)\Gamma(\mu_2)}\left(\frac{\zeta\rho(\beta_3 r+\beta_4)}{\beta_1-\beta_2\zeta\rho r}\right)^{\frac{\alpha_2(\mu_1+\mu_2)}{4}} G_{1,3}^{2,1}\left(\lambda_1\lambda_2\left(\frac{\zeta\rho(\beta_3 r+\beta_4)}{\beta_1-\beta_2\zeta\rho r}\right)^{\frac{\alpha_2}{2}}\middle| \begin{matrix}1-\frac{\mu_1+\mu_2}{2}\\ \frac{\mu_1-\mu_2}{2}, -\frac{\mu_1+\mu_2}{2}, \frac{\mu_2-\mu_1}{2}\end{matrix}\right) \tag{6.16}$$

transformation of RVs technique and is given by

$$F_{\bar{\gamma}_u}(\gamma) = \frac{\gamma\left(\mu_3, \frac{\mu_3\zeta\rho}{\Omega_3(1-\rho)}\gamma^{-\frac{\alpha_3}{2}}\right)}{\Gamma(\mu_3)}, \tag{6.13}$$

where $\gamma(s,x) = \int_0^x t^{s-1}\exp(-t)\,dt$ is the lower incomplete Gamma function.

The instantaneous SINR for UAV to G_d link is given by

$$\bar{\gamma}_d = \frac{d_d^{-\sigma(\phi_d)}\bar{P}_r|h_2|^2}{N_0} = \frac{\zeta\rho d_u^{-\sigma(\phi_u)}d_d^{-\sigma(\phi_d)}P_s|h_1|^2|h_2|^2}{N_0}. \tag{6.14}$$

Here, $|h_1|^2$ and $|h_2|^2$ follow the same distribution as given in (6.12), characterized by the fading parameters (α_1,μ_1) and (α_2,μ_2), respectively. Hence, the PDF of $Z=|h_1|^2|h_2|^2$, obtained using the transformation of Random Variables (RV) technique, is given by

$$f_Z(r) = C_z r^{\frac{\alpha_2(\mu_1+\mu_2)}{4}-1}K_{(\mu_1-\mu_2)}\left(2\sqrt{\lambda_1\lambda_2 r^{\frac{\alpha_2}{2}}}\right), \tag{6.15}$$

under the conditions $\alpha_1=\alpha_2$ and $\lambda_i = \frac{\mu_i}{\Omega_i}$. Here, $C_z = \frac{\alpha_2\lambda_1^{\mu_1}\lambda_2^{\mu_2}}{\Gamma(\mu_1)\Gamma(\mu_2)}$ and $K_n(\cdot)$ denotes the modified Bessel function of the second kind of order n.

Therefore, by employing [127, Eq. (03.04.26.0008.01)] and [128, Eq. (07.34.21.0003.01)], the CDF of $\bar{\gamma}_d$ is given by (6.16) at the top of next page.

The end-to-end instantaneous SINR $\hat{\gamma}_{_{Lin}}$ from B_s to G_d for linear EH-DF relaying is written as

$$\hat{\gamma}_{_{Lin}} = \min\{\bar{\gamma}_u, \bar{\gamma}_d\}. \tag{6.17}$$

6.2.1.2 Non-Linear Hybrid Power-Time Splitting-based EH

The UAV adopts a NL hybrid PTS-EH architecture. Traditional linear EH techniques lack practicality because the energy harvester does not perform EH when the input power is below a sensitivity threshold $P_{\min}$ and saturates when the input exceeds $P_{\max}$ [19]. To achieve efficient EH, we adopt a hybrid PTS-EH model [129]. In PTS-EH, the transmission phase T is divided into three intervals: τ_e, τ_p, and τ_t.

The average power of the harvested signal at the relay mounted on the UAV is given by

$$P_{tr} = d_u^{-\sigma(\phi_u)}|h_1|^2 P_s, \tag{6.18}$$

Thus, the harvested energy by the UAV in the first interval is estimated by

$$E_{\tau_e} = \tau_e T \zeta P_{tr}, \tag{6.19}$$

where ζ is the same as defined previously.

The harvested energy in the second interval the PS case is given by

$$E_{\tau_p} = \tau_p T \zeta \eta P_{tr}. \tag{6.20}$$

Thus, the total harvested energy at UAV with the hybrid PTS protocol is

$$\bar{\bar{E}}_r = E_{\tau_e} + E_{\tau_p} = \vartheta P_{tr}, \tag{6.21}$$

where $\vartheta = \tau_e T\zeta + \tau_p T\zeta\eta$. Finally, based on the harvested energy in the previous two intervals, UAV forwards the received signal to G_d. Therefore, $\bar{\bar{P}}r$ with NL-EH for UAV to G_d transmission can be expressed as

$$\bar{\bar{P}}_r = \begin{cases} 0, & P_{tr} < P_{\min}, \\ \delta P_{tr}, & P_{\min} \leq P_{tr} \leq P_{\max}, \\ \delta P_{\max}, & P_{tr} > P_{\max}, \end{cases} \tag{6.22}$$

where hybrid PTS factor is $\delta = \zeta(\frac{\tau_e+\tau_p\eta}{\tau_t})$. Based on the values of $\bar{\bar{P}}_r$ the SINR of $\bar{\bar{\gamma}}_u$ and $\bar{\bar{\gamma}}_d$ are respectively written as [19]

$$\bar{\bar{\gamma}}_u = \begin{cases} \dfrac{(1-\eta)P_{tr}}{\sigma_r^2}, & P_{tr} < P_{\min}, \\ \dfrac{(1-\eta)}{\delta|h_3|^2}, & P_{\min} \leq P_{tr} \leq P_{\max}, \\ \dfrac{(1-\eta)P_{tr}}{\delta P_{\max}|h_3|^2}, & P_{tr} > P_{\max}, \end{cases} \tag{6.23}$$

and

$$\bar{\bar{\gamma}}_d = \begin{cases} 0, & P_{tr} < P_{\min}, \\ \dfrac{\delta d_d^{-\sigma(\phi_d)}|h_2|^2 P_{tr}}{\sigma_d^2}, & P_{\min} \leq P_{tr} \leq P_{\max}, \\ \dfrac{\delta d_d^{-\sigma(\phi_d)}|h_2|^2 P_{\max}}{\sigma_d^2}, & P_{tr} > P_{\max}, \end{cases} \tag{6.24}$$

The channel power gain $|h_p|^2,\ \forall\ p \in (1,2,3)$, follow the same distribution as given

in (6.12), characterized by the fading parameters (α_p, μ_p). The CDF of $|h_p|^2$ is given by

$$F_{|h_p|^2}(r) = \frac{\gamma\left(\mu_p,\ \frac{\mu_p}{\Omega_p} r^{\frac{\alpha_p}{2}}\right)}{\Gamma(\mu_p)}. \tag{6.25}$$

The end-to-end instantaneous SINR for NL-EH is defined as

$$\hat{\gamma}_{_{NL}} = \min\left(\bar{\bar{\gamma}}_u,\ \bar{\bar{\gamma}}_d\right). \tag{6.26}$$

The CDF of $\hat{\gamma}_{_{NL}}$ is given by

$$\begin{aligned} F_{\hat{\gamma}_{_{NL}}}(\gamma) &= \Pr\left(\min(\bar{\bar{\gamma}}_u, \bar{\bar{\gamma}}_d) < \gamma\right) \\ &= 1 - \Pr\left(\bar{\bar{\gamma}}_u \geq \gamma \cap \bar{\bar{\gamma}}_d \geq \Upsilon_{\text{th}}\right) \\ &= 1 - \Pr\left((P_{tr} \geq P_{\min}) \cap (\bar{\bar{\gamma}}_u > \gamma) \cap (\bar{\bar{\gamma}}_d > \gamma)\right) \\ &= 1 - R_1 - R_2. \end{aligned} \tag{6.27}$$

The terms R_1 is defined as

$$\begin{aligned} R_1 &= \Pr(P_{\min} \leq P_{tr} \leq P_{\max} \ \cap\ \bar{\bar{\gamma}}_u > \gamma \ \cap\ \bar{\bar{\gamma}}_d > \gamma) \\ &= \begin{cases} 0, & |h_2|^2 < \dfrac{N}{M}, \\ \Pr(|h_3|^2 < K)\Pr\left(\dfrac{N}{|h_2|^2} < |h_1|^2 \leq M\right), & \dfrac{N}{M} < |h_2|^2 < \dfrac{N}{L}, \\ \Pr(|h_3|^2 < K)\Pr(L < |h_1|^2 \leq M), & |h_2|^2 > \dfrac{N}{L}, \end{cases} \end{aligned} \tag{6.28}$$

where the constants are defined as $K = \frac{1}{\delta\gamma}$, $L = \frac{P_{\min}}{P_s}$, $M = \frac{P_{\max}}{P_s}$, $N = \frac{\sigma_r^2\gamma}{\delta P_s}$, and $O = \frac{\sigma_r^2\gamma}{\delta P_{\max}}$.

$$R_1 = F_{|h_3|^2}(K)\Bigg[F_{|h_1|^2}(M)\Big(F_{|h_2|^2}\big(\tfrac{N}{L}\big) - F_{|h_2|^2}\big(\tfrac{N}{M}\big)\Big) - \frac{\frac{N}{L}+\frac{N}{M}}{2}\sum_{g=1}^{G}\frac{\pi}{G}\left(1-\phi_g^2\right) f_{|h_2|^2}(z_1)$$
$$F_{|h_1|^2}\Big(\tfrac{N}{z_1}\Big) + D_G\Bigg] + \Big(F_{|h_1|^2}(M) - F_{|h_1|^2}(L)\Big)\Big(1 - F_{|h_2|^2}\big(\tfrac{N}{L}\big)\Big), \tag{6.30}$$

$$R_2 = \Big(1-F_{|h_2|^2}(O)\Big)\Bigg[1-F_{|h_3|^2}(K)+K\sum_{c=1}^{C}\frac{\pi}{2C}\left(1-\phi_c^2\right) f_{|h_3|^2}(Kz_2)F_{|h_1|^2}(Mz_2) + D_C\Bigg]$$
$$+\Big(1-F_{|h_1|^2}(M)\Big)F_{|h_3|^2}(K). \tag{6.31}$$

Similarly, the term R_2 is defined as

$$\begin{aligned} R_2 &= \Pr(P_{tr} \geq P_{\max} \cap \bar{\bar{\gamma}}_u > \gamma \cap \bar{\bar{\gamma}}_d > \gamma) \\ &= \begin{cases} \Pr(|h_2|^2 > O)\Pr(|h_1|^2 > M), & |h_3|^2 < K, \\ \Pr(|h_2|^2 > O)\Pr\left(|h_1|^2 > \dfrac{M}{K|h_3|^2}\right), & |h_3|^2 > K. \end{cases} \end{aligned} \tag{6.29}$$

The final approximate closed-form expressions for R_1 and R_2 are given in (6.30) and (6.31), respectively, at the top of this page, with detailed derivations in Appendix C.1. Finally, substituting these into (6.27), the CDF of the end-to-end SINR is obtained.

6.2.2 UAV-assisted RIS transmission

In this mode, it is assumed that the relay remains inactive, while the RIS controller optimally adjusts the phase shift of each element. Specifically, the RIS maximizes signal power by optimizing the phase shifts of the incoming signals. The signal received at

G_d via N RIS elements is given by

$$y_i = \sum_{k=1}^{N} \sqrt{P_s d_u^{-\sigma(\phi_u)} d_d^{-\sigma(\phi_d)}} \bar{h}_{4,k} \Psi_k \bar{h}_{5,k} x + w_r. \tag{6.32}$$

The channels from the B_s to RIS and RIS to G_d can be assumed as $\bar{h}_{4,k} = |h_{4,k}| e^{j\varphi_{u,k}}$ and $\bar{h}_{5,k} = |h_{5,k}| e^{j\xi_{d,k}}$, respectively, with Ψ_k representing the PRC for the k-th element, and w_r denoting the AWGN with zero-mean and power spectral density N_0.

In practical RIS implementations, each reflecting element is typically equipped with a semiconductor component, designed with fixed geometric parameters, that modulates its impedance through a controllable bias voltage. This variation in impedance directly influences both the amplitude and phase response of the element [22]. The authors in [22] introduces a realistic hardware model capturing the behavior of the RIS PRC, highlighting how it varies with the phase shift and specific hardware configurations. Therefore, using [22, Eq. (2)], the PRC for the k-th element, denoted by Ψ_k, is mathematically expressed as

$$\Psi_k(\omega_k) = (1 - \Psi_{\min}) \left(\frac{\sin(\omega_k - \tau) + 1}{2} \right)^{\nu} + \Psi_{\min}, \tag{6.33}$$

where $\omega_k \in [-\pi, \pi)$ is the applied phase shift, $\tau \geq 0$ defines a phase offset related to the element's hardware characteristics, and $\nu \geq 0$ controls the sharpness of the PRC's transition curve. The parameter $\Psi_{\min}$ represents the minimum achievable amplitude and is itself a function of the phase shift. Notably, Ψ_k reaches lower values when ω_k is close to 0, and higher values near $\pm\pi$. From equation (6.33), it follows that if either $\Psi_{\min} = 1$ or $\nu = 0$, the PRC simplifies to $\Psi_k = 1$, indicating a case of ideal signal reflection, with no amplitude degradation. The instantaneous SNR at G_d via RIS is

written as

$$\check{\gamma} = \frac{P_s d_u^{-\sigma(\phi_u)} d_d^{-\sigma(\phi_d)}}{N_0} W, \tag{6.34}$$

where $W = \left(\sum_{k=1}^{N} |h_{4,k}|\Psi_k|h_{5,k}|\right)^2 = w^2$ is the square of the sum of non-negative independent RVs, whose PDF can be approximated by the Laguerre expansion [51]. Therefore, using [51, Eq. (5)], the PDF of W is respectively written as

$$f_W(x) = \frac{x^{a_k}}{(b_k)^{a_k+1}\Gamma(a_k+1)} \exp\left(-\frac{x}{b_k}\right), \tag{6.35}$$

where $\Gamma(\cdot)$ denotes the Gamma function, $a_k = \frac{\mu_W^2}{\sigma_W^2} - 1$, and $b_k = \frac{\sigma_W^2}{\mu_W}$. In addition, μ_W and σ_W^2 are the mean and variance of W, respectively. Firstly, the mean and variance of $w = \sum_{k=1}^{N} \Psi_k|h_{4,k}||h_{5,k}| = \sum_{k=1}^{N} \Psi_k l$ are respectively given by

$$\mathbb{E}[w] = N\mu_{\Psi_k}\mu_l, \tag{6.36}$$

$$\text{and } \mathrm{Var}[w] = N\left[\left((\sigma_{\Psi_k}^2 + \mu_{\Psi_k}^2)\mu_l^2\right) - (\mu_l.\mu_{\Psi_k})^2\right]. \tag{6.37}$$

Next, the mean (μ_{Ψ_k}) and variance ($\sigma_{\Psi_k}^2$) of Ψ_k are respectively given by

$$\mu_{\Psi_k} = \left(\frac{1-\Psi_{\min}}{\pi}\right) \mathrm{B}\left(\nu + \tfrac{1}{2}, \tfrac{1}{2}\right) + \Psi_{\min}, \tag{6.38}$$

$$\text{and } \sigma_{\Psi_k}^2 = \left[\pi \mathrm{B}\left(\tfrac{4\nu+1}{2}, \tfrac{1}{2}\right) - \mathrm{B}^2\left(\tfrac{2\nu+1}{2}, \tfrac{1}{2}\right)\right] \left(\frac{1-\Psi_{\min}}{\pi}\right)^2, \tag{6.39}$$

where $\mathrm{B}(\cdot,\cdot)$ denotes the Beta function.

Finally, the mean and variance of $W = w^2$ are respectively given by

$$\mu_W = (\mathbb{E}[w])^2 + \mathrm{Var}[w], \tag{6.40}$$

$$\text{and } \sigma_W^2 = 2\,\mathrm{Var}[w]\left(\mathrm{Var}[w] + 2\,\mathbb{E}[w]^2\right). \tag{6.41}$$

The CDF expression of $\check{\gamma}$ can be obtained from (6.35) as

$$F_{\check{\gamma}}(x) \approx \frac{\gamma\left(a_k+1, \frac{x}{b_k}\right)}{\Gamma(a_k+1)}. \tag{6.42}$$

6.2.3 UAV-assisted Relay-RIS Transmission

In the considered transmission scheme, both the relay transceiver and the RIS mounted on the UAV collaboratively forward the signal originating from the B_s. At the G_d, SC is performed based on the maximum of the instantaneous SNRs observed across the two transmission paths. Accordingly, the effective instantaneous SNR at the G_d can be written as

$$\tilde{\gamma}_{\max} = \max\left(\hat{\gamma}_t, \check{\gamma}\right), \tag{6.43}$$

where $\hat{\gamma}_t$=$\hat{\gamma}_{Lin}$ provides the SINR expression for linear EH-SWIPT relay and $\hat{\gamma}_t$=$\hat{\gamma}_{NL}$ gives the SINR expression for NL-EH SWIPT relay, with $\check{\gamma}$ represent the SNRs corresponding to the relay-assisted and RIS-assisted transmission paths, respectively.

The CDF of $\tilde{\gamma}_{\max}$ is given by

$$F_{\tilde{\gamma}_{\max}}(\gamma) = \Pr\left(\max\left(\hat{\gamma}_t, \check{\gamma}\right) < \gamma\right) = \Pr\left(\hat{\gamma}_t < \gamma,\ \check{\gamma} < \gamma\right), \tag{6.44}$$

where $\Pr(\cdot)$ denotes the probability operator.

By incorporating the expression of $\hat{\gamma}_{Lin}$ from (6.17), the CDF of $\tilde{\gamma}_{\max}$ can be reformulated as

$$\begin{aligned} F_{\tilde{\gamma}_{\max}}(\gamma) &= \Pr\left(\min\left\{\bar{\gamma}_u, \bar{\gamma}_d\right\} < \gamma,\ \check{\gamma} < \gamma\right) \\ &= \left[1 - \left(1 - F_{\bar{\gamma}_u}(\gamma)\right)\left(1 - F_{\bar{\gamma}_d}(\gamma)\right)\right] \cdot F_{\check{\gamma}}(\gamma), \end{aligned} \tag{6.45}$$

where $F_{\bar{\gamma}_u}(\gamma)$ and $F_{\bar{\gamma}_d}(\gamma)$ denote the CDFs of the instantaneous SINRs over the source-to-relay and relay-to-destination links, as defined in (6.13) and (6.16), respectively. Similarly, $F_{\check{\gamma}}(\gamma)$ represents the CDF of the instantaneous SNR corresponding to the RIS-assisted path, given in (6.42). Also, for $\hat{\gamma}_{_{NL}}$, the CDF of $\tilde{\gamma}_{\max}$ can be reformulated as

$$F_{\tilde{\gamma}_{\max}}(\gamma) = \Pr\left(\hat{\gamma}_{_{NL}} < \gamma,\, \check{\gamma} < \gamma\right) = F_{\hat{\gamma}_{_{NL}}}(\gamma) \cdot F_{\check{\gamma}}(\gamma). \tag{6.46}$$

6.3 Performance Analysis

In this section, the performance of the integrated relay-RIS transmission is assessed in terms of OP and EC.

6.3.1 Outage Probability

The integrated relay-RIS UAV-SWIPT system is considered to be in an outage state when the instantaneous SNR of the best available link falls below a predefined SNR threshold, denoted by γ_{th}. Accordingly, the OP of the system can be formulated as

$$\widehat{P} = \Pr\left(\tilde{\gamma}_{\max} < \gamma_{\text{th}}\right) = F_{\tilde{\gamma}_{\max}}(\gamma_{\text{th}}), \tag{6.47}$$

where $F_{\tilde{\gamma}_{\max}}(\cdot)$ denotes the CDF of the maximum instantaneous SNR, as derived in (6.45) and (6.46).

6.3.2 Ergodic Capacity

The EC of the integrated relay-RIS SWIPT system is expressed as

$$C = \frac{1}{\ln 2} \int_0^\infty \frac{1 - F_{\tilde{\gamma}_{max}}(\gamma)}{1+\gamma}\, d\gamma. \tag{6.48}$$

Since evaluating the closed-form expression of the integral in (6.48) is cumbersome, the generalized Gauss-Laguerre quadrature method is employed to approximate the EC as

$$C \approx \frac{1}{\ln 2} \sum_{j=1}^{n} W_j \cdot F_a(\Phi_j), \tag{6.49}$$

where W_j is the weight coefficient, Φ_j denotes the jth zero of the Laguerre polynomial, and $F_a(\Phi_j)$ is defined as

$$F_a(\Phi_j) = \frac{1 - F_{\tilde{\gamma}_{max}}(\Phi_j)}{(1+\Phi_j) \cdot \Phi_j^{-1/2} e^{-\Phi_j}}. \tag{6.50}$$

6.4 Optimization Problem Formulation

Herein, we maximize the SNR at G_d for optimizing the transmit power P_s , hybrid PTS factor (δ), and PRC. The optimization problem is defined as

$$\text{(P6.1)}: \underset{P_s,\delta,\{\Psi_k(\omega_k)\}_{k=1}^{N}}{\text{maximize}} \quad \Upsilon = \max\left(\gamma_d, \check{\gamma}\right), \tag{6.51}$$

$$\text{subject to :} \quad \text{(C1)}: \ \gamma_d \geq \gamma_{th}^{d}, \tag{6.52}$$

$$\text{(C2)}: \ \gamma_u \geq \gamma_{th}^{u}, \tag{6.53}$$

$$\text{(C3)}: \ \check{\gamma} \geq \gamma_{th}^{r}, \tag{6.54}$$

$$\text{(C4)}: \ \bar{\bar{P}}_r \geq P_{th}, P_{th} \neq 0 \tag{6.55}$$

$$\text{(C5)}: \ 1 < \delta \leq 2, \tag{6.56}$$

$$\text{(C6)}: \ 0 < P_s \leq P_T, \tag{6.57}$$

$$\text{(C7)}: \ 0<\Psi_k(\omega_k)\leq 1, \forall k \in \mathcal{N} \tag{6.58}$$

In the above-mentioned problem, assume that the hybrid PTS factor $\delta = 1 + \eta$. The constraints (C1)-(C3), makes sure that none of the links BS-UAV, UAV-G_d and BS-RIS-G_d, does not go into the outage. (C4) ensures that there is enough harvested power at UAV that it activates the UAV-G_d link to transmit signal. Combined (C1)-(C4), enables both relay and RIS link at G_d, where it selects the maximum SNR to have maximized gain, which becomes the problem of interest to be investigated in this Chapter. We know that PS factor in hybrid PTS case $\eta \in (0, 1]$, and keeping the assumptions intact, equates $\delta = 1 + \eta$, where $\delta \in (1, 2]$, as given in (C5). Constraint (C6), ensures transmit power is within the maximum allowed limit P_T. The PRC limit pertaining to RIS link is given by (C7), with implicit condition of $\omega_k \in [-\pi, \pi], \forall k$, with $\mathcal{N} = \{1, \ldots, N\}$ as the set of RIS elements. It also depends on the reflection

Algorithm 6.8 Total SNR maximization algorithm

Input: Channel parameters $(|h_1|^2, |h_2|^2, |h_3|^2, \bar{h}_{4,k}, \bar{h}_{5,k})$, SNR threshold γ_{th}^{u}, P_T, path losses $(d_u^{-\sigma(\phi_u)}, d_d^{-\sigma(\phi_d)})$, P_{min}, P_{max}.

Initialize: $A{=}d_u^{-\sigma(\phi_u)}|h_1|^2$, $B{=}\dfrac{\delta d_d^{-\sigma(\phi_d)}|h_2|^2}{\sigma_d^2}$, $P_s{=}P_T$,

If: $\left(\frac{P_{min}}{A} \leq P_s \leq \frac{P_{max}}{A}\right)$, **then** find δ_{lin} by (6.64), $\gamma_d = \beta_{lin} ABP_s$. Return P_s^* and $\delta^* \leftarrow \delta_{lin}$.

Else If: $(P_s > \frac{P_{max}}{A})$, **then** find δ_{sat} by (6.65) and $\gamma_d = \beta_{sat} BP_{max}$. Return P_s^* and $\delta^* \leftarrow \delta_{sat}$.

Solve: Find RIS link SNR $\check{\gamma}$ with $P_{s,RIS}$ (6.68), $\Psi_k^* \forall k$

Output: $\Upsilon = \max(\gamma_d, \check{\gamma}), P_s^*, \delta^*$

amplitude of RIS phase.

Since the multiple coupled optimization variables (transmit power, hybrid PTS factor and PRC) are engaged with optimizing function as well as constraints, the problem becomes non-convex programming and a direct solution is not possible [130]. Thus, we need to break down the problem into sub-problems and seek solution for the same. Subsequently, we develop an algorithm to solve the primal problem (P6.1). To begin with, we will keep P_s and δ fixed and optimize (P6.1) for PRC variable. This modifies the primal problem to selecting RIS link only, henceforth the constraints specific to relay link (C1), (C2), (C4)-(C6), do not participate in the corresponding Problem $(\text{P6.1})_\text{a}$. Thus, the objective considers maximization of $\check{\gamma}$ with respect to the (C3) and (C7) constraints, defined as follows

$$(\text{P6.1})_\text{a}: \underset{\{\Psi_k(\omega_k)\}_{k=1}^{N}}{\text{maximize}} \quad \Upsilon = \check{\gamma}, \tag{6.59}$$

$$\text{subject to :} \quad \text{(C3), (C7)} \tag{6.60}$$

The highest end-to-end SNR is obtained only when the channel phases are balanced

with the RIS elements phases. It is expressed as

$$\omega_k^* = -\angle(\bar{h}_{4,k} + \bar{h}_{5,k}) = -(\varphi_{u,k} + \xi_{d,k}). \tag{6.61}$$

Thus, optimized PRC $\Psi_k^*(\omega_k^*)$ is used for the remainder of the optimizing problem solution [131], [132].

Next, we take dual variables of P_s and δ to modify the problem and solve for the case when γ_d is selected. This changes the primal problem to following sub-problem

$$(\text{P6.1})_\text{b}\text{: } \underset{P_s,\delta}{\text{maximize}} \qquad \Upsilon = \gamma_d, \tag{6.62}$$

$$\text{subject to :} \qquad \text{(C1),(C2),(C4)-(C6).} \tag{6.63}$$

Constraints (C1), (C2) and (C4) belongs to the piece-wise linear function and their closed form solution is possible by dividing the regions of operation. The following closed form solutions are obtained as per their feasibilities.

Lemma 1: For the linear region,

$$P_{s,lin} = P_T,\ \delta_{lin} = \frac{2}{1 + \gamma_{th}^u |h_3|^2}. \tag{6.64}$$

For saturation region,

$$P_{s,sat}{=}P_T,\ \delta_{sat}{=}\frac{2d_u^{-\sigma(\phi_u)}|h_1|^2 P_{s,sat}}{d_u^{-\sigma(\phi_u)}|h_1|^2 P_{s,sat}{+}\gamma_{th}^u |h_3|^2 P_{max}}. \tag{6.65}$$

Proof. See Appendix C.2. ■

Now if instead of the relay, RIS link is active, then the primal problem (P6.1) has only a single constraint P_s with already optimized $\Psi_k^*(\omega_k^*)$ and δ will not be obtained, as it

vanishes from the objective and constraints as well. The modified problem is given as

$$(\text{P6.1})_{\text{c}}\text{: } \underset{P_s}{\text{maximize}} \quad \Upsilon = \check{\gamma}, \tag{6.66}$$

$$\text{subject to :} \quad \text{(C3), (C6).} \tag{6.67}$$

This is a single variable convex optimization problem and the closed-form solution is given as [132]

$$P_{s,RIS} = P_T. \tag{6.68}$$

Now, observing the solution obtained from various sub-solutions, the guaranteed optimized solution for the transmit power is

$$P_s^* = P_{s,lin} = P_{s,sat} = P_{r,RIS} = P_T. \tag{6.69}$$

This optimized value will now decide the region of operation and the optimized beta. To sum them up together, we propose the Algorithm 1. The optimized solution for P_s and δ for the relay link is closed and requires unity complexity. While for the RIS link, finding optimized PRC Ψ_k, the complexity majorly depends on the square of RIS elements as $\mathcal{O}(N^2)$. This makes total complexity for Algorithm 1 as $\mathcal{O}(1+N^2)$.

6.5 Numerical Results and Discussions

Herein, we present the numerical results for the FD integrated relay-RIS SWIPT system. The results are analyzed to understand the impact of various system parameters on performance metrics such as OP and EC. We validate the accuracy of the derived

Table 6.1: Simulation parameters values for proposed FD-UAV system

Parameter	**Value**
Coordinates of B_s (x_s, y_s)	(0,0) m
Coordinates of UAV (x_u, y_u)	(500,500) m
Coordinates of G_d (x_d, y_d)	(1000,1000) m
Number of RIS elements (N)	[2,4,8]
Uplink constant (m_u and m_d)	-1.7
Downlink constant (v_u and v_d)	0.12
Energy conversion efficiency (ζ)	0.6
PS factor (ρ and η)	0.5
Hybrid PTS factor (δ)	0.3
Minimum sensitive Power (P_{min})	0.9
Maximum sensitive Power (P_{max})	3
Phase shift $(\Psi_{\min})$	0.2
RIS hardware parameters (ν)	1.5
Number of Laguerre nodes (k)	20
GCQ accuracy–complexity factor (G)	60
Optimization thresholds $(\gamma_{th}^{u}=\gamma_{th}^{d}=\gamma_{th}^{r})$	5 dB
Maximum transmit power (P_T)	10 W

analytical expressions and provide insights into the influence of the channel parameters, number of RIS elements and the UAV height. Unless specified otherwise, the simulation parameters values, including the coordinates of B_s, UAV, and G_d, as well as the number of RIS elements, SNR threshold, uplink and downlink constants, energy conversion efficiency, and PS factor are provided in Table 6.1. All the parameter values used for simulations are taken from well-recognized works in the literature, specifically from [22] and [133]. We consider identical $\alpha - \mu$ channel parameters for both B_s-to-UAV and UAV-to-G_d links for relay mode and for each RIS element for simplicity without loss of generality.

In Fig. 6.3, the OP of the UAV-assisted relay transmission link is evaluated as a function of the energy conversion efficiency (ζ) for different transmit power levels. The SNR threshold is set to $\gamma_{\text{th}} = -10\,\text{dB}$. It is observed that as the ζ increases, the OP gradually decreases and eventually approaches a minimum value. This behavior

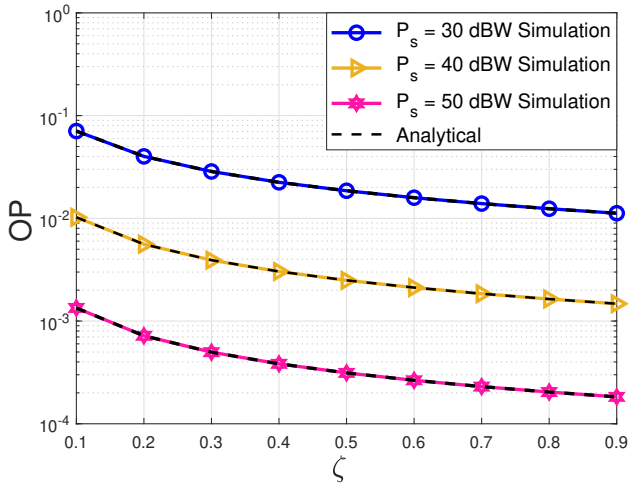

Fig. 6.3: OP versus ζ for varying transmit power (dBW) values.

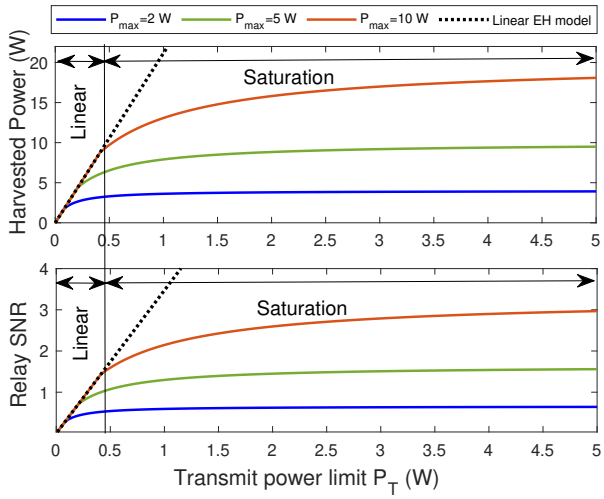

Fig. 6.4: Harvested power and relay SNR versus maximum allowed transmit power P_T under the hybrid PTS-EH model for different maximum harvested power levels $P_{\max}$. The linear and saturation regions are plotted for both metrics, along with the comparative linear EH model.

occurs because a higher value of ζ enables the relay to harvest more energy from the received signal, thereby improving the forwarding capability of the relay. Consequently, for all the considered transmit power levels, increasing ζ consistently leads to a reduction in the OP, highlighting its positive impact on improving the reliability of the communication link.

Fig. 6.4 illustrates the harvested power and the resulting relay SNR with respect to the transmit power P_T under the hybrid PTS-EH model for different saturation limits $P_{\max}$. For comparison, the conventional linear EH model is also included. We know that optimized $P_s^* = P_T$, which decides the region of operation as linear for range $\frac{P_{min}}{A} \leq P_s \leq \frac{P_{max}}{A}$ and harvested power $\bar{\bar{P}}_r \propto P_s$. While in saturation region : $P_s > \frac{P_{max}}{A}$, the harvested power no longer depends on P_s but on the P_{max} instead. Thus, we see the variation of plots only in saturation region. This behavior directly affects the relay performance, i.e., relay SNR γ_d initially increases with P_T in the linear region but eventually saturates once the harvested energy reaches the circuit limitation. Furthermore, larger values of $P_{\max}$ allows the system to harvest more energy before saturation occurs, thereby enabling higher relay SNR. In contrast, the linear EH model overestimates the harvested energy and relay SNR at high transmit power levels since it neglects the practical saturation effect.

Fig. 6.5 illustrates the OP performance of the proposed NTN system considering both linear EH and NL PTS-EH models. In Fig. 6.5, the OP is plotted as a function of the transmit power (dBW) for different values of the α–μ fading parameters under the linear EH model. The UAV altitude is fixed at $h = 100$ m. It is observed that improving the fading parameter from $\alpha = 1$ to $\alpha = 2$ results in a power gain of approximately 4 dBW to achieve an OP level of 10^{-3} for $N = 8$ RIS elements. Furthermore, increasing the number of RIS reflecting elements significantly enhances the system performance due to the additional passive beamforming gain provided by the RIS. Fig. 6.6 presents the OP performance for the NL PTS-EH model. Similar performance trends are observed; however, the required transmit power is higher due to the practical characteristics of NL-EH circuits. Specifically, when the fading parameter increases from $\alpha = 1$ to $\alpha = 2$, a power gain of approximately 9 dBW is

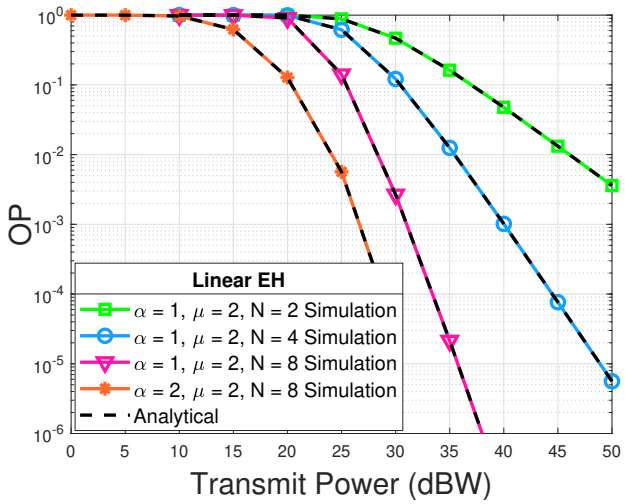

Fig. 6.5: OP versus transmit power (dBW) for varying N and α values for linear EH.

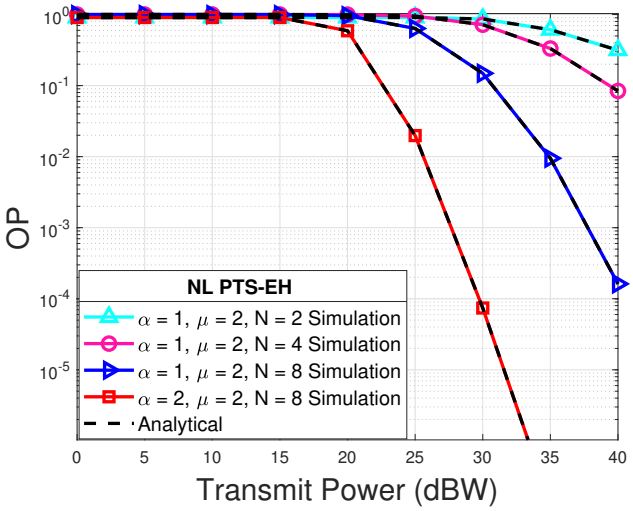

Fig. 6.6: OP versus transmit power (dBW) for varying N and α values for NL PTS-EH.

achieved to reach an OP of 10^{-2} for $N = 8$.

Fig. 6.7 compares the performance of the proposed integrated relay–RIS architecture with conventional standalone RIS-based systems. The results demonstrate that the integrated architecture consistently achieves superior OP performance. In addition, a comparison between the linear and NL-EH models shows that the NL-EH scheme exhibits slightly degraded performance, primarily due to its more realistic representation of practical RF EH circuits. For instance, to achieve an OP of 10^{-2}, the NL-EH

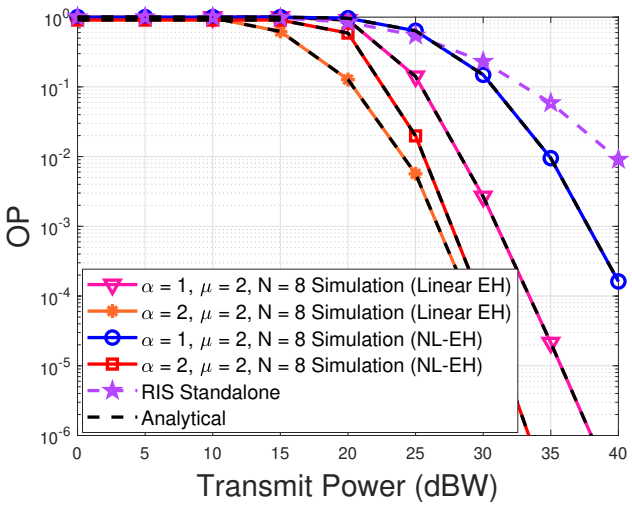

Fig. 6.7: OP versus transmit power (dBW) comparison for varying N and α values of linear EH and NL PTS-EH with standalone system.

model requires approximately 6 dBW higher transmit power compared to the linear EH model, which reduces to 2 dBW when the fading parameter changes from $\alpha = 1$ to $\alpha = 2$. Moreover, the joint utilization of relay transmission and RIS-assisted passive beamforming significantly improves the communication reliability by adapting to varying channel conditions. To achieve an OP of 10^{-2}, the standalone RIS-only configuration requires approximately 5 dBW higher transmit power than the integrated NL-EH relay–RIS SWIPT system, whereas the required power increases to 11 dBW for the linear EH case. These results highlight the effectiveness of the integrated architecture in overcoming the limitations of standalone RIS systems while also supporting the UAV energy sustainability through RF-EH.

Fig. 6.8 through to Fig. 6.10 shows the EC performance of the proposed integrated relay-RIS UAV-SWIPT system. The results indicate that the EC improves as the number of RIS reflecting elements N increases. This improvement arises from the enhanced passive beamforming gain, which effectively increases the number of signal components received at G_d. Moreover, an increase in the UAV altitude leads to higher

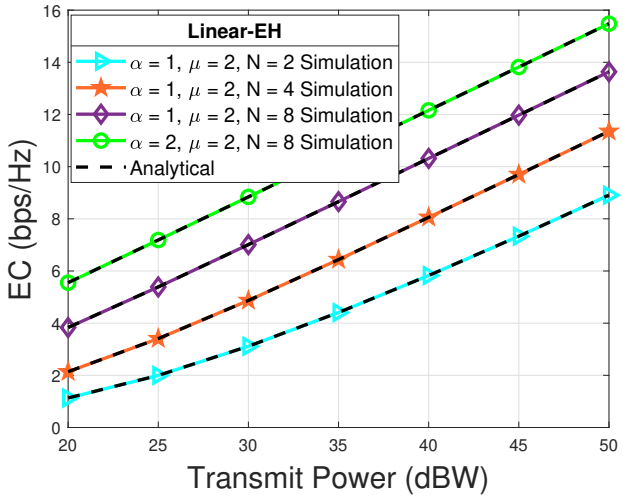

Fig. 6.8: EC versus transmit power (dBW) for varying N and α values for linear EH.

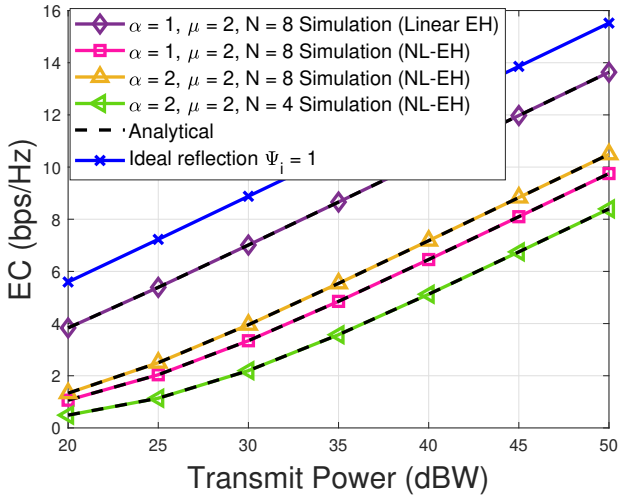

Fig. 6.9: EC versus transmit power (dBW) comparison for varying N and α values of linear EH and NL PTS-EH with standalone system.

EC. This is primarily due to the increased probability of establishing LoS communication links between B_s and the UAV, as well as between the UAV and G_d. Furthermore, the analytical results closely match the Monte-Carlo simulation results, confirming the accuracy of the derived expressions. The SNR threshold is set to $\gamma_{\text{th}} = -20\,\text{dB}$. Specifically, Fig. 6.8 presents the EC versus transmit power (dBW) for different values of N and α-μ fading severity parameters under the linear EH model. The UAV

altitude is fixed at $h = 100$ m. The results show that increasing the number of RIS elements from $N = 2$ to $N = 4$ provides an approximate power gain of 6 dBW in achieving an EC of 6 bps/Hz.

Fig. 6.9 presents the EC versus transmit power (dBW) for different values of N and α-μ fading parameters when the NL-EH model is considered. The UAV altitude remains $h = 100$ m. It is observed that increasing the number of RIS elements from $N = 4$ to $N = 8$ results in an approximate power gain of 4 dBW for achieving an EC of 6 bps/Hz. Additionally, when the fading parameter α increases from 1 to 2, a further power gain of approximately 2 dBW is achieved. A comparison between the linear EH and NL-EH shows that the linear model provides higher EC, whereas the NL-EH model offers a more accurate representation of practical EH circuits. Furthermore, a comparison between ideal RIS reflection (i.e., $\psi = 1$) and PRC (e.g., $\psi = 0.7$) for $N = 8$ is presented, demonstrating that PRC lead to some degradation in performance. Nevertheless, the proposed framework can be extended to larger RIS configurations to achieve higher beamforming gains, although this may introduce additional challenges such as increased channel estimation complexity, higher UAV payload requirements, and greater onboard power consumption.

Finally, Fig. 6.10 illustrates the variation of EC with respect to transmit power and the number of RIS elements N for different UAV altitudes. The results indicate that EC increases with higher transmit power and larger values of N. In addition, increasing the UAV altitude enlarges the slant distance between the UAV and the ground node. However, the corresponding increase in the elevation angle improves the probability of LoS communication, which reduces the elevation-dependent path-loss exponent $\sigma(\phi)$. As a result, the received SNR at G_d increases, thereby enhancing the overall system performance. This behavior highlights a tradeoff in which the gains from

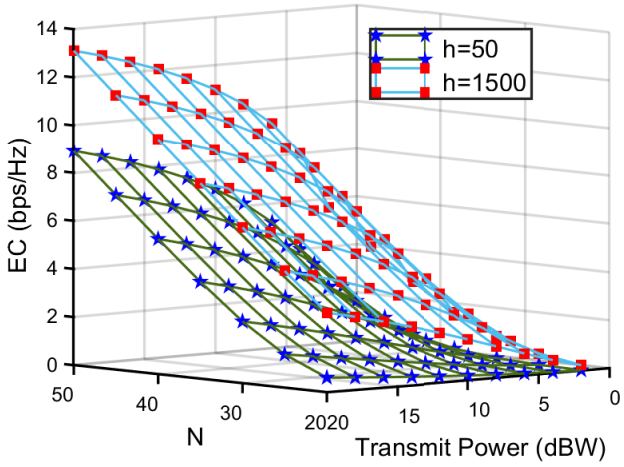

Fig. 6.10: EC versus transmit power (dBW) versus N for varying h (m) values.

improved LoS conditions dominate the free-space path loss within the considered high-altitude range.

In Fig. 6.11, the total SNR which takes maximum of RIS or relay SNR, is varied according to the RIS elements' numbers and the maximum allowed transmit power at BS. It is observed that for lower RIS elements ($N = 2,\ 6$), majorly relay selection happens leading to lesser dependency on N. While with higher $N = 62$, combined impact of P_T and N shoots up the SNR, as RIS link is selected for those cases.

Fig. 6.12 depicts the relay path SNR γ_d at G_d as a function of the desired SNR at UAV γ_u^{th} (BS-UAV link) for different transmit power levels P_T and UAV altitudes $h_{\max}$. It is seen that the relays' SNR decreases as γ_u^{th} increases. This behavior is due to the stricter communication requirement imposed on the user link, which limits the achievable relay path performance. Moreover, increasing the maximum allowed transmit power P_T improves the relay SNR. The impact of the UAV altitude from the adopted pathloss model, which implies stronger LoS for higher $h_{\max}$ is also evident from the results. When the UAV height increases from $h_{\max} = 100$ m to $h_{\max} = 500$

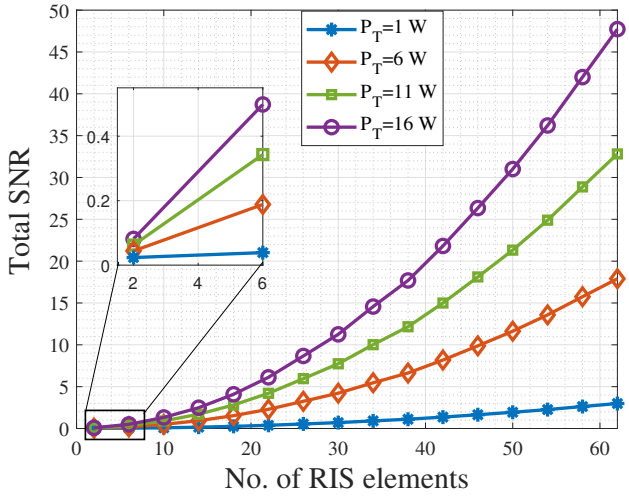

Fig. 6.11: Variation of total SNR with RIS element number and maximum allowed transmit power.

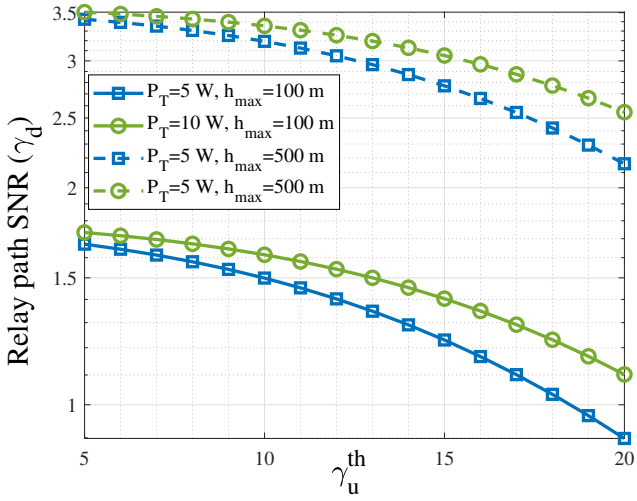

Fig. 6.12: γ_d versus γ_u^{th} for varying P_T and h_{max} values.

m, the relay SNR increases noticeably.

Fig. 6.13 illustrates the total SNR performance versus the transmit power under distinct RIS-PRC configuration schemes. As expected, the ideal PRC case with $\Psi_{min} = 1$, provides the upper performance bound, exhibiting a linear increase in SNR with P_T. The fixed reflection coefficient plot does not employ PRC rather used same reflection coefficient $\{\Psi_k\}_{k=1}^{N} = 0.5$, irrespective of the cascaded channel phases. It

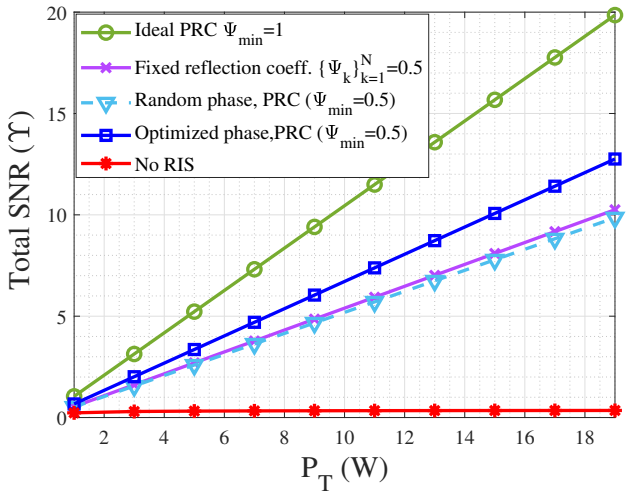

Fig. 6.13: Total SNR (Υ) versus transmit power P_T comparing RIS phase configuration strategies including PRC and baseline "No RIS".

is improved by the optimized phase shift and corresponding reflection coefficient with PRC of $\{\Psi_k\}_{k=1}^{N} = 0.5$. The optimized phase design significantly outperforms both the fixed reflection coefficient and random phase strategies across the entire transmit power range. Random phase shift selection and absence of RIS ('No RIS') serves a baseline comparison. This performance gain highlights the importance of phase optimization in compensating for practical reflection amplitude limitations of the RIS elements.

6.6 Chapter Summary

In this Chapter, the integration of UAV, relay, and RIS within an NTN framework is investigated to enhance UAV-based FD SWIPT communication. The proposed integrated relay–RIS architecture incorporates RIS-PRC with an SC scheme at the receiver to improve the communication reliability under the considered framework. Performance results show notable reductions in the OP in comparison to the stan-

dalone UAV–RIS systems, mainly due to cooperative relay–RIS operation and SC diversity gains. A comparison between the linear EH and NL-EH models indicates that although linear EH achieves a higher performance, the NL-EH provides a more practical representation of RF-EH circuits. The impact of RIS-PRC shows performance degradation compared to ideal reflections; however, the proposed system still outperforms the standalone schemes. Furthermore, the overall SNR is maximized through joint optimization of PRC, SWIPT-PS factor, and transmit power under the Quality-of-Service (QoS) constraints, supported by a well-structured optimization algorithm.

Chapter 7

Conclusion and Future Directions

7.1 Conclusion

This Thesis investigated the analysis and optimization of Simultaneous Wireless Information and Power Transfer (SWIPT)-enabled Reconfigurable Intelligent Surfaces (RISs)-assisted Uncrewed Aerial Vehicles (UAVs) and Vehicle-to-Everything (V2X) communication systems for future Sixth-Generation (6G) wireless networks. The primary objective of this work was to develop reliable, energy-efficient, and intelligent communication frameworks capable of supporting seamless connectivity in both urban vehicular environments and remote or disaster-prone scenarios. To achieve this objective, multiple system models incorporating RISs, SWIPT, UAVs, optimization techniques, and Deep Learning (DL) frameworks were comprehensively analyzed under realistic wireless propagation conditions.

First, a multi-RIS-assisted Vehicle-to-Vehicle (V2V) communication framework operating over the double generalized Gamma (dGG) fading channels was investigated. Two transmission schemes, namely Exhaustive RIS-aided Scheme (ERS) and Opportunistic RIS-aided Scheme (ORS), were proposed to improve communication relia-

bility and Spectral Efficiency (SE). Exact analytical expressions for Outage Probability (OP), Average Symbol Error Rate (ASER), and Ergodic Capacity (EC) were derived considering both perfect and imperfect Channel State Information (CSI). Furthermore, vehicle mobility effects were incorporated using the Random Waypoint (RWP) mobility model to realistically characterize dynamic vehicular environments. Optimization problems for rate maximization and power minimization were formulated and solved using the Karush-Kuhn-Tucker (KKT) conditions. In addition, a Deep Neural Network (DNN)-based framework was developed to reduce the computational complexity and enable an accurate low-latency prediction of the system performance. Numerical results demonstrated that the deployment of multiple RISs significantly improves the communication reliability and achievable performance under generalized fading environments.

Subsequently, a multi-RIS-assisted SWIPT-enabled V2V communication framework was investigated considering vehicular mobility and imperfect CSI. The proposed framework jointly optimized the harvested energy and achievable data rate under a Non-Linear Energy Harvesting (NL-EH) model using the Power-Splitting (PS)-based SWIPT architecture. A unified optimization framework employing an Alternating Optimization (AO) and the KKT-based closed-form solutions was developed respectively for an efficient resource allocation. Moreover, a DNN-assisted prediction model was proposed to reduce the optimization complexity and enable real-time intelligent vehicular communication. The obtained results demonstrated that multi-RIS-assisted SWIPT systems can effectively improve both communication reliability and EH efficiency in dynamic vehicular environments. Furthermore, the incorporation of DNN significantly reduced the computational time while maintaining a near-optimal system performance.

The Thesis further investigated an integrated relay-RIS-assisted UAV communication framework with SWIPT capability for remote connectivity and disaster-prone applications. The proposed system incorporated both Selection Combining (SC) and Maximal Ratio Combining (MRC) schemes to improve the communication reliability under Nakagami-m fading environments. Exact analytical expressions for the OP, ASER, Outage Capacity (OC), and EC were derived considering both Line-of-Sight (LoS) and Non-Line-of-Sight (NLoS) communication conditions. Optimization problems were formulated to maximize the achievable data rate, stored energy at the UAV, and overall Energy Efficiency (EE) under practical Quality-of-Service (QoS) constraints. The derived analytical results and optimization frameworks were validated through extensive Monte-Carlo simulations. The obtained results confirmed that the proposed integrated relay-RIS-assisted UAV communication framework significantly outperforms the conventional standalone relay and RIS-assisted systems in terms of communication reliability, SE, and energy sustainability.

Finally, a Full-Duplex (FD) SWIPT-enabled relay-RIS-assisted UAV communication framework for Non-Terrestrial Networks (NTNs) was investigated under realistic aerial propagation environments. The proposed framework incorporated practical RIS phase-response characteristics, residual Self-Interference (SI), and both linear and NL-SWIPT protocols for EH at the UAV relay. Exact analytical expressions for OP and EC were derived under generalized α–μ fading channels considering both LoS and NLoS propagation conditions. Furthermore, a joint optimization framework for RIS phase shifts, transmit power, and hybrid Power-Time Switching (PTS) factor was developed to maximize the received Signal-to-Noise Ratio (SNR) under QoS constraints. Numerical and simulation results demonstrated that the proposed FD relay-RIS-assisted UAV communication system achieves superior SE, communica-

tion reliability, and EH performance when compared with the conventional standalone architectures.

Overall, the contributions presented in this Thesis demonstrate the significant potential of RIS-assisted SWIPT-enabled UAV and vehicular communication systems for future intelligent wireless networks. The integration of RIS, SWIPT, UAV communication, optimization frameworks, and DL techniques offers an effective solution for addressing communication reliability, energy sustainability, and computational complexity challenges in future 6G wireless communication systems.

7.2 Future Directions

Although the proposed frameworks provide significant insights into the RIS-assisted SWIPT-enabled UAV and V2X communication systems, several promising research directions remain open for further investigation.

- Future work may extend the proposed multi-RIS-assisted vehicular communication framework to multi-user and dense vehicular communication scenarios involving multiple vehicles, interference management, and dynamic network topologies. Furthermore, the exact statistical characterization of the cascaded RIS channel gain, without relying on the CLT-based approximation, will be investigated to improve the accuracy of analytical performance results, particularly in the high-SNR region. Such investigations will provide more realistic evaluations for practical intelligent transportation systems.
- The incorporation of advanced vehicular mobility models such as Random Walk, Gauss–Markov, and Manhattan mobility models can further improve the realism

of the proposed V2V and V2I communication frameworks under temporally correlated vehicular movement.

- Future studies may investigate active RIS and hybrid active-passive RIS architectures to further improve communication coverage, EE, and reliability in highly obstructed urban environments.
- The integration of Deep Reinforcement Learning (DRL), federated learning, and distributed artificial intelligence techniques can enable real-time adaptive optimization for RIS configuration, power allocation, and SWIPT parameter optimization under highly dynamic wireless environments.
- Future work may consider practical hardware impairments such as phase noise, RIS element coupling, synchronization errors, and channel estimation overhead to further evaluate the performance of RIS-assisted communication systems under realistic implementation constraints.
- Future work may investigate the practical deployment of UAV-mounted RIS architectures by considering lightweight and flexible RIS designs, payload capacity, panel dimensions, aerodynamic drag, and UAV energy constraints. The joint optimization of RIS configuration and UAV trajectory under practical payload and flight-endurance limitations will also be explored.
- The proposed SWIPT-enabled UAV communication frameworks can be extended by incorporating UAV trajectory optimization and dynamic mobility control under time-varying wireless channels and energy constraints.
- Future research may investigate Integrated Sensing and Communication (ISAC)-enabled RIS-assisted UAV systems for simultaneously supporting wireless communication, localization, environmental sensing, and target detection function-

alities.

- The incorporation of Mobile Edge Computing (MEC), task offloading, and resource scheduling into RIS-assisted SWIPT-enabled UAV and vehicular communication systems are anticipated to provide efficient support for computationally intensive 6G applications.
- Future studies may investigate the performance of the proposed systems under the TeraHertz (THz) and the millimeter-wave (mm-Wave) communication bands for ultra-high-capacity 6G wireless networks.
- The integration of satellite communication, High-Altitude Platform Stations (HAPS), and UAV-assisted RIS systems within NTN architectures represents another promising research direction for achieving ubiquitous global connectivity.
- Future work may also explore secure communication frameworks incorporating physical layer security, blockchain-enabled authentication, and privacy-preserving machine learning for RIS-assisted UAV and vehicular communication systems.
- Experimental validation and hardware implementation of the proposed RIS-assisted SWIPT-enabled communication frameworks using SDR platforms, practical RIS prototypes, and DNN based approach can provide valuable insights into real-world deployment feasibility and implementation challenges.

In summary, RIS-assisted SWIPT-enabled UAV and V2X communication systems are expected to play a crucial role in enabling intelligent, sustainable, and resilient wireless communication infrastructures for beyond-5G (B5G) and 6G networks. The analytical frameworks, optimization techniques, and DL-based approaches presented

in this Thesis provide a strong foundation for future research and practical implementation of next-generation intelligent wireless communication systems.

Appendices

Appendix A

Cases of KKT Conditions

A.1 Evaluation of Various Cases From KKT Conditions for Rate Maximization Problem

To achieve a feasible solution, we analyze all possible cases for (5.75)-(5.78), defined as per standard KKT procedures.

Case I: $\nu_1 = 0 \Rightarrow g(P_t) \neq 0; \nu_2 = 0 \Rightarrow h(P_t) \neq 0$, no constraints are active and $\log_2(1+\gamma) = 0$. Hence, this case is not possible as $\log_2(1+\gamma) \neq 0$.

Case II: $\nu_1 = 0 \Rightarrow g(P_t) \neq 0; \nu_2 \neq 0 \Rightarrow h(P_t) = 0$ From (5.75), we find that $\nu_2 < 0$, which is contrary. Therefore, this case is not feasible.

Case III: $\nu_1 \neq 0 \Rightarrow g(P_t) = 0; \nu_2 = 0 \Rightarrow h(P_t) \neq 0$ then, we obtain: $-\nu_1(P_t - P_{max}) = 0 \Rightarrow P_{t,1} = P_{max}$.

Case IV: $\nu_1 \neq 0 \Rightarrow g(P_t) = 0; \nu_2 \neq 0 \Rightarrow h(P_t) = 0$, then from $g(P_t) = 0$, we have: $-\nu_1(P_t - P_{max}) = 0 \Rightarrow P_{t,1}$. Additionally, from $h(P_t) = 0$, we get: $-\nu_2(R_{th} - \log_2(1+\gamma)) = 0 \Rightarrow P_{t,2} = \frac{(2^{R_{th}}-1)N_o}{(p_l \tilde{\tilde{t}}_l)^2}$.

Based on the above-mentioned findings, the optimal value of the transmit power is

given by

$$P^{\circ} = \max(P_{t,1}, P_{t,2}). \tag{A.1}$$

A.2 Evaluation of Various Cases From KKT Conditions for Power Minimization Problem

To secure a feasible solution, an analysis of all potential cases is conducted for (3.54)-(3.57).

Case I: $\mu_1 = 0 \Rightarrow g(P_t) \neq 0; \mu_2 = 0 \Rightarrow h(P_t) \neq 0$, no constraints are active and $P_t = 0$. Hence, this case is not feasible as $P_t \neq 0$.

Case II: $\mu_1 = 0 \Rightarrow g(P_t) \neq 0; \mu_2 \neq 0 \Rightarrow h(P_t) = 0$, then from: $h(P_t) = 0$, we get: $P_{t,2}$.

Case III: $\mu_1 \neq 0 \Rightarrow g(P_t) = 0; \mu_2 = 0 \Rightarrow h(P) \neq 0$ From (3.54), we get $\mu_1 < 0$, which is contrary. Thus, this case is not tractable.

Case IV: $\mu_1 \neq 0 \Rightarrow g(P_t) = 0; \mu_2 \neq 0 \Rightarrow h(P_t) = 0$, then from: $g(P_t) = 0$, we obtain: $-\mu_1(P_t - P_{max}) = 0 \Rightarrow P_{t,1}$; and from: $h(P_t) = 0$, we get: $-\mu_2(R_{th} - \log_2(1+\gamma)) = 0 \Rightarrow P_{t,2}$.

Drawing from the mentioned observations, the optimal value of the transmit power is given by

$$P^{\bullet} = \min(P_{t,1}, P_{t,2}). \tag{A.2}$$

Appendix B

Solution for Various Cases From KKT Conditions

B.1 Evaluation of Various Cases From KKT Conditions for Unified Problem

Analyzing (5.75)-(5.78) using standard KKT procedures gives below feasible solutions.

Case I: $\mu_1, \mu_2, \mu_3 = 0$, this case is not possible as $\log_2(1+\gamma) \neq 0$ for both $\tilde{O}_w(P_t, \rho)$ and $\tilde{O}_z(P_t, \rho)$.

Case II: $\mu_1, \mu_3 = 0, \mu_2 \neq 0$, from (5.76) $\Rightarrow \mu_2 < 0$, which is contradictory for both $\tilde{O}_w(P_t, \rho)$ and $\tilde{O}_z(P_t, \rho)$.

Case III: $\mu_2, \mu_3 = 0, \mu_1 \neq 0$, from (5.76) $\Rightarrow \mu_1 < 0$, which is contradictory for both $\tilde{O}_w(P_t, \rho)$ and $\tilde{O}_z(P_t, \rho)$.

Case IV: $\mu_3 = 0, \mu_1, \mu_2 \neq 0$, from (5.76) and (5.77)$\Rightarrow \mu_2 < 0$, its contradictory for both $\tilde{O}_w(P_t, \rho)$ and $\tilde{O}_z(P_t, \rho)$.

Case V: $\mu_1, \mu_2 = 0, \mu_3 \neq 0$, from (5.77) $\Rightarrow P_t = 0$, which is contradictory for both $\tilde{O}_w(P_t, \rho)$ and $\tilde{O}_z(P_t, \rho)$.

Case VI: $\mu_1 = 0, \mu_2, \mu_3 \neq 0$, then for $\tilde{O}_w(P_t, \rho)$, from (5.77) $\Rightarrow \mu_2 < 0$, which is contradictory. For $\tilde{O}_z(P_t, \rho)$, from $i(P_t, \rho) = 0 \Rightarrow P_t = P_{max}$, $h(P_t, \rho_) = 0 \Rightarrow \rho_1 = \frac{b}{P_t s_{n,l}} - \frac{1}{aP_t s_{n,l}} \ln\left(\frac{1}{\frac{E_{th}(1-\Phi)}{\xi}+\Phi} - 1\right)$.

Case VII: $\mu_2 = 0, \mu_1, \mu_3 \neq 0$, for $\tilde{O}_w(P_t, \rho)$, from $i(P_t, \rho)$=0 $\Rightarrow \rho_2$ and for $\tilde{O}_z(P_t, \rho)$, from (5.77) $\Rightarrow \mu_3 < 0$, which is contradictory.

Case VIII: $\mu_1, \mu_2, \mu_3 \neq 0$, for $\tilde{O}_w(P_t, \rho)$, from $i(P_t, \rho) = 0 \Rightarrow P_t$, $g(P_t, \rho) = 0 \Rightarrow \rho_2$ and $h(P_t, \rho) = 0 \Rightarrow \rho_1$. For $\tilde{O}_z(P_t, \rho)$, from $i(P_t, \rho) = 0 \Rightarrow P_t$ and $g(P_t, \rho) = 0 \Rightarrow \rho_2 = 1 - (2^{R_{th}} - 1)\frac{N_o}{P_t s_{n,l}}$ and from $h(P_t, \rho) = 0 \Rightarrow \rho_1$.

Based on the above-mentioned findings, the optimal values of P_t^* and ρ^* are, respectively, given by (4.25).

Appendix C

Closed-form Solution for Relay Link

C.1 Approximate Closed-form Solution of R_1 and R_2

The approximate closed-form solution for R_1 is obtained as

$$\begin{aligned} R_1 &= \int_0^K f_{|h_3|^2}(x)\,dx \int_{N/L}^{N/M} f_{|h_2|^2}(z) \int_{N/z}^{C} f_{|h_1|^2}(y)\,dy\,dz \\ &\quad + \int_0^K f_{|h_3|^2}(x)\,dx \int_L^M f_{|h_1|^2}(y)\,dy \int_{N/L}^{\infty} f_{|h_2|^2}(z)\,dz. \\ &= F_{|h_3|^2}(K) \left[\left(F_{|h_1|^2}(M) - F_{|h_1|^2}(L)\right) \left(1 - F_{|h_2|^2}\left(\frac{N}{L}\right)\right)\right] \\ &\quad + F_{|h_3|^2}(K)\, R_3, \end{aligned} \tag{C.1}$$

where

$$\begin{aligned} R_3 &= \int_{N/L}^{N/M} f_{|h_2|^2}(z) \left[F_{|h_1|^2}(M) - F_{|h_1|^2}\left(\frac{N}{z}\right)\right] dz \\ &= F_{|h_1|^2}(M) \left[F_{|h_2|^2}\left(\frac{N}{L}\right) - F_{|h_2|^2}\left(\frac{N}{M}\right)\right] - R_4. \end{aligned} \tag{C.2}$$

The integral R_4 is

$$R_4 = \int_{N/L}^{N/M} f_{|h_2|^2}(z)\, F_{|h_1|^2}\left(\frac{N}{z}\right) dz. \tag{C.3}$$

Using Gaussian–Chebyshev quadrature (GCQ) [134],

$$R_4 = \frac{\frac{N}{L}+\frac{N}{M}}{2} \sum_{g=1}^{G} \frac{\pi}{G} \left(1-\phi_g^2\right) f_{|h_2|^2}(z_1) F_{|h_1|^2}\left(\frac{N}{z_1}\right) + D_G, \tag{C.4}$$

where $\phi_g = \cos\left(\frac{2g-1}{2G}\pi\right)$, $z_1 = \frac{\frac{N}{L}-\frac{N}{M}}{2}\phi_g + \frac{\frac{N}{L}+\frac{N}{M}}{2}$, G is the accuracy–complexity factor, and D_G is the negligible remainder. The final expression for R_1 is given in (6.30).

Similarly, R_2 is expressed as

$$\begin{aligned} R_2 &= \int_O^\infty f_{|h_1|^2}(y)\, dy \int_K^\infty f_{|h_3|^2}(x) \int_{M/(Kx)}^\infty f_{|h_1|^2}(z)\, dz\, dx \\ &\quad + \int_O^\infty f_{|h_1|^2}(y)\, dy \int_M^\infty f_{|h_1|^2}(z)\, dz \int_0^K f_{|h_3|^2}(x)\, dx. \\ &= \left(1 - F_{|h_2|^2}(O)\right) \left[I_5 + \left(1 - F_{|h_1|^2}(M)\right) F_{|h_3|^2}(K)\right], \end{aligned} \tag{C.5}$$

where

$$\begin{aligned} R_5 &= \int_K^\infty f_{|h_3|^2}(x) \left[1 - \int_0^{M/(Kx)} f_{|h_1|^2}(y)\, dy\right] dx \\ &= 1 - F_{|h_3|^2}(K) + R_6. \end{aligned} \tag{C.6}$$

The term R_6 is

$$R_6 = \int_0^K f_{|h_3|^2}(x)\, F_{|h_1|^2}\left(\frac{M}{Kx}\right) dx. \tag{C.7}$$

Substituting $x = Ky$,

$$R_6 = K \int_0^1 f_{|h_3|^2}(Ky)\, F_{|h_1|^2}(My)\, dy. \tag{C.8}$$

Using GCQ,

$$R_6 = K \sum_{c=1}^{C} \frac{\pi}{2C} \left(1-\phi_c^2\right) f_{|h_3|^2}(Kz_2) F_{|h_1|^2}(Mz_2) + D_C, \tag{C.9}$$

where $\phi_c = \cos\left(\frac{2c-1}{2C}\pi\right)$ and $z_2 = \frac{\phi+1}{2}$. The final expression for R_2 is given in (6.31).

C.2 Closed-form Solution for Relay Link for $P1$

First, we find the optimized value of P_s. Since the constraints (C1), (C2) and (C4) are piecewise-linear functions, we will consider the linear and saturation regions and find the upper and lower limits of P_s.

For (C1) $\gamma_d \geq \gamma_{th}^d$,

$$\text{Linear: } P_s \geq \frac{\gamma_{th}^d}{\delta AB};\ \forall \frac{P_{min}}{A} \leq P_s \leq \frac{P_{max}}{A}. \tag{C.10}$$

For (C2) $\gamma_u \geq \gamma_{th}^u$,

$$\text{Sat: } P_s \geq \frac{\delta P_{max}|h_3|^2\gamma_{th}^u}{(-\delta+2)A};\ \forall P_s > \frac{P_{max}}{A}. \tag{C.11}$$

For (C4) $P_r \geq P_{th}$,

$$\text{Linear: } P_s \geq \frac{P_{th}}{\delta A};\ \forall \frac{P_{min}}{A} \leq P_s \leq \frac{P_{max}}{A}, \tag{C.12}$$

where $A = d_u^{-\sigma(\phi_u)}|h_1|^2$ and $B = \frac{\delta d_d^{-\sigma(\phi_d)}|h_2|^2}{\sigma_d^2}$. Combining (C.10), (C.11) and (C.12)

makes lower limit of P_s and upper limit by (C6) given as

$$\check{P}_s = \max\left(\frac{\gamma_{th}^d}{\delta AB}, \frac{\delta P_{max}|h_3|^2\gamma_{th}^u}{(-\delta+2)A}, \frac{P_{th}}{\delta A}\right),\ \hat{P}_s = P_T. \tag{C.13}$$

Our aim is to maximize the relay SNR, which is made possible by selecting the upper limit and hence for both the regions, i.e., linear and saturation, the optimized value is

$$P_{s,lin} = P_{s,sat} = P_T. \tag{C.14}$$

As the optimized value is not dependent on δ, we use this value to find optimized δ in the respective region of operation.

Following the same procedure by taking constraints (C1), (C2), (C4) and (C5), for the linear region we find the respective lower and upper bounds as

$$\check{\delta}_{lin} = \max\left(\frac{\gamma_{th}^d}{P_{s,lin}AB}, \frac{P_{th}}{P_{s,lin}A}, 1\right), \tag{C.15}$$

$$\hat{\delta}_{lin} = \min\left(\frac{2}{1+\gamma_{th}^u|h_3|^2}, 2\right). \tag{C.16}$$

Similarly for the saturation region, the lower and upper bounds are respectively written as follows

$$\check{\delta}_{sat} = \max\left(\frac{\gamma_{th}^d}{P_{max}B}, \frac{P_{th}}{P_{max}}, 1\right), \tag{C.17}$$

$$\hat{\delta}_{sat} = \min\left(\frac{2AP_{s,sat}}{AP_{s,sat}+\gamma_{th}^u|h_3|^2P_{max}}, 2\right). \tag{C.18}$$

Since, maximizing the objective relay SNR (γ_d) requires higher δ value in both the regions and selecting $\delta = 2$ tend the make BS-Relay link towards an outage. Thus,

the corresponding optimized values are given by

$$\delta_{lin} = \frac{2}{1+\gamma_{th}^{u}|h_3|^2};\ \delta_{sat} = \frac{2AP_{s,sat}}{AP_{s,sat}+\gamma_{th}^{u}|h_3|^2 P_{max}}. \tag{C.19}$$

Bibliography

[1] P. S. Bithas, A. G. Kanatas, D. B. da Costa, P. K. Upadhyay, and U. S. Dias, "On the double-generalized gamma statistics and their application to the performance analysis of V2V communications," *IEEE Trans. Commun.*, vol. 66, no. 1, pp. 448–460, May. 2018.

[2] V. K. Chapala, A. Malik, and S. M. Zafaruddin, "RIS-assisted vehicular network with direct transmission over double-generalized gamma fading channels," in *proc.IEEE Veh. Technol. Conf. (VTC2022-Spring)*, 2022, pp. 1–6.

[3] M. Aldababsa, A. M. Salhab, A. A. Nasir, M. H. Samuh, and D. B. da Costa, "Multiple RISs-aided networks: Performance analysis and optimization," *IEEE Trans. Veh. Technol.*, vol. 72, no. 6, pp. 7545–7559, Jun. 2023.

[4] V. K. Chapala and S. M. Zafaruddin, "Multiple RIS-assisted mixed FSO-RF transmission over generalized fading channels," *IEEE Syst. J.*, vol. 17, no. 3, pp. 3515–3526, 2023.

[5] D. T. Tam, N. V. Vinh, and B. C. Nguyen, "Improving the performance of multi-IRS aided millimeter-wave communication systems by transmit antenna selection," *Elsevier Phys. Commun.*, vol. 56, p. 101957, 2023.

[6] H. Ren, K. Wang, and C. Pan, "Intelligent reflecting surface-aided URLLC

in a factory automation scenario," *IEEE Trans. Commun.*, vol. 70, no. 1, pp. 707–723, 2022.

[7] S. Kosu, M. Babaei, S. Ö. Ata, L. Durak-Ata, and H. Yanikomeroglu, "Linear/non-linear energy harvesting models via multi-antenna relay cooperation in V2V communications," *IEEE Trans. Green Commun. Netw.*, vol. 7, no. 4, pp. 1725–1738, 2023.

[8] N. Mensi and D. B. Rawat, "Reconfigurable intelligent surface selection for wireless vehicular communications," *IEEE Wirel. Commun. Lett.*, vol. 11, no. 8, pp. 1743–1747, 2022.

[9] D. L. Galappaththige, D. Kudathanthirige, and G. Amarasuriya, "Performance analysis of distributed intelligent reflective surface aided communications," in *proc. IEEE Global Commun. Conf. (GLOBECOM)*, 2020, pp. 1–6.

[10] M. H. N. Shaikh, K. Rabie, X. Li, T. Tsiftsis, and G. Nauryzbayev, "On the performance of dual RIS-assisted V2I communication under Nakagami-m fading," in *proc. IEEE Veh. Technol. Conf. (VTC2022-Fall)*, 2022, pp. 1–5.

[11] M. Chen, A. Liu, N. N. Xiong, Y. Ren, and H. H. Song, "ANNS: An intelligent advanced non-convex non-smooth scheme for IRS-aided next generation mobile communication networks," *IEEE Trans. Mob. Comput.*, vol. 24, no. 9, pp. 8959–8973, 2025.

[12] M. Chen, H. Xie, X. Wang, W. Xiao, A. Farouk, Z. Liu, M. Chen, and H. H. Song, "Holographic counterpart computation offloading via reconfigurable intelligent surfaces in VEC consumer electronics," *IEEE Trans. Consumer Electronics*, vol. 71, no. 2, pp. 5275–5286, 2025.

[13] L. Yang, Y. Yang, D. B. d. Costa, and I. Trigui, "Outage probability and capacity scaling law of multiple RIS-aided networks," *IEEE Wirel. Commun. Lett.*, vol. 10, no. 2, pp. 256–260, Feb. 2021.

[14] K. Yu, X. Yu, and J. Cai, "UAVs assisted intelligent reflecting surfaces SWIPT system with statistical CSI," *IEEE J. Sel. Top. Signal Process.*, vol. 15, no. 5, pp. 1095–1109, 2021.

[15] L. Yang, J. Chen, M. O. Hasna, and H.-C. Yang, "Outage performance of UAV-assisted relaying systems with RF energy harvesting," *IEEE Commun. Lett.*, vol. 22, no. 12, pp. 2471–2474, 2018.

[16] S. Gautam, T. X. Vu, S. Chatzinotas, and B. Ottersten, "Cache-aided simultaneous wireless information and power transfer (SWIPT) with relay selection," *IEEE J. Sel. Areas Commun.*, vol. 37, no. 1, pp. 187–201, 2019.

[17] P. K. Singh, S. K. Nandi, and S. Nandi, "A tutorial survey on vehicular communication state of the art, and future research directions," *Elsevier Veh. Commun.*, vol. 18, p. 100164, Aug. 2019.

[18] Z. Peng, Z. Zhang, C. Pan, L. Li, and A. L. Swindlehurst, "Multiuser full-duplex two-way communications via intelligent reflecting surface," *IEEE Trans. Signal Process.*, vol. 69, pp. 837–851, 2021.

[19] N. Sharma, S. Gautam, S. Chatzinotas, and B. Ottersten, "Integrating multiple RIS for enhanced SWIPT-IoT performance: Optimization strategies," *IEEE Access*, vol. 12, pp. 182 841–182 855, 2024.

[20] J. Jose, S. Bisen, P. Shaik, S. Biswas, K. Singh, O. Krejcar, and V. Bhatia, "Performance analysis of IRS assisted full-duplex systems with different down-

link and uplink users," *IEEE Trans. Veh. Technol.*, vol. 73, no. 10, pp. 15 848–15 853, 2024.

[21] T. Wang, G. Chen, and J. P. Coon, "Performance analysis of RIS-assisted full-duplex communication over correlated Nakagami-m fading channel," *IEEE Trans. Veh. Technol.*, vol. 73, no. 3, pp. 3430–3444, 2024.

[22] A. M. Tota Khel and K. A. Hamdi, "Performance analysis of IRS-assisted full-duplex wireless communication systems with interference," *IEEE Commun. Lett.*, vol. 26, no. 9, pp. 2027–2031, 2022.

[23] Y. Zhang, J. Zhang, M. D. Renzo, H. Xiao, and B. Ai, "Performance analysis of RIS-aided systems with practical phase shift and amplitude response," *IEEE Trans. Veh. Technol.*, vol. 70, no. 5, pp. 4501–4511, 2021.

[24] D. K. P. Asiedu and J.-H. Yun, "Full-duplex multiuser wireless information and power transfer with a multistage nonlinear rectifier energy harvesting model," *IEEE Wirel. Commun. Lett.*, vol. 13, no. 1, pp. 183–187, 2024.

[25] K. Hirashima and T. Miyajima, "Sum rate maximization for multiuser full-duplex wireless powered communication networks," *IEICE Trans. Commun.*, vol. E107-B, no. 8, pp. 564–572, 2024.

[26] S. K. Singh, K. Agrawal, K. Singh, S. Prakriya, and C.-P. Li, "SWIPT for battery-assisted full-duplex relaying networks with finite blocklength codes," *IEEE Trans. Commun.*, vol. 73, no. 5, pp. 3013–3030, 2025.

[27] S. Zhang, Q. Ma, H. Cheng, and R. Song, "Achievable rate optimization of RIS-assisted multi-antenna FD DF relay cooperation system with SWIPT technology," *IEEE Trans. Netw. Sci. Eng.*, vol. 12, no. 3, pp. 2243–2253, 2025.

[28] T. Wang, G. Chen, and J. P. Coon, "Performance analysis of RIS-assisted full-duplex communication over correlated nakagami-m fading channel," *IEEE Trans. Veh. Technol.*, vol. 73, no. 3, pp. 3430–3444, 2024.

[29] L. Kong, J. He, Y. Ai, S. Chatzinotas, and B. Ottersten, "Channel modeling and analysis of reconfigurable intelligent surfaces assisted vehicular networks," in *proc. IEEE Int. Conf. Commun. Workshops (ICC)*, 2021, pp. 1–6.

[30] E. Basar, M. Di Renzo, J. De Rosny, M. Debbah, M.-S. Alouini, and R. Zhang, "Wireless communications through reconfigurable intelligent surfaces," *IEEE Access*, vol. 7, pp. 116 753–116 773, Aug. 2019.

[31] M. Di Renzo, K. Ntontin, J. Song, F. H. Danufane, X. Qian, F. Lazarakis, J. De Rosny, D.-T. Phan-Huy, O. Simeone, R. Zhang, M. Debbah, G. Lerosey, M. Fink, S. Tretyakov, and S. Shamai, "Reconfigurable intelligent surfaces vs. relaying: Differences, similarities, and performance comparison," *IEEE Open J. Commun. Soc.*, vol. 1, pp. 798–807, Jun. 2020.

[32] R. Alghamdi, R. Alhadrami, D. Alhothali, H. Almorad, A. Faisal, S. Helal, R. Shalabi, R. Asfour, N. Hammad, A. Shams, N. Saeed, H. Dahrouj, T. Y. Al-Naffouri, and M.-S. Alouini, "Intelligent surfaces for 6G wireless networks: A survey of optimization and performance analysis techniques," *IEEE Access*, vol. 8, pp. 202 795–202 818, 2020.

[33] C. Pan, G. Zhou, K. Zhi, S. Hong, T. Wu, Y. Pan, H. Ren, M. D. Renzo, A. Lee Swindlehurst, R. Zhang, and A. Y. Zhang, "An overview of signal processing techniques for RIS/IRS-aided wireless systems," *IEEE J. Sel. Top. Signal Process.*, vol. 16, no. 5, pp. 883–917, 2022.

[34] S. Gong, X. Lu, D. T. Hoang, D. Niyato, L. Shu, D. I. Kim, and Y.-C. Liang, "Toward smart wireless communications via intelligent reflecting surfaces: A contemporary survey," *IEEE Commun. Surv. Tutor.*, vol. 22, no. 4, pp. 2283–2314, 2020.

[35] Q. Wu, S. Zhang, B. Zheng, C. You, and R. Zhang, "Intelligent reflecting surface-aided wireless communications: A tutorial," *IEEE Trans. Commun.*, vol. 69, no. 5, pp. 3313–3351, May. 2021.

[36] K. Zhi, C. Pan, H. Ren, K. K. Chai, and M. Elkashlan, "Active RIS versus passive RIS: Which is superior with the same power budget?" *IEEE Commun. Lett.*, vol. 26, no. 5, pp. 1150–1154, 2022.

[37] I. Yildirim, A. Uyrus, and E. Basar, "Modeling and analysis of reconfigurable intelligent surfaces for indoor and outdoor applications in future wireless networks," *IEEE Trans. Commun.*, vol. 69, no. 2, pp. 1290–1301, Feb. 2021.

[38] H. Du, J. Zhang, J. Cheng, and B. Ai, "Millimeter wave communications with reconfigurable intelligent surfaces: Performance analysis and optimization," *IEEE Trans. Commun.*, vol. 69, no. 4, pp. 2752–2768, Apr.. 2021.

[39] Y. Zhu, B. Mao, Y. Kawamoto, and N. Kato, "Intelligent reflecting surface-aided vehicular networks toward 6G: Vision, proposal, and future directions," *IEEE Veh. Technol. Mag.*, vol. 16, no. 4, pp. 48–56, Dec. 2021.

[40] Z. Huang, B. Zheng, and R. Zhang, "Roadside IRS-aided vehicular communication: Efficient channel estimation and low-complexity beamforming design," *IEEE Trans. Wirel. Commun.*, vol. 22, no. 9, pp. 5976–5989, Sep. 2023.

[41] J. Wang, W. Zhang, X. Bao, T. Song, and C. Pan, "Outage analysis for intelligent reflecting surface assisted vehicular communication networks," in *proc. 2020 IEEE Glob. Commun. Conf.*, 2020, pp. 1–6.

[42] A. U. Makarfi, K. M. Rabie, O. Kaiwartya, X. Li, and R. Kharel, "Physical layer security in vehicular networks with reconfigurable intelligent surfaces," in *proc. IEEE Veh. Technol. Conf. (VTC2020-Spring)*, 2020, pp. 1–6.

[43] E. Björnson, Özdogan, and E. G. Larsson, "Intelligent reflecting surface versus decode-and-forward: How large surfaces are needed to beat relaying?" *IEEE Wirel. Commun. Lett.*, vol. 9, no. 2, pp. 244–248, Feb. 2020.

[44] Y. Chen, Y. Wang, J. Zhang, and Z. Li, "Resource allocation for intelligent reflecting surface aided vehicular communications," *IEEE Trans. Veh. Technol.*, vol. 69, no. 10, pp. 12 321–12 326, Oct. 2020.

[45] S. Solanki, S. Gautam, S. K. Sharma, and S. Chatzinotas, "Ambient backscatter assisted co-existence in aerial-IRS wireless networks," *IEEE Open J. Commun. Soc.*, vol. 3, pp. 608–621, Mar. 2022.

[46] C. D. Ho, T.-V. Nguyen, T. Huynh-The, T.-T. Nguyen, D. B. da Costa, and B. An, "Short-packet communications in wireless-powered cognitive IoT networks: Performance analysis and deep learning evaluation," *IEEE Trans. Veh. Technol.*, vol. 70, no. 3, pp. 2894–2899, Mar. 2021.

[47] B. Sagir, E. Aydin, and H. Ilhan, "Deep-learning-assisted IoT-based RIS for cooperative communications," *IEEE Internet Things J.*, vol. 10, no. 12, pp. 10 471–10 483, Jun. 2023.

[48] W. Song, S. Rajak, S. Dang, R. Liu, J. Li, and S. Chinnadurai, "Deep learning enabled IRS for 6G intelligent transportation systems: A comprehensive study," *IEEE Trans. Intell. Transp. Syst.*, vol. 24, no. 11, pp. 12 973–12 990, Nov. 2023.

[49] X. Chen, S. Leng, J. He, and L. Zhou, "Deep-learning-based intelligent intervehicle distance control for 6G-enabled cooperative autonomous driving," *IEEE Internet Things J.*, vol. 8, no. 20, pp. 15 180–15 190, Oct. 2021.

[50] C. Zhang, Y. Huang, C. He, C. Pan, and K. Wang, "Energy optimization for IRS-aided SWIPT under imperfect cascaded channels," *IEEE Trans. Veh. Technol.*, vol. 72, no. 9, pp. 11 631–11 643, 2023.

[51] N. Sharma, S. Gautam, S. Chatzinotas, and B. Ottersten, "Fractional programming based optimization techniques for RIS-assisted SWIPT-IoT system," *IEEE Commun. Lett.*, vol. 28, no. 12, pp. 2819–2823, 2024.

[52] N. Sharma, S. Gautam, S. Chatzinotas, and B. Ottersten, "Integrating multiple RIS for enhanced SWIPT-IoT performance: Optimization strategies," *IEEE Access*, vol. 12, pp. 182 841–182 855, 2024.

[53] A. Khalili, S. Zargari, Q. Wu, D. W. K. Ng, and R. Zhang, "Multi-objective resource allocation for IRS-aided SWIPT," *IEEE Wirel. Commun. Lett.*, vol. 10, no. 6, pp. 1324–1328, 2021.

[54] A. Mohamed, A. Zappone, and M. Di Renzo, "Bi-objective optimization of information rate and harvested power in RIS-aided SWIPT systems," *IEEE Wirel. Commun. Lett.*, vol. 11, no. 10, pp. 2195–2199, 2022.

[55] A. Magbool, V. Kumar, A. Bazzi, M. F. Flanagan, and M. Chafii, "Multi-functional RIS for a multi-functional system: Integrating sensing, communication, and wireless power transfer," *IEEE Net.*, vol. 39, no. 1, pp. 71–79, 2025.

[56] D. Han, P. Wang, W. Ni, W. Wang, A. Zheng, D. Niyato, and N. Al-Dhahir, "Multi-functional RIS integrated sensing and communications for 6G networks," *IEEE Trans. Wirel. Commun.*, vol. 24, no. 2, pp. 1146–1161, 2025.

[57] P. Mukherjee, C. Psomas, H. A. Suraweera, and I. Krikidis, "Chaotic noncoherent SWIPT in multi-functional RIS-aided systems," 2025. [Online]. Available: https://arxiv.org/abs/2506.01051

[58] C. K. Singh, P. K. Upadhyay, J. Lehtomäki, and M. Juntti, "Performance analysis with deep learning assay for cooperative UAV-borne IRS NOMA networks under non-ideal system imperfections," *IEEE Trans. Veh. Technol.*, vol. 73, no. 1, pp. 1065–1083, 2024.

[59] S. M. Alqaraghuli, O. Karan, "Using deep learning technology based energy-saving for software defined wireless sensor networks (SDWSN) framework ," *Babylon. J. Artif. Intell.*, vol. 2024, p. 34–45, Apr. 2024.

[60] W. M. S. Abed, G. Al-Kateb, H. Alkattan, "DPON: A novel deep learning framework for efficient image processing," *Babylon. J. Mach. Learn.*, vol. 2025, p. 126–140, Aug. 2025.

[61] M. Burhanuddin, "Efficient hardware acceleration techniques for deep learning on edge devices: A comprehensive performance analysis," *Khwarizmia*, vol. 2023, p. 103–112, 2023.

[62] S.S. Qasim , S.H. Oleiwi, "Advancing arabic handwritten digit recognition with AI-enhanced neural network architectures," *Babylon. J. Artif. Intell.*, vol. 2024, p. 146–157, Nov. 2024.

[63] N.A. Lafta, "A comprehensive analysis of keras: Enhancing deep learning applications in network engineering," *Babylon. J. Artif. Intell.*, vol. 2023, p. 94–100, Nov. 2023.

[64] M. Shujairi, "Developing IoT performance in healthcare through the integration of machine learning and software-defined networking (SDN)," *Babylon. J. Internet Things*, vol. 2025, p. 77–88, Feb. 2025.

[65] I. Rasheed, "Dynamic mode selection and resource allocation approach for 5G-vehicle-to-everything (V2X) communication using asynchronous federated deep reinforcement learning method," *Elsevier Veh. Commun.*, vol. 38, p. 100532, 2022.

[66] S. Gautam, E. Lagunas, S. Chatzinotas, and B. Ottersten, "Relay selection and resource allocation for SWIPT in multi-user OFDMA systems," *IEEE Wirel. Commun. Lett.*, vol. 18, no. 5, pp. 2493–2508, 2019.

[67] S. Ghosh, A. Bhowmick, S. D. Roy, and S. Kundu, "UAV-RIS enabled NOMA network for disaster management with hardware impairments," *IEEE Trans. Aerosp. Electron. Syst.*, vol. 60, no. 6, pp. 7995–8009, 2024.

[68] O. S. Badarneh, M. K. Awad, S. Muhaidat, and F. S. Almehmadi, "Performance analysis of intelligent reflecting surface-aided decode-and-forward UAV communication systems," *IEEE Syst. J.*, vol. 17, no. 1, pp. 246–257, 2023.

[69] N. Vishwakarma, R. Swaminathan, P. D. Diamantoulakis, and G. K. Karagiannidis, "Cascaded FSO systems with optical reflecting surfaces," *IEEE Internet Things J.*, pp. 1–1, 2024.

[70] A. Singh, S. Redhu, B. Beferull-Lozano, and R. M. Hegde, "Network-aware RF-energy harvesting for designing energy efficient IoT networks," *Elsevier Internet Things*, vol. 22, p. 100770, 2023.

[71] H. Hashida, Y. Kawamoto, and N. Kato, "Intelligent reflecting surface placement optimization in air-ground communication networks toward 6G," *IEEE Wirel. Commun.*, vol. 27, no. 6, pp. 146–151, 2020.

[72] Lu, Weidang and Ding, Yu and Gao, Yuan and Chen, Yunfei and Zhao, Nan and Ding, Zhiguo and Nallanathan, Arumugam, "Secure NOMA-based UAV-MEC network towards a flying eavesdropper," *IEEE Trans. Commun.*, vol. 70, no. 5, pp. 3364–3376, 2022.

[73] Ding, Yu and Feng, Yunqi and Lu, Weidang and Zheng, Shilian and Zhao, Nan and Meng, Limin and Nallanathan, Arumugam and Yang, Xiaoniu, "Online edge learning offloading and resource management for UAV-assisted MEC secure communications," *IEEE J. Sel. Top. Signal Process.*, vol. 17, no. 1, pp. 54–65, 2023.

[74] L. Zhi, N. Hehao, H. Yuanzhi, A. Kang, Z. Xudong, C. Zheng, and X. Pei, "Self-powered absorptive reconfigurable intelligent surfaces for securing satellite-terrestrial integrated networks," *China Commun.*, vol. 21, no. 9, pp. 276–291, 2024.

[75] Z. Lin, H. Niu, K. An, Y. Wang, G. Zheng, S. Chatzinotas, and Y. Hu, "Refract-

ing RIS-aided hybrid satellite-terrestrial relay networks: Joint beamforming design and optimization," *IEEE Trans. Aerosp. Electron. Syst.*, vol. 58, no. 4, pp. 3717–3724, 2022.

[76] Z. Lin, M. Guo, C. Han, Y. Sun, R. Ma, K. An, Y. He, and N. Al-Dhahir, "Wireless endogenous security for SAGINs: Achieving ubiquitous access and secure communication in symbiosis," *IEEE Netw.*, vol. 39, no. 6, pp. 155–163, 2025.

[77] Z. Lin, M. Lin, T. de Cola, J.-B. Wang, W.-P. Zhu, and J. Cheng, "Supporting IoT with rate-splitting multiple access in satellite and aerial-integrated networks," *IEEE Internet Things J.*, vol. 8, no. 14, pp. 11 123–11 134, 2021.

[78] N. Ashraf, S. A. Sheikh, and S. A. Khan, "Performance analysis of SWIPT assisted cooperative internet of things (IoT) network under optimal and adaptive power splitting schemes," *Elsevier Internet Things*, vol. 20, p. 100630, 2022.

[79] M. A. Aboulhassan, A. H. A. El-Malek, A. M. Salhab, and S. A. Zummo, "Performance analysis and path-planning for self-energized UAV-assisted relay networks," *IEEE Trans. Aerosp. Electron. Syst.*, vol. 60, no. 1, pp. 907–917, 2024.

[80] B. Fang, X. Chen, and B. Huang, "Computational rate maximization for SWIPT-based mobile edge computing with alternative optimization algorithm," *Elsevier Internet Things*, vol. 22, p. 100826, 2023.

[81] Y. Chen, X. Shen, P. Zhang, S. Lu, L. Wang, Z. Wu, and X. Xie, "Joint optimization of UAV-WPT and mixed task offloading strategies with shared mode

in SAG-PIoT: A MAD4PG approach," *Elsevier Internet Things*, vol. 24, p. 100970, 2023.

[82] Q. Li, P. Si, Y. Zhang, J. Wang, D. Zhang, and F. R. Yu, "UAV altitude, relay selection, and user association optimization for cooperative relay-transmission in UAV-IRS-based THz networks," *IEEE Trans. Green Commun. Netw.*, vol. 8, no. 2, pp. 815–826, 2024.

[83] Z. Su, W. Feng, J. Tang, Z. Chen, Y. Fu, N. Zhao, and K.-K. Wong, "Energy-efficiency optimization for D2D communications underlaying UAV-assisted industrial IoT networks with SWIPT," *IEEE Internet Things J.*, vol. 10, no. 3, pp. 1990–2002, 2023.

[84] Y. Liu, F. Han, and S. Zhao, "Flexible and reliable multiuser SWIPT IoT network enhanced by UAV-mounted intelligent reflecting surface," *IEEE Trans. Reliab.*, vol. 71, no. 2, pp. 1092–1103, 2022.

[85] D. Kumar, P. K. Singya, O. Krejcar, and V. Bhatia, "On performance of a SWIPT enabled FD CRN with HIs and imperfect SIC over α–μ fading channel," *IEEE Trans. Cogn. Commun. Netw.*, vol. 9, no. 1, pp. 99–113, 2023.

[86] S. Wang, L. Gao, Z. Zhao, J. Dai, W. Xu, W. Xu, and K. Niu, "RIS-assisted two-way full-duplex 6G IoT communication: A unified framework for modeling and analysis over fading channels," *IEEE Internet Things J.*, vol. 13, no. 1, pp. 1554–1568, 2026.

[87] W. Mei, B. Zheng, C. You, and R. Zhang, "Intelligent reflecting surface-aided wireless networks: From single-reflection to multireflection design and optimization," *Proc. IEEE*, vol. 110, no. 9, pp. 1380–1400, 2022.

[88] Q. Wu and R. Zhang, "Intelligent reflecting surface enhanced wireless network via joint active and passive beamforming," *IEEE Trans. Wirel. Commun.*, vol. 18, no. 11, pp. 5394–5409, 2019.

[89] Q. Wu and R. Zhang, "Beamforming optimization for wireless network aided by intelligent reflecting surface with discrete phase shifts," *IEEE Trans. Commun.*, vol. 68, no. 3, pp. 1838–1851, 2020.

[90] E. Basar, "Reconfigurable intelligent surfaces for doppler effect and multipath fading mitigation," *Frontiers in Communications and Networks*, vol. 2, May. 2021.

[91] J. Andersen, "Statistical distributions in mobile communications using multiple scattering," *Proc. 27th URSI Gen. Assembly*, pp. 1–4, Jan. 2002.

[92] J. Salo, H. El-Sallabi, and P. Vainikainen, "Impact of double-Rayleigh fading on system performance," in *proc. 2006 International Symposium on Wireless Pervasive Computing*, 2006, p. pp. 5.

[93] G. K. Karagiannidis, N. C. Sagias, and P. T. Mathiopoulos, "$N*$Nakagami: A novel stochastic model for cascaded fading channels," *IEEE Trans. Commun.*, vol. 55, no. 8, pp. 1453–1458, Aug. 2007.

[94] B. Ashrafzadeh, E. Soleimani-Nasab, M. Kamandar, and M. Uysal, "A framework on the performance analysis of dual-hop mixed FSO-RF cooperative systems," *IEEE Trans. Commun.*, vol. 67, no. 7, pp. 4939–4954, Jul. 2019.

[95] T. N. Do, G. Kaddoum, T. L. Nguyen, D. B. da Costa, and Z. J. Haas, "Multi-RIS-aided wireless systems: statistical characterization and performance analysis," *IEEE Trans. Commun.*, vol. 69, no. 12, pp. 8641–8658, Dec. 2021.

[96] A. Sikri, A. Mathur, and G. Kaddoum, "Joint impact of phase error, transceiver hardware impairments, and mobile interferers on RIS-aided wireless system over $\kappa - \mu$ fading channels," *IEEE Commun. Lett.*, vol. 26, no. 10, pp. 2312–2316, 2022.

[97] L. Han, X. Liu, Y. Wang, and B. Li, "Joint impact of channel estimation errors and pointing errors on fso communication systems over $\mathcal{F}$ turbulence channe," *J. Light. Technol.*, vol. 40, no. 14, pp. 4555–4561, 2022.

[98] S. Uniyal, N. Vishwakarma, and R. Swaminathan, "Multihop IRS-assisted free space optics communication with DF relaying: A performance analysis," *Appl. Opt.*, vol. 62, no. 18, pp. 4716–4726, Jun. 2023.

[99] S. Li, S. Yan, L. Bariah, S. Muhaidat, and A. Wang, "IRS-assisted full duplex systems over Rician and Nakagami fading channels," *IEEE Open J. Veh. Technol.*, vol. 4, pp. 217–229, Jan. 2023.

[100] D.-A. Clevert, T. Unterthiner, and S. Hochreiter, "Fast and accurate deep network learning by exponential linear units (ELUs)," 2016. [Online]. Available: https://arxiv.org/abs/1511.07289

[101] C. Nwankpa, W. Ijomah, A. Gachagan, and S. Marshall, "Activation functions: comparison of trends in practice and research for deep learning," in *proc. Int. Conf. Comput. Sci. Technol. (INCCST 20)*, 2020, pp. 124–133.

[102] T. Dozat, "Incorporating nesterov momentum into adam," in *proc. Int. Conf. Learn. Represent. (ICLR)*, 2016, pp. 1–4.

[103] R. Swaminathan, R. Roy, and M. D. Selvaraj, "Performance comparison of selection combining with full CSI and switch-and-examine combining with and

without post-selection," *IEEE Trans. Veh. Technol.*, vol. 65, no. 5, pp. 3217–3230, May 2016.

[104] G. Singh, A. Srivastava, V. A. Bohara, M. Noor-A-Rahim, Z. Liu, and D. Pesch, "Toward 6G-V2X: Aggregated RF-VLC for ultra-reliable and low-latency autonomous driving," *IEEE Commun. Mag.*, vol. 8, no. 4, pp. 80–87, 2024.

[105] B. P. Nayak, L. Hota, A. Kumar, A. K. Turuk, and P. H. J. Chong, "Autonomous vehicles: Resource allocation, security, and data privacy," *IEEE Trans. Green Commun. Netw.*, vol. 6, no. 1, pp. 117–131, 2022.

[106] E. Boshkovska, D. W. K. Ng, N. Zlatanov, and R. Schober, "Practical non-linear energy harvesting model and resource allocation for SWIPT systems," *IEEE Commun. Lett.*, vol. 19, no. 12, pp. 2082–2085, 2015.

[107] S. Boyd and L. Vandenberghe, *Convex optimization*. Cambridge university press, 2004.

[108] S. Gautam and P. Ubaidulla, "Relay selection and transceiver design for joint wireless information and energy transfer in cooperative networks," in *proc. IEEE Veh. Technol. Conf. (VTC2017-Spring)*, 2017, pp. 1–5.

[109] T. M. Inc., "Matlab version: 9.13.0 (r2022b)," Natick, Massachusetts, United States, 2022. [Online]. Available: https://www.mathworks.com

[110] A. Saif, K. Dimyati, K. A. Noordin, N. A. Mosali, D. GC, and S. H. Alsamhi, "Skyward bound: Empowering disaster resilience with multi-UAV-assisted B5G networks for enhanced connectivity and energy efficiency," *Elsevier Internet Things*, vol. 23, p. 100885, 2023.

[111] J. Sharma and P. S. Mehra, "Secure communication in IOT-based UAV networks: A systematic survey," *Elsevier Internet Things*, vol. 23, p. 100883, 2023.

[112] M. Kim and J. Lee, "Outage probability of UAV communications in the presence of interference," in *Proc. IEEE Global Commun. Conf. (GLOBECOM)*, 2018, pp. 1–6.

[113] C. You, Z. Kang, Y. Zeng, and R. Zhang, "Enabling smart reflection in integrated air-ground wireless network: IRS meets UAV," *IEEE Wirel. Commun.*, vol. 28, no. 6, pp. 138–144, 2021.

[114] Q. Wu and R. Zhang, "Towards smart and reconfigurable environment: intelligent reflecting surface aided wireless network," *IEEE Commun. Mag.*, vol. 58, no. 1, pp. 106–112, 2020.

[115] Z. Zhang, L. Dai, X. Chen, C. Liu, F. Yang, R. Schober, and H. V. Poor, "Active RIS vs. passive RIS: Which will prevail in 6G?" *IEEE Trans. Commun.*, vol. 71, no. 3, pp. 1707–1725, 2023.

[116] A. Al-Hourani and K. Gomez, "Modeling cellular-to-UAV path-loss for suburban environments," *IEEE Wirel. Commun. Lett.*, vol. 7, no. 1, pp. 82–85, 2018.

[117] M. M. Azari, F. Rosas, K.-C. Chen, and S. Pollin, "Ultra reliable UAV communication using altitude and cooperation diversity," *IEEE Trans. Commun.*, vol. 66, no. 1, pp. 330–344, 2018.

[118] M. Aldababsa, A. M. Salhab, A. A. Nasir, M. H. Samuh, and D. B. da Costa, "Multiple RISs-aided networks: Performance analysis and optimization," *IEEE Trans. Veh. Technol.*, vol. 72, no. 6, pp. 7545–7559, 2023.

[119] Y. Lee and M.-H. Tsai, "Performance of decode-and-forward cooperative communications over Nakagami- m fading channels," *IEEE Trans. Veh. Techno.*, vol. 58, no. 3, pp. 1218–1228, 2009.

[120] I. S. Gradshteyn and I. M. Ryzhik, *Table of integrals, series, and products*, 7th ed. Amsterdam, Elsevier/Academic Press, 2007.

[121] S. Primak, V. Kontorovich, and V. Lyandres, *Stochastic methods and their applications to communications: Stochastic differential equations approach*. West Sussex, U.K.: John Wiley Sons, Ltd, 2004.

[122] D. Diao, B. Wang, K. Cao, B. Zheng, R. Dong, T. Cheng, and J. Chen, "Reflecting elements analysis for secure and energy-efficient UAV-RIS system with phase errors," *IEEE Wirel. Commun. Lett.*, vol. 13, no. 2, pp. 293–297, 2024.

[123] K. Shen and W. Yu, "Fractional programming for communication systems—part I: power control and beamforming," *IEEE Trans. Signal Process.*, vol. 66, no. 10, pp. 2616–2630, 2018.

[124] M. M. Azari, S. Solanki, S. Chatzinotas, O. Kodheli, H. Sallouha, A. Colpaert, J. F. Mendoza Montoya, S. Pollin, A. Haqiqatnejad, A. Mostaani, E. Lagunas, and B. Ottersten, "Evolution of non-terrestrial networks from 5G to 6G: A survey," *IEEE Commun. Surv. Tutor*, vol. 24, no. 4, pp. 2633–2672, 2022.

[125] M. A. Jamshed, A. Kaushik, M. Toka, W. Shin, M. Z. Shakir, S. P. Dash, and D. Dardari, "Synergizing airborne non-terrestrial networks and reconfigurable intelligent surfaces-aided 6G IoT," *IEEE Internet Things Mag.*, vol. 7, no. 2, pp. 46–52, 2024.

[126] M. D. Yacoub, "The α-μ distribution: A physical fading model for the stacy distribution," *IEEE Trans. Veh. Technol.*, vol. 56, no. 1, pp. 27–34, 2007.

[127] The Wolfram Functions Site, "BesselK-Function," Accessed: Aug. 2025. [Online]. Available: https://functions.wolfram.com/Bessel-TypeFunctions/BesselK/26/02/

[128] The Wolfram Functions Site., "Meijer G-Function," Accessed: Aug. 2025. [Online]. Available: https://functions.wolfram.com/HypergeometricFunctions/MeijerG/

[129] V. Panse and T. K. Jain, "Full-duplex cooperative relaying with non-linear energy harvesting for vehicular communication," *J. Commun. Info. Net.*, vol. 8, no. 4, pp. 369–377, 2023.

[130] S. Boyd and L. Vandenberghe, *Convex optimization*. Cambridge university press, 2004.

[131] S. Abeywickrama, R. Zhang, Q. Wu, and C. Yuen, "Intelligent reflecting surface: Practical phase shift model and beamforming optimization," *IEEE Trans. Commun.*, vol. 68, no. 9, pp. 5849–5863, 2020.

[132] N. Sharma, S. Gautam, S. Chatzinotas, and B. Ottersten, "Fractional programming based optimization techniques for RIS-assisted SWIPT-IoT system," *IEEE Commun. Lett.*, vol. 28, no. 12, pp. 2819–2823, 2024.

[133] T. Shafique, H. Tabassum, and E. Hossain, "Optimization of wireless relaying with flexible UAV-borne reflecting surfaces," *IEEE Trans. Commun.*, vol. 69, no. 1, pp. 309–325, 2021.

[134] M. Abramowitz, *Handbook of Mathematical Functions, With Formulas, Graphs, and Mathematical Tables*. USA: Dover Publications, Inc., 1974.